Corrosion evaluation of Super 13Cr martensitic stainless steel under high temperature and high pressure downhole environments

Zezhou Wen

Submitted in accordance with the requirements for the degree of
Doctor of Philosophy

The University of Leeds
Institute of Functional Surfaces
School of Mechanical Engineering

January 2026

Publication Statement

The candidate confirms that the work submitted is his/her own, except where work which has formed part of jointly-authored publications has been included. The contribution of the candidate and the other authors to this work has been explicitly indicated below. The candidate confirms that appropriate credit has been given within the thesis where reference has been made to the work of others.

In the paper listed below, authorship contribution statement for the involved publication: Zezhou Wen: writing-original draft, validation, methodology, investigation, formal analysis, data curation, conceptualization. Jiong Qian: methodology. Qiang Zhong: methodology. Chun Wang: methodology. Richard Barker: writing-review & editing, supervision. Anne Neville: supervision, funding acquisition, resources. Yong Hua: writing-review & editing, supervision.

Z. Wen, J. Qian, Q. Zhong, C. Wang, R. Barker, A. Neville, Y. Hua. Corrosion and Stress Corrosion Cracking Behaviour of Super 13Cr Martensitic Stainless Steel in CO_2-Saturated High Temperature and High Pressure (HTHP) Downhole Environment. In: *AMPP Annual Conference + Expo*, Paper No. 17559, San Antonio, Texas, USA, March 2022.

Acknowledgements

First of all, I wish to express my highest respect and deepest gratitude to the late Prof. Anne Neville, my former supervisor. My sincere thanks go to Prof. Anne Neville for initiating this special PhD project, which granted me the privilege of conducting research under her guidance during the early stage of my PhD project. Her passion for science, rigorous academic attitude, and professional dedication have left a profound impact on me. And I wish to express my sincere appreciation to my supervisor, Prof. Richard Barker, for his invaluable guidance during the middle and late stages of my PhD project and in the writing of this thesis. I also wish to thank my former supervisor, Dr. Yong Hua, for his supervising during the early stage of my PhD project.

I wish to thank Zhejiang Jiuli Hi-Tech Metals Co., Ltd. for sponsoring this project, and to thank Dr. Jiong Qian and Qiang Zhong from the company for providing test materials and helping in the slow strain rate tensile tests.

My thanks also go to Dr. Joshua Owen for his constructive suggestions during the thesis review process. I'd like to thank to Dr. Xiaoqi Yue and Dr. Huifeng Liu for their professional support in high temperature and high pressure experiments and Pourbaix diagram calculations.

I'd like to thank the Jordan Thomas and iFS technicians for all of their hard work to maintain the labs and provide equipment and materials. Thanks also to Zabeada Aslam and Stuart Micklethwaite from LEMAS and Dr. Chun Wang from iFS for their brilliant work on surface analysis.

I am also thankful to the members of iFS research group, especially to Dr. Qingyang Liu and Dr. Dongze Wang for their kind help and support.

I would like to give special thanks to my girlfriend, Ms. Yingxuan Liu, for her unwavering emotional support and understanding throughout my research and especially during the writing of this thesis.

Lastly, my deepest gratitude goes to my parents for their endless love and support.

Abstract

The service environments of tubing materials in deep/ultra-deep oilfields and geothermal wells are particularly corrosive due to the extremely high chloride content, temperature and CO_2 partial pressure, which pose significant challenges to the integrity of tubing materials. Super 13Cr martensitic stainless steel (S13Cr MSS) is widely employed in high temperature and high pressure (HTHP) downhole environments owing to its excellent mechanical properties and corrosion resistance. Nevertheless, its corrosion behaviour under extreme downhole conditions remains to be further investigated to facilitate its application and modification.

The current study aimed to identify the failure modes of S13Cr MSS in HTHP CO_2-saturated formation brine by HTHP immersion test, slow strain rate tensile test (SSRT), *in-situ* electrochemical measurements, and surface analysis technologies. The study also investigated the influence of environmental factors (temperature and CO_2 partial pressure) as well as austenite content on the corrosion behaviour of S13Cr MSS and the evolution of corrosion product films.

This thesis demonstrates that S13Cr MSS faces a severe risk of uniform corrosion under HTHP condition (200°C/5.2 MPa CO_2). The research suggests that the corrosion process occurs in three distinct stages: 1) Early stage: native passive film degradation; 2) Middle stage: localized preferential corrosion; 3) Final stage: uniform corrosion. Variations in CO_2 partial pressure (0.27/5.2 MPa CO_2 at 200°C) affected the precipitation behaviour of calcium carbonate, and altered the corrosion morphology during the middle stage as well as the composition of the corrosion product film. Increasing temperature did not change the thermodynamic mechanism of corrosion, but kinetically accelerated each corrosion stage. The relationship between the native passive film degradation time and temperature was found to obey the Arrhenius law. Austenite, acting as a cathode, forms a galvanic couple with the martensite matrix, thereby accelerating the corrosion of S13Cr MSS. The austenite-free S13Cr MSS demonstrated the best corrosion resistance.

Table of Contents

List of Tables

List of Figures

List of Abbreviations

13Cr	13% Chrome
AES	Auger electron spectroscopy
Af	Finishing temperature of austenite formation
AIDE	Adsorption-induced dislocation emission
APT	Atom probe tomography
As	Starting temperature of austenite formation
BCT	Body-centred tetragonal
CO_3^{2-}	Carbonate ion
CPDP	Cyclic potentiodynamic polarisation
CPE	Constant phase element
CPE_{dl}	Capacitance of the electrical double layer
CPE_f	Capacitance related to the corrosion scale
DI	Deionized
EBSD	Electron backscatter diffraction
E_{corr}	Corrosion potential
EDX	Energy dispersive X-ray spectroscopy
EEC	Equivalent electrical circuit
EGS	Enhanced geothermal system
EIS	Electrochemical Impedance Spectroscopy
E_{pit}	Pitting potential
ER	Elongation ratio
E_{rep}	Repassivation potential
FCC	Face-centered cubic
FE	Finite element
FIB	Focused ion beam
FIC	Film-induced cleavage
FLW	Finite-length Warburg
FPB	Four-Point Bend
FSW	Finite-space Warburg
GDP	Gross Domestic Product
HCO_3^-	Bicarbonate ion
HE	Hydrogen embrittlement

HEDE	Hydrogen-enhanced decohesion
HELP	hydrogen-enhanced localized-plasticity
HFM	High field model
HTHP	High temperature and high pressure
IEA	The International Energy Agency
IMPACT	International Measures of Prevention, Application and Economics of Corrosion Technology
IRENA	The International Renewable Energy Agency
IW	Infinite Warburg
K_{sp}	Solubility product
MCM	Mixed Conduction Model
Ms	Martensitic start temperature
MSS	Martensitic stainless steels
NACE	The National Association of Corrosion Engineers
OCP	Open circuit potential
OCTG	Oil country tubular goods
PBR	Pilling-Bedworth ratio
PDM	Point defect model
PEEK	Polyetheretherketone
PTFE	Polytetrafluoroethylene
RAR	Reduction in area ratio
R_{ct}	Charge transfer resistance
R_f	Resistance of the corrosion scale
S13Cr	Super 13% Chrome
SCC	Stress corrosion cracking
SEM	Scanning electron microscopy
SHE	Standard hydrogen electrode
SPM	Solution Pores Model
SR	Supersaturation
SSRT	Slow strain rate tensile test
STEM	Scanning transmission electron microscopy
TEM	Transmission electron microscopy
TRIP	Transformation-induced plasticity
UTS	Ultimate tensile strength
W_s-R	Warburg resistance
XPS	X-ray photoelectron spectroscopy
XRD	X-ray diffraction

1. Chapter 1 Introduction

1.1. Project background

Under the background of the global energy transition and the reshaping of geopolitical landscapes, ensuring the security and resilience of energy supplies has emerged as a core concern for nations worldwide. The global pursuit of energy security, coupled with the trend of low-carbon energy transition, is propelling the frontiers of resource exploration deep into the Earth's crust. As engineering operations venture into deeper formation, the service environment for engineering materials undergoes extreme HTHP conditions. In these downhole environments, the synergistic interplay of elevated temperatures, high mechanical stresses, and aggressive corrosive media (e.g., high salinity brines, CO_2, and H_2S) is pushing engineering materials to their physical limits [1].

Corrosion in such extreme downhole environments has become one of the most common and costliest challenges to the energy industry [2]. Corrosion not only damages the structural integrity of tubing, leading to catastrophic failures and environmental hazards, but also brings a staggering economic burden. As estimated by the National Association of Corrosion Engineers (NACE) International in the International Measures of Prevention, Application and Economics of Corrosion Technology (IMPACT) Study (2016), the annual global cost of corrosion was at around $2.5 trillion, representing approximately 3.4% of the global Gross Domestic Product (GDP) [3]. Particularly within the energy industry, corrosion-related expenditures (including material replacement, unplanned downtime, and chemical inhibition treatments) incur losses amounting to billions of dollars annually.

The corrosion in extreme HTHP downhole environments mainly occurs in two critical sectors: oil and gas exploitation and geothermal development. Both industries rely on the development of deep reservoirs where HTHP conditions are the norm, thereby

posing an urgent request for advanced material solutions to ensure the long-term serviceability and integrity of downhole infrastructure.

1.1.1. Oil and natural gas

Despite the rapid development of renewable energy, oil and natural gas remains the cornerstone of the global energy system for the next few decades [4]. This is due to their irreplaceable energy density and their essential role as industrial raw materials. According to the World Energy Outlook 2023 [5] pressed by the International Energy Agency (IEA), the demand for oil and natural gas is expected to remain at high level until 2050, as shown in Figure 1-1.

To meet sustained energy demand and offset the production decline in mature fields, the global oil and gas industry is continuously moving into areas with more complex geology and higher costs. Specifically, deep and ultra-deep formations. Among them, deep and ultra-deep regions have become the most important areas for reserve replacement and the investment hotspots. The reservoir temperature rises with depth at a rate of about 25-30°C/km [6]. Therefore, the deep and ultra-deep zones usually correspond to a HTHP reservoir condition. As shown in Figure 1-2, for oil and gas industry, HTHP can be defined as a reservoir temperature greater than 150°C and a pressure greater than 69 MPa [7].

(a)

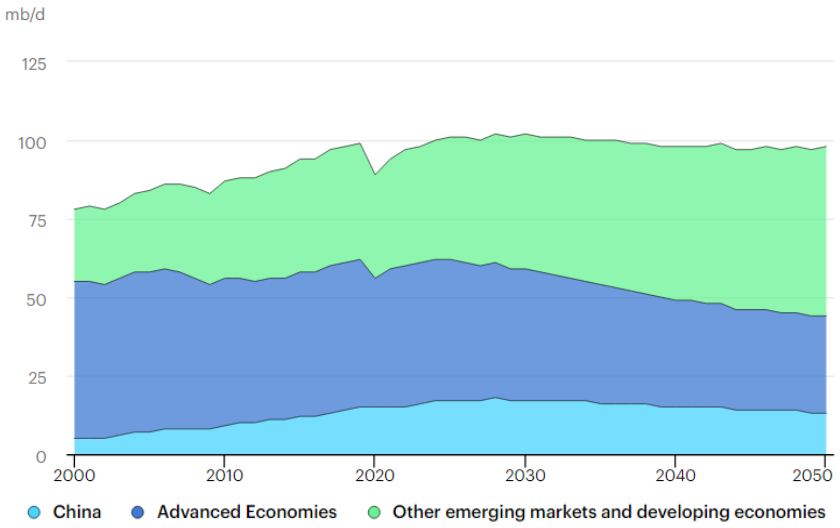

(b)

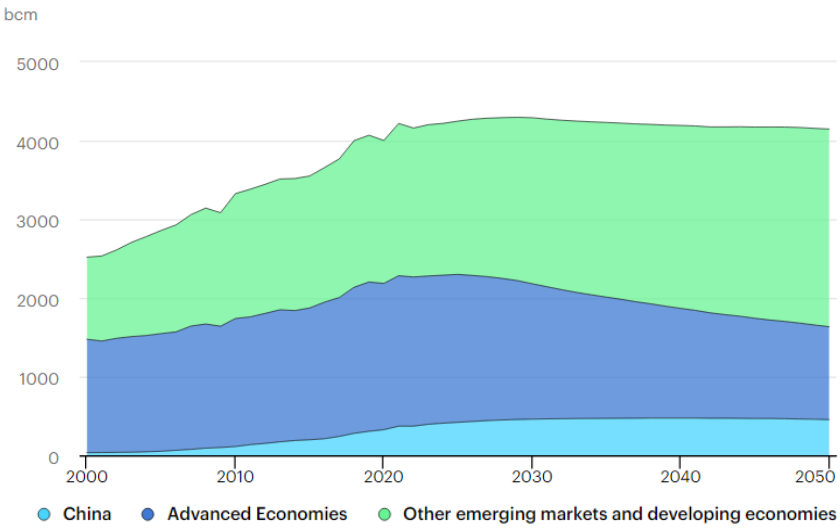

Figure 1-1. (a) Oil and (b) natural gas demand by region in the Stated Policies Scenario, 2000-2050 [5].

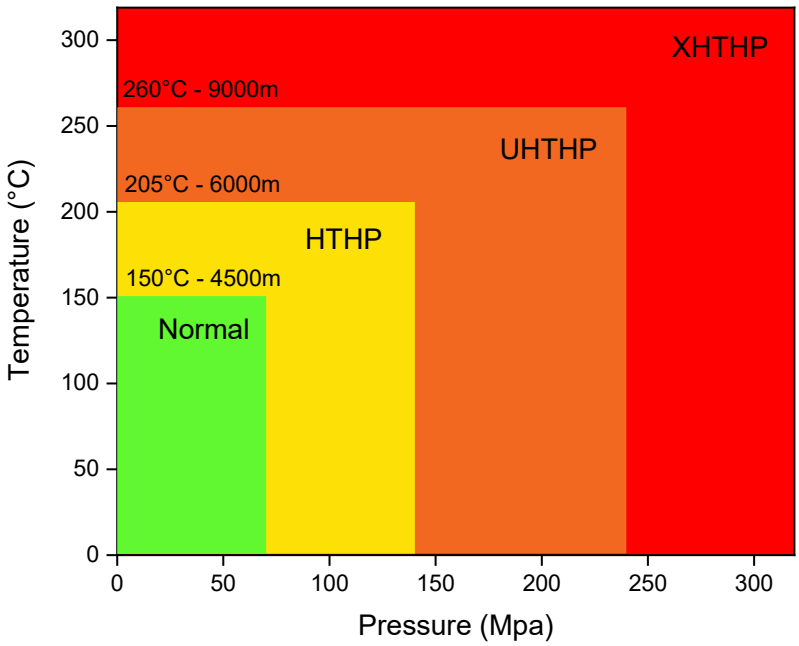

Figure 1-2. Classification of reservoirs based on pressure and temperature [7].

As shown in Figure 1-3, the HTHP resources are widely distributed in regions such as the Americas, Asia-Pacific, and the Middle East, including the Gulf of Mexico (depth > 8000 m), the North Sea, and China's Tarim Basin (depth > 9000 m) [8].

Developing these resources means that production facilities must withstand extremely harsh downhole environments: high temperatures, high pressures, and fluids containing high concentrations of CO_2 and high-salinity formation water (rich in Cl^- ions). This aggressive downhole environment poses an unprecedented and severe challenge to the long-term integrity and safety of downhole tubing, which is in direct contact with the produced fluids [1].

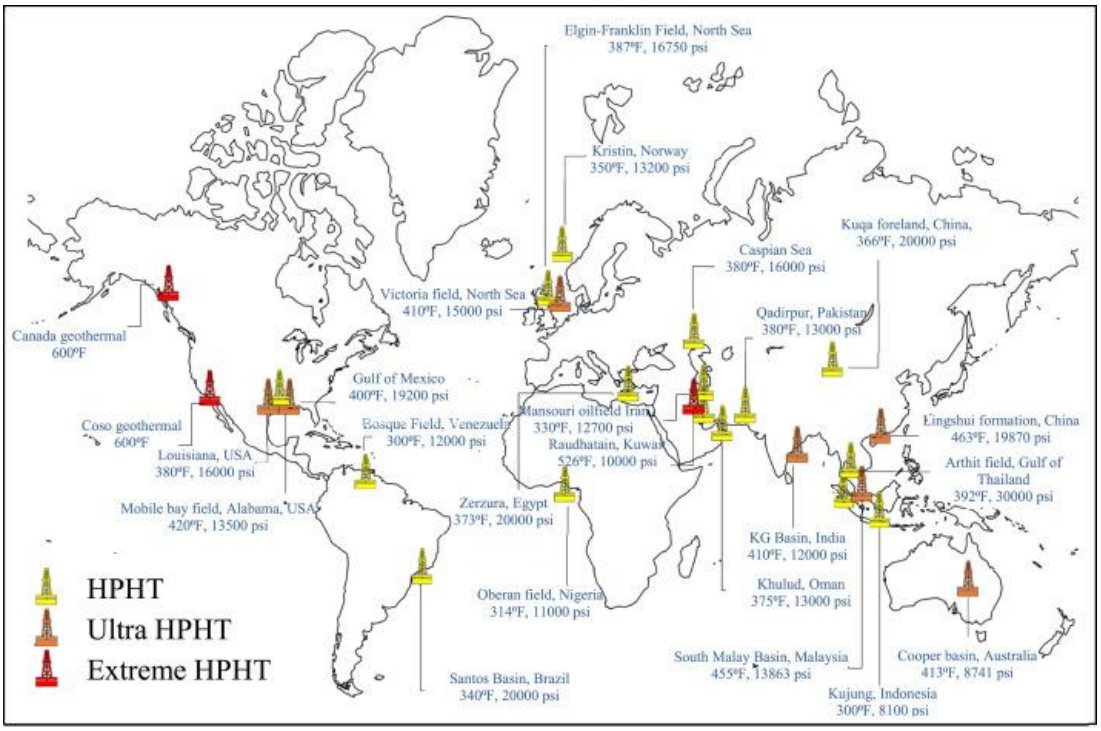

Figure 1-3. World HTHP resources' location [8].

1.1.2. Geothermal

In order to against climate change and achieve energy transition, deep geothermal energy, especially Enhanced Geothermal Systems (EGS) as shown in Figure 1-4 [9], is emerging as a zero-carbon energy option. It was reported by the IEA [10] in 2024 that the full technical potential of next-generation geothermal systems to generate electricity is second only to solar photovoltaic among renewable technologies and is sufficient to meet global electricity demand 140-times over. EGS extracts heat from deep, low-permeability hot dry rocks by creating artificial reservoirs. The target zones are typically with temperatures ranging from 150°C to 300°C or even higher [9].

Similar to deep oil and gas wells, both production and injection wells in EGS face harsh HT environments. The chemistry of geothermal fluids is highly corrosive, they are usually rich in aggressive ions like Cl^- and SO_4^{2-} and may also contain dissolved gases such as CO_2 and H_2S [11]. This poses a severe corrosion threat to tubing materials.

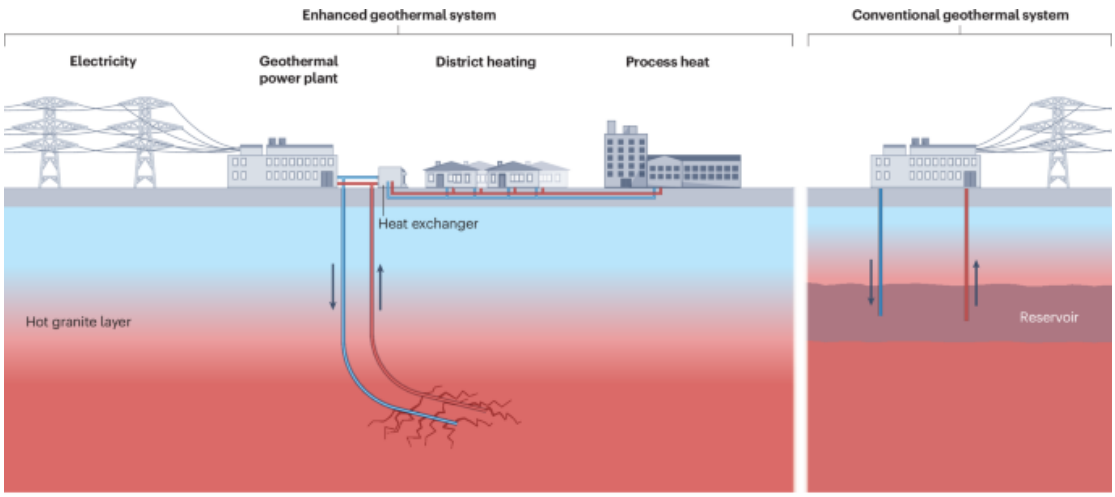

Figure 1-4. Enhanced geothermal systems [9].

Since the downhole environment of geothermal wells is very similar to that of HTHP oil and gas wells, the corrosion challenges they faced and the demand for cost-effective materials are almost exactly the same.

1.2. Application of S13Cr MSS

Figure 1-5 presents a widely accepted material selection guide for downhole tubing in the oil and gas industry [12]. Traditionally, carbon steel/low alloy steel combined with inhibitors has been the most cost-effective solution for downhole conditions. However, in HTHP environments (>150°C), most commercial organic inhibitors face severe thermal degradation [13]. This causes a sharp drop in inhibition efficiency, making this approach unreliable. Duplex stainless steels (22Cr/25Cr) and nickel-based alloys offer excellent corrosion resistance at high temperature, but their high costs limit their large-scale application.

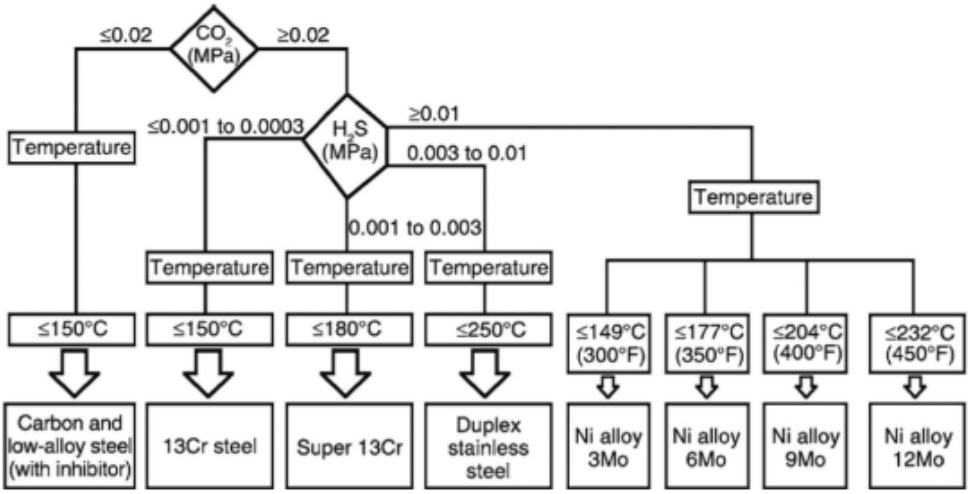

Figure 1-5. A flow chart for the selection of tubing material for H_2S and/or CO_2 service [12].

The successful development of S13Cr MSS bridges the gap in both performance and cost between cheap carbon steels/low alloy steels and expensive duplex stainless steels. The traditional material selection map as provided in Figure 1-5 set the safe application temperature limit of S13Cr MSS below 180°C. However, advancements in corrosion research and field experience have led some manufacturers to suggest that the service temperature limit of S13Cr MSS could be extended to 200°C under specific field conditions (as shown in Figure 1-6) [14].

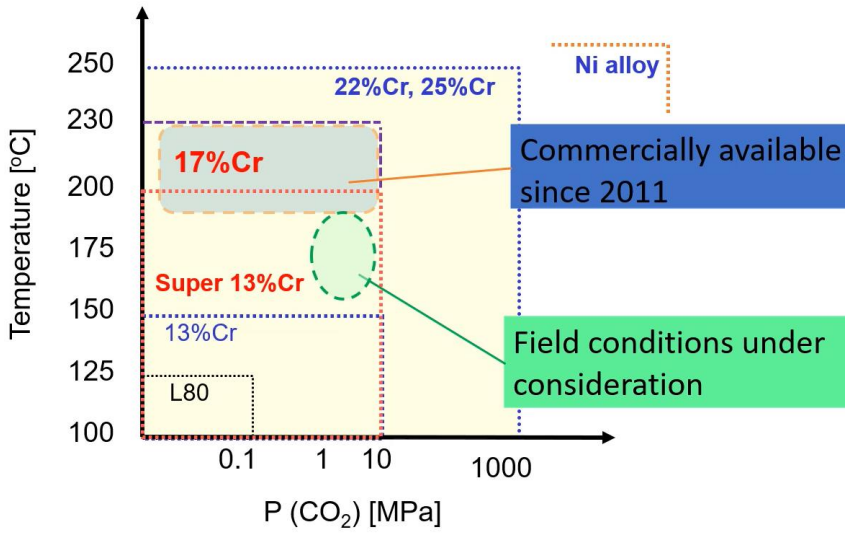

Figure 1-6. Application limits of tubing materials proposed by manufacturers [14].

Therefore, systematically study on the corrosion and stress corrosion cracking (SCC) behaviour of S13Cr MSS at high temperatures, especially around 200°C, is crucial. This is not only essential for clarifying the failure mechanisms of S13Cr MSS in HTHP downhole environments and extending the application temperature range, but also holds significant engineering importance for reducing the development costs of deep oil and gas resources.

1.3. Objectives of this study

Corrosion in HTHP downhole environments is a significant challenge during the development of HTHP wells. In collaboration with Zhejiang Jiuli Hi-Tech Metals Co., Ltd., this project aims to identify the primary failure mode of S13Cr MSS under HTHP downhole environment. Additionally, by investigating the corrosion behaviour and the evolution of the corrosion product film at high temperatures, this study aims to improve the understanding of S13Cr MSS applications under HTHP environments. It also aims to provide corrosion-related insights for material optimization. The specific research objectives of this study can be outlined as follows:

- To systematically assess the susceptibility of S13Cr MSS to general corrosion, localized corrosion, and SCC under specific aggressive HTHP downhole environment, and to identify the primary failure mode of S13Cr MSS in such environment.
- To develop an autoclave system capable of performing *in-situ* electrochemical measurements under HTHP environments, providing a reliable experimental platform to observe transient corrosion processes.
- To investigate the influence of CO_2 partial pressure on the evolution of the composition and structure of the corrosion product film, as well as on the scaling behaviour.
- To study the impact of temperature variation on the evolution of composition and structure of the corrosion product film, and to establish a comprehensive corrosion model covering the full process from native passive film degradation to steady-state corrosion under HTHP environments.

- To utilize *in-situ* electrochemical techniques to monitor the degradation behaviour of the native passive film in real-time, and to accurately identify the failure time of the native passive film in order to study the kinetic characteristics of the transition from passivity to active dissolution.
- To investigate the thermodynamic processes regarding the formation and evolution of corrosion products on S13Cr MSS under HTHP environments by combining chemical composition characterization with Pourbaix diagram.
- To propose and experimentally validate a material optimization strategy for S13Cr MSS based on corrosion performance improvement.

1.4. Outline of thesis

The thesis is broken down into ten chapters as follows:

Chapter 1 is the introduction and justification for the project.

Chapter 2 introduces essential theoretical concepts relevant to CO_2 corrosion of stainless steel, and the basic principles of passive behaviour and SCC.

Chapter 3 is a review of literature on the development of 13%Cr MSS and its corrosion and cracking performance under HTHP downhole environments.

Chapter 4 covers the full experimental methodology employed in the research project, including a description of all HTHP testing equipment and the surface analysis techniques applied.

Chapter 5 is the first of four results chapters. The general corrosion rate, localized corrosion rate, and the evolution of pitting morphology of S13Cr MSS under specific HTHP condition were obtained through immersion tests combined with surface profilometry and weight loss measurements. Subsequently, the SCC susceptibility in this harsh downhole environment was evaluated by slow strain rate tensile tests (SSRT) and scanning electron microscopy (SEM) fracture analysis. The susceptibility to general corrosion, localized corrosion, and SCC was classified, and the primary failure mode of S13Cr MSS in this environment was identified.

Chapter 6 compares the composition evolution and microstructural differences of corrosion product films, as well as the scaling behaviour, under high and low CO_2 partial pressures through immersion tests of varying durations and surface analysis techniques (including SEM, energy dispersive X-ray spectroscopy (EDX), transmission electron microscopy (TEM), X-ray diffraction (XRD), and Raman spectroscopy). A corrosion stage division model was proposed based on the evolution of surface morphology. *In-situ* electrochemical measurements were employed to monitor and compare the real-time electrochemical response characteristics of the S13Cr MSS under different CO_2 pressure conditions.
Chapter 7 first investigates the corrosion rates through long-term experiments to understand the usability of the S13Cr MSS at different temperatures. Subsequently, immersion tests combined with surface analysis were used to observe the degradation of the native passive film and the subsequent growth of the corrosion product film. *In-situ* electrochemical monitoring was conducted to compare the electrochemical response at each corrosion stage under different temperatures. The corrosion evolution stage model proposed in the previous chapter were improved.

Chapter 8 proposes an optimization strategy to improve the corrosion resistance of S13Cr MSS by adjusting the reversed austenite content. S13Cr MSS specimens with varying austenite contents were prepared. The impact of austenite content on corrosion resistance was evaluated through immersion tests. Surface analysis techniques were employed to investigate the effect of austenite content on the corrosion behaviour of S13Cr MSS during each corrosion stage under HTHP downhole environments.

Chapter 9 is the discussion section which pulls together all of the results chapters and compares and contrasts this with the currently available literature.

Chapter 10 is the final conclusions of the project and also includes recommendations for future work.

2. Chapter 2 Theory of carbon dioxide corrosion of stainless steel

2.1. Mechanisms of the CO_2 corrosion

CO_2 corrosion is the chemical/electrochemical reaction of the pipeline material in the presence of water and CO_2. It is a complex process in which a number of chemical reactions, electrochemical reactions and transport processes occur simultaneously which can be divided into both anodic and cathodic reactions. The presence of CO_2 in an aqueous solution promotes the hydrogen evolution reaction, increasing the rate of corrosion of iron [15].

The chemical process of CO_2 corrosion commences by the dissolution of CO_2 in water. Depending on the conditions within the flow, a percentage of the carbon dioxide gas dissolves in the produced water and results in the formation of weak carbonic acid as shown in the reactions 2-1 and 2-2 [15].

$$CO_{2(g)} \rightleftharpoons CO_{2(aq)} \quad (2\text{-}1)$$

$$CO_{2(aq)} + H_2O \rightleftharpoons H_2CO_{3(aq)} \quad (2\text{-}2)$$

Carbonic acid is considered a weak acid as it does not fully dissociate. It is diprotic and partially dissociates in two steps to form bicarbonate (HCO_3^-) and carbonate (CO_3^{2-}), and releases H^+ ions in both steps. This separation provides the necessary H^+ ions to enable the corrosion reaction.

$$H_2CO_{3(aq)} \rightleftharpoons H^+ + HCO_3^- \quad (2\text{-}3)$$

$$HCO_3^- \rightleftharpoons H^+ + CO_3^{2-} \quad (2\text{-}4)$$

2.1.1. Anodic reactions

The primary anodic dissolution of metal is given in reaction 5-7:

$$Fe_{(s)} \rightarrow Fe^{2+} + 2e^- \quad (2\text{-}5)$$

$$Ni_{(s)} \rightarrow Ni^{2+} + 2e^- \quad (2\text{-}6)$$

$$Cr_{(s)} \rightarrow Cr^{3+} + 3e^- \quad (2\text{-}7)$$

The corrosion product film formed at high temperature is mainly composed of spinel (Fe_3O_4, $FeCr_2O_4$, $NiFe_2O_4$, etc.), hematite (Fe_2O_3), Cr_2O_3, etc. Cr_2O_3 could be formed and controlled by the electro-migration process according to the following reactions at high temperature CO_2 environments [16, 17]:

$$2Cr + 3H_2O \rightleftharpoons Cr_2O_3 + 6H^+ + 6e^- \quad (2\text{-}8)$$

$$Cr + 3H_2O \rightleftharpoons Cr(OH)_3 + 3H^+ + 3e^- \quad (2\text{-}9)$$

$$2Cr(OH)_3 \rightleftharpoons Cr_2O_3 + 3H_2O \quad (2\text{-}10)$$

$Cr(OH)_3$ can be deposited to form as an amorphous phase during a dissolution-precipitation process and then transform into Cr_2O_3 [16]:

$$Cr^{3+} + 3OH^- \rightleftharpoons Cr(OH)_3 \quad (2\text{-}11)$$

$$Cr(OH)_3 + Cr + 3OH^- \rightleftharpoons Cr_2O_3 + 3H_2O + 3e^- \quad (2\text{-}12)$$

Fe and Ni can form oxides or hydroxides on the surface via the following reactions [18]:

$$3Fe + 4H_2O \rightleftharpoons Fe_3O_4 + 8H^+ + 8e^- \quad (2\text{-}13)$$

$$Ni^{2+} + 2OH^- \rightleftharpoons Ni(OH)_2 \quad (2\text{-}14)$$

According to the potential (E)-pH diagram of the Ni-H_2O system and Fe-H_2O system at 250°C, the following reactions may occur:

$$Ni + 2H_2O \rightleftharpoons NiO + 2H^+ + 2e^- \quad (2\text{-}15)$$

$$2Fe_3O_4 + H_2O \rightleftharpoons 3Fe_2O_3 + 2H^+ + 2e^- \quad (2\text{-}16)$$

Fe_2O_3 forms on the metal surface at a relatively positive potential as a metastable oxide phase.

The formation of spinel $FeCr_2O_4$ can occur via reactions 2-17, 2-18 and 2-19 (noting that all these reactions produce H^+ ions, potentially acidifying the interface during formation)

$$Fe + 2Cr + 4H_2O \rightleftharpoons FeCr_2O_4 + 8H^+ + 8e^- \quad (2\text{-}17)$$

$$2Fe^{2+} + Cr_2O_3 + H_2O \rightleftharpoons FeCr_2O_4 + 2H^+ \quad (2\text{-}18)$$

$$Fe^{2+} + 2Cr(OH)_3 \rightleftharpoons FeCr_2O_4 + 2H^+ + 2H_2O \quad (2\text{-}19)$$

The growth of oxide particles can occur via the precipitation of cations from solution. The formation of $NiFe_2O_4$ by precipitation can be expressed as reaction 2-20 [19]:

$$2Fe^{2+} + Ni^{2+} + 4H_2O \rightleftharpoons NiFe_2O_4 + 8H^+ + 2e^- \quad (2\text{-}20)$$

Another corrosion process is the formation of carbonate via the following reaction [20]:

$$Fe^{2+} + CO_3^{2-} \rightleftharpoons FeCO_3 \quad (2\text{-}21)$$

2.1.2. Cathodic reactions

The main cathodic reaction on the steel surface in the presence of CO_2 is the hydrogen evolution reaction (i.e. the reduction of H^+ ions). In CO_2-containing environments, the production of hydrogen at the steel surface is facilitated through a collection of cathodic reactions. Initially, the hydrogen evolution reaction was widely considered to include the below reactions, which consist of the reduction of H^+ as well as the direct reduction of H_2CO_3, HCO_3^- and H_2O [21]. However, recent studies point out that the direct reduction of H_2CO_3, HCO_3^- (reactions 2-23 and 2-24) is insignificant in CO_2 corrosion. H_2CO_3, HCO_3^- mainly contribute to the cathodic reaction through dissociation (reactions 2-23 and 2-24) to supply H^+ [22, 23]. The direct reduction of water (reaction 2-25) is thermodynamically feasible, but is often neglected due to its kinetically insignificant contribution in CO_2 corrosion process [23, 24].

$$2H^+_{(aq)} + 2e^- \rightleftharpoons H_{2(g)} \quad (2\text{-}22)$$

$$2H_2CO_{3(aq)} + 2e^- \rightleftharpoons H_{2(g)} + 2HCO_3^-{}_{(aq)} \quad (2\text{-}23)$$

$$2HCO_3^-{}_{(aq)} + 2e^- \rightleftharpoons H_{2(g)} + 2CO_3^{2-}{}_{(aq)} \quad (2\text{-}24)$$

$$2H_2O_{(l)} + 2e^- \rightleftharpoons H_{2(g)} + 2OH^-{}_{(aq)} \quad (2\text{-}25)$$

Hydrogen ion reduction (reaction 2-22) has been studied extensively [25-27]. The commonly understanding is that this reaction can be described using three steps, which involve electrochemical adsorption of H^+ (reaction 2-26), followed by either electrochemical desorption (reaction 2-27) or chemical desorption (reaction 2-28).

$$H^+_{(aq)} + e^- \rightleftharpoons H_{ads} \quad (2\text{-}26)$$

$$H_{ads} + H^+_{(aq)} + e^- \rightleftharpoons H_{2(g)} \quad (2\text{-}27)$$

$$H_{ads} + H_{ads} \rightleftharpoons H_{2(g)} \quad (2\text{-}28)$$

2.2. Passive behaviour of stainless steel

Passivity is a property of some metals or alloys, which are thermodynamically unstable, and react inherently with environment (water or oxygen) forming a stable passive oxide film on the material surface. The metal surface is protected against the corrosive environments by the passive layer [28].

The passive film was first separated by the scratch experiment. Later, combined with modern research methods, including X-ray Photoelectron Spectroscopy (XPS) and Auger Electron Spectroscopy (AES), researchers gradually deepened their researches on passive film. Macdonald believed that the passive film of stainless steel has a double-layer structure, as shown in Figure 2-1 [29]. The outer membrane is a sedimentary membrane, which is formed by the cation diffusion of the inner membrane to the surface and hydrolysis. However, the results of the literature show that the composition, structure and thickness of the passive film change with the composition of the material and the environment [30]. For metals such as (Cr, Co, Ni, Mo) and their alloys it is tens to hundreds of angstroms while the thickness of passive film for the other metals (Zn, Cd, Mg, Cu, Pb) could be in micro meter range [31].

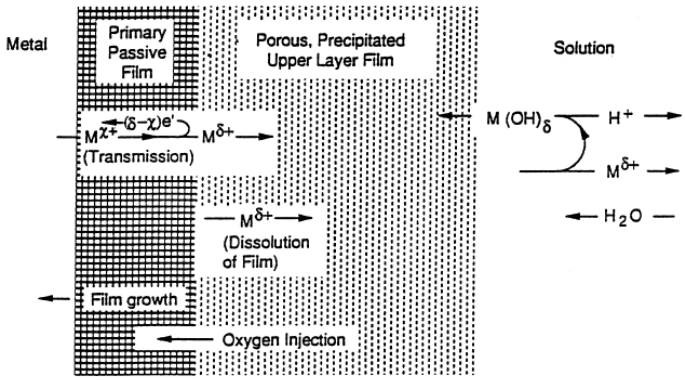

Figure 2-1. Schematic diagram illustrating the structure of the passive film [29].

2.2.1. The passive film growth model

Passivation has been the subject of discussion for more than 200 years. Researchers have systematically studied the passivation of

various metals and their alloys. During those researches, many theories and models have been proposed to explain the growth of passivation films, including High Field Model (HFM), Mixed Conduction Model (MCM), Solution Pores Model (SPM) and Point Defect Model (PDM), etc., so far, no unified theory has emerged to explain the growth kinetics of passive films.

2.2.1.1. Point Defect Model

Of all the models which make analytical predictions that can be tested, the Point Defect Model is the most widely accepted model for corrosion in aqueous solution. The PDM was originally proposed by C. Y. Chao and D. D. Macdonald in the early 1980s [32], and has now developed into the third generation [33].

According to the PDM, the passive film is generally considered to be a highly defective semiconductor with vacancies (including metal vacancies and oxygen vacancies) and metal interstitials. As illustrated in Figure 2-2, the formation and consumption of vacancies and metal interstitials occur at the interface. Under anodic polarisation conditions, oxygen vacancies migrate from the metal/ barrier layer interface to the outer layer or solution direction, while metal vacancies migrate from the barrier layer /outer layer interface or barrier layer/solution interface to the metal direction. The migration of these vacancies may eventually lead to the movement of the passive film interface. When the film formation and dissolution rate are consistent, the thickness of the corrosion film will be stable and the passive film can reach an equilibrium state [33].

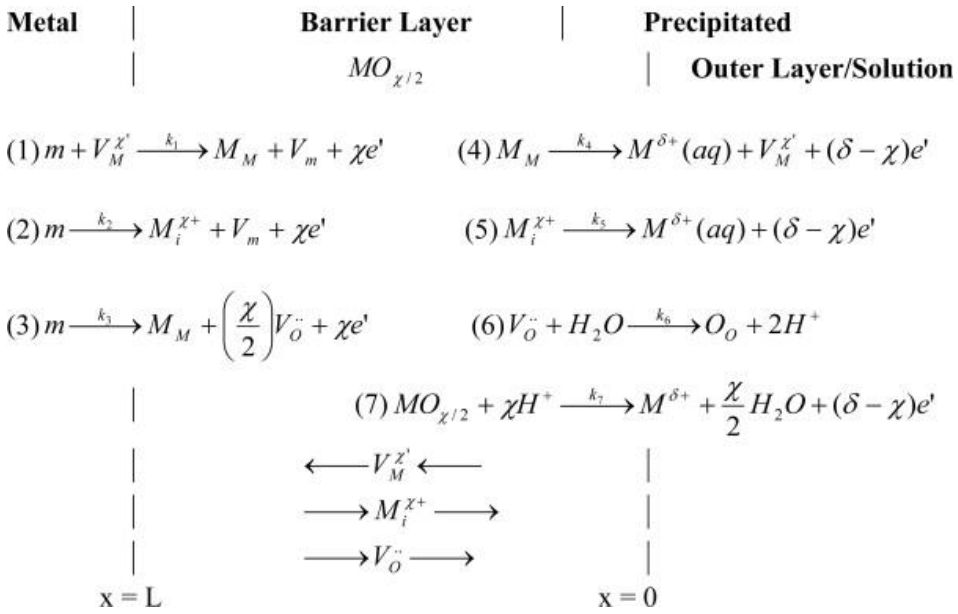

Figure 2-2. Summary of the defect generation and annihilation reactions envisioned in PDM to occur at the interfaces of the barrier oxide layer on the metal [33].

Following the PDM, the electrostatic potential is distributed across the interphase with drops across the metal/barrier layer interface, the barrier layer, and the barrier layer/outer layer interface as shown in Figure 2-3. The strength (ε) of the electric field in the barrier layer is independent of voltage and distance through the barrier layer. The voltage drop across the barrier layer/outer layer interface is linearly dependent upon the applied voltage and the pH [33, 34].

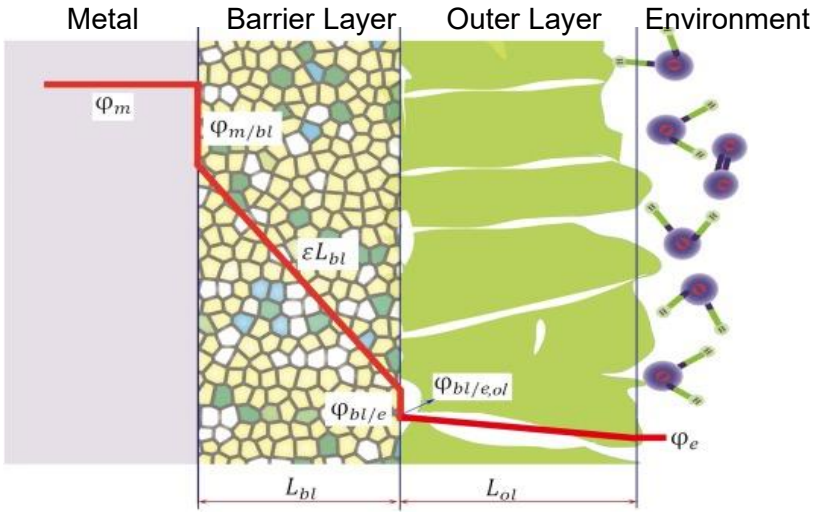

Figure 2-3. Distribution of the potential across the barrier layer [34].

2.2.1.2. High Field Model

High Field Model was proposed by E.J.W. Verwey in 1935 [35]. According to the HFM, a significant electric field is assumed to exist across the thin oxide film. The high field assisted ionic transport through the film is considered to be the rate-limiting processes during the film growth process, often leading to a linear growth law for the oxide film thickness over time. Unlike the PDM, the strength of the electric field in the film is not constant according to the assumption of HFM [36]. As shown in Figure 2-4, according to the HFM, the electric field is assumed to change upon a change in potential while the potential drop across the metal/film interface and film/solution interface remains unchanged, the film growth will be limited by high field ion conduction through the oxide [37].

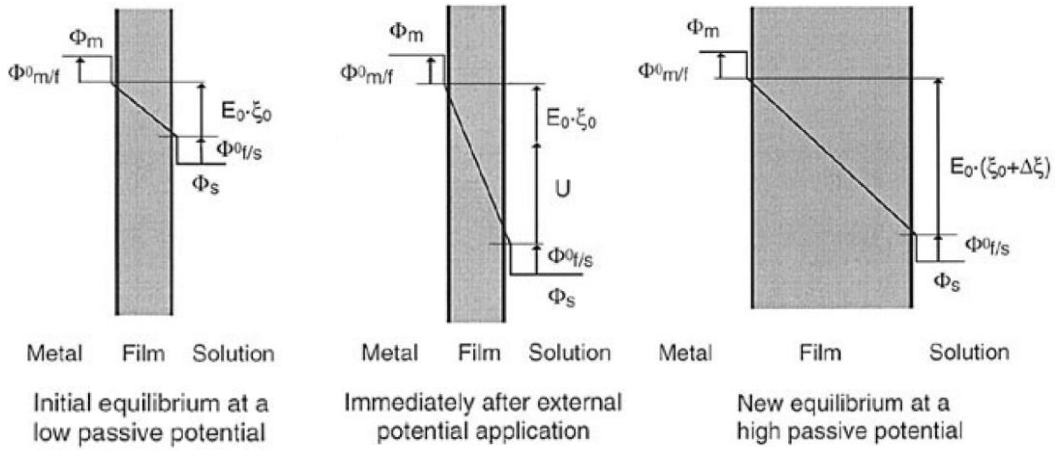

Figure 2-4. Schematic diagram illustrating the response to an applied potential according to HFM [37].

2.2.1.3. Mixed Conduction Model

Mixed Conduction Model was proposed by M. Bojinov in the late 20th century. A simplified scheme of the processes taking place in the metal/oxide/electrolyte system according to the MCM is provided in Figure 2-5 [38]. From the schematic view of it only, to a large extent, the MCM is similar to the early generation PDM. But the MCM emphasises the coupling between the ionic defect structure and electronic conduction. It is assumed in the MCM that positive ionic defects generated at the metal/film interface and consumed at the film/electrolyte interface play the role of electron donors, while negative defects generated at the film/electrolyte

interface and consumed at the metal/film interface play the role of acceptors. The electronic conductivity of the steady-state passive film is considered to be proportional to the concentration of ionic defects [39].

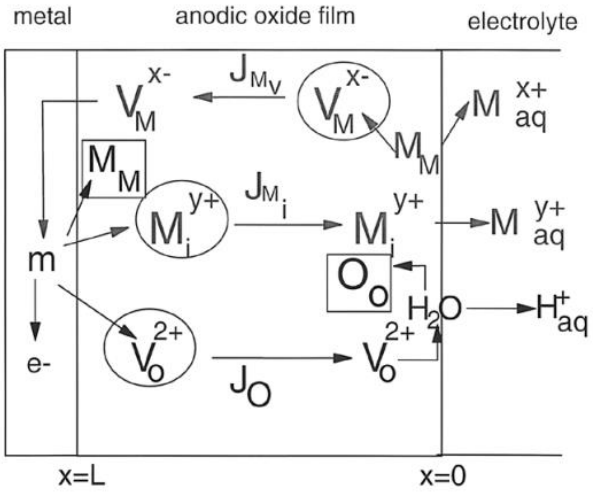

Figure 2-5. A scheme of the processes taking place in the metal/anodic layer/solution system according to MCM [38].

2.2.1.4. Solution Pores Model

In many cases, the passive oxide film is porous. Solution Pores Model particularly focus on the presence and role of pores within the film.

In the case of the film growth control by reactant diffusion, it can be categorized into two cases based on the activation energy required for diffusion: in one case, reactant diffusion through the oxide lattice, which requires an activation energy of 120-135 kJ/mol [40]; and in the other case, reactant diffusion through the solution in the pores of the porous oxide layer, where the activation energy for liquid phase diffusion generally lies below a value of 41.84 kJ/mol [41]. The second case which the reactant diffusion through the solution in the pores of the porous oxide layer is known as the SPM [40].

2.2.2. Protectiveness of passive film

The protective oxide film could be destroyed by electrochemical and mechanical methods. For example, putting the passivated metal in a solution containing the aggressive ions is a common degrading condition. Localized corrosion (pitting corrosion, crevice corrosion

and stress corrosion cracking) occurs by the breakdown of the passive film in the presence of aggressive ions (such as Cl^-, Br^-, etc.). Electrochemical investigation of passivity is a common method used to evaluate the resistance of the material to localised corrosion. Studying the material polarisation treatment by polarisation techniques especially cyclic potentiodynamic polarisation (CPDP) technique is a suitable way for investigation of the beginning of passivity, breakdown of oxide film, susceptibility to repassivation and calculation of the rate of pitting corrosion due to the vast range of scanning potential [31].

The general shape of CPDP curve is as follows; after passing through the region of active corrosion, the current density decreases to a critical potential, called the “Flade potential” or “primary passivation potential”. This decrease is due to the formation of the passive layer on metal surface. The passive current density is the current density in the passive region. With further increase in the potential in the passive region, a rapid rise in the anodic current can be detected. This rise is due to either the evolution of oxygen by the decomposition of water or breaking the passive film and localized corrosion. If the increase of current density is due to the decomposition of water and evolution of oxygen gas, the region is called “transpassive region” (Figure 2-6) [28]. Finally, the scanning potential direction is reversed to the starting point. Along with the continuous scanning potential, the current response is monitored. According to ASTM F2129 standard [42], there are three different states: the scanning potential continues until the hysteresis loop is completed indicating repassivation (Figure 2-6 a) or oxygen evolution occurs and the anodic to cathodic transition potential is reached (Figure 2-6 b) or the hysteresis loop is not completed and corrosion potential is reached (Figure 2-6 c). According to ASTM G61 standard [43], the reverse scan continues until the hysteresis loop is completed or the corrosion potential is reached.

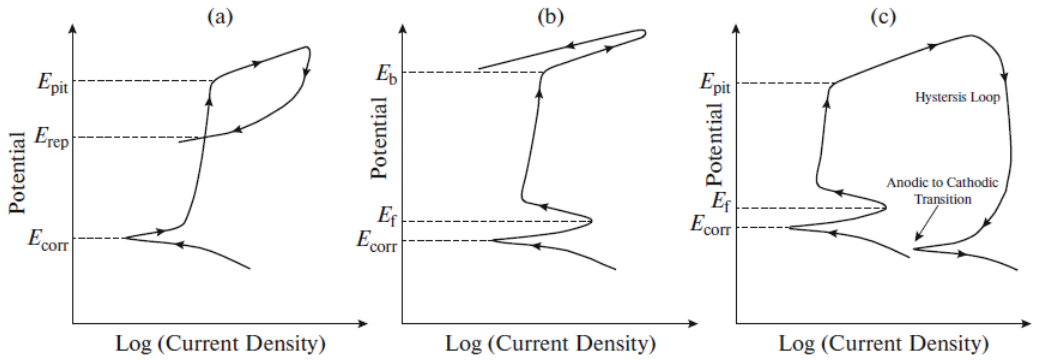

Figure 2-6. Schematic illustration of CPDP tests for three different conditions, (a) exhibiting protection potential, (b) with oxygen evolution, (c) without protection potential [28].

The parameters used to interpret the CPDP curves include: pitting potential, repassivation or protection potential, the potential of anodic to cathodic transition and hysteresis. In the CPDP test, relative position of pitting potential and repassivation potential or protective potential with respect to the corrosion potential is the most important parameter for evaluating the pitting susceptibility [44].

2.2.2.1. Pitting potential

In the anodic polarisation scanning, scanning starts from corrosion potential after reaching a steady state. Before reaching the potential of oxygen evolution, a rapid increase in the current density occurs. Two reasons have been mentioned for this increase. One is that if the surface of oxide is not perfect, for example, some defects exist in the film; the passive film will not be stable over the passive region. At a potential below the oxygen evolution potential, the surface defects will be active and begin to propagate which can increase the current density. The other reason for the increase in the current density earlier than the oxygen evolution can be the breakdown of the oxide film and occurrence of the pitting corrosion in the presence of aggressive ions. In the absence of aggressive ions, the passive film will be stable over the electrode potential of O_2 evolution. The potentials at which the current density increases rapidly for either of two above reasons are given names such as critical pitting potential, pitting potential, breakdown potential or rupture potential [45, 46].

2.2.2.2. Repassivation potential

In the CPDP curve, for investigating the material resistance to localized corrosion after increasing the current density at pitting corrosion, the scanning direction changed. The potential reduction toward the negative potentials, the current density in the reverse scan is higher than the current density in the forward scan (positive hysteresis). The scanning continues until the reverse curve crosses the forward polarisation curve. This intersection point was named as protection potential or repassivation potential (E_{rep}). Repassivation potential is the potential at which the growth rate of pits is stopped [28].

The resistance of the material to localized corrosion is evaluated on the basis of the E_{rep} measurement to the corrosion potential (E_{corr}). If E_{rep} lies in the more noble values than the E_{corr}, the propagation of active pits is diminished or stopped. Therefore, at the potentials between the protection potential and corrosion potential, the passive film is stable and no pits will initiate or grow. Also, in this region crevice corrosion and crack initiation and propagation will not take place. This region is called perfect passivity. At the potential between the pitting potential (E_{pit}) and repassivation potential (E_{rep}), only old pits propagate and no new pits nucleate (Figure 2-7). If E_{corr} lies between E_{pit} and E_{rep}, the repassivation of pits will not take place completely and preformed pits continue to grow and propagate (Figure 2-6(c)) [31].

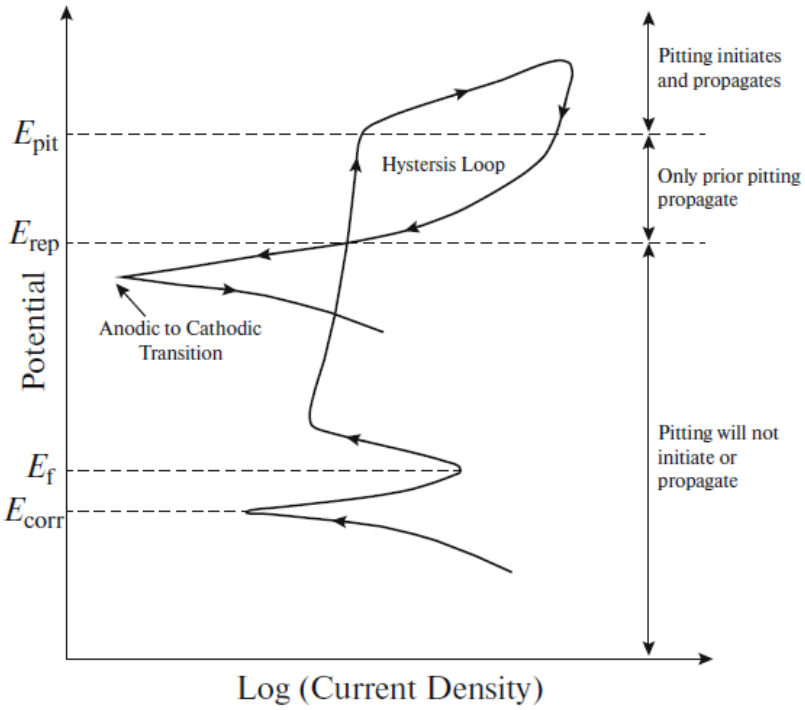

Figure 2-7. Schematic illustration of CPDP curve and corrosion parameters. The arrows show the direction of polarisation [28].

Pitting potential is the minimum potential at which the material tends to the pitting corrosion. Above the pitting potential, new pits will initiate and develop. The difference between the E_{pit} and E_{rep} and also the area of the hysteresis loop indicates the probability of pitting corrosion. The more difference between the E_{pit} and E_{rep} and the larger area of positive loop demonstrate the probability of low pitting corrosion resistance [31, 46, 47].

2.3. Factors that influence the CO_2 corrosion process

For CO_2 corrosion, research has been carried out to study the influence factors of CO_2 corrosion, such as CO_2 partial pressure, temperature, pH value, Cl^-, flow rate, etc. on the corrosion processes as well as the corrosion rate.

2.3.1. Temperature

The influence of temperature on CO_2 corrosion mainly due to the following reasons [48, 49]:(1) Temperature affects the solubility of

CO_2 in the medium that CO_2 concentration decreases with the increase of temperature; (2) Temperature affects the reaction speed of the corrosion reaction and the transmission speed of anode and cathode ions; (3) Temperature also affects the film-forming mechanism of the corrosion product film as well as the stability of the passive film on the steel surface.

The corresponding temperature deviated with the change of matrix material, medium composition and state parameters. As shown in Figure 2-8, 9% and 13% Cr steels indicated the maximum corrosion rate of 4.1 mm/y and 4.0 m/y were observed at 150°C and 200°C respectively at 3 MPa CO_2, but 25% Cr showed better corrosion resistance in this environment [50]. In high temperature CO_2 environments, the increase in temperature, the corrosion scales on stainless steel surface undergo significant microstructural changes. Therefore, the protection of the corrosion scales changes with increasing temperatures. For example, the decrease of the pitting potential and repassivation potential accompanied by the increasing density and diffusivity of acceptor in the scales [51]. As the temperature increase to a critical value, the stainless steel move into an active state [52].

Moreover, in addition to the change of corrosion rate as well as the corrosion products on the surface, the number of pits decreased. However, the increase in pits' size and depth have been reported with increasing temperatures.[28]

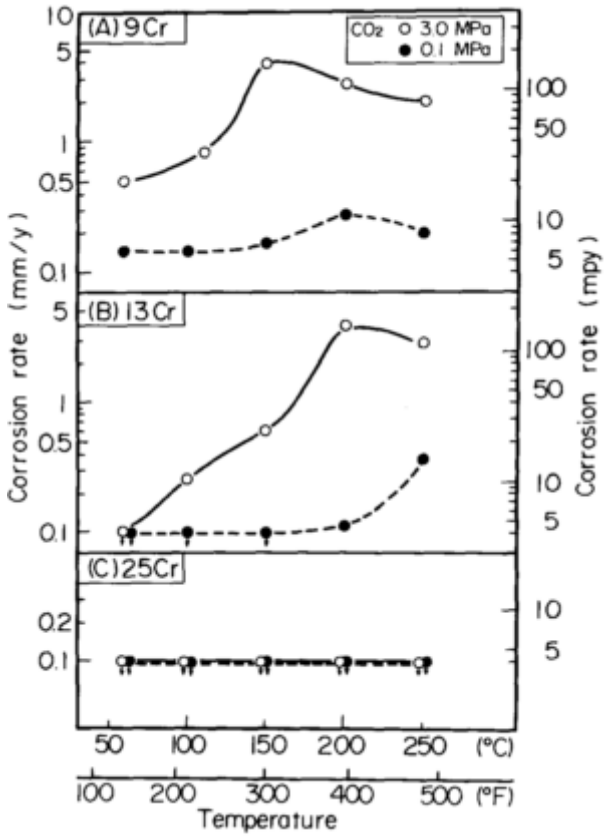

Figure 2-8. Effect of CO_2 partial pressure and temperature on corrosion rate of Cr steel in the autoclave. (5% NaCl; 0.1 and 3.0 MPa CO_2 at 25°C; test duration, 96 h; flow velocity, 2.5 m/s.) [50].

2.3.2. CO_2 partial pressure

CO_2 gas dissolves into the solution and results in the formation of weak carbonic acid, which partially dissociates and provides H^+ ions, thereby lowering the pH of the environment [21]. The reduction in pH promotes the dissolution of materials [53]. On the other hand, the increased partial pressure of CO_2 results in the easier precipitation of carbonates, which inhibit the subsequent corrosion processes. Hence, higher CO_2 partial pressure does not necessarily lead to a higher corrosion rate, this is a matter of environmental conditions [54, 55]. In general, under film-free conditions, higher CO_2 partial pressure results in higher corrosion rate by reducing the pH [56].

Bicarbonate (HCO_3^-) and carbonate (CO_3^{2-}) ions which were formed by the dissociation of carbonic acid, were described as non-aggressive anions [57].

2.3.3. pH

Generally, materials show better resistance to the corrosion/pitting under high pH conditions. As the pH increased, the metastable pitting nucleation potential and point of stainless steel in the same concentration of NaCl solution shift positively [58]. When the polarisation potential is fixed, the increase rate of the point current, volume depth and orifice diameter of a single etch hole varied with the pH values [59].

According to the thermodynamic properties of Cr-H_2O and Fe-H_2O system at 300 °C, the equilibrium electrode potential of oxidation of Cr and Fe degraded with increasing pH, resulting in the anodic reaction shifted to the left and decrease of E_{corr} [60].

The pH affects the stability of the corrosion products from the perspective of thermodynamics, and the composition of the corrosion products can be predicted by Pourbaix diagram. Due to the change in pH, the structure and composition of the corrosion product films change, resulting in the change in the protective properties [61].

The pH also effects the formation of corrosion product films from the perspective of kinetic. For example, the solution pH affects significantly the precipitation of $FeCO_3$ on the surface.[21] Since the kinetics of the precipitation of $FeCO_3$ is relatively slow, it is believed that the supersaturation of the steel surface needs to reach 10 ~ 100 to form a protective layer [62]. And the pH is one of the most important factors which affect the required supersaturation of $FeCO_3$. The increase of pH significantly reduces the Fe^{2+} concentration required to reach the solubility of $FeCO_3$, promoting the formation of the carbonate on the surface [49].

2.3.4. Chloride ion

Chloride ions (Cl^- ions) are one of the most important factors leading to the pitting corrosion of stainless steel. Cl^- ions not only destroy the passive film of stainless steels and lead to the occurrence of the

pitting corrosion, but also promote the growth of the pitting on the surface due to the concentration of Cl^- ions is high within the pit [63]. The passive film is mostly amorphous, with some nanocrystals [64]. There are boundaries between nanocrystals and the amorphous phase and the interface between nanocrystals and the amorphous zone assume a special kind of grain boundaries and provide ready paths for Cl^- ions transport. Cl^- ions accumulate at the metal/film interface through the path, cause lattice expansion of the passive film on the metal side and undulations at the interface, then result in the breakdown of the passive film at adjacent locations [64]. When the concentration of Cl^- ions increase, the catalytic effect of Cl^- ions promoting the breakdown of the passive film is enhanced, and the active points in the passive film increase, so does the susceptibility to pitting corrosion. The pitting potential reduces (shift to the active direction) as the Cl^- ions concentration increases. Conversely, as the solution containing chloride ions is more dilute, the value of the pitting potential is observed at higher (more noble) potentials [28].

2.3.5. Flow

Fluid velocity is one of the effective parameters on the corrosion/pitting resistance of some alloys in CO_2 environments. The flow velocity influences the transport of cathodic species towards the steel surface, resulting in increased metal dissolution rates at higher flow velocities [15]. For alloys such as nickel chromium alloy, iron nickel alloy and iron chromium alloy, the high velocity of fluid does not permit to deposit suspended solids on the surface. This will cause changes in the composition and structure of the corrosion product films on the surface of the material and further affect the general corrosion and pitting behaviour of the material [28]. For example, the corrosion product film of HP-13Cr SS in the highly aggressive formation water was composed of $Cr(OH)_3$ and Cr_2O_3, of which $Cr(OH)_3$ was controlled by the dissolution-precipitation process and Cr_2O_3 was controlled by the electromigration process. The rotation speed would have a significant influence on the dissolution-precipitation process, resulting in decrease of the volume fraction of an amorphous $Cr(OH)_3$. Then, the density of the $Cr_2O_3/Cr(OH)_3$ phase boundary and the donor densities increased so as to the pitting corrosion was easier to occur [16].

Flow also alters the flow state within the pits, promoted the pitting geometry changes from bullet shape to shallow-disk shape. Furthermore, both the uniform corrosion and pitting corrosion would be accelerated in flowing solution and exhibited deeper pits. In brief, flow can promote the pitting growth rate in different directions [16].

2.4. Basic theory of stress corrosion cracking

Stress corrosion cracking (SCC) is defined as “spontaneous failure by cracking of metal under the combined action of high stress and corrosion”. There has been approved in the literature, the stress corrosion cracking resulted from tensile stress and the nucleation of crack at the metal surfaces required an incubation period [65].

Stress corrosion cracking can be divided into anodic dissolution mechanism and hydrogen-based mechanism according to the macroscopic mechanism. If the corresponding cathodic process during the dissolution of the anode metal is a hydrogen evolution reaction, and the generated atomic hydrogen can diffuse into the sample and control the nucleation and propagation of cracks, then this type of stress corrosion is a hydrogen-based stress corrosion cracking. If the corresponding cathodic reaction is an oxygen absorption reaction, or although the corresponding hydrogen evolution reaction, but the hydrogen concentration entering the sample is lower than the threshold value of hydrogen-induced cracking caused by the material, then it is a typical anodic dissolution stress corrosion [66].

2.4.1. Anodic dissolution mechanisms

Anodic dissolution mechanisms can be divided into film-induced cleavage mechanism, cracking of oxide film along grain boundary mechanism, slip dissolution-based mechanism, preferential dissolution mechanism, corrosion enhanced localized-plasticity mechanism and film-induced stress enhanced localized-plasticity mechanism. The preferred dissolution mechanism is proposed for aluminum alloys, which is not suitable for downhole corrosion resistant alloys so we don’t introduce it here. A brief introduction of the remaining mechanisms is provided in the following sections.

2.4.1.1. Film-induced cleavage

The film-induced cleavage (FIC) model for SCC of normally ductile materials, face-centred cubic (FCC) materials, was proposed by Sieradzki and Newman in 1985 [67, 68]. The model involves repeated sequences of (i) the formation of an environmentally induced brittle film at crack tips, (ii) rapid brittle fracture of the film, (iii) continuation of brittle fracture into the underlying substrate for distances that are much greater (10-1000x) than the film thickness, and (iv) crack-arrest and blunting (Figure 2-9). Thus, the model predicts that crack growth is discontinuous and that crack-arrest markings should be present on fracture surfaces, as sometimes observed. FIC has been proposed for both transgranular (cleavage-like) and intergranular cracking, although the term should not, strictly speaking, be applied to the latter since cleavage is transgranular.

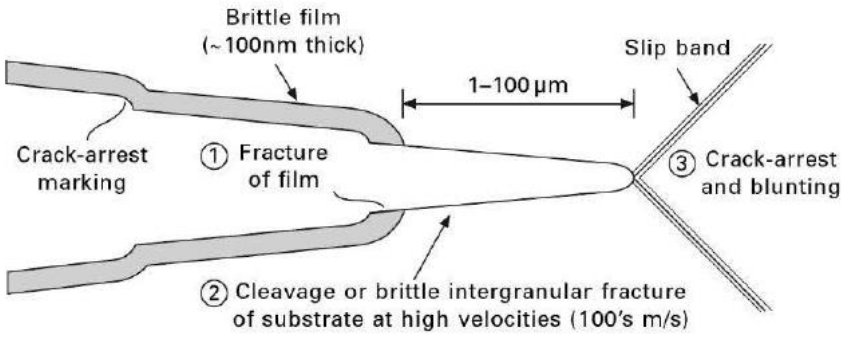

Figure 2-9. Schematic diagram illustrating the film-induced cleavage mechanism [69].

A basic assumption of the model is that a crack in the brittle film propagated at such high velocities (hundreds of meters per second or more), and continues to propagate into the substrate without slowing down, only very limited dislocation activity occur. It is assumed that due to occasional dislocation emission from crack tips or because crack encounters obstacles such as slip bands, the crack velocities decrease as cracks propagate. Then extensive dislocation activity (as usually occurs in FCC materials) take place, leading to crack arrest.

For FIC to occur, the film needs to be brittle and also be strongly bonded to the substrate. Other film properties, such as the degree

of coherency with the substrate, elastic modulus and film-thickness, are also important. Nano-porous, de-alloyed films are considered to be particularly effective in promoting cleavage in the substrate, providing that the porosity is sufficiently fine. Coarsening of de-alloyed films is thought to somehow destroy their ability to inject a brittle crack into the substrate.

2.4.1.2. Cracking of the oxide film along with grain boundary mechanism

The cracking of oxide film along the grain boundary mechanism was first used to explain the stress corrosion of brass in ammonia water. Grain boundary oxide film cracking refers to the alloy in a specific corrosion medium produce a very brittle or weak passive film, it forms along the grain boundary. Due to the limitation of the migration process, the grain boundary film is not very thick. If there is stress, the grain boundary film perpendicular to the stress will be brittlely broken, exposing fresh metal and corroded into a fracture. Under the applied stress, the fracture then is opened and the solution enter the crack. In this way, the brittle oxide film forms along the grain boundary along the crack tip. The repetition of this process causes stress corrosion to propagate along the grain boundaries. Because crack growth is achieved by the fracture of the brittle film that penetrates into the grain boundary, it is discontinuous, and the distance of each step is equal to the depth of the grain boundary film [70]. In this way, some fatigue-like patterns can be seen at the epitaxial fracture.

The schematic diagram is shown in Figure 2-10, and the stages in the figure are as follows: First oxide film and pitting form on the surface and oxide film grow along the grain boundary at the location where the surface oxide film break. After that, under the effect of external stress and film-induced stress, the oxide film along the grain boundary crack locally, and discontinuous microcracks appears in the grain boundary oxide film in front of the crack tip. Then discontinuous microcracks grow and connect, and oxide film continues to grow along the grain boundary. The above process repeats, leading to crack propagation [66].

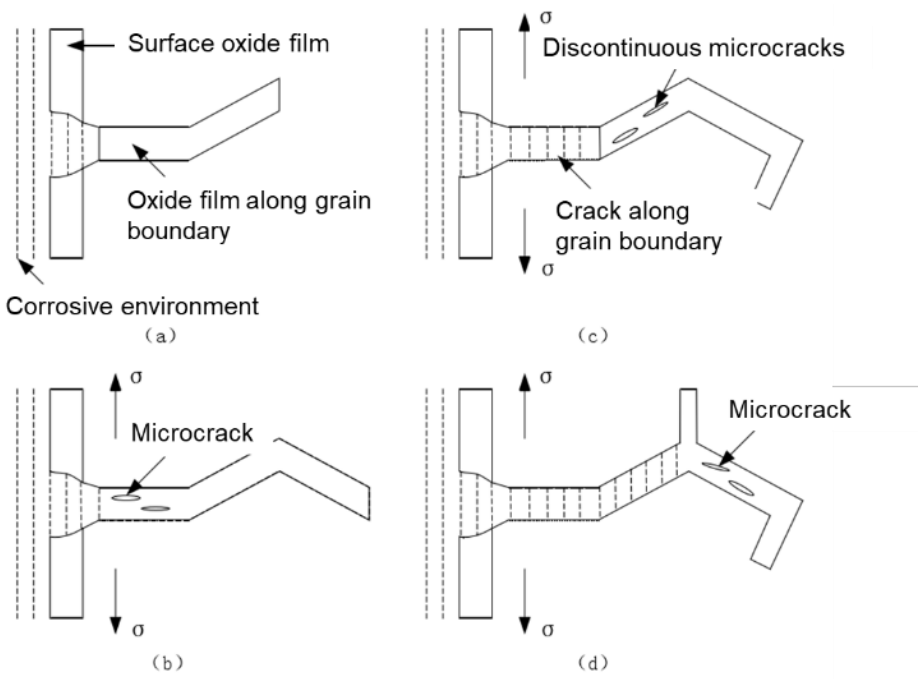

Figure 2-10. Schematic diagram illustrating the cracking of oxide film along with the grain boundary mechanism for SCC [66].

2.4.1.3. Dissolution-based mechanisms

Mechanisms of SCC based on dissolution require atoms at the crack tips to be removed preferentially in a direction approximately normal to the applied stress, with only limited dissolution behind the crack tip. Direct dissolution could be promoted by either a chemically active path, such as grain boundaries, or an active path generated by stress/strain concentrated at crack tips.

The slip-dissolution mechanism (also known as the film-rupture/anodic dissolution mechanism) is the most widely cited dissolution-based SCC process. It involves the rupture of protective films by slip bands intersecting the crack tip, then dissolution along grain boundaries or low-index crystallographic planes until repassivation occurs. Alternatively, crack tips may remain essentially film-free if the crack-tip strain-rate is high compared with the repassivation rate. In addition to rupturing protective films, slip processes increase the crack-tip-opening displacement, allowing solvent ions and solvated ions to diffuse to crack tips more rapidly so that dissolution does not inhibited by salt films or other corrosion products (Figure 2-11) [71].

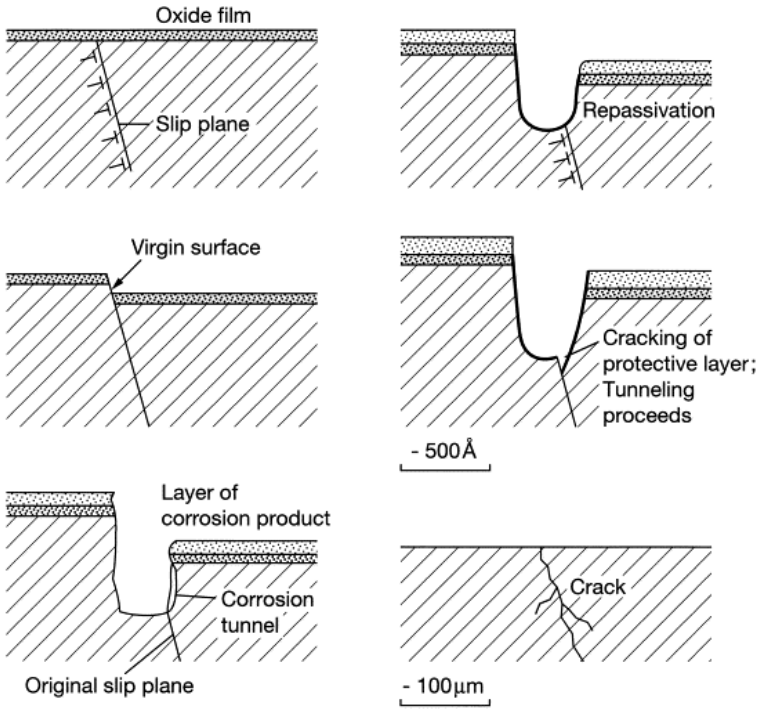

Figure 2-11. Schematic diagram illustrating the slip-dissolution mechanism for SCC [71].

2.4.1.4. Corrosion enhanced localized-plasticity mechanism and film-induced stress enhanced localized-plasticity mechanism

Corrosion enhanced localized-plasticity mechanism was thought to occur by the following sequence of events: stress leads the rupture of the passive film, in the meantime, adsorption of chloride ions at the rupture position inhibit the repassivation. At these ruptured locations, anodic dissolution occurs, generating a high density of vacancies. These vacancies diffuse into the metal matrix and interact with dislocations, lowering the barrier to dislocation motion. As a result, dislocations can move under lower applied stress, enhancing local plastic deformation. The increased local plastic deformation produces a triaxial stress state, which in turn facilitates crack nucleation along active slip planes [72].

Film-induced stress enhanced localized-plasticity mechanism is also a form of corrosion enhanced localized-plasticity mechanism. It proposes that the formed corrosion product film can impose tensile stress on the underlying metal substrate. Once the superimposition

of the applied tensile stress and tensile stress caused by the corrosion product film make the local plastic deformation develop to a critical state, SCC initiates and propagates. In this case, the sensitivity of stress corrosion was related to the thickness and properties of the corrosion product film, the greater the additional stress caused by the film, the more sensitive the stress corrosion was [73].

2.4.2. Hydrogen-based mechanisms

Mechanisms of SCC based on the effects of hydrogen on deformation and fracture are widely accepted for many materials, e.g. high-strength steels, nickel alloys, titanium alloys, aluminium alloys and magnesium alloys, since (i) hydrogen can be generated at crack tips by chemical dissociation of water molecules or by electrochemical reactions, (ii) these materials are known to be embrittled by hydrogen (after hydrogen-charging and testing in inert environments or during testing in gaseous hydrogen), and (iii) SCC in some of these materials can occur in moist air where dissolution and some other environmental interactions can be discounted.

The characteristics of fracture surfaces produced by stress corrosion cracking and hydrogen embrittlement (HE) in the materials mentioned above are similar (except for differences in films or corrosion on fracture surfaces). Hence, mechanisms of SCC based on hydrogen are thought to be essentially the same as those proposed for HE, and involve either adsorbed hydrogen, dissolved hydrogen, or hydrides at crack tips. The mechanisms of SCC induced by hydrogen are summarised in the following.

2.4.2.1. Mechanisms based on adsorbed hydrogen

These mechanisms involve the weakening of substrate interatomic bonds leading to easier dislocation emission (adsorption-induced dislocation emission (AIDE)) or decohesion at crack tips. Adsorbed hydrogen can readily diffuse ahead of crack tips compare to other adsorbed species, so that adsorption of hydrogen could occur not only at external crack tips but also at internal cracks (and voids just ahead of cracks) [74]. When hydrogen adsorption promotes dislocation emission from crack-tips, a greater proportion of the

dislocation activity results in crack growth since dislocation emission on suitably inclined slip planes produces crack advance as well as crack opening. Hence, coalescence of cracks with voids occurs at lower strains and shallower dimples were produced on fracture surfaces when AIDE occurs (Figure 2-12) [75]. Another difference between hydrogen and other adsorbed species, related to the ease of hydrogen diffusion, is that high hydrogen concentrations are likely to be present within the first few atomic layers beneath crack tips as well as on the surface. Interatomic bonds involved in dislocation emission or decohesion at crack tips would probably be weakened to greater extents when hydrogen is present within the first few atomic distances as well as on the surface compared with when hydrogen is present only on the surface. For convenience, hydrogen on the surface and within a few atomic distances of surfaces is defined as 'adsorbed hydrogen' for the purposes of discussing mechanisms of HE and SCC, as already mentioned [69].

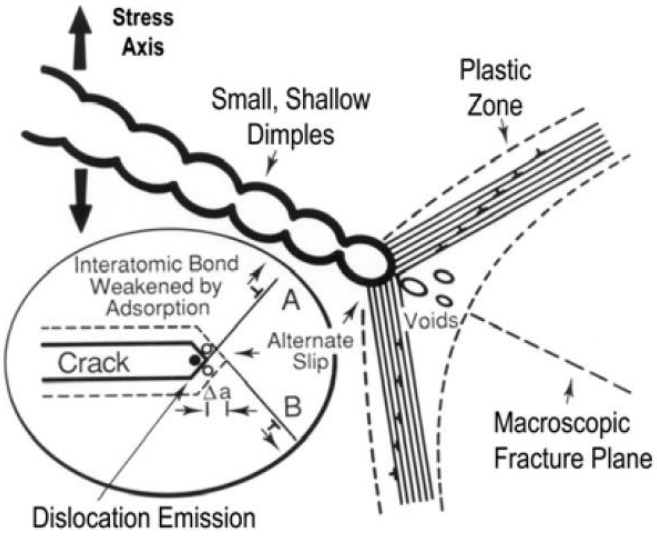

Figure 2-12. Schematic diagrams illustrating the adsorption-induced dislocation emission mechanism for transgranular crack growth [75].

2.4.2.2. Mechanisms based on solute hydrogen

The mechanisms based on solute hydrogen can be divided into two categories:

(1) Hydrogen-enhanced decohesion (HEDE) mechanism: solute hydrogen weakens interatomic bonds and facilitates decohesion (as for adsorbed hydrogen but further ahead of crack tips).

(2) Hydrogen-enhanced localized-plasticity (HELP) mechanism: solute hydrogen facilitates dislocation activity in the plastic zone ahead of cracks and promotes crack growth by a more localized slip/microvoid-coalescence process than that which occurs in inert environments.

The HEDE mechanism involve hydrogen concentrating in regions of high hydrostatic stress where the lattice is slightly dilated, at particle-matrix interfaces, or at grain boundaries. The HELP mechanism also involves localized hydrogen concentrations ahead of crack tips due to high hydrostatic stresses (or due to hydrogen entry at crack tips), and it is based on hydrogen atmospheres around dislocations, or hydrogen at dislocation cores, facilitating dislocation movement in the localized regions where hydrogen is concentrated [76].

2.4.2.3. Combinations of mechanisms

Combinations of AIDE, HELP and HEDE mechanisms could occur in many cases [77]. For example, dislocations nucleated from crack tips (due to AIDE) may move away from crack tips more readily due to HELP, thereby decreasing the back-stress on subsequent dislocation emission. For crack growth predominantly by AIDE, void-nucleation ahead of cracks could be promoted at slip-band intersections by HELP or by HEDE at particle- matrix interfaces. AIDE and HEDE could also occur sequentially, with AIDE occurring until the back-stress from emitted dislocations increased somewhat so that HEDE then occurred, followed by AIDE again when the crack tip had moved away from the stress-field of dislocations previously emitted. As well as AIDE and HELP possibly acting conjointly to localize plasticity, additional strain-localization could occur due to the effect of vacancies on deformation and fracture, with hydrogen reducing the vacancy-formation energy and stabilizing vacancies produced by dislocation-dislocation interactions, as discussed in the next section [69].

3. Chapter 3 13%Cr martensitic stainless steel for HTHP downhole environments and its corrosion and cracking performance.

3.1. Development of martensitic stainless steel

Martensitic stainless steel is named after its microstructure, which is martensitic, a metastable interstitial solid solution of carbon in iron. Martensite (α' Fe) is a supersaturated solid solution of carbon in α-Fe with a body-centred tetragonal (BCT) crystal structure, it is not shown in the equilibrium phase diagram of the iron-carbon system as it is not an equilibrium phase. Martensite always forms in carbon-containing steel by a rapid cooling (quenching) of the austenite as carbon atoms do not have enough time to diffuse to form Fe_3C [78-80]. Compared to other types of stainless steel such as austenitic stainless steel, ferritic stainless steel, duplex stainless steel, and precipitation hardened stainless steel, martensitic stainless steel is known for its high strength, hardness, and wear resistance which contributed by its martensitic microstructure [81].

Usually the phase composition of stainless steel can be simply predicted by the Schaeffler constitutional diagram [82] as shown in Figure 3-1. Martensitic stainless steels are typically made up of high amounts of chromium (11.5%-18%), as well as varying amounts of carbon, silicon, nickel, molybdenum, and other elements. The high chromium content gives martensitic stainless steel its excellent corrosion resistance, while the carbon content contributes to its high strength and hardness [83, 84].

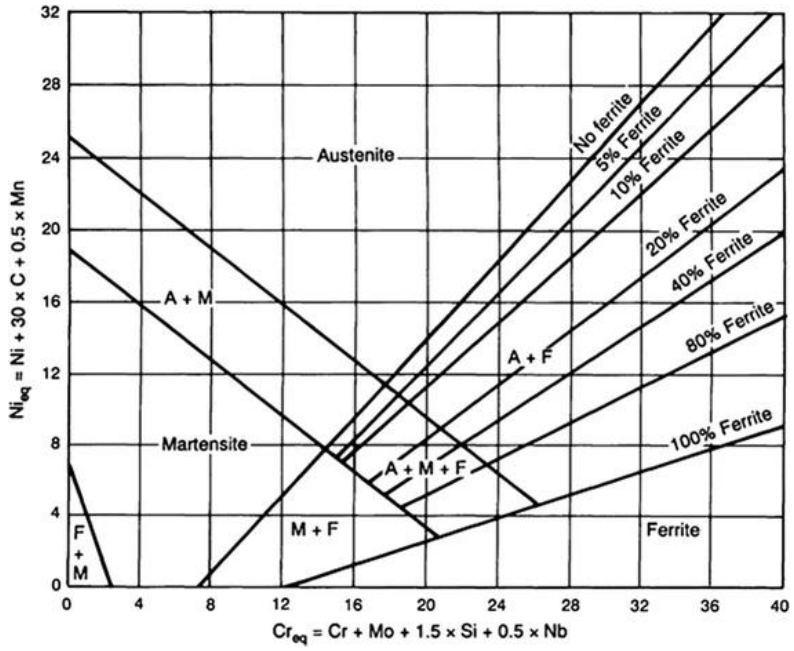

Figure 3-1. Schaeffler constitutional diagram [82].

Martensite microstructure was first observed by German microscopist Adolf Martens at around 1890 and then officially named after him. Then in 1913, Harry Brearley of the Brown-Firth research laboratory in Sheffield, England discovered the industrialized first commercial martensitic stainless steel (12.8% Cr, 0.24% C, 0.44% Mn, Bal. Fe) [85]. In the decades since then, researchers continued to refine the composition and heat treatment of martensitic stainless steel to improve the its performance. Today, martensitic stainless steel has been widely used in a variety of industrial applications, such as aerospace, automotive, medical industries, oil and gas, chemical industry and etc due to its high strength, hardness, and wear resistance, making it ideal for applications that require these properties.

In terms of the application in oil and gas industry, 13% Chrome (13Cr) martensitic stainless steels (MSS) debuted as oil country tubular goods (OCTG) during the early 1980s owing to its good corrosion resistance in the high carbon dioxide and chloride environment, and have been beneficial cost solution for many fields [86]. However, the high carbon content poses problems for its welding as well as corrosion resistance [87]. The limitation of 13Cr MSS strength capabilities due to heat treatment and chemistry, and the susceptibility to CO_2 corrosion at elevated temperature and

cracking in H_2S environments restricted the usability of this material beyond 80 ksi grade. Under this circumstance, a great metallurgical effort has been undertaken to enhance the performance of 13Cr materials. With the metallurgical technology progress, argon oxygen furnace/vacuum decarburisation furnace refining technology became widely used in the refining of stainless steel, the carbon content of stainless steel was therefore capable to be controlled under 0.03%, low carbon martensitic stainless steels, called super martensitic stainless steels, then were developed and been used as line pipes since the late 1990's.

In the meantime, the effect of alloying elements on the corrosion performance of modified 13Cr MSS were widely studied to improve the performance of 13Cr MSS. Among the numerous alloying elements, Ni and Mo are the most common alloying elements in 13Cr MSS. The addition of Ni stabilizes the martensitic phase without ferrite, and the addition of Mo is to improve the resistance to localized corrosion and sulphide stress cracking (SSC) [86, 88]. Within a range of modified 13Cr MSS, 13Cr MSS with 5% Ni and 2% Mo stands out due to its excellent corrosion resistance as shown in Figure 3-2 [89].

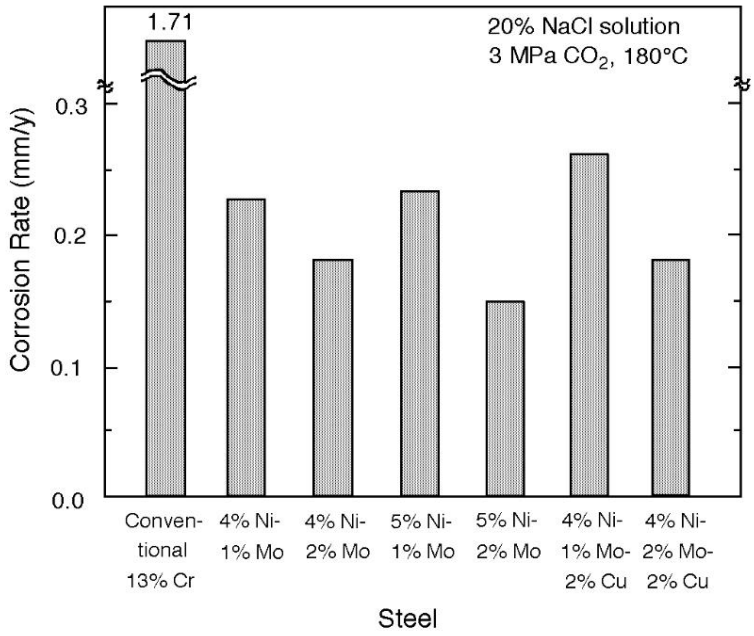

Figure 3-2. Effect of alloying element on CO_2 corrosion rate [89].

3.2. Austenite in martensitic stainless steel

The widely application of martensitic stainless steel is mainly due to its excellent strength and wear resistance provide by its martensitic structure, but the martensitic structure also has the obvious defect of being brittle. Introducing precipitated austenite into the martensitic matrix is a common method of adjusting the mechanical properties [84, 90].

Austenite, also known as gamma-phase iron (γ-Fe), is a solid solution of iron and carbon and has a face-centred cubic (FCC) structure. Austenite, compared to martensite, is relatively soft and ductile. In general, a higher austenite content in martensitic stainless steels results in improved toughness and ductility, but reduced hardness and strength. Conversely, a lower austenite content results in increased hardness and strength, but decreased toughness and ductility [84, 91]. Overall, the presence of austenite in martensitic stainless steels can be both beneficial and detrimental depending on the specific application and desired properties.

3.2.1. Formation of austenite in martensitic stainless steel

Austenite introduced in martensitic stainless steel by heat treatment can be divided into retained austenite and reversed austenite according to their heat treatment process [92]. Austenite forms when the steel is heated and then cooled from fully austenite region is called “retained austenite”. Correspondingly, the austenite obtained when steel is heated and then cooled from incomplete austenite region is called “reversed austenite”.

3.2.1.1. Formation of remained austenite in martensitic stainless steel

Retained austenite forms when the steel is heated to the fully austenite region and then quenched. During the quenching process, once the temperature lowers the martensitic start temperature (Ms), austenite will gradually transform to martensite by shear transformation without element diffusion. The shear transformation from austenite to martensite causes volume expansion, leading to an increase in the resistance to shear transformation of the

austenite between martensite [93], resulting in the inhibition of transformation of the rest austenite to martensite. Austenite that does not transform to martensite upon quenching is called “retained austenite” and mainly distribute between martensite laths.

The Ms temperature is the temperature that austenite to martensite transformation begins at, it is a very useful parameter for estimating the stability of austenite. Ms temperature can be described as a parameter that affected by steel chemistry as the following equation proposed by Ishida [94]:

$$\text{Ms (°C, wt.\%)} = 545\text{-}330\text{C}+2\text{Al} +7\text{Co}-14\text{Cr}-13\text{Cu}-23\text{Mn}-5\text{Mo}-4\text{Nb} -13\text{Ni}-7\text{Si}+3\text{Ti}+4\text{V}+0\text{W} \quad (3\text{-}1)$$

A lower Ms temperature might associated with a more stable austenite, make it more easy to get a high amount of retained austenite in material after quenching process as illustrated in Figure 3-3 [95].

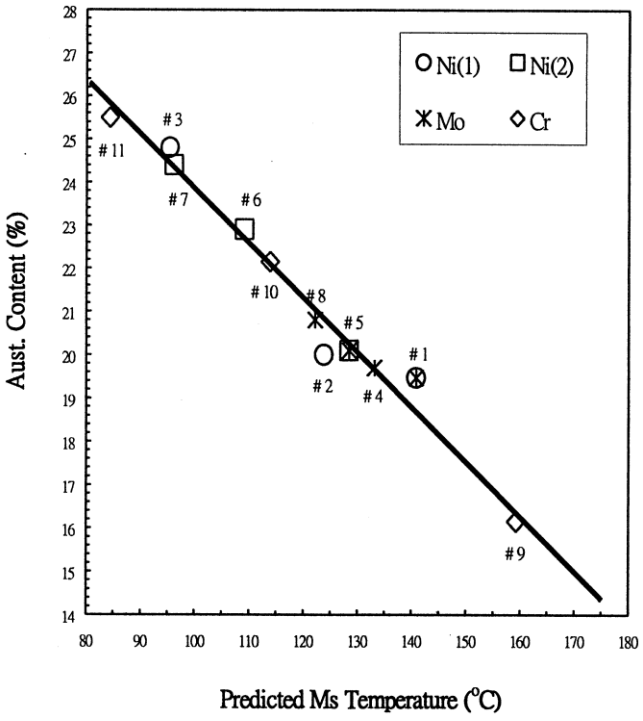

Figure 3-3. Relationship between retained austenite and the predicted Ms temperature [95].

Besides steel chemistry, austenitization temperature and cooling rate also effects the stability of austenite by effect the Ms temperature. According to the research provide by Tsai [96], higher

austenitization temperature and cooling rate tend to result in lower Ms temperature.

3.2.1.2. Formation of reversed austenite in martensitic stainless steel

In martensitic stainless steels, the reversed austenite formation is a two-stage process during an entire tempering process. During the first stage, the steel is heated to an incomplete austenitization temperature and held at that temperature for a period of time to allow the martensite transform to austenite, called “reversed austenite”. During the second stage, the steel is rapidly cooled, part of the reversed austenite will transform back to martensite, a proportion of reversed austenite remains in steel after cooling to room temperature during this process.

During the first stage, which is the heating stage, the martensite to reversed austenite phase transformation begins at As (starting temperature of austenite formation), and fully transform to austenite at temperature above Af (finishing temperature of austenite formation). The austenite fraction increases with temperature between As and Af as shown in Figure 3-4 [97].

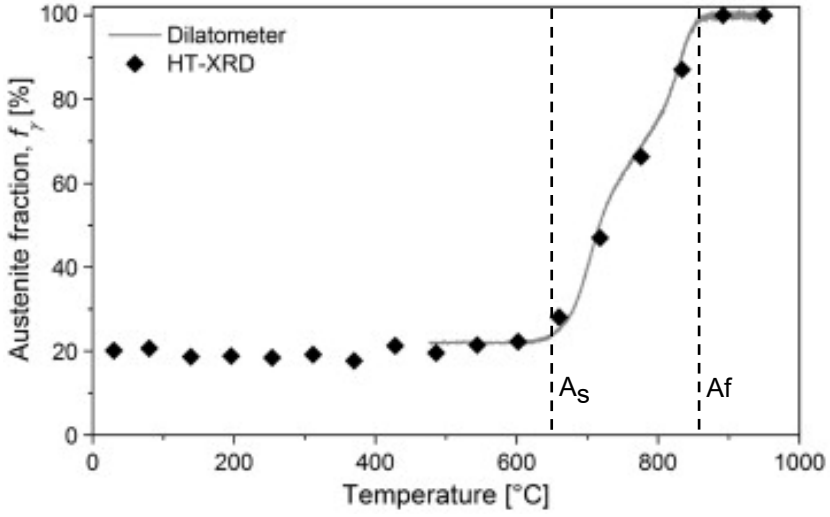

Figure 3-4. Austenite fraction of 13Cr6Ni2Mo SMSS during heating obtained from dilatometry and HT-XRD experiment [97].

Similar to Ms, As can be also described as a parameter that affected by steel chemistry and effect by heating rate as well. An approximation for the As temperature of 13%Cr steels with less than 0.05 wt.% C can be described as the following equation [98]:

$$As\ (°C, wt.\%) = 850-1500(C+N)-50Ni-25Mn+25Si+25Mo+20(Cr-10) \quad (3\text{-}2)$$

The martensite to austenite phase transformation occurring during the heating and holding steps of tempering is a diffusional phase transformation which represent the formation of reversed austenite not only undergoes phase transformation, but also undergoes element diffusion, resulting in a different composition of reversed austenite from the surrounding martensite. According to thermodynamic equilibrium, growth of austenite requires an inward-flux of Ni and outward-flux of Cr as shown in Figure 3-5 [81]. Ni-enrichment in austenite decreases with increasing annealing temperature, indicating the reversed austenite form at a lower temperature is more stable (with lower Ms).

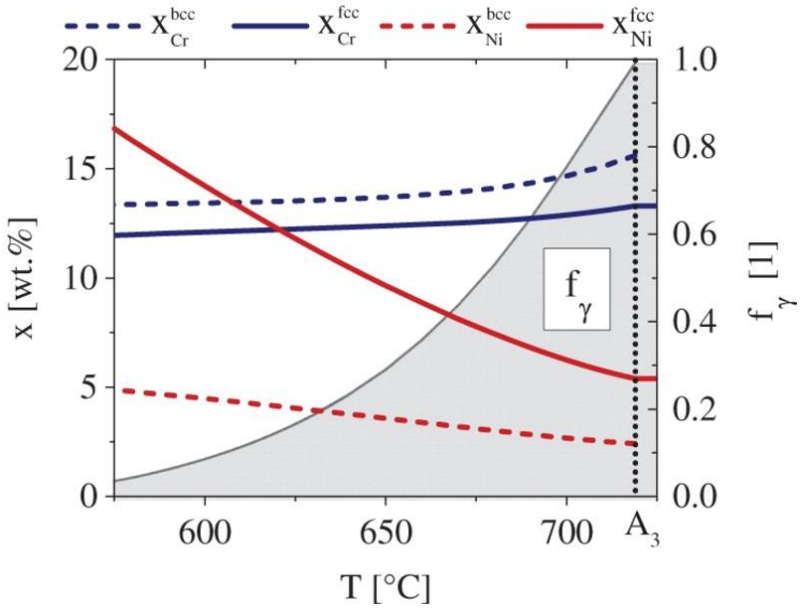

Figure 3-5. Ni and Cr concentration in austenite (fcc) and ferrite (bcc) as well as the molar fraction of austenite (grey area) from an equilibrium calculation of a representative Fe-3.3Cr-5.4Ni (wt%) ternary alloy [81].

During the second stage, which is the cooling stage, austenite transforms to martensite, which controlled by the stability of

austenite. The stability of austenite in martensitic stainless steel in this cooling process is affected by several factors, as introduced before, including the carbon content, the alloying elements, the heating temperature, and the cooling rate. The less stable the austenite, the higher the fraction of transformation from austenite to martensite during the cooling process.

Thus, it can be summarized that during tempering, the amount of reversed austenite is controlled by two factors: the transformation volume of austenite under high temperature and the stability of austenite in tempering cooling process. On one hand, a higher tempering temperature can induce a higher transformation volume of austenite under high temperature. One the other hand, As the tempering temperature increases, the concentration of austenite forming element such as Ni in reversed austenite decreases, resulting in a decrease in the stability of the reversed austenite, reversed austenite becomes easier to transform to martensite during cooling process. So there exists an optimal temperature under which the volume fraction of reversed austenite is maximum in the temperature range from As to Af as shown in Figure 3-6 [99].

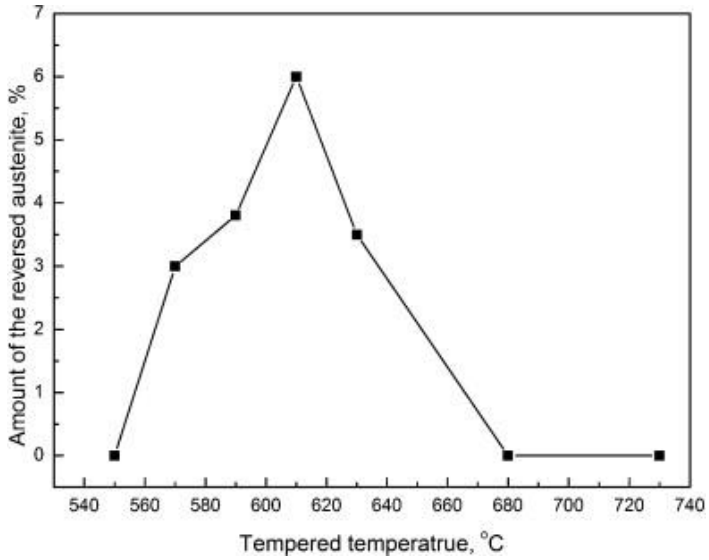

Figure 3-6. Variation in room temperature amount of the reversed austenite with the tempering temperature [99].

Besides the heating temperature, cooling rate also significantly affects the retained reversed austenite content at room temperature. As shown in Figure 3-6, the air-cooled (high cooling rate) specimen

has smaller amount of reversed austenite than the furnace-cooled (low cooling rate) specimen at all tempering treatment temperatures. The smaller amount of retained austenite for a higher cooling rate is attributable to more unstable austenite due to introduction of a higher thermal stress and higher concentration of quenched-in vacancies at the Ms temperature from higher cooling rate [91].

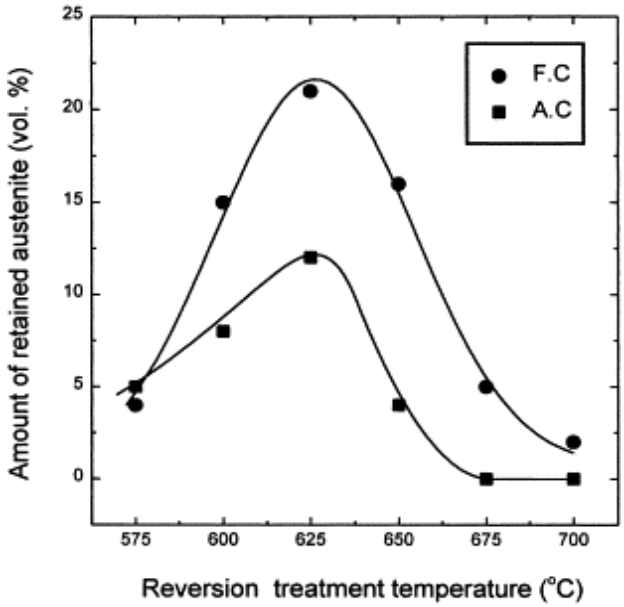

Figure 3-7. Variation in amount of retained reversed austenite with reversion treatment temperature by air cooling (A.C) and furnace cooling (F.C) [91].

The tempering holding time is an important parameter that effect the reversed austenite content as well. As indicated in Figure 3-8, the amount of reversed austenite is reported to reached the maximum when the holding time reaching critical value at which thermodynamic equilibrium is attained. After that, with increasing holding time, the reversed austenite decrease as the growth of $M_{23}C_6$ consumes carbon and chromium in the reversed austenite, therefore decrease the stability of austenite and resulting a reversed austenite content decrease after cooling [79].

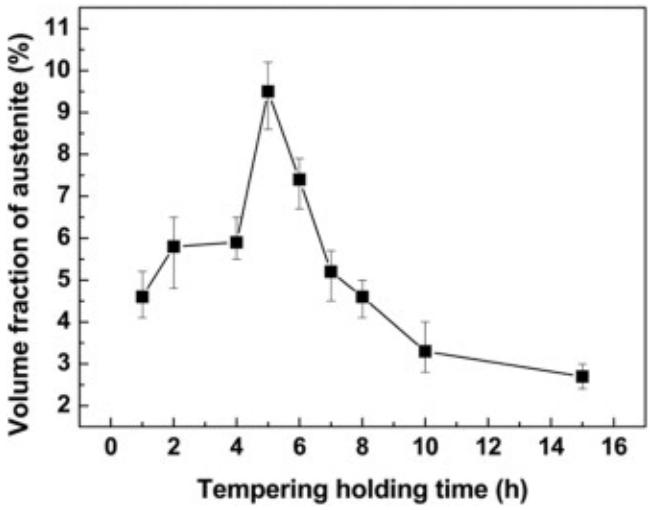

Figure 3-8. The amount of retained austenite obtained after tempering at 620°C for different holding times [79].

The distribution and morphology of austenite is widely reported to be significant influenced by the heating temperature [100, 101]. As indicated in Figure 3-9(a), reversed austenite with film morphology forms at lath boundaries when temperature slightly above As, it is worth noting that austenite grows from the lath boundary into only one of the laths in this stage [102]. Above this temperature, austenite films begin to grow into both laths adjacent to a lath boundary as shown in Figure 3-9(b) [101, 103]. At elevated temperature lower than Af, reversed austenite tends towards a blocky morphology, first at prior austenite grain boundaries (Figure 3-9(c)) and at higher temperature within martensite laths (Figure 3-9(d)) [92, 104]. This mainly because of lower required partitioning of Ni as shown in Figure 3-5 at higher temperature, resulting in easier formation of nucleation sites inside martensite laths.

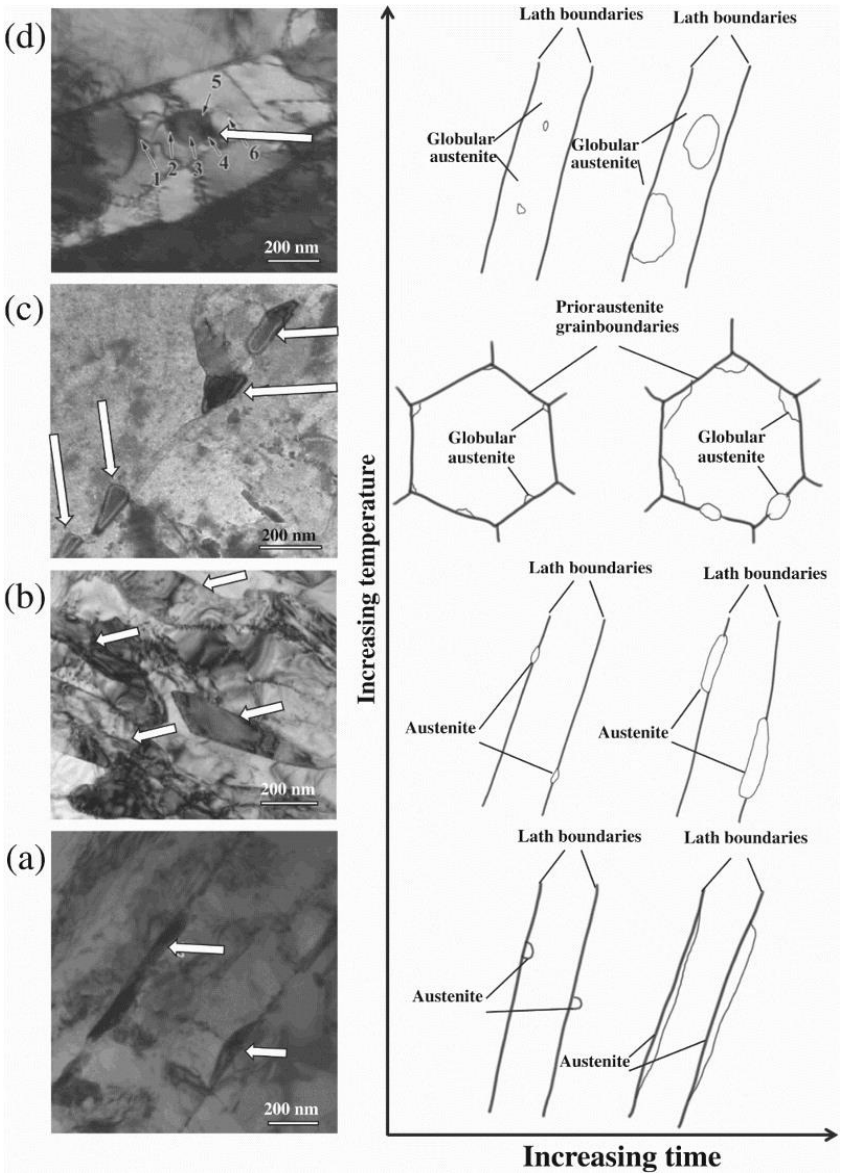

Figure 3-9. Bright-field micrographs and schematics of the evolution of the reversed austenite morphology with temperature and time in low C martensitic stainless steels: (a) low temperature film morphology; (b) elevated temperature film morphology; (c) globular morphology at prior austenite grain boundaries; (d) globular morphology inside martensite laths [81].

Carbides in martensite stainless steel shows a strong relationship with the nucleation of reversed austenite. The $M_{23}C_6$ carbide precipitates are commonly observed in martensitic stainless steel after tempering as Cr is a strong carbide former alloying element. During tempering, the $M_{23}C_6$ carbides are precipitated preferentially at the martensite lath boundaries as the boundary sites are

preferred because of the greater ease of diffusion in these regions [78]. The $M_{23}C_6$ carbides have a limited solubility in Ni, which also causes the Ni atoms to diffuse to the adjacent area, providing the nucleate site for the reversed austenite formation. Thus the reversed austenite formed adjacent to the carbides with the Ni-enrichment as the nucleation sites at the tempered temperature above the As temperature [105].

3.2.2. The role of austenite in mechanical property of martensitic stainless steel

Martensite is a type of phase that is characterized by high strength, hardness, and wear resistance, but relatively low ductility and toughness; while austenite is characterized by highly ductile and toughness. Therefore, introducing a certain amount austenite into martensite can achieve a good combination of strength-ductility by martensite for strength while austenite for ductility.

Generally, an increase in the austenite content of martensitic steel leads to a decrease in the hardness, yield strength as well as the ultimate tensile strength, and an increase in the impact toughness and elongation of the material [84, 106, 107]. This is well summarized by Niessen [81] as shown in Figure 3-10. It should be notice that the maximum hardness, yield strength and ultimate tensile strength obtained at temperature around 475°C which is not the maximum austenite content temperature, this was identified to be an effect of secondary hardening from precipitation of Mo_2C.

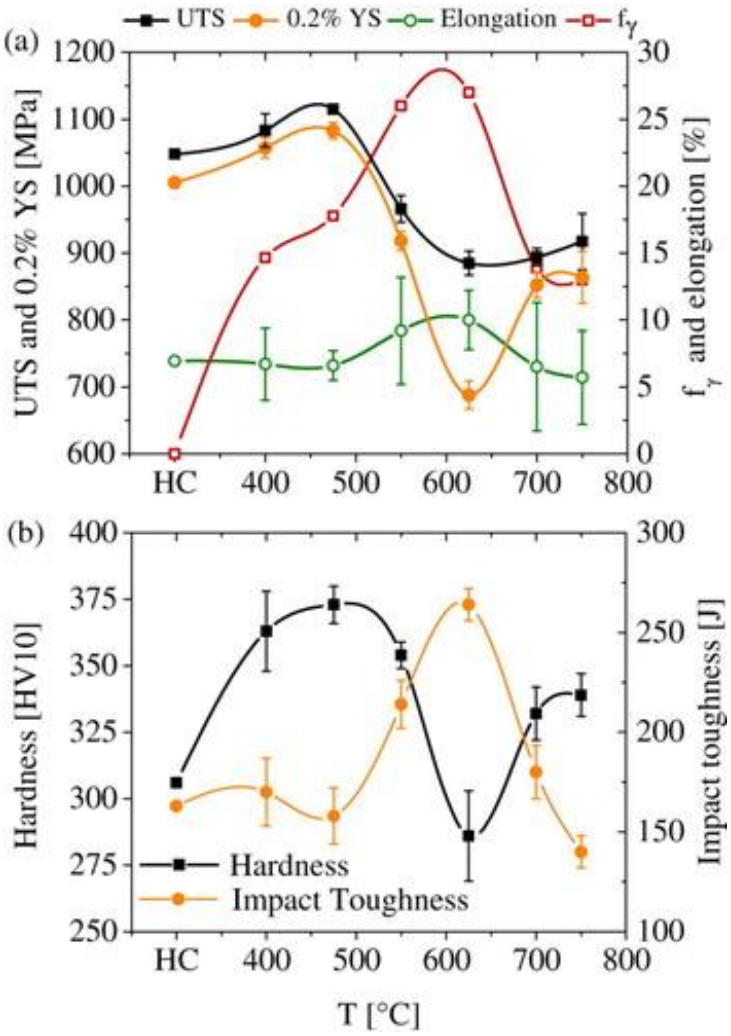

Figure 3-10. Fraction austenite and mechanical properties of a 16Cr–5Ni–1Mo stainless steel at room temperature in the hardened condition (HC) and after 4 h soaking at various temperatures: (a) ultimate tensile strength (UTS), 0.2% yield strength (YS), elongation and fraction austenite (); (b) hardness and Charpy V impact toughness; the lines are spline functions of measured data (symbols) and do not represent physical valuesm [81].

Low yield to tensile ratio and high ductility were achieved at high austenite content condition, this is reported to be contributed by transformation-induced plasticity (TRIP) effect from high volume fraction of austenite. When the crack propagated to the reversed austenite phase, the austenite consumed a large amount of deformation work while transform to martensite, and hinder the further propagation of the crack and thus increase the total elongation, ultimate tensile strength and toughness [108].

3.2.3. The role of austenite in corrosion of martensitic stainless steel

There are different opinions on the effect of increasing the austenite content by tempering on the corrosion properties of the steels. Some researchers believe that increasing the austenite content will improve the pitting resistance of the steels, while some hold the opposite view.

Zhao et al. [109] proved that the pitting resistance of S13Cr MSS increased with increasing reversed austenite content by Electrochemical Impedance Spectroscopy (EIS) and potentiodynamic polarisation measurement. As shown in Figure 3-11, the Electron Backscatter Diffraction (EBSD) results indicated that reversed austenite formation restricted the movement of dislocations, and reduced the dislocations density. Therefore, the increasing in the reversed austenite content could improve the passive film compactness, and inhibit the penetration of Cl^-, thus reducing the risk of pitting corrosion. Accordingly, the pitting corrosion resistance of S13Cr MSS was enhanced as the tempering temperature increased as shown in Figure 3-12. Similar result was also reported by Wang et al. [110].

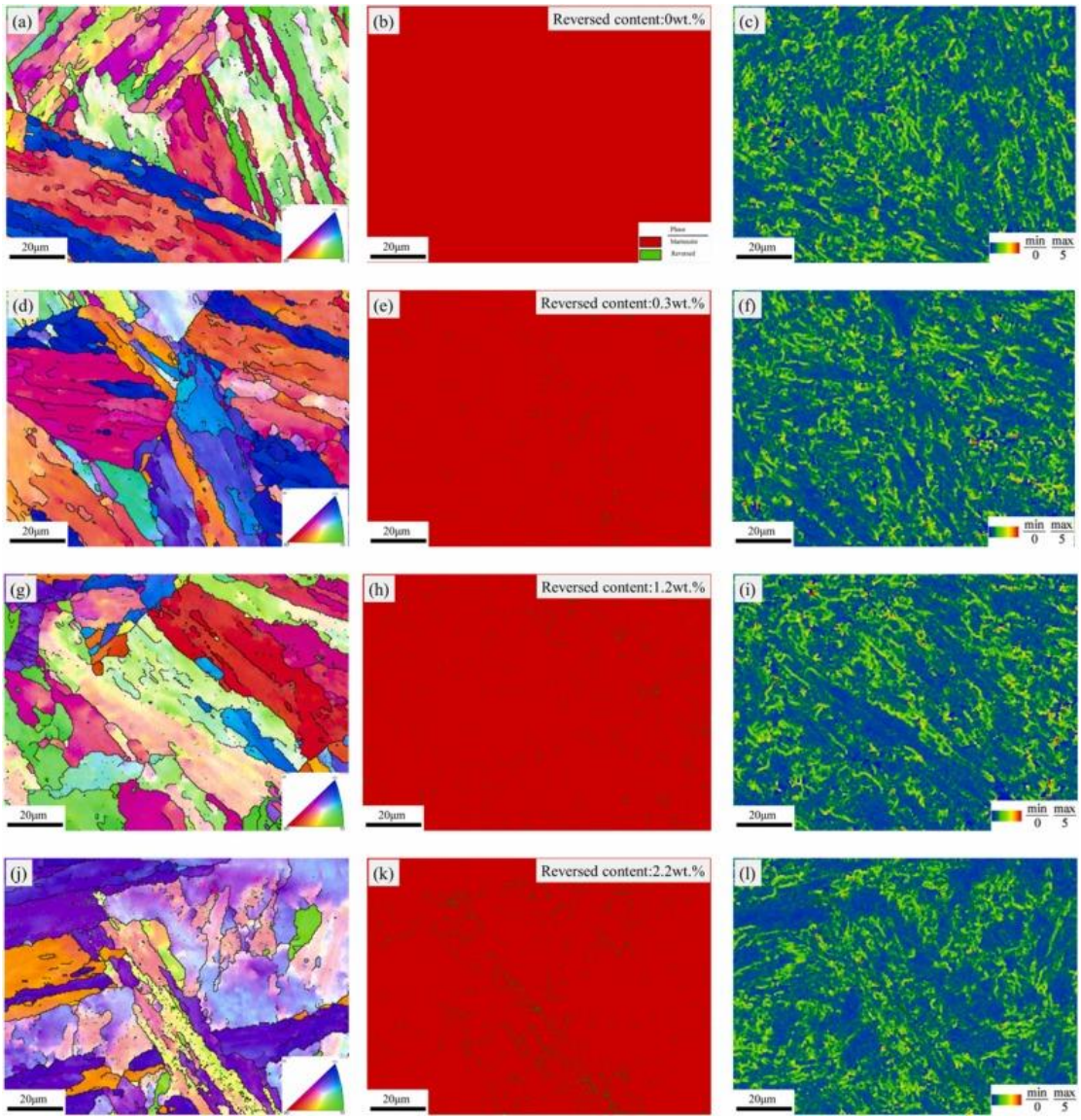

Figure 3-11. Inverse pole figure (left), phase(middle) and KAM (right) maps of S13Cr MSS with different tempering temperatures: (a) (b) (c) as-quenched; (d) (e) (f) 750°C; (g) (h) (i) 850°C; (j) (k) (l) 950°C [109].

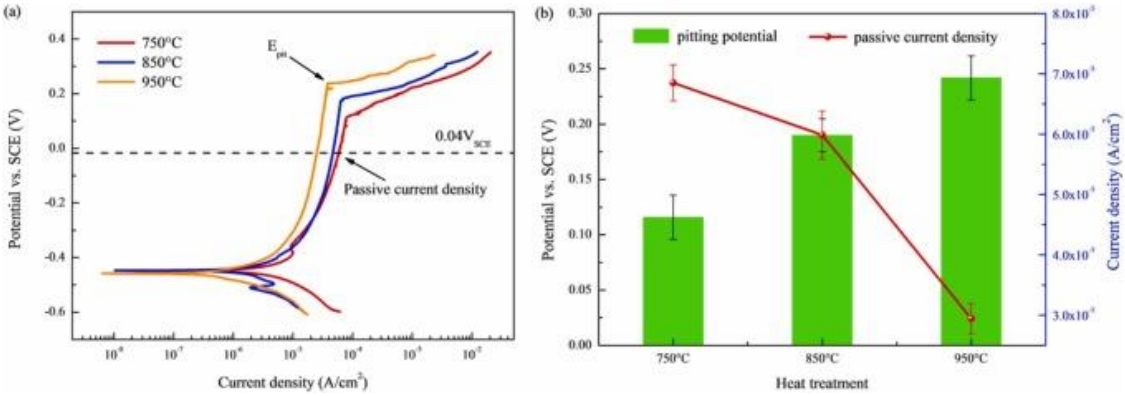

Figure 3-12. Polarisation curves of S13Cr MSS exposed to the 3.5 wt% NaCl solution: (a) after tempering process; (b) relative parameters [109].

However, Carvalho et al. [111] reported that the Ni-partitioning resulting from austenite reversion process led to an increase in the susceptibility of the alloy to pitting corrosion. Santos et al. [112] also found that the great fractions of austenite decrease corrosion resistance by electrochemical tests. But they observed a different behaviour at the immersion test, the austenite ennoblement due to higher Ni content decreases the corrosion rate during immersion in 0.5 M H_2SO_4 solution.

Moreover, Mitsuo et al. [113] reported that the pitting potential for modified 13% Cr steel were independent of the retained austenite content.

When discussing the effect of austenite content on corrosion resistance, in addition to the austenite phase itself, it is also necessary to consider carbides, precipitates or intermetallic compounds which formed associated with the tempering process when adjusting the austenite content in martensitic stainless steel.

Carbides, especially $M_{23}C_6$, are widely discussed when evaluating the effect of austenite/tempering on the corrosion behaviour of MSSs. However, there are two different views on the influence of reversed austenite on the pitting resistance of MSSs in the coexistence of austenite and carbides condition. Both Lei et al. [114] and Man et al. [115] observed that the reversed austenite nucleated around the Cr-rich carbides and reduced the extent of Cr depletion around carbides and enhances the stability of passive film. Zhao et al. [116] and Bonagani et al. [117] found that the Cr

contents in the Cr-depleted regions increased with increasing tempering temperature, but remained lower than the value of the steel matrix, Meanwhile, the austenite content decreased, and the size as well as the density of Cr-depleted regions were also reduced with increasing tempering temperature. These factors together led to an enhanced pitting corrosion resistance as the tempering temperature increased. However, Abbasi et al.[118] reported that the corrosion resistance of AISI420 MSS decreased with increasing austenite content. This is believed to be related to the formation of the carbides and associated Cr-depleted region at high temperature while a high austenite content is obtained, thus reduced the corrosion resistance of AISI420 MSS.

Besides, Wang et al. [119] investigated the effect of tempering temperature on the corrosion resistance of Custom 465 nickel-rich martensitic stainless steel. As indicated in the Figure 3-13, increasing tempering resulted in coarsening of the η-Ni_3Ti precipitates and increasing reversed austenite content. The coarsening of the η-Ni_3Ti precipitates caused the reduction of the nickel content in the matrix, which resulted in a decrease of the stability of the matrix passive film. But when the tempering temperature was higher than 648°C, the amount of reversed austenite gradually increased to 14%. Therefore, the passive film stability and pitting corrosion resistance gradually increased attributed to the nickel enrichment in reversed austenite, which was beneficial for passive film stability. Thus, in summary, when the tempering temperature increased from 482°C to 648°C, the η-Ni3Ti precipitates gradually coarsened to 150 nm and the reversed austenite gradually increased to 14%, which first decreased and then increased the passive film stability.

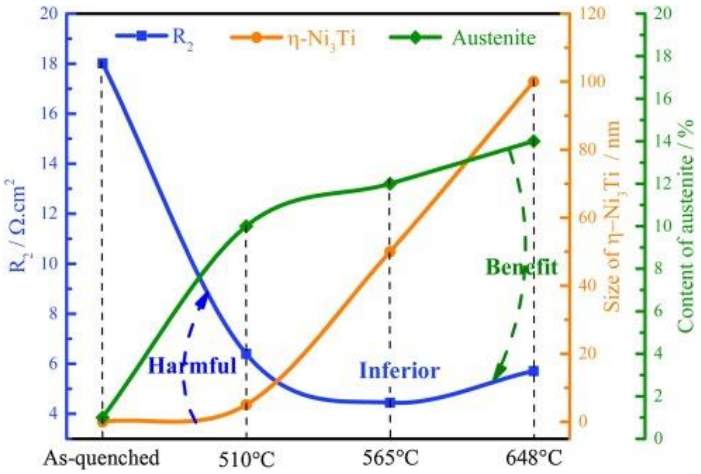

Figure 3-13. Correlation between the passive film stability, η-Ni3Ti precipitates and reversed austenite [119].

Research work presented by Zhao and co-workers [120] on S13Cr MSS showed tempered specimens exhibited worse pitting resistance than as-quenched specimen. This can be contributed to the formation of Mo-rich intermetallic compounds and related Mo-depleted region during tempering process. As shown in Figure 3-14, the Mo-rich intermetallic compound is accompanied with a Mo-depleted region which had an approximately 7 mV Volta potential lower than the matrix and destroying the corrosion film stability.

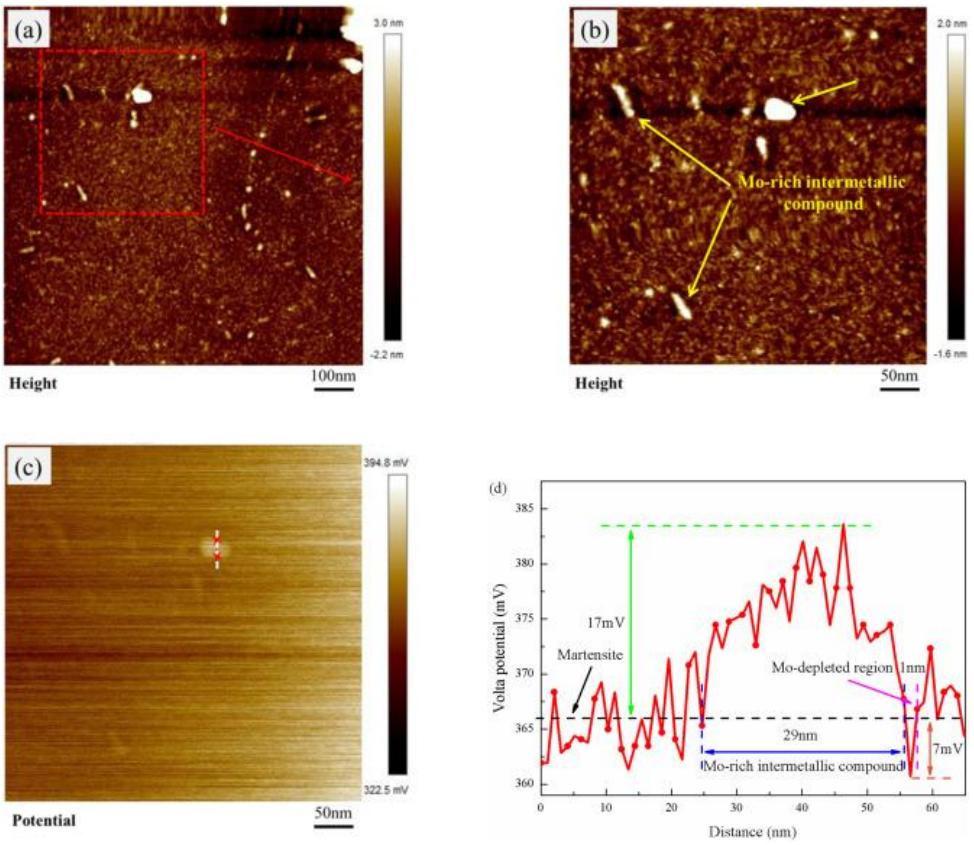

Figure 3-14. SKPFM analysis of S13Cr MSS tempered at 500°C: (a) surface morphology of the specimen; (b) local area of (a); (c) Volta potential of the specimen; (d) the line analysis of surface potential [120].

3.2.4. The role of austenite in stress corrosion cracking of martensitic stainless steel

Stress corrosion cracking is another major concern in addition to corrosion during the service of martensitic stainless steel in oil and gas. Martensitic stainless steels are sensitive to hydrogen embrittlement compared to austenitic stainless steels and duplex stainless steels. Austenite has a higher hydrogen embrittlement resistance compared to martensite due to its face-centered cubic (FCC) structure [121]. Hence, increasing the austenite content is a common method of improving the HE resistance of martensitic stainless steels [113, 122-125].

Fan et al. [126] applied atom probe tomography (APT) to confirm that reversed austenite is the H trapping site in martensitic stainless steel as shown in Figure 3-15. It was reported by Zhu et al. [127]

that the hydrogen was three times more soluble in austenite than that in martensite. Hydrogen distribution is largely modified with introducing reversed austenite in martensitic stainless stee, and hydrogen would be mainly trapped in reversed austenite rather than in the prior austenite grain boundaries or other sites where stress is concentrated. Thus, it can be expected that the weakest link of fracture path would not be the prior austenite boundaries any more.

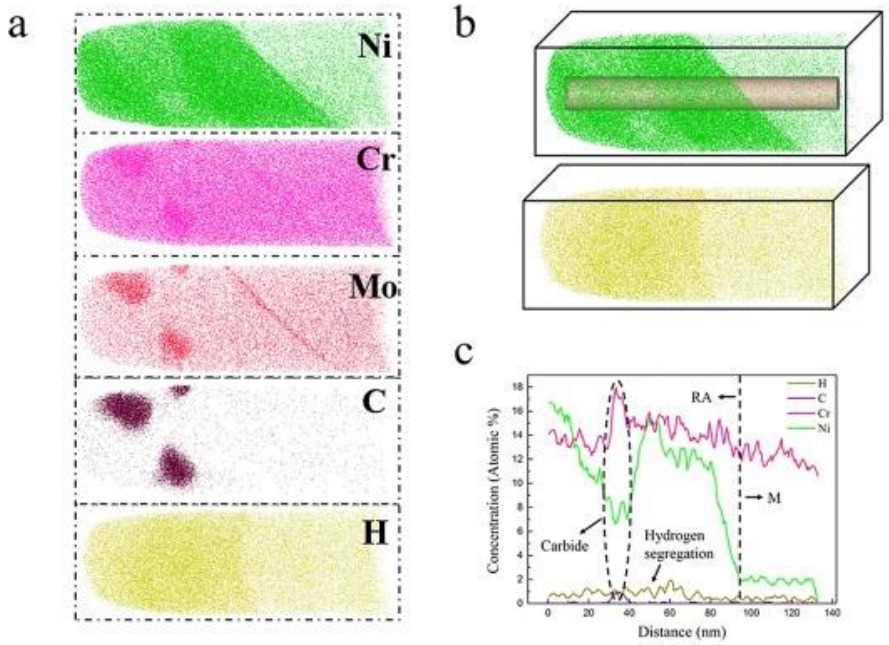

Figure 3-15. APT atom maps of double tempered sample. (a) elemental distributions of Ni, Cr, Mo, C and H; (b) reconstructed 3-dimensional atom maps of Ni and H with a selected cylinder across the reversed austenite (RA) and martensite (M); (c) the compositional profiles of H, C, Ni and Cr measured using cylinder in (b) [126].

However, it is noteworthy that the reversed austenite can transform to martensite when sufficient hydrogen and severe plastic deformation are presented. In this situation, a large quantity of hydrogen is inherited from the austenite which previously trapped a substantial amount of hydrogen, making the newly formed martensite the most susceptible phase to HE in MSSs. As a result, a hydrogen induced crack is very likely to initiate or propagate in these regions, which causes premature failure. Hence, the beneficial effect of austenite is limited [122, 126, 128].

3.3. Research work on the corrosion and SCC behaviour of 13Cr MSS under HTHP CO_2-containing downhole environments

Normal 13Cr MSS (UNS S41000) is considered as a cost-effective material for downhole injection or production tubing and casing due to its excellent mechanical & corrosion properties and economic applicability. However, normal 13Cr undergoes a relatively server corrosion when the temperature reaches 150°C [129]. In this situation, modified 13Cr MSSs were developed to increase the upper limit temperature of the application of 13Cr MSS. Among a range of modified 13Cr MSSs, an appropriate candidate structural material known as Super 13Cr MSS (UNS S41427, S13Cr MSS) containing extra low carbon grade and approximately 5 wt% Ni and 2 wt% Mo has been shown to improve corrosion resistance compared to normal 13Cr and other modified 13Cr MSSs at a higher temperature with CO_2 presence. S13Cr MSS can provide more cost-effective performance compared to duplex stainless steels and Ni-based austenitic stainless steels in some cases and is extensively used in high CO_2 downhole environments.

With the widespread usage of 13Cr type MSS in the oil and gas industry, attention has been drawn to its corrosion and fracture issue as corrosion and fracture failures were reported regarding the application in HTHP CO_2-containing downhole environments [130, 131]. Attention has been paid to reveal the corrosion and fracture behaviour of 13Cr type MSSs to improve the understanding of the application of 13Cr type MSSs.

3.3.1. Research work on the corrosion behaviour of 13Cr MSS and the formation mechanism of the corrosion scales under HTHP CO_2-containing downhole environments

Under mild service environments, the 13Cr MSS surface covered by a passive film which mainly comprised of Cr_2O_3, $Cr(OH)_3$, Fe_3O_4/Fe_2O_3 and FeOOH, the added of Ni and Mo in S13Cr MSS can form MoO_2/MoO_3 and NiOOH to enhance the protective

properties of the passive film [132-134]. The passive film on the surface of the passivated material is in a dynamic generation-dissolution process during the service which can be described using the Point Defect Model as mentioned in Chapter 2. The low corrosion rate of the material is attributed to the presence of the protective passive film which act as a barrier between the substrate and the aggressive electrolyte to prevent the substrate from server corrosion.

Under an aggressive HTHP environment, the air-formed native passive film degraded and is replaced by a corrosion product film which mainly comprised $FeCO_3$, Cr_2O_3, $Cr(OH)_3$, $FeCr_2O_4$ [51, 135]. 5% Ni endow S13Cr MSS with the ability to form a Ni-rich layer at the material-corrosion scale interface which plays an important role in the corrosion resistance at high temperature by blocking the material interface and acting as a barrier to restrict the corrosive species pass through and reduce material degradation [52].

The evolution of the corrosion scales formed on 13Cr MSS including the structure and composition of corrosion scales, the protective property of the corrosion scales, etc. has been reported to be greatly influenced by environmental factors such as temperature, CO_2 partial pressure, flow condition, etc., and has recently received a lot of attention with the widespread use of 13Cr type MSS in HTHP downhole environments.

3.3.1.1. High temperature

Temperature has been wildly accepted as an important factor that related to the survey of 13Cr type martensitic stainless steel. As shown in Figure 3-16, the flow chart proposed by Ueda [129] suggest that the threshold temperature for the application of conventional 13Cr MSS to be 150°C in terms of corrosion and localized corrosion in an environment with very limited H_2S content, while for S13Cr MSS the temperature limit is 180°C.

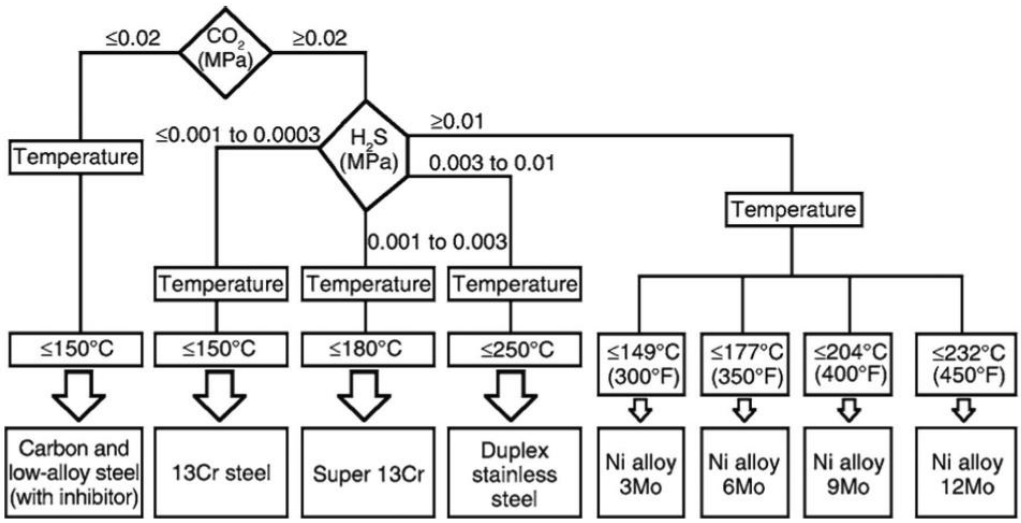

Figure 3-16. A flow chart for the selection of CRA for H_2S and/or CO_2 service [129].

The temperature is not only an important factor that determine the application limit of the material by itself, but also influences the acceptable range of other service determining factors such as CO_2 partial pressure, H_2S partial pressure, Cl^- concentration, etc. For example, as shown in Figure 3-17(a), a material selection map based on the general corrosion rates obtained by 7 days tests in 20% NaCl solution provide by Kimura [136] indicates that with the temperature increasing from 100°C to 150°C, the acceptable CO_2 partial pressure of conventional 13Cr MSS reduced from above 2 MPa to 0.5 MPa. Modified 13Cr MSS (with Ni and Mo addition) exhibited a same corrosion trend but has significantly higher corrosion resistance than conventional 13Cr MSS. Similar trend also reported by Ishiguro [137] based on general corrosion rate obtained by 14 days tests in 20% NaCl solution, as shown in Figure 3-17(b). It should be notice Ishiguro claimed in their report that pitting attack absented in any of the test conditions reported, suggesting that the main corrosion rate to be concerned during the material selection process for pure CO_2 downhole environments which limit the application of 13Cr MSS is generation corrosion rate instead of pitting rate [137].

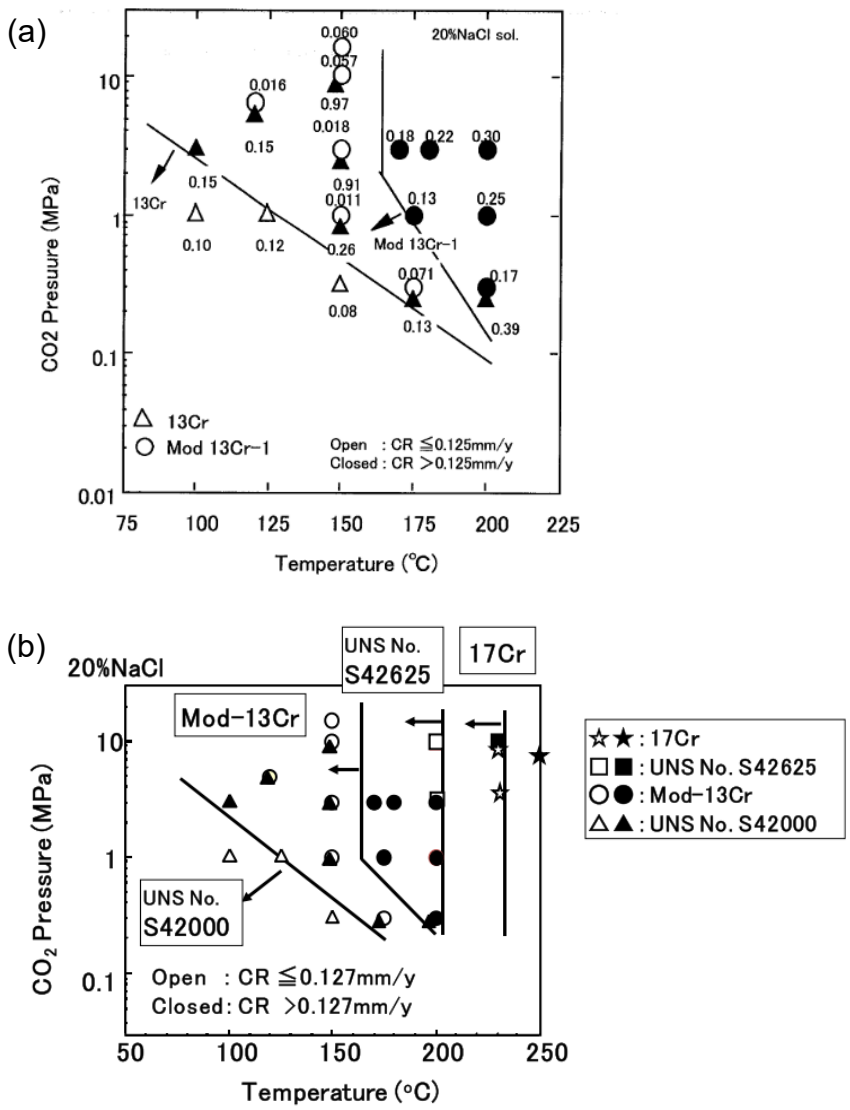

Figure 3-17. CO_2 corrosion resistance plotted along temperature and CO_2 partial pressure provide by (a) Kimura and (b) Ishiguro [136, 137].

As introduced in Chapter 2, temperature affects the film-forming mechanism of the corrosion product film as well as the stability of the passive film on the steel surface. This topic has come into focus in recent years regarding the study of the corrosion behaviour of 13Cr MSS under HTHP conditions.

Moreira et al. [138] studied the corrosion product film formed on 13Cr/S13Cr MSS in 3.2 M/L NaCl solution with CO_2 from 125°C to 175°C. The results indicated that the thickness, as well as the Cr/Fe ratio of the corrosion product films, increased with the temperatures. The corrosion rates obtained from the mass loss data and

electrochemical data increased for both testing materials under dynamic and static conditions.

Zhao et al. [17] systematically investigated the corrosion behaviour of HP-13Cr MSS (containing 2.19 wt% Mo and 5.36 wt% Ni), including the evolution of corrosion scales and their thermodynamic prediction, in downhole environments from 95°C to 180°C. The calculated Pourbaix diagram as shown in Figure 3-18 is consistent with the XPS test results, Cr_2O_3 and $Cr(OH)_3$ were detected as the composition of the corrosion scales. In addition to this, the XPS test results provides more detail regarding the composition of the corrosion scales, that the content of Cr_2O_3 falls with the increasing the temperature, this is beyond Pourbaix diagram's capabilities as the chemical reaction 2-10 (the transition between Cr_2O_3 and $Cr(OH)_3$) could not be represented in a Pourbaix diagram because no e^- and H^+ involved. Moreover, the Pourbaix diagrams predict the passivity region of HP-13Cr MSS in HTHP CO_2-containing simulated formation brine and have been confirmed by the potentiodynamic polarisation curve measurements.

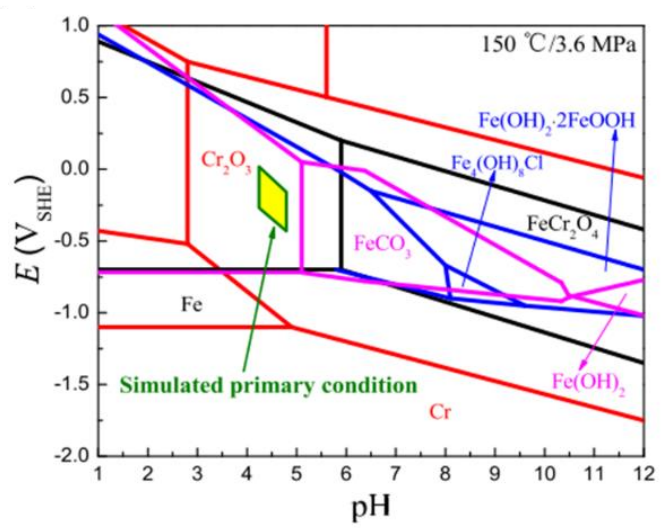

Figure 3-18. Pourbaix diagrams for 13Cr MSS in the aggressive oilfield environment with $[Fe(aq)]_{tot} = [Cr(aq)]_{tot} = 10^{-6}$ mol/L [17].

The structure and composition of the corrosion scales was further investigated by means of microstructure characterization [51]. The corrosion scales undergo significant microstructural changes as the

Scanning transmission electron microscopy (STEM) mapping images shown in Figure 3-19 with a schematic diagram shown in Figure 3-20, the results indicate that the corrosion product layers changed from monolayer corrosion scales comprised Cr_2O_3, $Cr(OH)_3$, MoO_2 and $FeCO_3$ at 95°C to an bilayer at 120°C and 150°C, within the bilayer, the inner layer mainly comprised Cr_2O_3, $Cr(OH)_3$, MoO_2 and $FeCO_3$, while the $FeCO_3$ is absent in the outer layer. The corrosion scale changed back to a single layer comprised Cr_2O_3, $Cr(OH)_3$ and MoO_2 as the temperature further increased to 180°C.

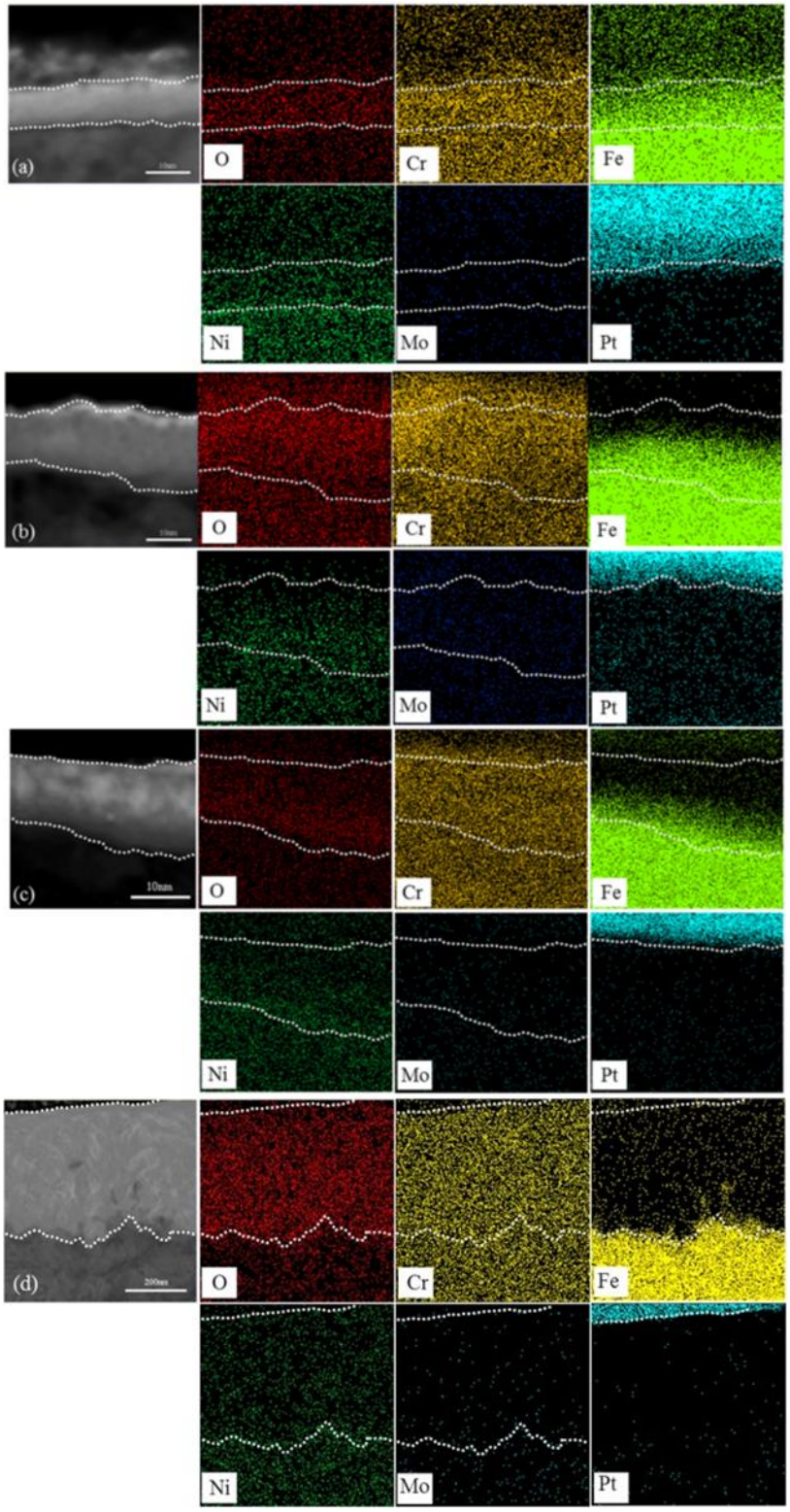

Figure 3-19. STEM image and the corresponding EDS maps of the corrosion scales formed on HP-13 Cr MSS in various extremely aggressive environments: (a) 95°C/2.8 MPa,(b) 120°C/3.2 MPa, (c) 150°C/3.6 MPa, (d) 180°C/3.8 MPa [51].

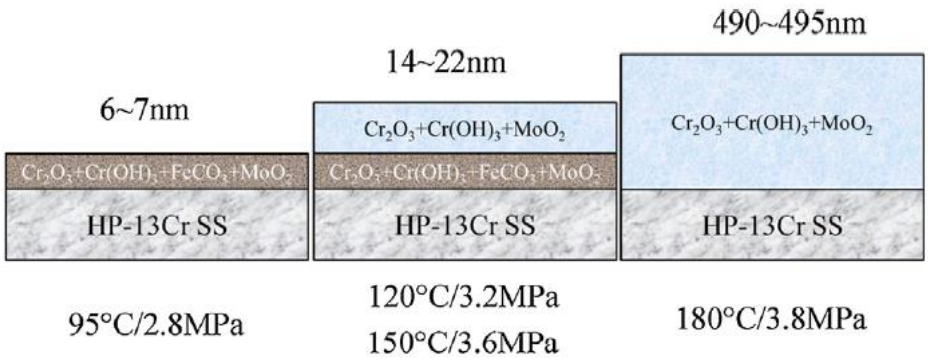

Figure 3-20. Schematic diagrams of composition and its distribution in corrosion scales in various extremely aggressive environments [51].

The semiconductive property of the corrosion scales formed under high temperature environments was studied by means of Mott-Schottky test in Cai's report as shown in Figure 3-21 [139]. The corrosion scale formed at 100°C represented n-p-type semiconductor behaviour but changed into p-type as temperature increased to 150°C, implying the transition of the corrosion scale composition. Meantime, the doner and accepter density within the corrosion scale increased with the increasing temperature, indicating the reduction in the protection of corrosion scale.

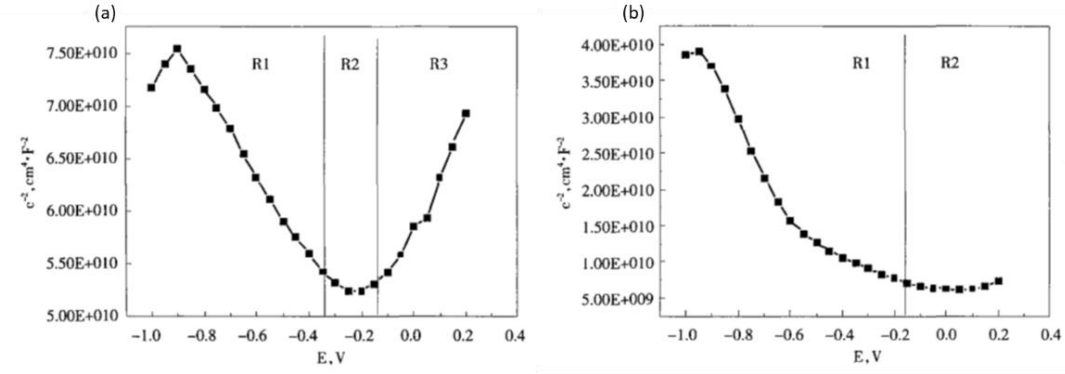

Figure 3-21. The M-S curves of the passive film of S13Cr MSS formed at 100°C(a) and 150°C(b) in simulated formation solution [139].

3.3.1.2. CO_2 partial pressure

As mentioned in Chapter 2, CO_2 gas dissolved in the solution and resulted in the formation of weak carbonic acid which partially dissociated and providing H^+ ions causing the decrease in pH and

will also take part in the cathodic reaction happened on the metal surface.

Yue [140] investigated the effect of CO_2 partial pressure on the evolution of the corrosion scales on 13Cr MSS in a $NaHCO_3$-containing NaCl solution (29503 mg/L Cl^-,HCO_3^{2-} 585mg/L) at 200°C by means of immersion test combined with Pourbaix diagram calculation. The results indicate that the CO_2 partial pressure has a significant effect on the composition of the corrosion scales on 13Cr MSS formed at HTHP conditions as shown in Figure 3-22: when the CO_2 partial pressure was below 0.65 MPa, the primary composition of the corrosion scales was $FeCr_2O_4$; as the CO_2 partial pressure beyond 1.54 MPa, the corrosion scales mainly comprised of $Cr(OH)_3$.

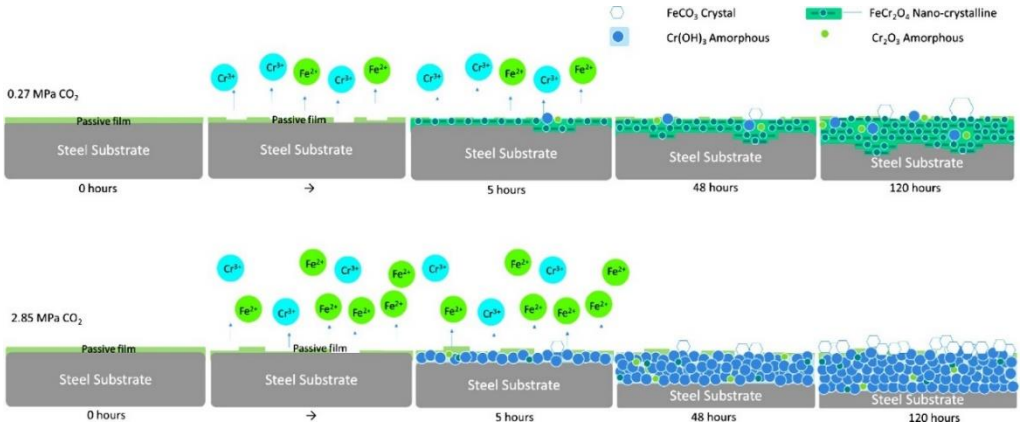

Figure 3-22. The formation and evolution of the films on the 13Cr SS surface at 200°C and various CO_2 partial pressure [140].

Besides, the precipitation behaviour of $FeCO_3$ during the corrosion process was also affected by the CO_2 partial pressure as shown in Figure 3-23, the number of the crystalline $FeCO_3$ significantly increase with the increasing CO_2 partial pressure. It's also worth noting that the number of the crystalline $FeCO_3$ did not significantly increase with immersion time prolong in this report, only the size of the crystalline $FeCO_3$ increased with immersion time.

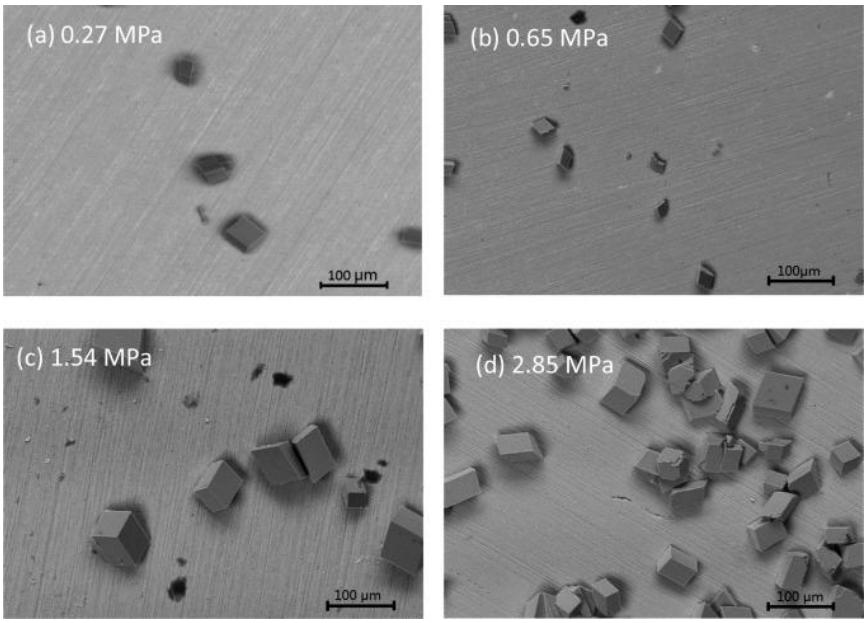

Figure 3-23. Top-view SEM images of 13Cr SS immersed in the solution at a constant temperature of 200°C and (a) 0.27 MPa, (b) 0.65 MPa, (c) 1.54 MPa, and (d) 2.85 MPa of CO_2 partial pressure for 48 h [140].

3.3.1.3. Flow velocity

The flow velocity was reported to have a significant influence on the mass transfer processes on near surface of metal, thereby effect the specimen dissolution-precipitation process, resulting in the change in composition/structure of corrosion scales. Under HTHP environments, the formation of $Cr(OH)_3(_s)$ was believed to be controlled by the dissolution-precipitation process while Cr_2O_3 was controlled by the electro-migration process. Hence, the flow is believed to have a significant effect in the precipitation of $Cr(OH)_3$, subsequently, affect the composition of the corrosion scales, resulting in the change in corrosion behaviour. As shown in Figure 3-24, Zhao [16] reported that due to the effect of the flow on the precipitation of $Cr(OH)_3$, the volume fraction of an amorphous $Cr(OH)_3$ decreased in the temperature range from 95°C to 180°C. Furthermore, the density of the $Cr_2O_3/Cr(OH)_3$ phase boundary and the donor densities increased in flow condition, resulting a higher general corrosion rate.

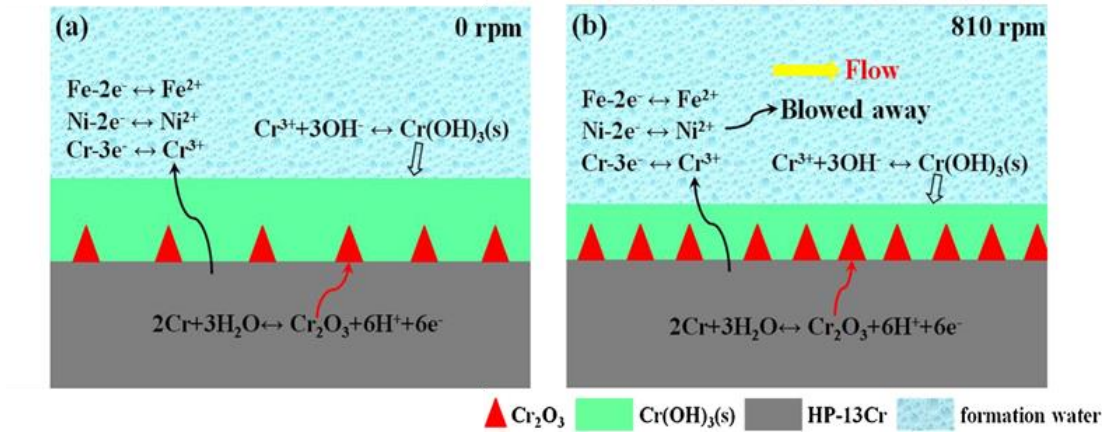

Figure 3-24. Schematic of influence of the flow conditions on the formation mechanism of the scale films of the HP-13Cr MSS [16].

Besides the general corrosion, flow also have a significant effect on the pitting behaviour. As shown in Figure 3-25, the H^+ generated by metal irons hydrolysis could accumulate within the pitting cavity under static condition, therefor accelerated the growth of the pitting in the vertical direction. Under flow condition, Yue [141] reported that the precipitation of $FeCO_3$ crystals turned the uncovered region as a concave, resulting in a relatively asymmetric distribution of H^+ ions as shown in Figure 3-25(b). The localised corrosion occurs at the precipitated regions of porous $Cr(OH)_3$ due to the acidification, and the level of H^+ ions accumulates at upstream which widen the pits along the flow direction, forming pits with disk-like shape.

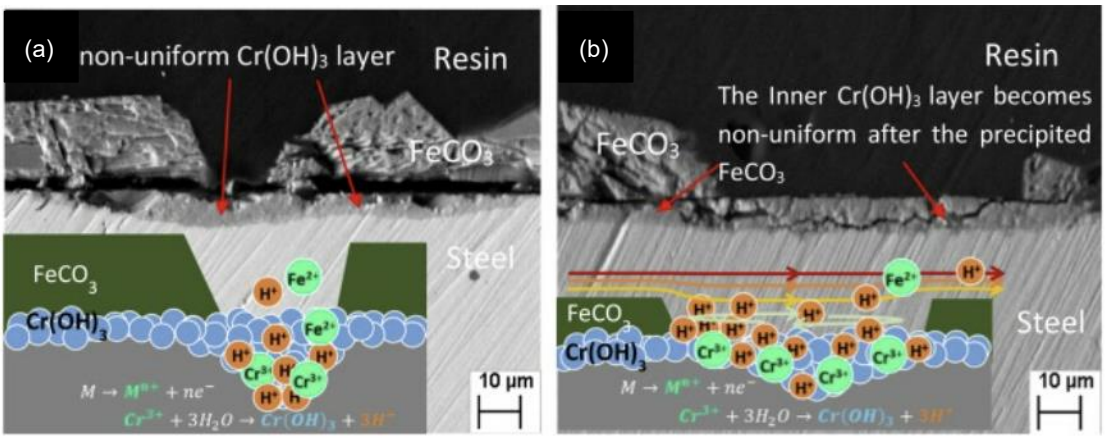

Figure 3-25. Schematic diagram of the porous corrosion product film-induced localised corrosion at 200°C and 28.5 bar CO_2 conditions (a) 120 h in static and (b) 120 h in rotation speed of 188 rpm [141].

A similar transform in the shape of pitting was also observed while no carbonate precipitated on the sample surface [16]. This was believed to related to the vortex flow within the pitting cavity, the vortex flow causes the metal irons concentration to have a maximum value along the upstream wall of the pitting. On the contrary, the region where H^+ concentration is highest shifts to the downstream portion of the pitting cavity. Hence, the pitting growth rate would also be accelerated in the horizontal direction, and formed the shallow-disk shape pitting.

The flow not only effect the formation of the oxides/hydroxides inner layer, but also reported to affect the precipitation of the $FeCO_3$ outer layer as shown in Figure 3-26. The effect of flow delays the Fe^{2+} and CO_3^{2-} to reach the critical supersaturation ratio (SR_C), resulting in the delayed precipitation of the crystalline $FeCO_3$ on the surface [141].

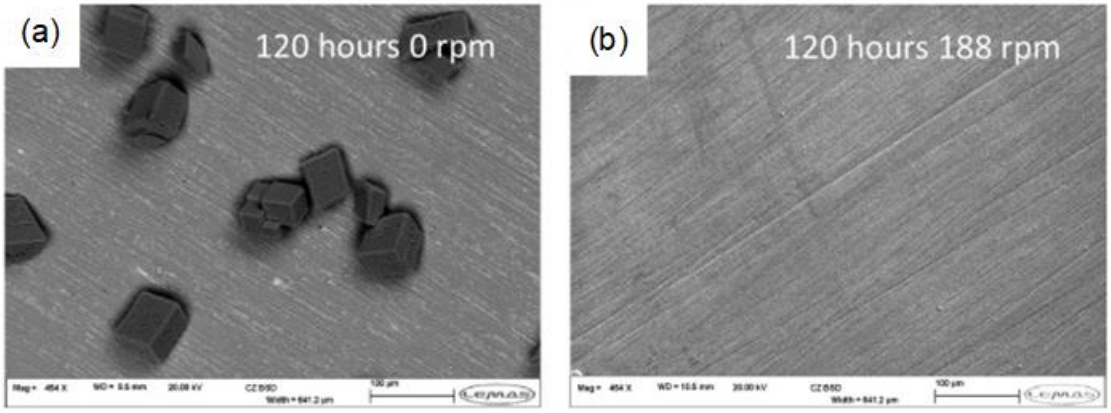

Figure 3-26. SEM images of the corrosion products at various immersion times at 200°C and 2.7 bar CO_2 (a) 120 h in static and (b) 120 h in rotation speed of 188 rpm [141].

3.3.2. Research work on the SCC behaviour of 13Cr MSS under HTHP CO_2-containing downhole environments

Stress corrosion cracking resistance, in addition to corrosion resistance, is also an important performance to consider when selecting material for a particular environment. During the service, downhole tubing often experiences complex stress, including tensile stress caused by the weight of the tubing itself, stress induced by temperature effect, stress caused by operation, internal/external

pressures, etc. The combination of these stresses and the corrosive environment may lead to a risk of SCC of the material.

Research on the SCC behaviour of 13Cr MSS has never ceased since the early 1980s when the 13Cr type MSS casing and tubing started to be applicated in downhole environments. In the same time, there are also reports regarding the failure of 13Cr MSS casing and tubing due to SCC in HTHP CO_2-containing downhole environments [131, 142-144]. Early research mainly focused on determining the domain diagrams of 13Cr MSS in different application conditions, a large number of domain diagrams with different variables (e.g. temperature, pH, CO_2 partial pressure, H_2S partial pressure, Cl^- concentration, etc.) for various environments were proposed to facilitate the understanding of the application of 13Cr MSS in HTHP conditions [89, 145-148]. In the meantime, the applications of different modified 13Cr MSSs have also been extensively studied for comparison with the conventional 13Cr MSS [89, 145-148]. For instance, 13Cr-5Ni-2Mo, the so-called Super 13Cr MSS, is reported to have a significant improvement in SCC resistance compared to conventional 13Cr MSS which mainly attributed to the Mo addition. The Mo was reported to play an important role in improving the SCC resistance by enhancing the passive film [88, 133, 145].

However, these studies mainly focused on the SCC resistance of 13Cr type MSS in environments containing small or trace amounts of H_2S, and relatively little research has been carried out on high temperature downhole environments where the atmosphere is pure CO_2. Zhao et al. [149]. applied slow strain rate tensile (SSRT) tests on 13Cr MSS in various solutions with different concentrations of NaCl at 90°C under 3 MPa CO_2, the results indicate that the SCC behaviour of the specimen in the 5% NaCl is supposed to be controlled by hydrogen-induced cracking, the cathodic reactions under this condition are the H evolution reactions, and the dissociation of H_2CO_3 serves as an additional source of H. But as

the NaCl concentration increase to 20%, the cathodic reaction was believed to be inhibited by the high concentration of Cl^-. In the meantime, the passive film of the specimen in the 20% NaCl solution is unstable. Consequently, the SCC behaviour of the specimen in the 20% NaCl solution is supposed to be controlled by anodic dissolution.

Subsequently, Yue et al. [150] increased the experimental temperature for corrosion tests and SSRT tests to 150°C in 16% NaCl brine solution with 1 MPa CO_2. Their results indicate the S13Cr MSS was highly resistant to SCC at temperatures less than 140°C. However, material failure in terms of embrittlement cracking was observed as the temperature increased up to 150°C. This change was believed to related to the corrosive pitting; the film corrosion resistance decreased with the increase in temperature according to the EIS test results, the high concentration of Cl^- also attributed to the film degradation and finally causes pitting corrosion. When the pitting corrosion is developed up to a certain depth in a direction perpendicular to the applied stresses, the occurrence of crack propagation originating from the pits is observed. However, in this study, there is no direct observational evidence to support the association between pitting and cracking.

Recently, Qi et al. [151] published their research regarding the SCC behaviour of HP-13Cr MSS (containing 2.19 wt% Mo and 5.36 wt% Ni) in CO_2-containing simulated formation water with temperature up to 180°C. The relationship between pitting and cracks was investigated by observing the surface morphology of the specimens after immersion test with different levels of plastic deformation as shown in Figure 3-27. The conversion from pitting to cracking was simulated by applying finite element (FE)analysis. A hemi-spherical shaped pit model was used for the FE simulation, the diameter of the pit was based on the measurement results of the max pitting depth while the max pitting depth increased with increasing temperature. The FE results indicated that the stress and

plastic strain were concentrated at the bottom of pitting, the degree of stress and strain concentration increased with the increasing of pitting depth. Therefore, under the same stress level, the cracks will more preferentially nucleate at deeper pit cavities at HTHP environment. However, pits usually have different morphologies under different conditions, e.g. wide & shallow shaped, narrow & deep shaped, and the shape of pits has a strong influence on the degree of stress concentration within the pits. But the authors have not taken the shape into consideration here but simply used hemisphere to simulate pits.

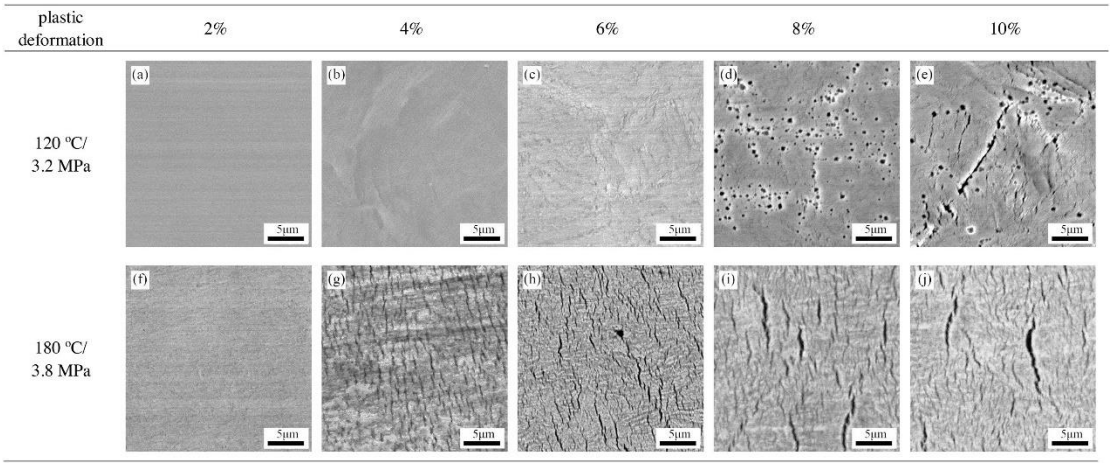

Figure 3-27. Surface morphology of HP-13Cr SS in the formation water during the SSRT process with the plastic deformation of (a) 2%, (b) 4%, (c) 6%. (d) 8% and (e) 10% at 120°C/3.2 MPa and (f) 2%, (g) 4%, (h) 6%, (i) 8% and (j) 10% at 180°C/3.8 MPa [151].

3.4. Summary of the corrosion and cracking behaviour of 13%Cr MSS at HTHP conditions and knowledge gap

Research on corrosion and SCC behaviour of 13%Cr MSS has never stopped since the early 1980s when the 13%Cr type MSS casing and tubing started to be applicated in oil and gas downhole environments. Early studies were mainly carried out by the research

departments of steel companies to determining the domain diagrams of 13%Cr MSS in different application conditions. Therefore, the main focus was on the corrosion rates and the stress corrosion cracking behaviour at elevated temperatures and pressures. According to those researches, 13%Cr MSS is normally recommended for service environments below 180°C. The research on corrosion and SCC mechanism of 13%Cr MSS under HTHP conditions mainly carried out on the recent ten years. The corrosion and SCC behaviour of 13%Cr MSS at temperatures ranging from 120°C to 200°C has been widely studied by Xiaoqi and Yang et al. through *ex situ* surface analysis methods such as XRD, SEM-EDS, TEM, XPS and Raman. These studies mainly explain the effects of temperature, partial pressure of carbon dioxide and flow rate on the structure and composition on the corrosion product films as well as the corrosion rate, the relationship between pitting corrosion and SCC has also been investigated.

Austenite, as the second phase, plays an essential role in the modification of 13%Cr MSS. The addition of ductile austenite improves mechanical property of the brittle martensitic matrix by increases its toughness. Moreover, the higher hydrogen embrittlement resistance of austenite and its greater hydrogen dissolution capacity compared to the martensite matrix allows the addition of austenite to have a limited beneficial effect on the hydrogen embrittlement resistance of 13%Cr MSS. However, the effect of austenite on the corrosion resistance of the 13%Cr MSS is not clear. Both enhanced and reduced the corrosion resistance of 13%Cr MSS have been reported. Since current researches on the effect of austenite on the corrosion resistance of martensitic stainless steels are mainly carried out at room temperature, at which the material is in a passive state, the investigations are mainly focused on the effect of austenite on the pitting behaviour of 13%Cr MSS. Increasing the austenite content usually means a higher tempering temperature or longer tempering duration, during

which the content and size of precipitates such as carbides and nitrides will inevitably change. The precipitation of precipitates leads to compositional fluctuations in the surrounding matrix, such as the formation of Cr-depletion zone, which are considered to be closely related to the pitting resistance of the 13%Cr MSS. However, the influence of the galvanic coupling effect between the austenitic and martensitic matrix on the corrosion was usually neglected in these studies as the impact of this galvanic effect on corrosion (primarily pitting) is less pronounced compared to the effects of Cr-depleted zones and precipitates. Nevertheless, the role of the galvanic coupling between austenite and martensite in HTHP corrosion is beginning to show significance as evidenced by the retention of uncorroded austenite within the corrosion product films observed by Yue at 200°C [141, 152], though this influence has not yet been intensively investigated.

Based on these findings the following knowledge gaps can be summarised:

1. Current researches have not identified the main problems faced by S13Cr MSS when applied under HTHP CO_2-containing environments among general corrosion, pitting and SCC.
2. The current researches under HTHP conditions are mainly carried out through *ex situ* surface analysis methods, *in situ* methods are required to further understand the corrosion behaviour of S13Cr MSS under HTHP CO_2-containing environments.
3. The protection of the air-formed native passive film on S13Cr MSS under HTHP environments and its degradation process is not clear.
4. The effect of austenite on corrosion behaviour of S13Cr MSS under HTHP CO_2-containing environments is not clear.

4. Chapter 4 Experimental procedures

This chapter is divided into three main sections: The first section describes the material and solution used throughout this research project. The second section describes the test setup, procedures for corrosion experiments, including HTHP immersion tests and HTHP electrochemical tests. The third section describes various surface analysis techniques used to investigate and identify the chemistry and morphology of corrosion product layers and pitting corrosion.

4.1. Material and solution used for this study

4.1.1. Raw material and sample preparations

The material used in this work was an API-P110 grade S13Cr MSS provided by Zhejiang Jiuli Hi-Tech Metals Co., Ltd., manufactured by hot rolling, solid solution at 1020°C for 30 min followed by quenching, then tempered at 620°C for 60 min followed by air cooling, the compositions of S13Cr MSS are provided in Table 4-1.

Table 4-1. The chemical composition of S13Cr MSS (wt.%).

Elements	C	Cr	Ni	Mo	Mn	Si	S	P	Fe
S13Cr MSS	0.01	12.6	5.1	1.6	0.4	0.3	0.002	0.01	Bal.

The mass loss samples for immersion tests were machined into 23 mm x 13 mm x 5 mm as shown in Figure 4-1(a). Prior to each test, the sample surface was ground to 1200 # by silicon carbide paper, then rinsed with Deionized (DI) water and acetone, respectively, followed by cold-air drying. The cleaned samples were weighed (w_0) using an analytical balance with an accuracy of 10^{-5} g.

Samples for electrochemical tests are cylindrical specimens with a diameter of 10 mm and high of 7 mm as shown in Figure 4-1(b), the specimens were sealed inside resin by hot mounting, exposing rounded metal surfaces on both sides, one of the exposed rounded surfaces was used for electrochemical test and the other one is for connecting Kapton insulated copper wire by soldering. In order to prevent the occurrence of the galvanic corrosion, the soldering joint

was subsequently shielded by high temperature resistant insulating glue to avoid exposure of solder, copper wire and S13Cr MSS and make sure the corrosion only resulted from specimens with a specific exposure surface. The test surface was ground to 1200 using silicon carbide paper, then rinsed with distilled water, acetone and dried with compressed air.

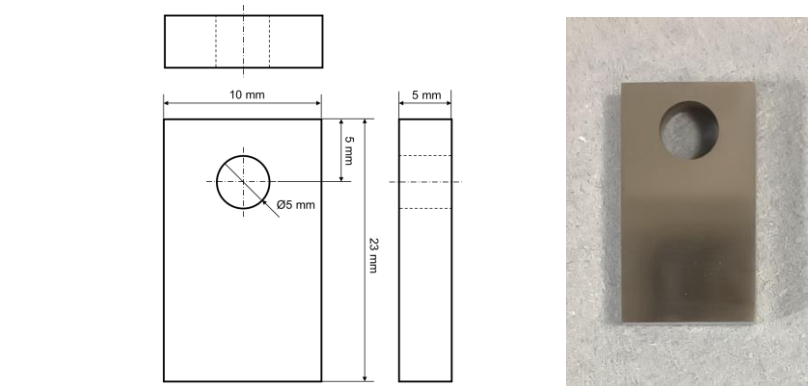

(a)

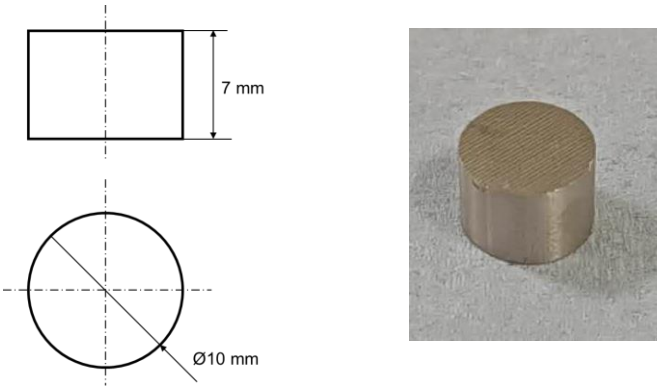

(b)

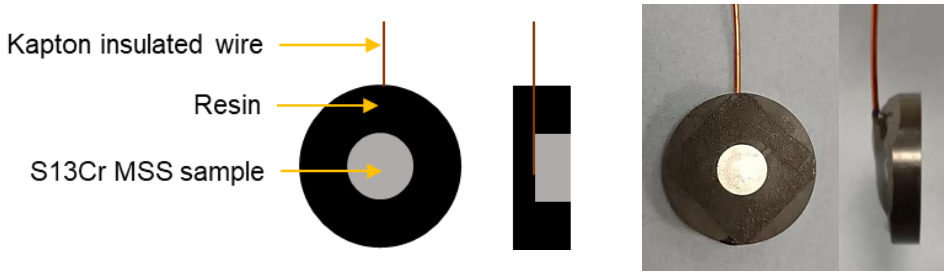

(c)

Figure 4-1. (a) Test sample used for HTHP immersion tests; sample used for the HTHP electrochemical tests: (b) before sealed and (c) after sealed.

4.1.2. Solution preparation

The test solution, simulating the aggressive downhole formation brine, was made by the analytical grade reagents and deionized (DI) water, the composition of the formation brine is provided in Table 4-2. Prior to the tests, the solution was de-aerated by CO_2 bubbling for at least 2 hours per litre solution before introduced into the autoclave.

Table 4-2. The chemical composition of simulated formation brine

Composition	Na^+	K^+	Mg^{2+}	Ca^{2+}	SO_4^{2-}	Cl^-	HCO_3^-
Content (mg/L)	68850	5960	505	7479	387	115200	170

4.2. HTHP tests

4.2.1. Immersion test

A schematic and real picture representation of the autoclave setup is shown in Figure 4-2. The test samples were fixed using a holder made of polyetheretherketone (PEEK) to prevent galvanic effects. The prepared, CO_2-saturated brine was carefully transferred into the autoclave at ambient pressure and temperature and evacuated to ensure removal of O_2 within the system, high pressure CO_2 was then transferred into the autoclave and heated and pressurized to 25°C and target pressure. The starting point of the test was taken from the time at which the autoclave reached the required temperature.

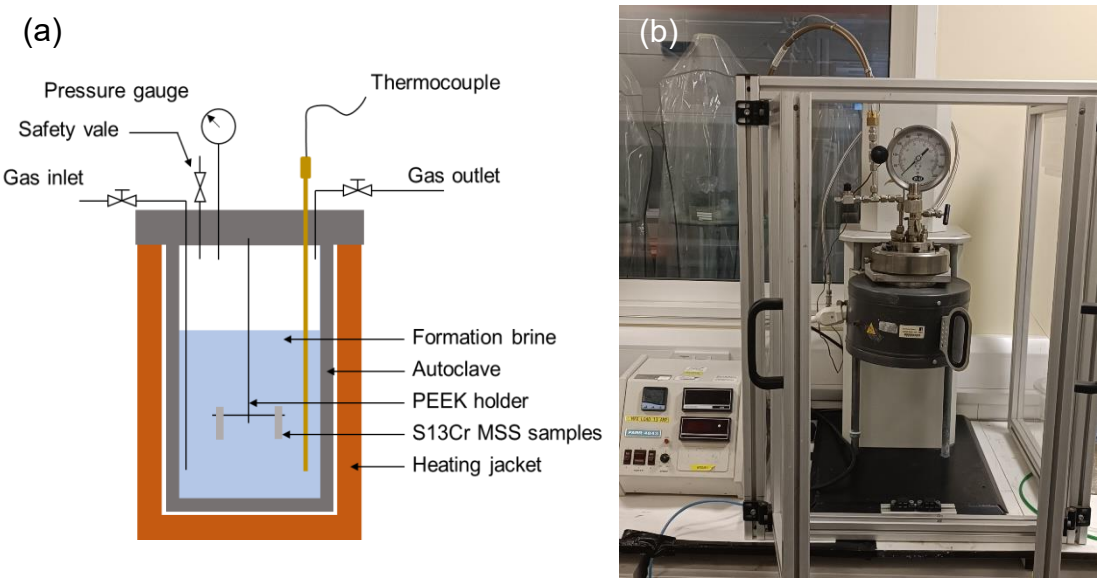

Figure 4-2. (a) Schematic and (b) real picture of the experimental setup for the HTHP immersion tests.

After the immersion test, the autoclave was cooled down to 80°C within 10 minutes and then depressurised, the corroded specimens were extracted from the autoclave and immediately rinsed with distilled water and dried with compressed air.

After immersion tests, the corroded specimens were extracted from the autoclave and immediately rinsed with absolute ethyl alcohol and DI water. The corrosion products were removed according to ASTM G1-03 standard [153] using Clarke's solution, then rinsed, dried, and reweighed to obtain the final weight of the specimen. The corrosion rate was calculated by the following equation:

$$R_{Gcorr} = \frac{8.76 \times 10^7 \times \Delta m}{S \times T \times \rho} \quad (4\text{-}1)$$

Where R_{Gcorr} is the general corrosion rate, mm/y; Δm is the weight loss, g; S is the exposed surface area, cm^2; ρ is the density of the steel, g/cm^3; and T is the immersion time, h.

4.2.2. Electrochemical test

The electrochemical measurements were carried out in the high temperature and high pressure electrochemical autoclave, and the schematic is shown in Figure 4-3. All the electrochemical tests were performed in a conventional three-electrode cell with a working electrode, platinum counter electrode and an Ag/AgCl reference

electrode. The reference solution was 0.1M KCl. All electrode potentials in the present work have been converted to the standard hydrogen electrode (SHE) according to the following relationship[16]:

$$E_{SHE} = E_{obs} + 0.2866 - 0.001(T-T_0) + 1.754 \times 10^{-7}(T-T_0)^2 - 3.03 \times 10^{-9}(T-T_0)^3 \quad (4\text{-}2)$$

Where E_{SHE} represents the electrode potential vs SHE, E_{obs} is the measured electrode potential vs the Ag/AgCl reference electrode, T is the experimental temperature and T_0 is the room temperature (25 °C).

Note that as labelled in the Figure 4-3, two block samples with specific dimensions were placed in the autoclave for controlling the total area of the specimen exposed to the solution in order to adjust the solution volume/sample surface area ratio consistent with the immersion tests.

In addition to the electrochemical sample, two additional block samples were placed in the autoclave with a PEEK holder to maintain the exposure sample area/solution volume ratio at around 33 mL/cm^2, other operating steps were consistent with immersion tests.

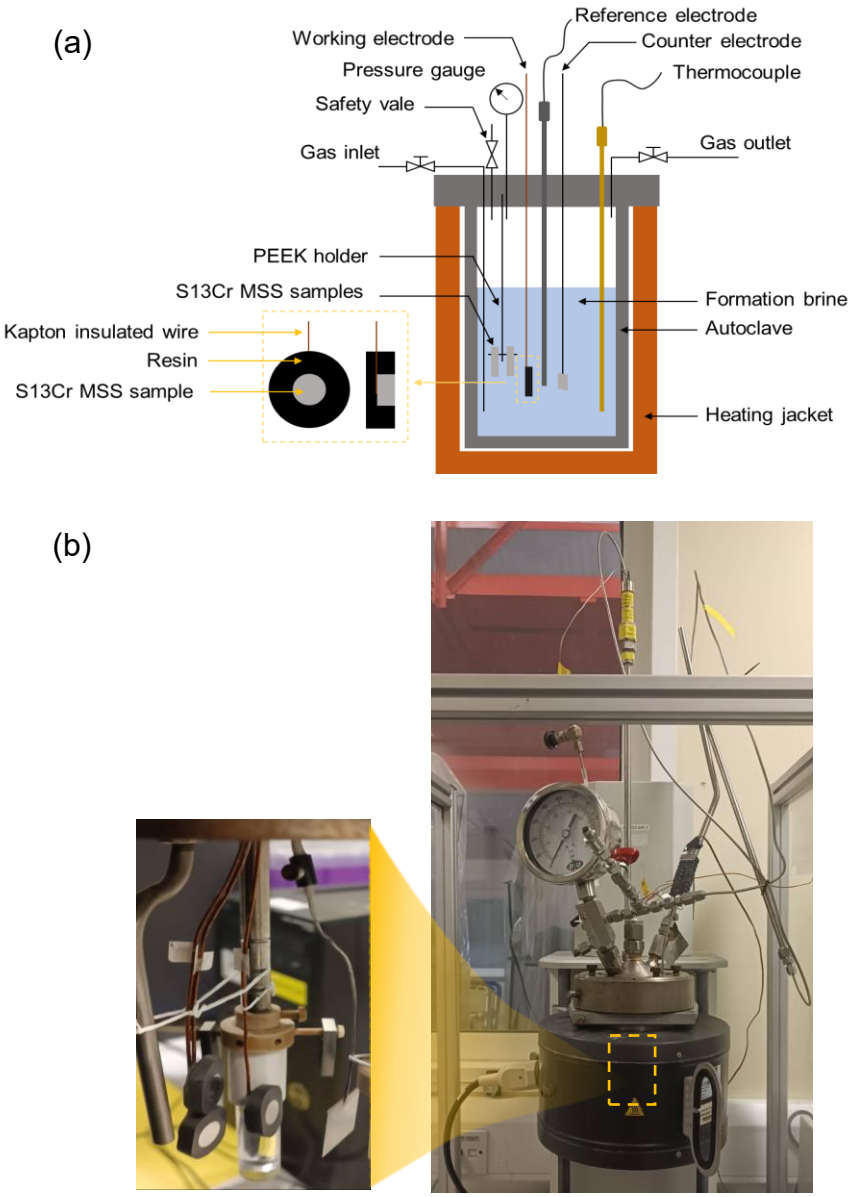

Figure 4-3. (a) Schematic and (b) real picture of the experimental setup for the HTHP electrochemical tests.

4.2.2.1. Polarisation measurements

Polarisation measurements were performed at the corresponding time after the temperature reach the test temperature. For the potentiodynamic polarisation curve measurement, the scan started from -100mV vs. open circuit potential (OCP) with a scan rate of 1 mV/s until the current density reached 5 mA/cm^2.

4.2.2.2. Electrochemical impedance spectroscopy (EIS) measurements

Electrochemical impedance spectroscopy measurements were performed at the corresponding time after the temperature reach the test temperature. All the EIS measurements were performed at OCP over a frequency range from 10^5 to 10^{-2} Hz with an amplitude of 10 mV. To analysis the impedance data, the equivalent electrical circuit parameter was obtained by ZView4 software.

4.2.3. Slow strain rate tensile test (SSRT)

Tensile specimens were cut parallel to the rolling direction from the alloy plate as shown in Figure 4-4(a) based on NACE TM0177-2016 [154], sample dimensions are illustrate as Figure 4-4(b) which is 3.81 ± 0.05 mm (0.150 ± 0.002 in) in diameter by 25.4 mm (1.00 in) long. Prior to the test, all the surfaces were ground with grit SiC paper to a 1200 grit finish sequentially and the final grinding was performed perpendicular to the tensile axis of the specimen. Samples were then cleaned with alcohol, and dried in cold air.

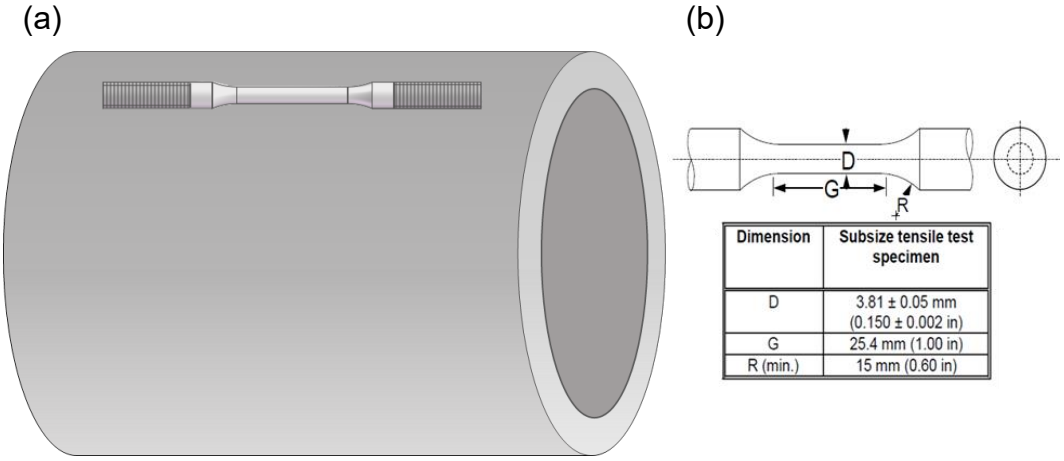

Figure 4-4. (a) Schematic diagram of the SSRT sample processing and (b) dimensions of SSRT sample.

The specimen was wrapped with polytetrafluoroethylene (PTFE) tape on the threaded part to ensure the insulation between the specimen and the holder and then installed on the holder, other operating steps were consistent with immersion tests. To fracture

the specimen, the SSRTs were performed with a strain rate of $4*10^{-6}$ s^{-1} after reaching the testing conditions.

The elongation ratio (ER) and reduction in area ratio (RAR) were used to determine the index of relative susceptibilities to the SCC of the specimens in different test conditions. ER and RAR can be expressed as follows:

$$ER\ (\%) = (\frac{\mathrm{E}_E}{\mathrm{E}_A}) \times 100 \quad (4\text{-}3)$$

$$RAR\ (\%) = (\frac{\mathrm{RA}_E}{\mathrm{RA}_\mathrm{A}}) \times 100 \quad (4\text{-}4)$$

Where E_E and RA_E are the plastic strain to failure and reduction in area in different test conditions; E_A and RA_A are the plastic strain to failure and reduction in area in N_2 without pre-heating for 7 days.

4.3. Surface analysis

4.3.1. Scanning electron microscopy (SEM)/energy dispersive X-ray spectroscopy (EDX)

Scanning electron microscope (SEM) is a type of electron microscope that produces images of a sample by scanning the surface with a focused beam of electrons. These electrons interact with the surface and produce an array of scattered signals which are then analysed for information about the surface topography and composition of the sample. These could span a wide range of secondary electrons, backscattered electrons, characteristics X-rays and other photons. In this project, SEM was used to obtain images of the surface morphology of S13Cr MSS after corrosion tests. Energy Dispersive X-Ray (EDX) analysis was used to identify and quantify the elemental composition of the corrosion products on the sample surfaces.

The scanning electron microscope used for surface analysis throughout this project was a Carl Zeiss EVO MA15 SEM which was integrated with an Oxford instruments AZtecEnergy energy dispersive X-ray system with an 80mm X-max SDD detector which provided secondary and backscattered imaging, EDX elemental

mapping and line scans. Two types of samples were used for analysis: top-view samples and cross-sectional samples. The block samples used in the autoclave experiments were carbon coated along the height of their circumference to eliminate any surface charging effect and could then be used for top-view analysis using both the SEM and the EDX. For cross-section analysis the samples had to immersed in a resin. Then samples were polished using 600 grit up to 1200. The cross-section sample was then rinsed with distilled water and dried with an air gun. The resin on the outside of the cross-sectioned sample was then carbon coated and the cross-sectioned steel surface was iridium coated to diminish any surface charging effect.

The secondary electron function was used for the top-view SEM images. This function was selected for the top-view images as it provides a higher resolution due to it being more surface sensitive. However, for the cross-section images, the backscattered electron function was used as the backscattered electrons are more sensitive to the scattered atomic mass of the nuclei which provides a greater contrast between the elements in the backscattered electron image.

4.3.2. X-ray diffraction (XRD)

The X-ray diffraction (XRD) technique is a unique method used for identifying the chemistry of a compound. The XRD consists of an X-ray tubing, an X-ray detector, and a sample holder. The cathode X-ray tubing generates X-rays which were then filtered, collimated, and then directed towards the surface of the sample. The incident rays then interacted with the surface and produces constructive interference as well as a diffracted ray when the conditions met and satisfy Bragg's law which relates the electromagnetic wavelength to the diffraction angle and the lattice spacing as shown in equation (4-5), where θ is the incident angle, d is the spacing between the diffraction planes, λ is the wavelength of the X-ray, n is the diffraction order. The diffracted rays were then detected by the X-ray detector where they get counted.

$$n\lambda = 2dsin\theta \qquad (4\text{-}5)$$

Identification of the mineral can then be achieved by converting diffraction peaks to d-spacings as all minerals have their own unique set of d-spacings.

The Bruker D8 X-ray diffractometer was used for phase identification throughout this project, employing Cu Kα radiation with an active area of 10mm × 10 mm, with a range of 2θ = 20 - 70° using a step size of 0.033° per second. The samples required no preparation beforehand and could simply be inserted onto a sample holder and then be analysed using the Bruker D8.

4.3.3. Surface profilometry

NPFLEX 3D surface metrology was used for surface profilometry analysis. Surface profilometry was used to determine whether there were any pits on the surface. The samples used for this type of analysis had to be cleaned using acid solution to remove any corrosion product on the steel surface according to ASTM G3 standard [155]. This was necessary for identification of any pits as the localised areas of pitting corrosion may could have been filled with corrosion products during the experiments. Two random 3*3 mm regions where targeted on each sample (Two for each experimental time and condition). A 2.5X objective was used with a working distance of approximately 3.5 mm. The results gathered were then analysed using Vision64 software the top 10 deepest pits were used for pit damage characterization of each scanned area. The localized corrosion rate was calculated by the following equation:

$$R_{Lcorr} = \frac{\mathrm{D} \times 8.76}{T} \quad (4\text{-}6)$$

Where R_{Lcorr} is the localized corrosion rate, mm/y; D is pit depth, μm; and T is the immersion time, h.

4.3.4. Raman Spectroscopy

Raman spectroscopy is a spectroscopic technique based upon the interaction of light with the chemical bonds within a material, it is commonly used in chemistry to provide a structural fingerprint by which molecules can be identified. Renishaw inVia confocal Raman microscope instrument was used to identify the nature of corrosion

products locally on the sample surface in this project. 错误!未找到引用源。 presents a picture of the Renishaw inVia confocal Raman microscope instrument used in this work. Two laser wavelengths of 488 nm and 785 nm are available for the Renishaw inVia confocal Raman microscope instrument. In this study, 488 nm wavelength radiation from an Ar ion laser was used as the excitation source for all the experiments to make sure the results are always comparable.

4.3.5.Focused Ion Beam sample preparation (FIB)

A focused ion beam (FIB) instrument resembles a SEM. However, while the SEM uses a focused beam of electrons to image the sample in the chamber, a FIB setup uses a focused beam of ions instead. Besides obtaining surface image, the ion beam allows etching of the sample at well localised sites, so that cross-sectional images of the structure can be obtained or that preparation of specimens for transmission electron microscopy (TEM) can be achieved. In this project, a FEI Helios G4 CX DualBeam was used to prepare TEM samples to investigate the cross section of the corrosion product layers. The region of interest was first coated with a protective layer of platinum, followed by bulk removal of the material. The sample was then lifted out in situ, attached to a Cu TEM grid, and then thinned to a final thickness of approximately 100 nm for TEM analysis.

4.3.6. Transmission Electron Microscopy (TEM)

Transmission electron microscopy (TEM) is a microscopy technique in which a beam of electrons is transmitted through a specimen to form an image. The accelerated and concentrated electron beam is projected onto a very thin sample, the electrons interact with sample as the beam is transmitted through the specimen to create an image on the imager after magnification and focusing. Due to the very short wavelength of electrons, the resolution of transmission electron microscopy is much higher than that of optical microscopy, reaching 0.1 to 0.2 nm with a magnification of tens of thousands to millions of times. The use of transmission electron microscopy can therefore

be used to observe the fine structure of a sample, or even the structure of just one column of atoms.

5. Chapter 5 General understanding of the corrosion and cracking behaviour of S13Cr MSS under HTHP downhole environment.

5.1. Introduction

Based on the literature review, the maximum operating temperature for S13Cr MSS in engineering applications is typically restricted to the range of 180-185°C. Relevant studies on the corrosion and cracking behaviour of S13Cr MSS are generally performed at temperatures below 180°C and mainly below 150°C. Research on the corrosion and cracking behaviour of S13Cr MSS at temperatures above 180°C is generally limited. The aim of this chapter is therefore to further understand the limitations of S13Cr MSS application in high temperature conditions by investigating its corrosion and cracking behaviour at 200°C under high pressure CO_2 and high Cl^- content environment and to clarify the risks of S13Cr MSS failure when applied to temperatures higher than the typically recommended operating conditions. The immersion test conditions for obtaining the corrosion rates presented in this chapter are summarized in Table 5-1.

Table 5-1. Test matrix for the immersion tests.

Temperature (°C)	Gas	Solution	Immersion time (hours)
200	5.2 MPa CO_2 at 200°C	Formation brine	5
			20
			48
			168

The SSRT conditions which were used to obtain the fracture characteristics of S13Cr MSS presented within this chapter are illustrated in Table 5-2.

Table 5-2. Test matrix for the SSRTs.

Temperature (°C)	Gas	Solution	Strain rate (s^{-1})	Exposure time in SSRT environments (without load) before tensile (hours)
200	6.8 MPa N_2 at 200°C	/	$4*10^{-6}$	0
				168
	5.2 MPa CO_2 at 200°C	Formation brine		0
				168

5.2. General corrosion of S13Cr MSS under HTHP environment

Figure 5-1 shows the general corrosion rates of S13Cr MSS at different immersion times in the formation brine at 200°C. It can be seen from figure that the general corrosion rates were recorded as 1.70 mm/y and 1.37 mm/y after 5 hours and 20 hours respectively, then dropped to a rate of 1.04 mm/year over 7 days of exposure. The slight reduction in corrosion rates can be attributed to the formation of the corrosion scales on the metal surface, suggesting that the corrosion scales can inhibit the mass transfer process during the corrosion process and thereby slow the corrosion rate.

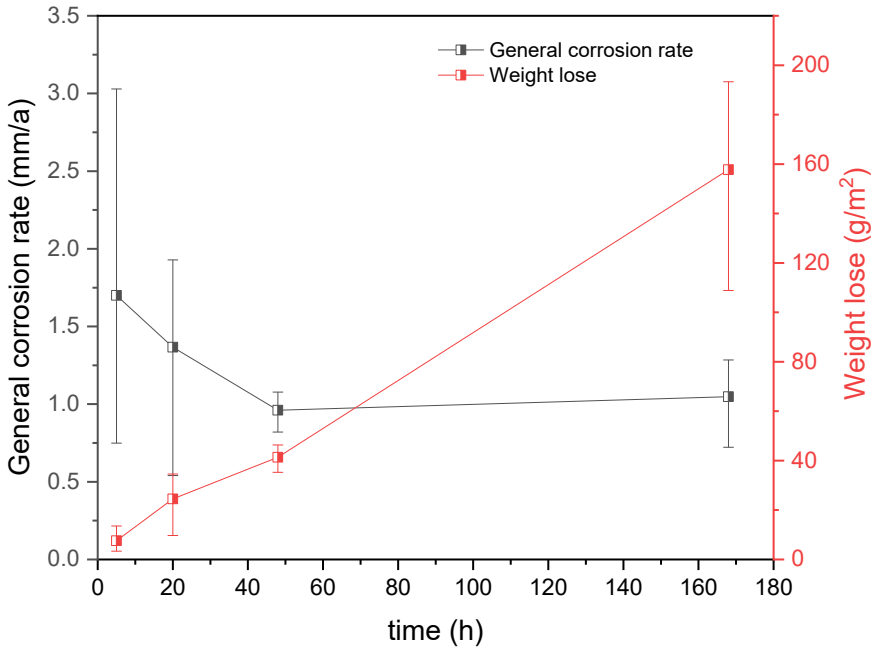

Figure 5-1. General corrosion rate of S13Cr MSS with various immersion times at 200°C.

In order to have an intuitive understanding of the degree of corrosion of S13Cr MSS in the formation brine at 200°C, the corrosion rate obtained through immersion tests was evaluated with reference to the NACE standard RP0775-2005-Qualitative categorization of carbon steel corrosion rates for oil production systems (as provide in Table 5-3) [156].

Table 5-3. Qualitative categorization of corrosion rates for oil production systems [156].

Level	Average corrosion rate (mm/y)	Maximum pitting rate (mm/y)
Low	< 0.025	< 0.13
Moderate	0.025-0.12	0.13-0.20
High	0.13-0.25	0.21-0.38
Severe	> 0.25	> 0.38

Note the qualitative categorization provide above is the qualitative categorization for carbon steel in oil and gas field, but not for stainless steel. However, based on the general corrosion rates

provide above and the results obtained from electrochemical methods which will mentioned in the next few chapters, the S13Cr MSS was considered in an active dissolution state at elevated temperature conditions which is more similar to service state of carbon steel but not a common service state of stainless steel, in this case, the categorization for stainless steel is no longer suitable here and we tend to use the qualitative categorization for carbon steel to evaluate the corrosion resistance of the S13Cr MSS at elevated temperature conditions.

The previous general corrosion rate curve shows that during a 7 days corrosion period, the general corrosion rate of S13Cr MSS gradually decreases and then stabilizes with the growth of the corrosion time, therefore, among these obtained corrosion rates, the corrosion rate with a corrosion period of 7 days is more suitable to be used for corrosion interpretation of S13Cr MSS at 200°C in formation brine and be provide as a reference for the downhole applications in oil and gas fields. As provided in Figure 5-1, the general corrosion rate of S13Cr MSS at 200°C in formation brine with a corrosion period of 7 days reached 1.04 mm/y, this can be classified as severe level which means that in terms of safety requirements, S13Cr MSS is not suitable for a long-term project with application temperature up to 200°C. However, for short-lived projects with application temperature up to 200°C, there is still potential for S13Cr MSS to be applied, considering both economic considerations and safety requirements.

5.3. Localized corrosion behaviour of S13Cr MSS under HTHP environment

5.3.1. Localized corrosion rate

As illustrated in Figure 5-2, the pit depth continually increased with increasing immersion time, however, the growth rate of the pit slowed down with immersion time, which corresponds to a decrease in pitting rate from 2.27 mm/y after 5 hours to 0.37 mm/y after 7 days.

Refer to the localized corrosion level qualitative categorization guidelines in Table 5-1, the localized corrosion rate of S13Cr MSS

at 200°C in formation brine obtained after 7 days of immersion was 0.37 mm/y, which is lower than 0.38 mm/y that required to achieve severe level, and is classified as high level. Compared to the general corrosion rate, which is at severe level, the localized corrosion rate is at a slightly lower level. This implies that in downhole environments with application temperatures up to 200°C, the general corrosion of S13Cr MSS poses a higher failure risk than localized corrosion and requires more attention.

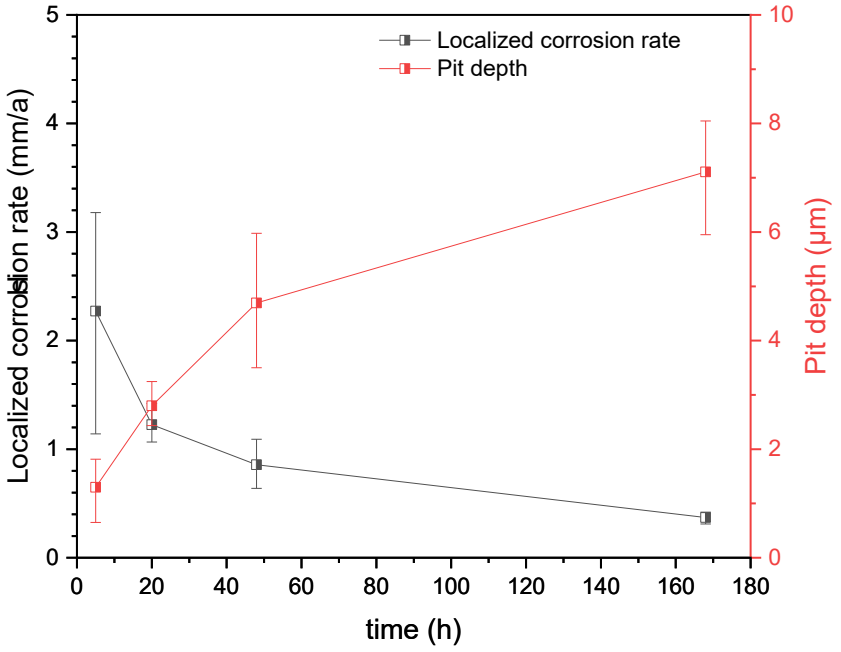

Figure 5-2. Localized corrosion rate of S13Cr MSS with various immersion times at 200°C.

5.3.2. Pit morphology

Surface profilometry analysis were performed using NPFLEX 3D interferometer to obtain the pit depth and pit morphology (radius/depth ratio (R/D ratio)) for further analysis in section 5.4.

As results shown in Figure 5-3, the R/D ratio followed a decreasing trend with the immersion times and decreased dramatically from 7.28 at 5 h to 3.54 at 20 h, then reached and maintained at 1.15 after 168 h. This suggests that the morphology of the pits

transformed from a wide-shallow shape to a hemisphere with the corrosion progressed.

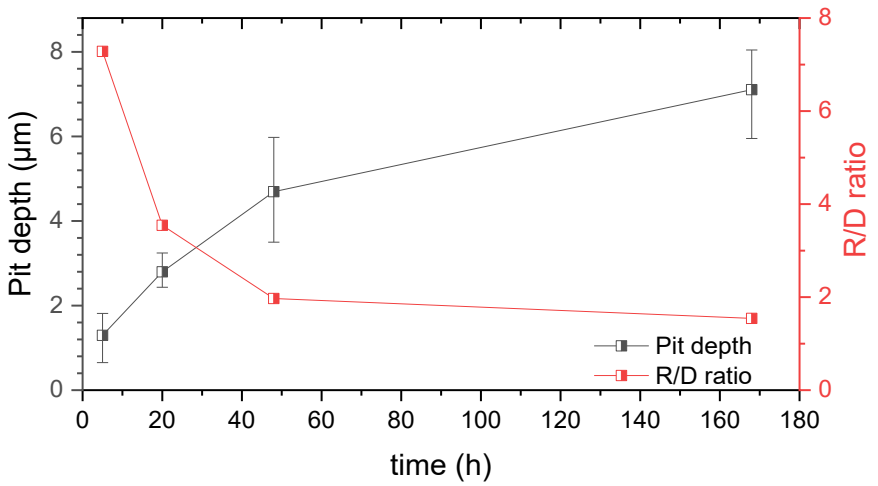

Figure 5-3. Pit depth and R/D ratio of S13Cr MSS with various immersion times at 200°C.

5.4. Stress corrosion cracking behaviour of S13Cr MSS under HTHP environment

Figure 5-4 provides the stress-strain curves of S13Cr MSS in the inert gas (N_2) and CO_2-saturated formation brine at 200°C, the samples under the N_2 environment were considered as a baseline for comparison purposes. In the N_2 environment, there was no significant difference from the results. As for the test in the CO_2-saturated formation brine without 7 days pre-corrosion, there was no obvious decrease in the ultimate tensile strength compared to those of the tests in the N_2 environment. However, a significant decrease in fracture strain was observed, suggesting that the presence of CO_2 can increase the susceptibility of S13Cr MSS to fracture. The necking process for each test was marked in the stress-strain curves. It is obvious that the necking of the pre-corrosion sample tested in the CO_2 saturated formation brine occurred earlier compared to that of the non-pre-corroded sample, indicating an increase in SCC susceptibilities of S13Cr MSS after 7 days pre-corrosion.

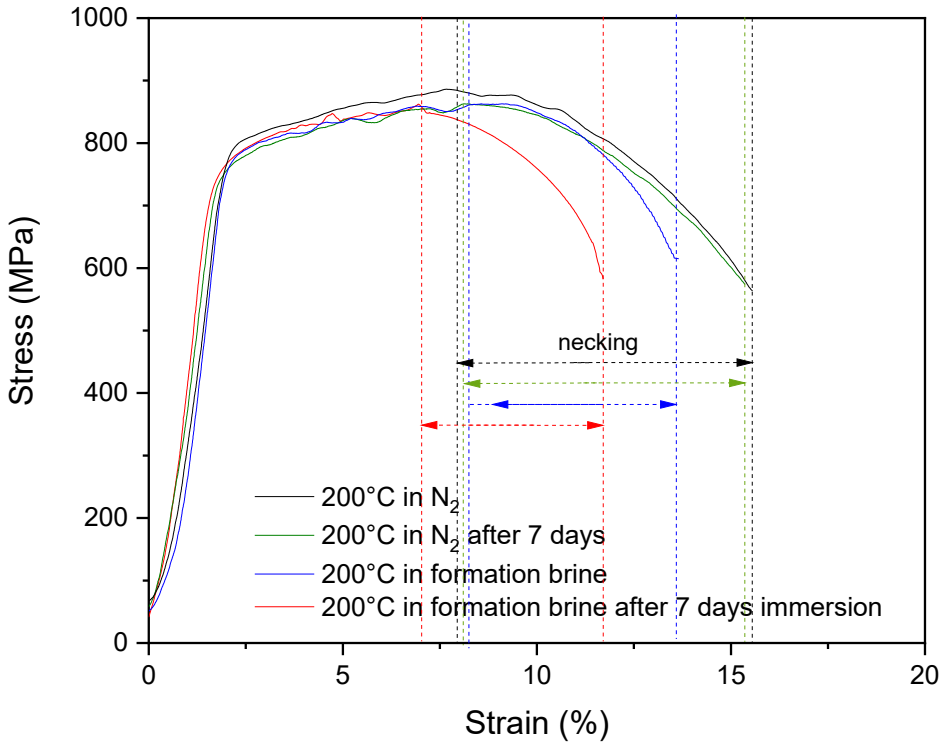

Figure 5-4. The stress-strain curves of S13Cr MSS in the N_2 environment and CO_2-saturated formation brine at 200°C.

To further analyse the SCC susceptibilities of S13Cr MSS at 200°C, the elongation ratio (ER) and reduction in area ratio (RAR) were calculated and shown in Figure 5-5. It was found that the ER and RAR of S13Cr MSS in the N_2 environment were higher than those of S13Cr MSS in the CO_2-saturated formation brine at 200°C. In addition, in the CO_2 saturated formation brine at 200°C, both the ER and RAR of S13Cr MSS after 7 days pre corrosion were reduced compared to sample without pre-corrosion, which supports the higher SCC susceptibility in Figure 5-5. Table 5-4 provides the criteria used to categorize the SCC sensitivity levels according to NACE TM0198 standard [157]. The ER and RAR obtained in the CO_2-saturated formation brine without pre-corrosion are slightly lower than 20%, indicating a slight loss of ductility according to NACE TM0198 standard which can be classified as class 2. Both reductions in ER and RAR exceed 20% obtained in the CO_2-saturated formation brine with pre-corrosion in comparison to the results obtained in the N_2 environment, which can be classified as class 3-substantial loss of ductility. It should be noted that the

above classification results are all based on the condition that no indications of cracking on the primary fracture surface and no indications of secondary cracking are permitted. Therefore, obtaining an accurate classification of SCC susceptibility requires fractographic analysis of the fracture surface.

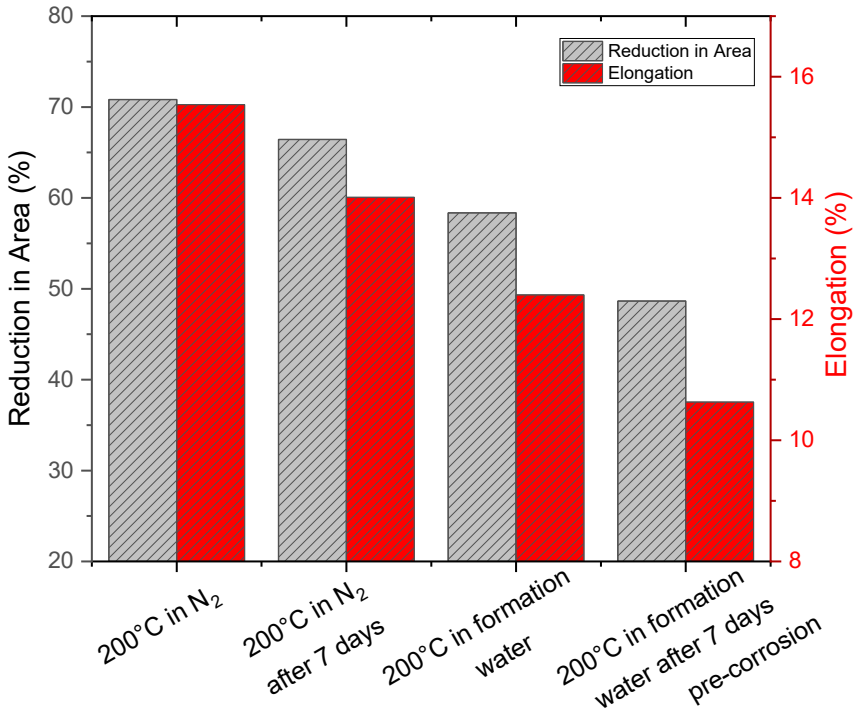

Figure 5-5. The calculated ER and RAR values of S13Cr MSS in the N_2 environment and CO_2-saturated formation brine at 200°C.

Figure 5-6 compares the fracture morphology of S13Cr MSS after SSRTs in the N_2 environment and CO_2-saturated formation brine at 200°C. It can be seen in Figure 5-6(a)-(f) that the fracture surface of S13Cr MSS tested in the N_2 environment with/without 7 days pre-exposure at 200°C exhibited typical ductile fracture characteristics, which is comprised of ductile dimples in “region A” and shear lips around the periphery designated as B in Figure 5-6(a) and (d). The details of regions A and B are shown in Figure 5-6(b), (e) and (c), (f) separately. Ductile dimples can be found in region A whilst shear dimples occurred throughout region B, which suggests that the fracture can be characterized as micro void coalescence (MVC) mechanism of ductile rupture.

Table 5-4. Classification of SCC susceptibility for oil production systems [157].

Level	Criteria
Class 1	Normal ductile behaviour comparable with the baseline value determined in the air/inert tests (i.e. loss in ductility <10%), with no indication of cracking on the primary fracture surface, and no indication of secondary cracking (i.e. cracking in the reduced section outside of the necked region).
Class 2	Ductile behaviour with only slight loss of ductility from the baseline value determined in the air/inert tests (i.e., loss in ductility < 20%). Fissures may develop in the necked region of the reduced section immediately adjacent to the primary fracture surface, and isolated spots of dark staining may be present on the primary fracture surface. No indications of cracking on the primary fracture surface and no indications of secondary cracking are permitted.
Class 3	Substantial loss of ductility from the baseline value determined in the air/inert tests (i.e., loss in ductility > 20%). Fissures may develop in the necked region of the reduced section immediately adjacent to the primary fracture surface, and areas of dark staining may be present on the primary fracture surface. No indications of cracking on the primary fracture surface and no indications of secondary cracking are permitted.
Class 4	Evidence of SCC in the reduced section by observation of either (a) cracking on the primary fracture surface, or (b) secondary cracking located in the reduced section outside of the necked region, or (c) both.

The fracture morphologies of samples tested in the CO_2-saturated formation brine with/without 7 days pre-corrosion are shown in Figure 5-6(g)-(i) and (j)-(l), respectively. Secondary cracks were observed on the fracture surface for both samples with/without 7 days pre-corrosion as shown in Figure 5-6(g) and (j) respective. For samples tested in the CO_2-saturated formation brine without pre-corrosion, magnification of region A marked in Figure 5-6(g) shows that the fracture in this region presents obvious tearing and cleavage as shown in Figure 5-6(h), indicating the quasi-cleavage fracture

characteristic. In region B, the fracture morphology changed to a ductile fracture characteristic; dimples can be observed as shown in Figure 5-6(i). For the pre-corrosion sample, the fracture surface appeared similar as shown in Figure 5-6(j), with both quasi-cleavage and ductile fracture in regions A and B, Figure 5-6(k) and (l), respectively. Given that secondary cracks were observed on the fracture surfaces of both sample with/without 7 days pre-corrosion, the previous assessment of SCC susceptibility based on the ER and RAR criteria is invalidated. Under the HTHP downhole environment (200°C, CO_2-saturated formation brine), the SCC susceptibility of S13Cr MSS is rated as Class 4 (on a scale of Class 1 to Class 4) for both sample with/without 7 days pre-corrosion.

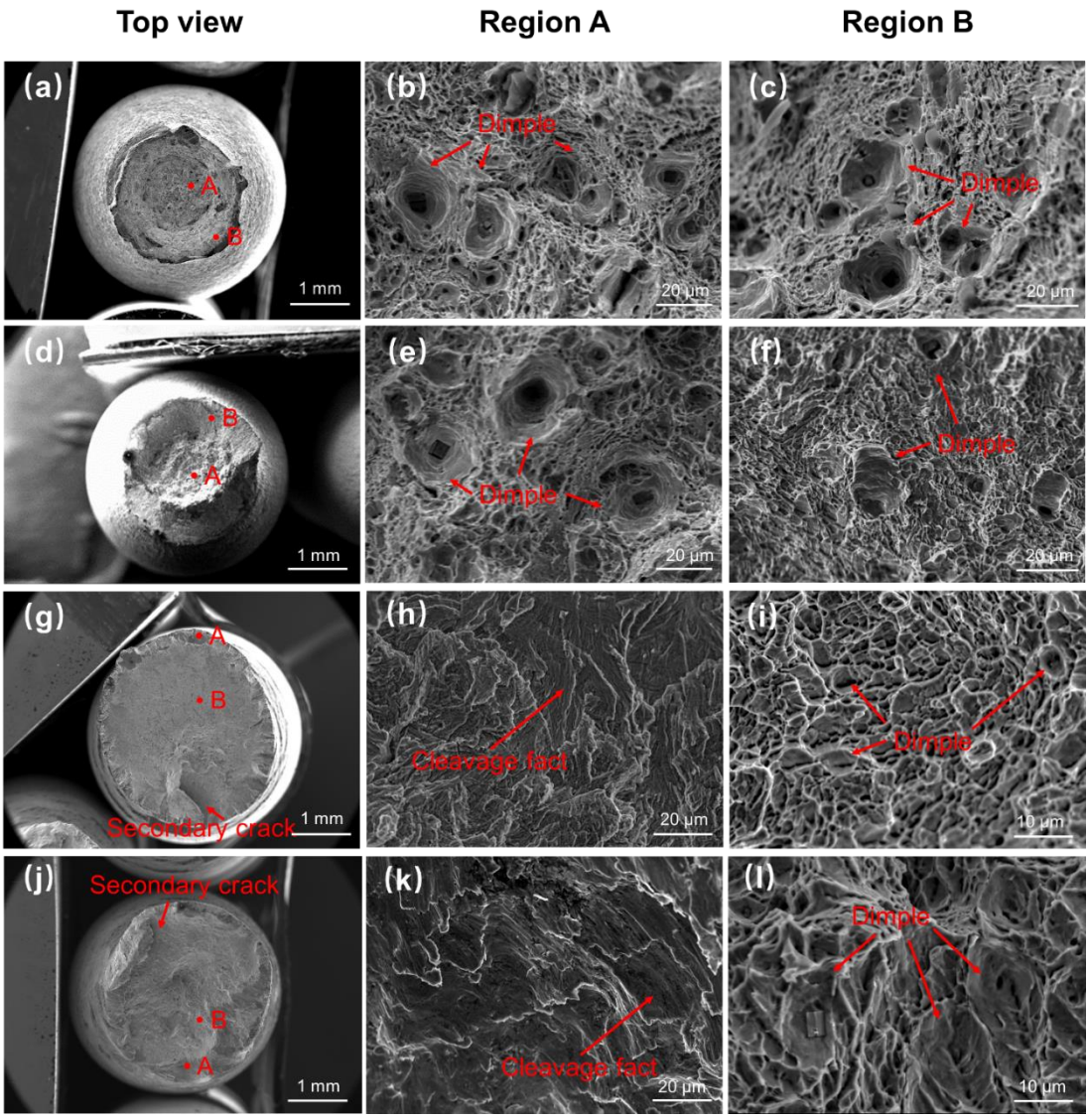

Figure 5-6. The fracture morphology of S13Cr after SSRT tests at 200°C (a)(b)(c) in N_2 and (d)(e)(f) in N_2 after 7 days tempering; in the CO_2-saturated formation brine (g)(h)(i) without and (j)(k)(l) with 7 days pre-corrosion.

To further understand the failure mode of the S13Cr MSS at 200°C, the micromorphology of the fracture from a side-view was assessed. For samples tested in the N_2 environment (Figure 5-7(a), (b)), typical tensile necking was observed, as-along with “cup and cone” fracture, indicative of good ductility. However, for samples tested in the CO_2-saturated formation brine (Figure 5-7(c), (d)), brittle shear-type fractures were observed, with fractures at a 45° plane to the direction of the applied tensile stress. Besides the main fracture, many cracks can be observed near the necking position of the samples tested in the CO_2-saturated formation brine, these cracks are perpendicular to the direction of the applied tensile stress and characteristic of environmentally assisted cracking.

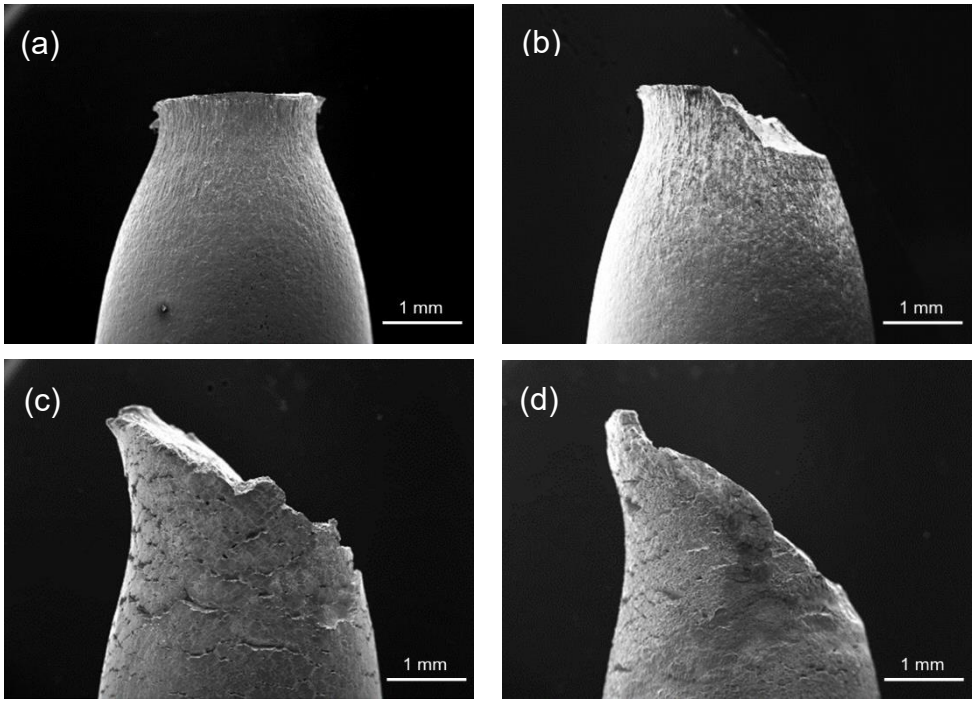

Figure 5-7. Side view of the fractured surface of S13Cr after SSRT at 200°C (a) in N_2 and (b) in N_2 after 7 days tempering; in the CO_2-saturated formation brine (c) without and (d) with 7 days pre-corrosion.

5.5. Relationship between pit and SCC

As shown previously, in the inert N_2 environment, prolonged insulation treatment at temperature up to 200°C does not affect the cracking behaviour of S13Cr MSS, however, the presence of CO_2 accompanied with high Cl^- content formation brine increased SCC susceptibility of S13Cr MSS. Figure 5-8 illustrates the local magnified images of S13Cr MSS samples after exposure in the CO_2-saturated formation brine. Both the pre-corrode and non-pre-corroded samples indicate that the early stage of cracks initiated from pits and propagated perpendicular to the tensile stress, revealing a clear correlation between pitting corrosion and crack initiation.

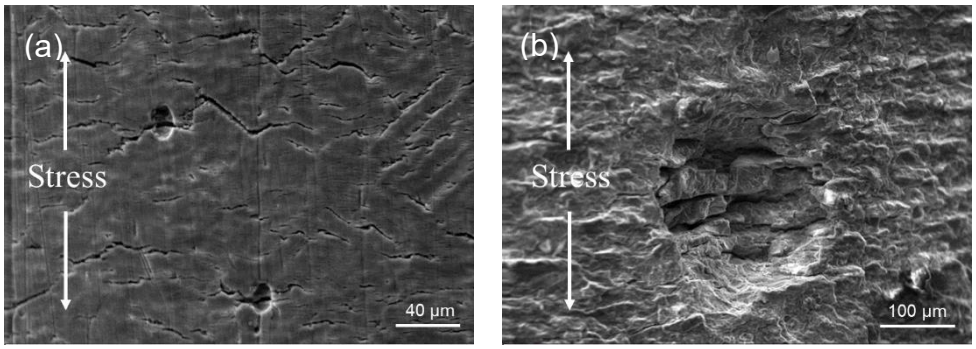

Figure 5-8. The side-view SEM images of S13Cr MSS surface after SSRT at 200°C in the CO_2-saturated formation brine (a) without and (b) with 7 days pre-corrosion.

Finite element (FE) analysis was performed in order to understand the effect of pit depth and morphology on stress concentration by using ANSYS V19.2 software. A bar with 3.81 mm in diameter and 25.4 mm in length was modelled to simulate the tensile specimen. Simplified pits with a half-ellipse section were created at the middle of the sample surface, the size of pits was set according to the measured radius to depth ratio (R/D ratio) and depth of the pits provided in Figure 5-3. Tensile stress (90% yield strength of API-P110 grade S13Cr MSS) was applied at both ends of the bar to obtain the distribution of stress within the pits.

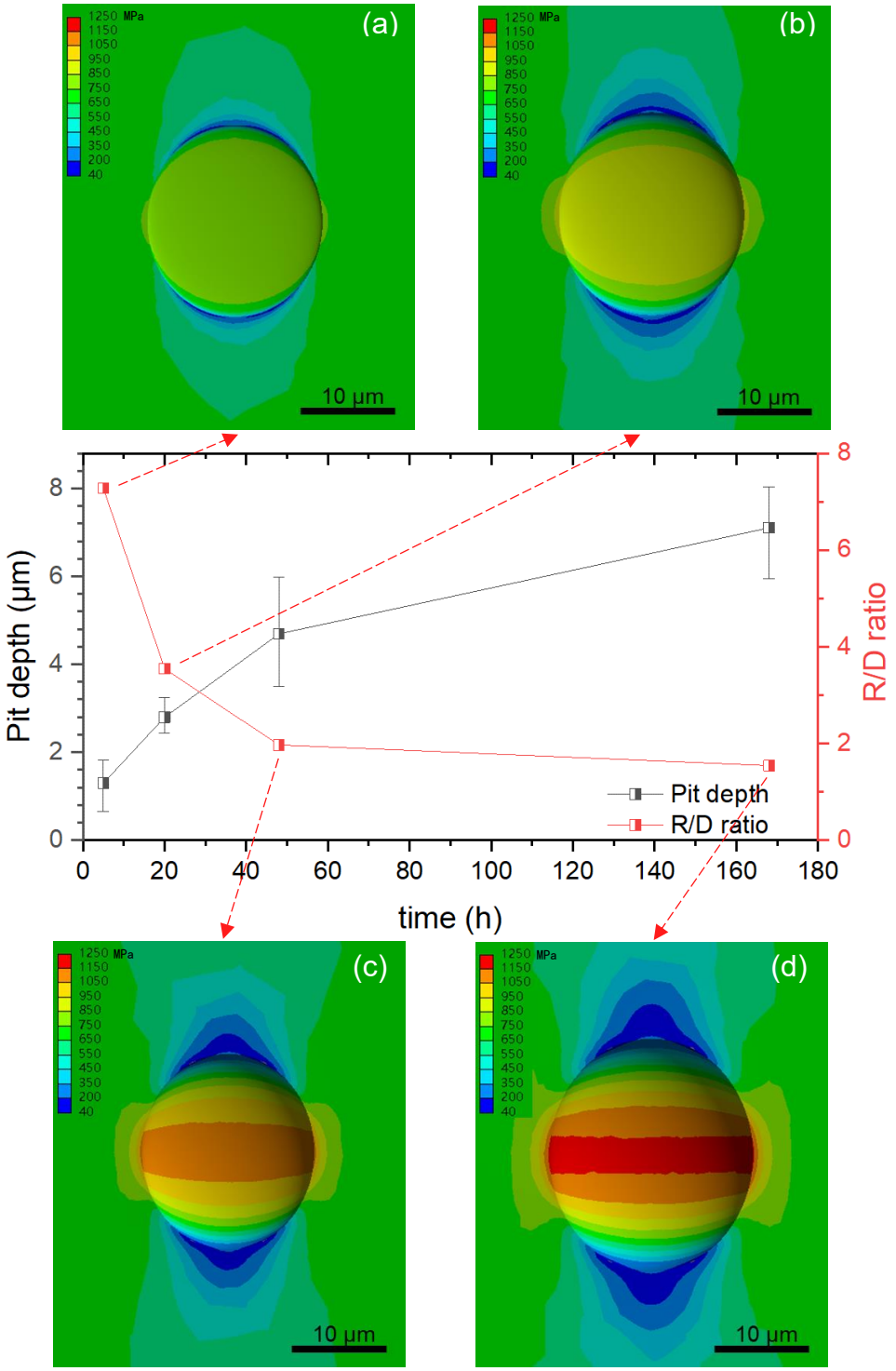

Figure 5-9. Stress distribution of pits with hemispherical cross-section under a loading of 90% yield strength.

The FE analysis results are displayed in shown in Figure 5-9. It is obvious that the stress was concentrated at the bottom of the pits and the maximum stress within the pits was perpendicular to the

applied tensile stress. Pits with smaller R/D ratio which corresponds to shorter corrosion period produced higher level of stress concentration. Therefore, the SCC susceptibility of S13Cr MSS in HTHP formation brine is positively related to immersion time.

To further investigate the SCC behaviour of S13Cr MSS in HTHP CO_2-saturated formation brine, as well as the relationship between pitting and crack initiation, a 15 days Four-Pint Bend (FPB) constant load test was conducted with an applied stress of 90% of the yield strength. The results are presented in Figure 5-10. Although the SSRT results indicated a high SCC susceptibility of the S13Cr MSS in HTHP CO_2-saturated formation brine under the continuous plastic deformation, and microstructural observations confirmed that cracks initiated from pits, however, no fracture occurred in the specimen subjected to the 15-day FPB test (as shown in Figure 5-10(a)). Moreover, as shown in Figure 5-10(b), no cracks were observed within the loaded region. Meanwhile, Figure 5-10(c) reveals that no distinct evidence of crack initiation at the bottom of the pits. The cracking observed in Figure 5-10(c) is attributed to the dehydration of the corrosion product film after the test.

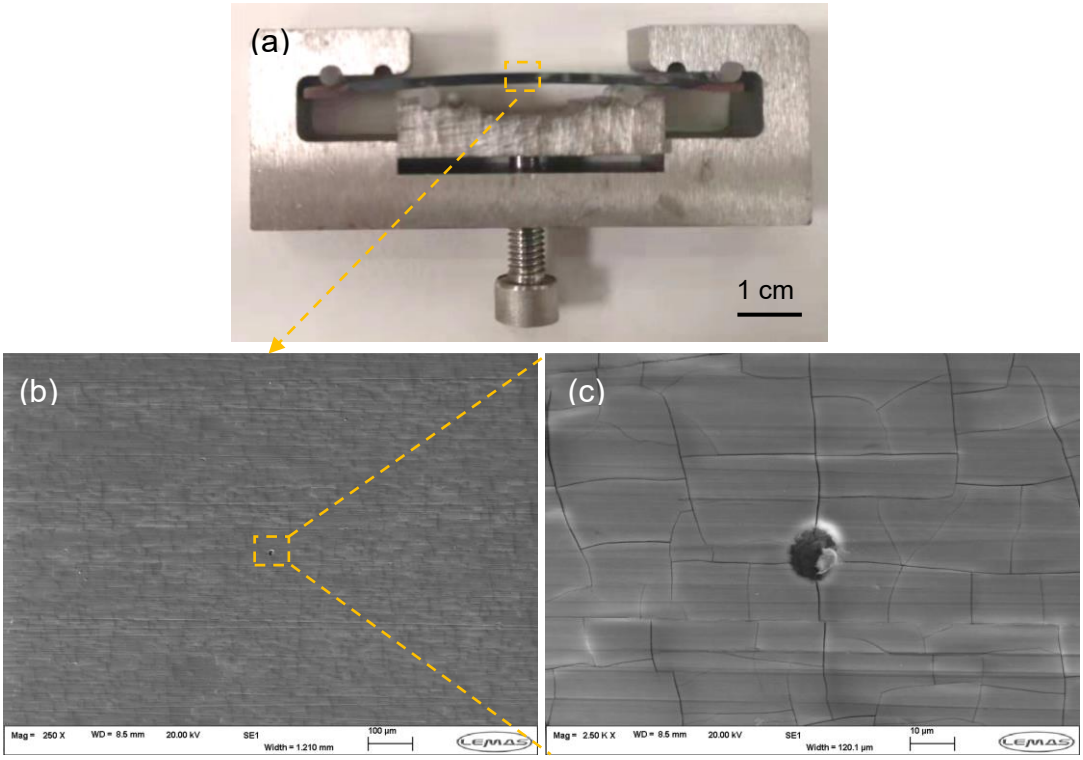

Figure 5-10. (a) Macroscopic morphology and (b),(c) surface microscopic morphology of FPB sample with a loading of 90% yield strength at 200°C in the CO_2-saturated formation brine for 15 days.

These findings demonstrate that under constant load condition, pits do not necessarily lead to crack initiation. In the absence of continuous dynamic plastic strain which could force specimen fracture, a static high stress alone is insufficient to induce crack initiation at pits.

Based on the above results, it is concluded that the high SCC susceptibility observed in the SSRT tests is largely induced by the unrealistic dynamic strain imposed during the accelerated test. In contrast, under static loading condition, which is more closely resemble actual service condition, S13Cr MSS remained intact. Hence, compared to the SCC behaviour, the severe general corrosion of S13Cr MSS in HTHP downhole environments requires particular attention, as it may be the dominant factor governing tube integrity throughout the full-lifecycle service of S13Cr MSS under such extreme HTHP downhole condition. Therefore, the subsequent chapters of this thesis will shift the research focus to the general corrosion behaviour of S13Cr MSS in HTHP downhole environments.

5.6. Conclusions

1. The general corrosion rate of S13Cr MSS in a simulated downhole environment was 1.70 mm/y in the first 5 hours and reached a rate of 1.04 mm/year over 7 days exposure. In the meantime, the localized corrosion rate was high (2.27 mm/year) in the first 5 hours with a corresponding pit depth of 1.30 μm and dropped to 0.37 mm/y with the pit depth of 7.11 μm after 7 days.
2. Cracking in S13Cr MSS in the CO_2-saturated formation brine at 200°C initiated at pits. The morphology of the pits became steeper during the corrosion process as the R/D ratio decreasing from 7.28 to 1.15 between 5h and 168h of exposure. The level of stress concentration at the bottom of the pits increased and thereby resulted in an increase in the SCC susceptibility of S13Cr MSS.

3. The general corrosion rate of S13Cr MSS is more severe compared to the localized corrosion rate over 7 days exposure at 200°C, the attention needs to be focused on its general corrosion behaviour when the S13Cr MSS is in service at HTHP condition.

6. Chapter 6 Formation/evolution of corrosion product film formed on S13Cr MSS in aggressive HTHP downhole environments: effect of CO_2 partial pressure

6.1. Introduction

In the previous chapter, we identified the general corrosion as the main failure risk of S13Cr MSS in an aggressive HTHP downhole environment. Therefore, we specifically focus on the general corrosion behaviour of S13Cr MSS in the following study. In this chapter, to investigate the corrosion mechanisms and associated corrosion product film evolution at 200°C, we conducted systematic experiments under two CO_2 partial pressures (5.2 MPa and 0.27 MPa) with varying exposure times through immersion tests (Table 6-1) and electrochemical measurements combined with surface characterization using SEM, EDS, Raman spectroscopy, etc..

Table 6-1. Test matrix for the immersion tests.

Temperature (°C)	P_{CO2} at 200°C (MPa)	Solution	Immersion time (hours)
200	5.2	Formation brine	5
			20
			48
			168
	0.27		5
			20
			48
			168

6.2. Film formation and morphology observation at 200°C with pCO_2 of 5.2 MPa

6.2.1. Overall observation of the surface morphology at 200°C with pCO_2 of 5.2 MPa

Figure 6-1 provides the typical top-view and cross-section images of S13Cr MSS exposed to CO_2-saturated formation brine at 200°C with CO_2 partial pressure of 5.2 MPa at different immersion times. As shown in Figure 6-1(a), local magnified view shows distinct dark areas which represent a higher content of light elements than lighter areas in backscattered electron imaging. Cross-section as provided in Figure 6-1(b) shows a discontinuous layer of corrosion products, indicating preferential corrosion in the darker area during the first 5 h of immersion. After 20, 48 and 168 h of exposure, polishing marks were still visible from top-view images, cracks due to the dehydration of the corrosion product film after removal from the test solution can be observed on the sample surface [158]. Cross-section images (Figure 6-1(d) and (f)) indicate that a uniform corrosion product film formed at 20 h and 48 h, and it covered the entire surface of the sample. The thickness of the corrosion product film increased with immersion time. As the immersion time increased to 168 h, a double-layer corrosion product was evident, the corrosion product film can be divided into a uniform outer layer and an inner layer containing white spots. More details on analysing this film are given in the later sections.

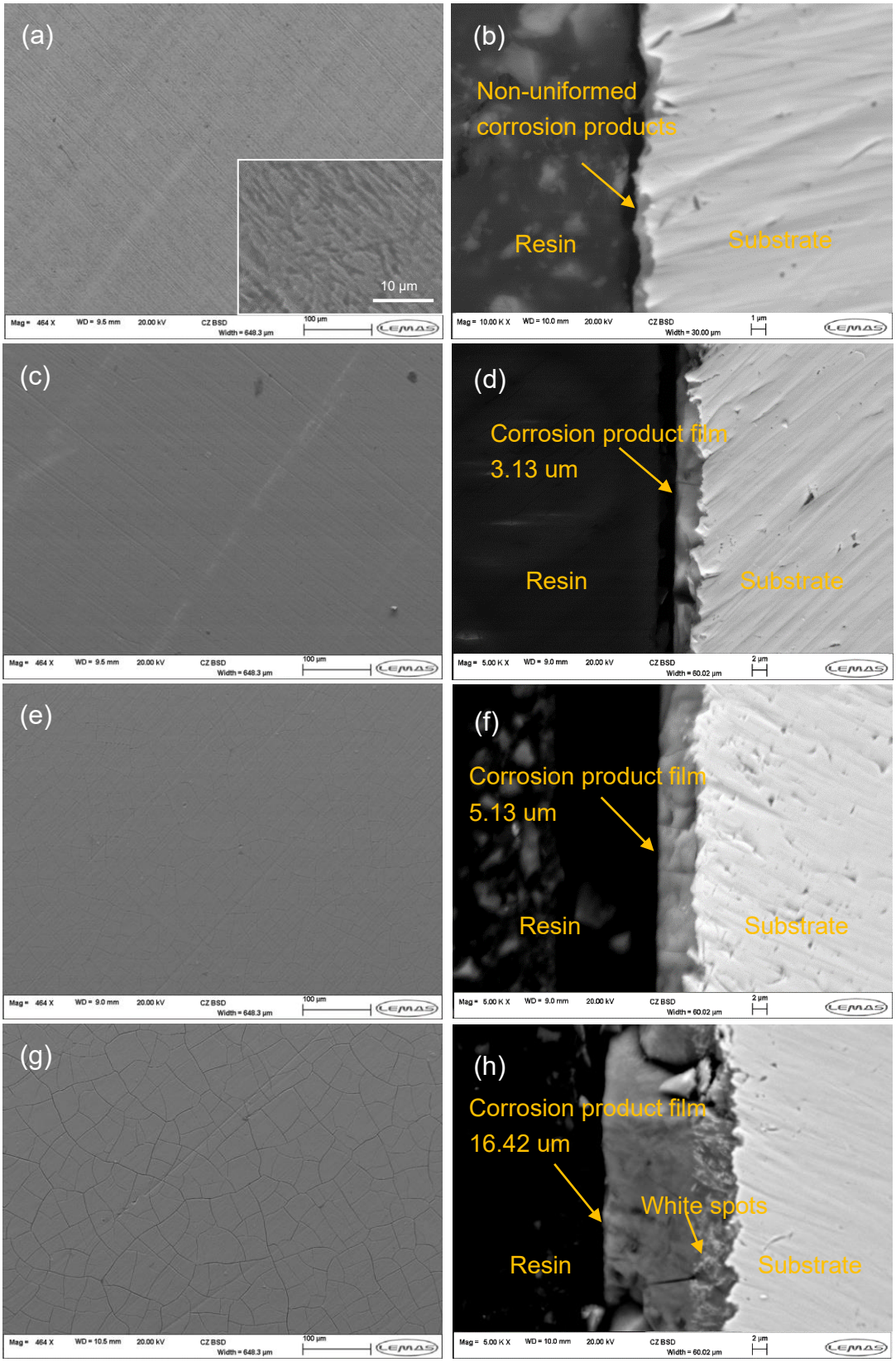

Figure 6-1. Surface and cross-sectional morphologies of corrosion product film on S13Cr MSS under 200°C and 5.2 MPa CO_2 for (a)(b) 5, (c)(d) 20, (e)(f) 48 and (g)(h) 168 hours.

Figure 6-2 (a) provides the XRD patterns of the corroded S13Cr MSS obtained at 200°C and 5.2 MPa CO_2 partial pressure with various durations. No peaks belonging to corrosion products can be detected by XRD, indicating the corrosion products on the sample surface were in an amorphous state. Raman spectroscopy was employed to further understand the chemical composition of amorphous corrosion products. The characteristic spectra obtained are presented in Figure 6-2 (b). Peaks located at around 552 cm^{-1} and 717 cm^{-1} were observed, confirming that the corrosion products are mainly Cr_2O_3 and $Cr(OH)_3$ [125, 143]. Meanwhile, the number and position of the corrosion product peaks did not show significant change with the increase of immersion time, indicating that the types of corrosion products did not change significantly with increasing immersion time.

Based on the above observations, the corrosion process of S13Cr MSS at 200°C and 5.2 MPa CO_2 can be divided into three stages:

1. Early stage: characterised by a non-uniform corrosion product film formed on the surface;
2. Middle stage: characterised by the formation of a uniform single-layer corrosion product film;
3. Final stage: characterised by the formation of a double-layer corrosion product film which including a uniform outer layer and an inner layer containing white spots.

A more detailed analysis of these three stages is provided in the subsequent sections.

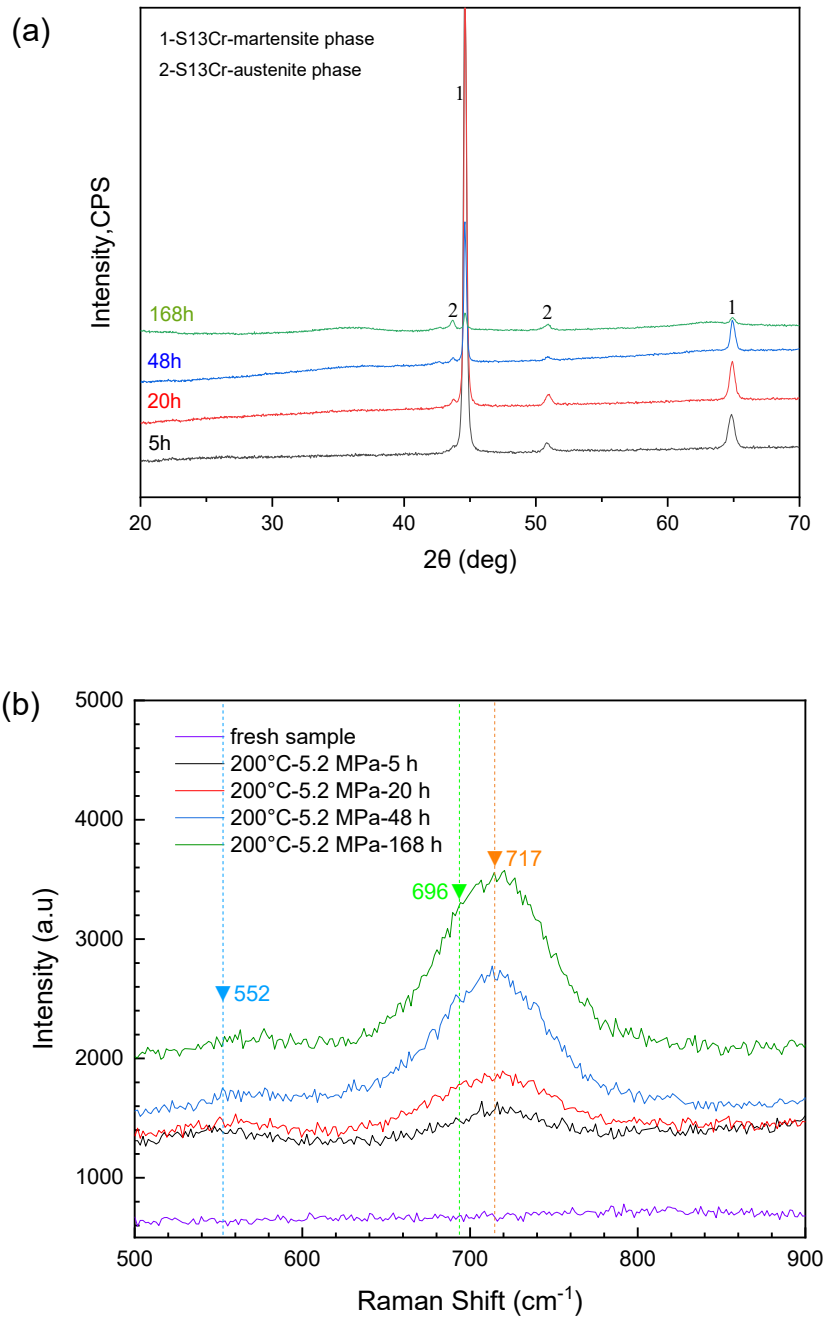

Figure 6-2. XRD patterns and Raman spectroscopy of S13Cr MSS specimens exposed at 200°C and 5.2 MPa CO_2 for 5, 20, 48 and 168 hours.

6.2.2. Early stage of the corrosion scales formation and evolution during long-term corrosion at 200°C with pCO_2 of 5.2 MPa

Figure 6-3(a), (b) and (c) provide the typical top-view images of S13Cr MSS exposed to CO_2-saturated formation brine at 200°C with CO_2 partial pressure of 5.2 MPa at different immersion times during the early stage. As shown in Figure 6-3(a), there were no visible signs of corrosion on sample surface after 1 h of immersion. After 3 h, scattered dark regions, which were related to the preferential corrosion area, appeared as marked in Figure 6-3(b), and became larger and more obvious after 5 h of immersion as shown in Figure 6-3(c). In the backscattered electron (BSE) image, the darker regions have a higher content of lighter elements than the lighter regions, implying preferential corrosion in the black regions in this study. Cross-section after 5 h of immersion as provided in Figure 6-3(d) shows a discontinuous layer of corrosion products, indicating preferential corrosion in the darker regions.

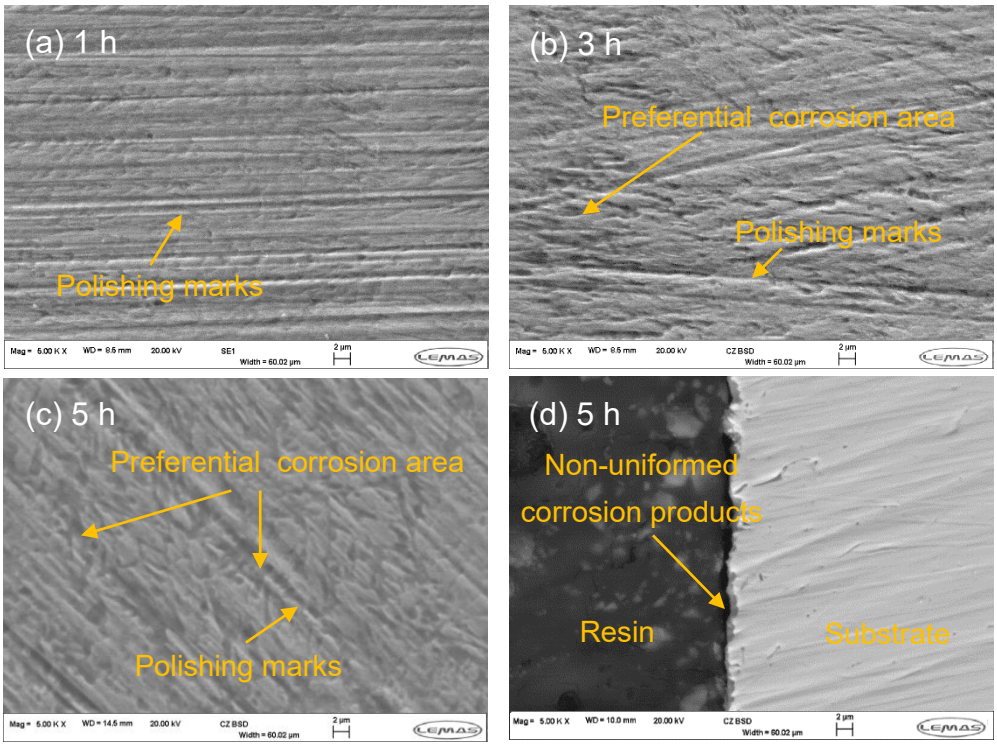

Figure 6-3. BSE surface morphologies of S13Cr MSS immersed in formation brine under 200°C and 5.2 MPa CO_2 for (a) 1, (b) 3 and (c) 5 hours; (d) cross-sectional for 5 hours.

To understand the chemistry of the corrosion products on S13Cr MSS at 200°C and 5.2 MPa CO_2 for 5 hours, EDS line scanning was performed on the surface of S13Cr MSS as shown in Figure 6-4. Figure 6-4(a) shows the region designated for EDS line scanning, encompassing both light and dark areas within the scanned line.

The line scan results in Figure 6-4(b) reveal that the dark region, as compared to the light region, has higher content of Cr and O while lacking in Fe. This confirms that the dark region experiences more significant corrosion compared to the light region, indicating a non-uniform corrosion at the early stage. It is noteworthy that in Figure 6-4(b-4) and (b-5), the distribution of Ni and Mo element follow a similar trend to that of Cr and O.

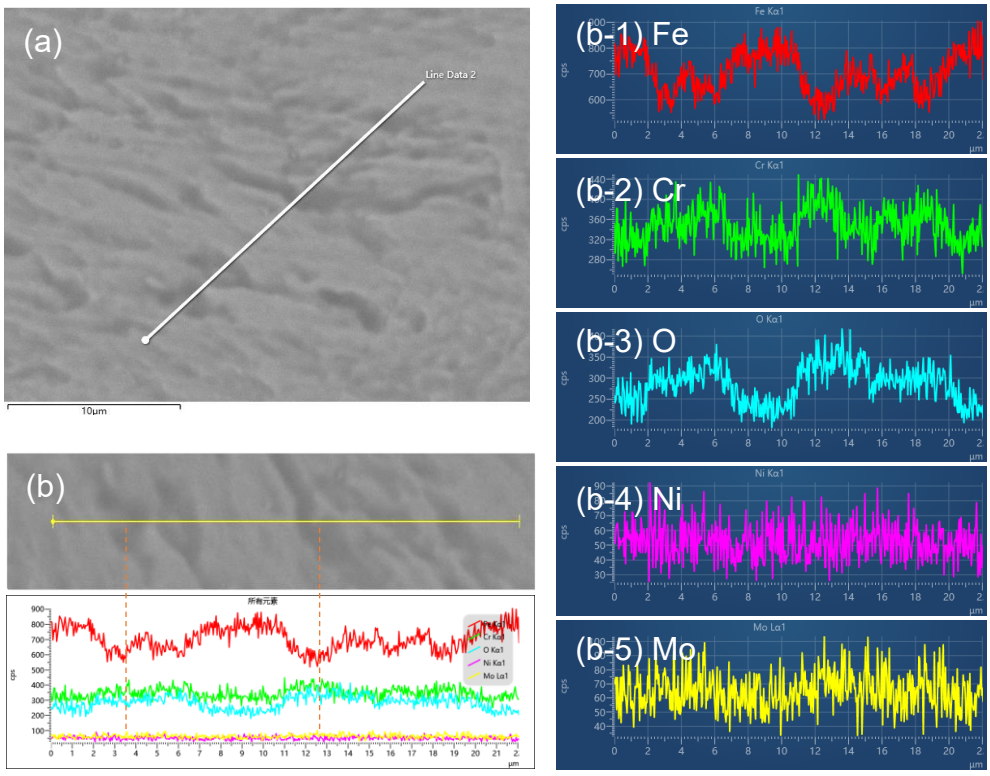

Figure 6-4. (a) SEM image of selected area used for EDS line scanning obtained from S13Cr MSS exposure to formation brine under 200°C and 5.2 MPa CO_2 for 5 hours and (b) EDS line scanning results of the selected position.

To further analysis the chemistry of the corrosion products on S13Cr MSS at 200°C and 5.2 MPa CO_2 for 5 hours, Raman spectroscopy was performed on the surface of S13Cr MSS locally as shown in

Figure 6-5. Figure 6-5(a) shows the Raman point identify results at dark region and light region as well as the fresh sample. For fresh sample, no obvious peaks can be observed, indicating the limitation to analysis the atmosphere-formed passive film by using Raman spectroscopy. Peaks located at around 552 cm^{-1} and 712 cm^{-1} were observed in both dark and light region, confirming that the corrosion products are mainly Cr_2O_3 and $Cr(OH)_3$ [140, 159]. More visual line scanning results of the intensity of the Cr_2O_3 and $Cr(OH)_3$ signal at 552 cm^{-1} and 712 cm^{-1} obtained from a line scanning alone the marked line in Figure 6-5(b) are shown in Figure 6-5(c) and (d), respectively. It is obvious that the intensity of signals at 552 cm^{-1} and 712 cm^{-1} in dark regions were higher than those in light region, indicating that the dark region endured a stronger corrosion.

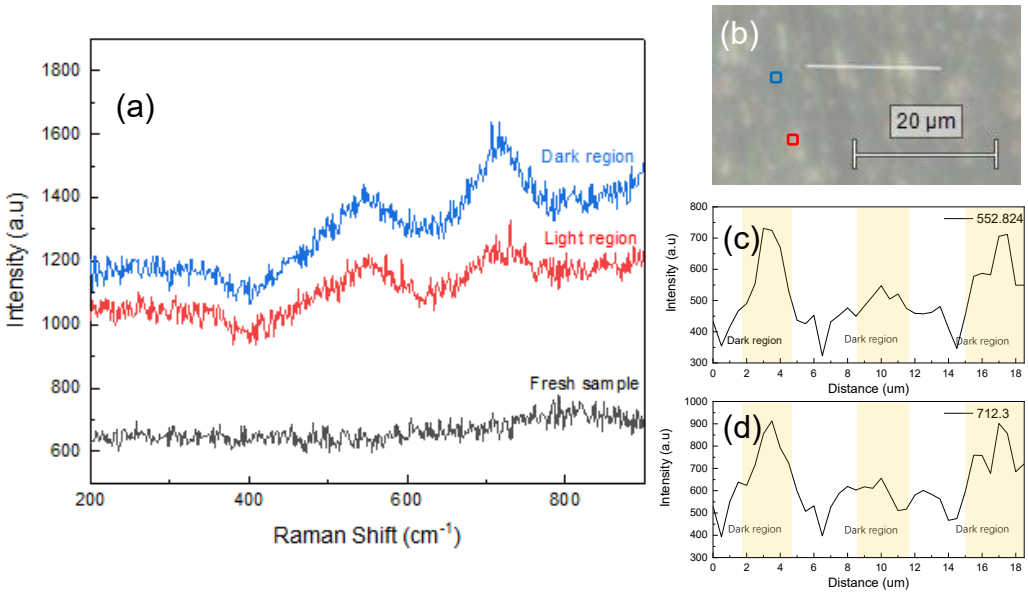

Figure 6-5. Raman spectroscopy and line scanning of S13Cr MSS specimen exposed at 200°C and 5.2 MPa CO_2 for 5 hours: (a) point identify of different regions, (b) schematic diagram of scanning area and (c), (d) line scanning results at 552 cm^{-1} and 712 cm^{-1}.

6.2.3. Middle stage of the corrosion scales formation and evolution during a long-term corrosion at 200°C with pCO_2 of 5.2 MPa

After 20 and 48 h of exposure, cracks due to the dehydration of the corrosion scales after removal from the test solution can be observed on the entire sample surface, indicating a fully covered film formed at middle stage [158]. The polishing marks on the sample surface produced during sample preparation before corrosion test were still apparent after corrosion, suggesting the growth direction of the corrosion products is towards the metal matrix. Cross-sectional images (Figure 6-1(b) and (d)) indicate that uniform corrosion scales formed on sample surface at 20 and 48 h. The thickness of corrosion product scale increased with immersion time.

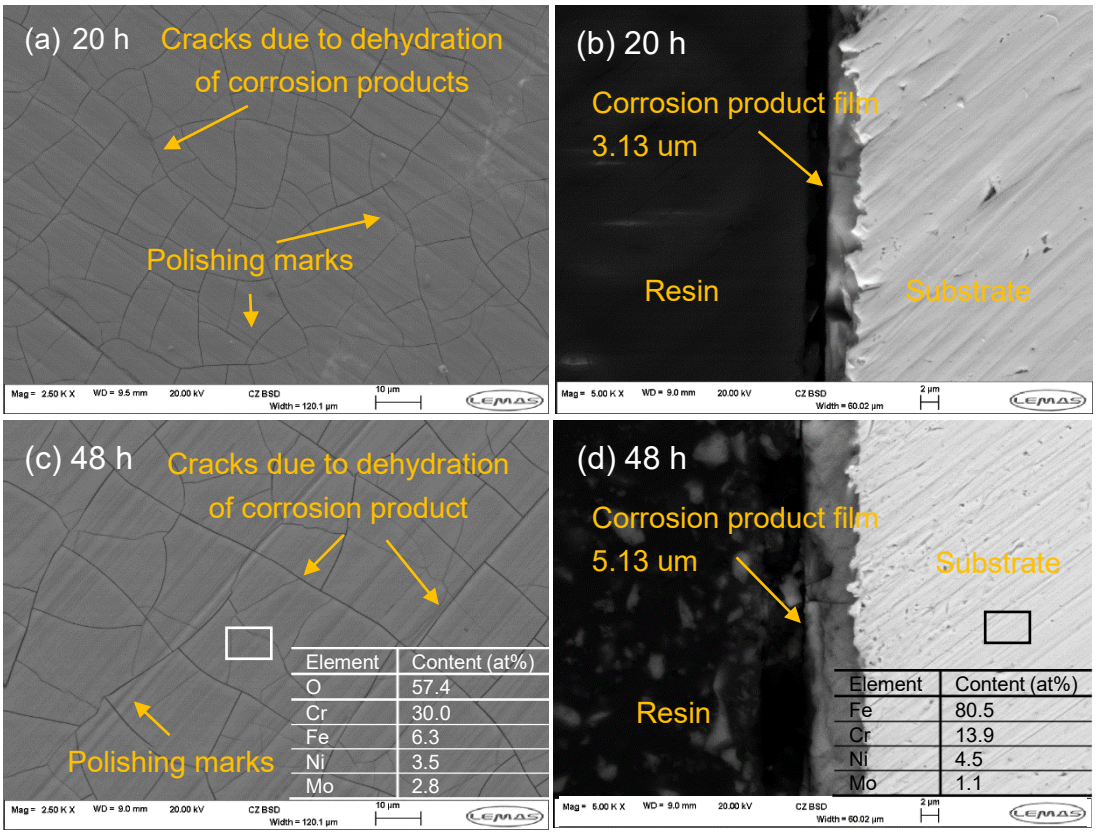

Figure 6-6. Surface and cross-sectional morphologies of corrosion product film on S13Cr MSS under 200°C and 5.2 MPa CO_2 for (a)(b) 20 and (c)(d) 48 hours.

Figure 6-7 illustrates the Raman spectroscopy of the corrosion products formed on S13Cr MSS at 200°C and 5.2 MPa CO_2 for 20 and 48 h. Similar to the corrosion products formed at early stage, Raman spectroscopy of corrosion products formed at middle stage shows peaks located at 556 cm^{-1} and 717 cm^{-1} were observed at both 20 and 48 h, suggesting that the corrosion products are mainly Cr_2O_3 and $Cr(OH)_3$.

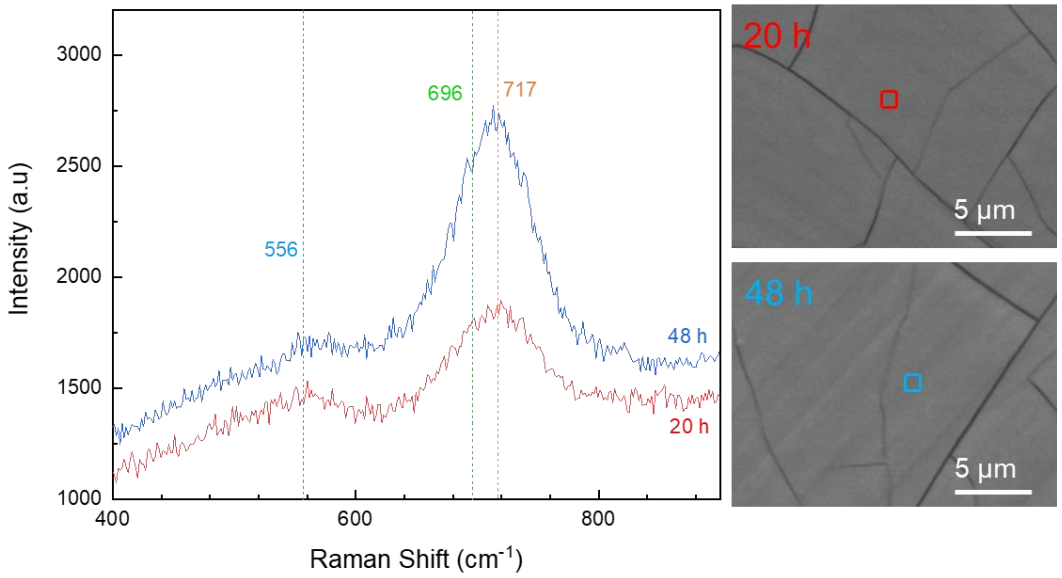

Figure 6-7. Raman spectroscopy of S13Cr MSS specimens exposed at 200°C and 5.2 MPa CO_2 for 20 and 48 hours.

The EDS analysis in Figure 6-1(c) demonstrates that while chromium and oxygen dominate the corrosion product film, small amount of Mo, Ni, and Fe are also present. It is noteworthy that the proportion of Fe in the metallic elements of the corrosion product film is markedly lower than its proportion in the S13Cr MSS alloy, this suggests that most of Fe preferentially dissolves into the corrosive medium rather than participating in the formation of the corrosion product film. The Fe and Ni incorporated into the corrosion product film are typically considered to form spinel-type oxides [141]. However, the characteristic Raman peak of spinal (~696 cm^{-1}) is very close to the $Cr(OH)_3$ peak (~717 cm^{-1}). In this study, The intense $Cr(OH)_3$ peak likely obscured the weaker spinel signals, making the spinel difficult to resolve in the Raman spectra.

6.2.4. Final stage of the corrosion scales formation and evolution during a long-term corrosion at 200°C with pCO_2 of 5.2 MPa

Figure 6-8 indicates the top-view and cross-sectional images of corrosion scale formed on S13Cr MSS under 200°C and 5.2 MPa CO_2 for 168 hours. As the immersion time increase to 168 h, there was no significant morphological change in the corrosion scale compared to that formed at middle stage from top-view, cracks due to the dehydration of the corrosion scale and polishing marks produced before corrosion test were still apparent as shown in Figure 6-8(a). However, a double-layered corrosion scale was evident in cross section as shown in Figure 6-8(b), the corrosion scale can be divided into a uniform outer layer and a white spot-containing inner layer. More details on analysing this film are given in the later sections.

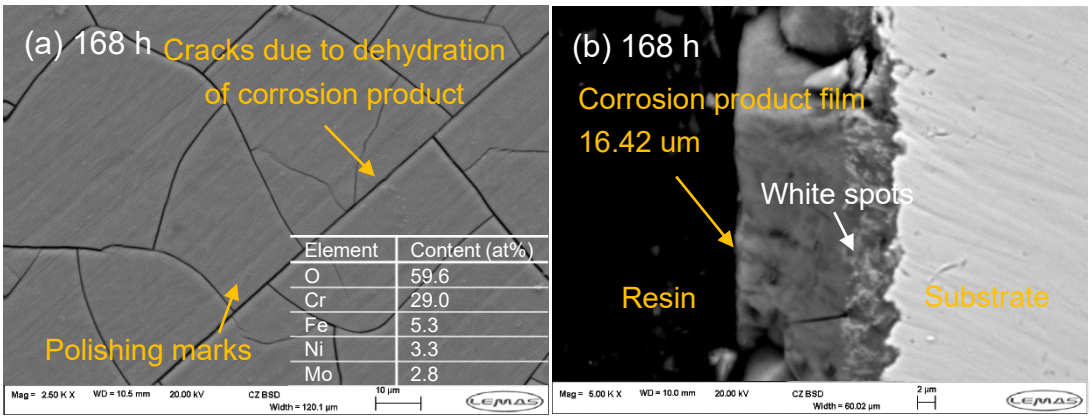

Figure 6-8. (a) Top-view and (b) cross-sectional images of corrosion film on S13Cr MSS under 200°C and 5.2 MPa CO_2 for 168 hours.

A combination of FIB-SEM and TEM was employed to further understand the nature of the corrosion product film formed on the surface of S13Cr MSS at 200°C and 5.2 MPa CO_2 partial pressure after 168 h of exposure in terms of the composition/phase and distribution of white spots. Figure 6-9(a) shows the SEM image of the selected area used for TEM sample preparation prepared using FIB. The corrosion product film was clearly divided into two layers, EDS line scanning results as presented in Figure 6-9(b) indicate that

the composition of the dark area in the inner corrosion product layer is similar to the outer corrosion product layer, containing a higher concentration of Cr and O. But white spots which contains higher Fe, Ni and lower Cr, O cause the fluctuations in composition in EDS line scan results.

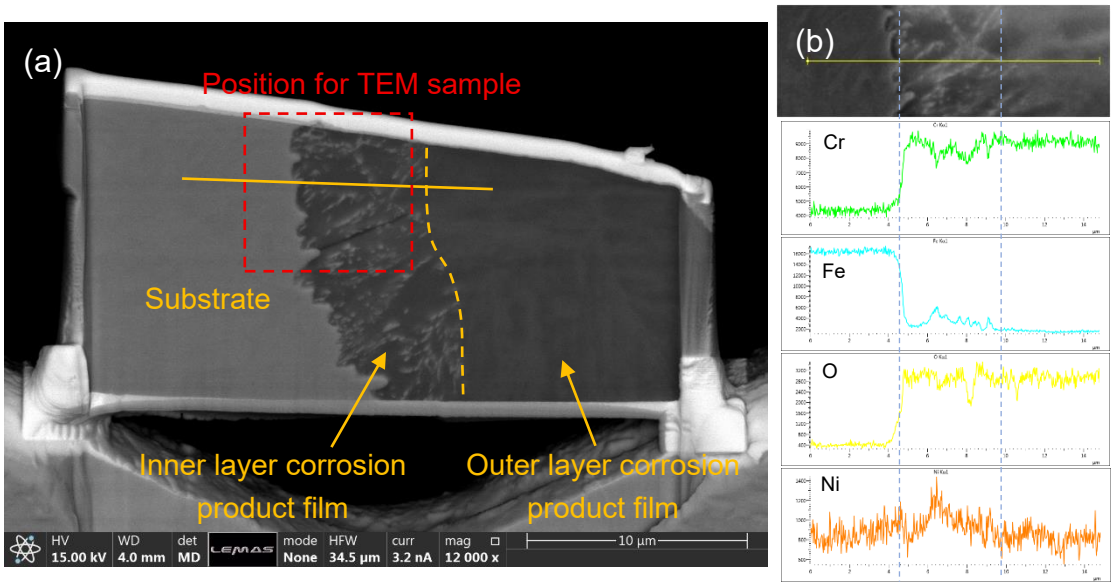

Figure 6-9. (a) SEM image of selected area used for TEM sample preparation obtained from S13Cr MSS exposure to formation brine under 200°C and 5.2 MPa CO_2 for 168 hours and (b) EDS line scanning results.

FIB was used to further thinning the sample for TEM observation to confirm the phase/distribution of white particles in the inner corrosion product layer. As shown in Figure 6-10(a), in the TEM image, the white particles have a darker lining which is similar to the substrate. The electron diffraction pattern for the selected region 1 which contains few particles as shown in Figure 6-10(b) and (c) indicates the particles in the inner corrosion product layer are confirmed as austenite. Furthermore, the austenite particles in the inner corrosion product layer were mainly distributed along lines, which is consistent with the distribution pattern of reversed austenite in S13Cr MSS, along the martensitic slat boundaries and ex-austenitic grain boundaries. As shown in Figure 6 10(d), the electron diffraction pattern for the selected region 2 which does not contain austenite particle indicates the corrosion products are mainly Cr_2O_3 and $Cr(OH)_3$.

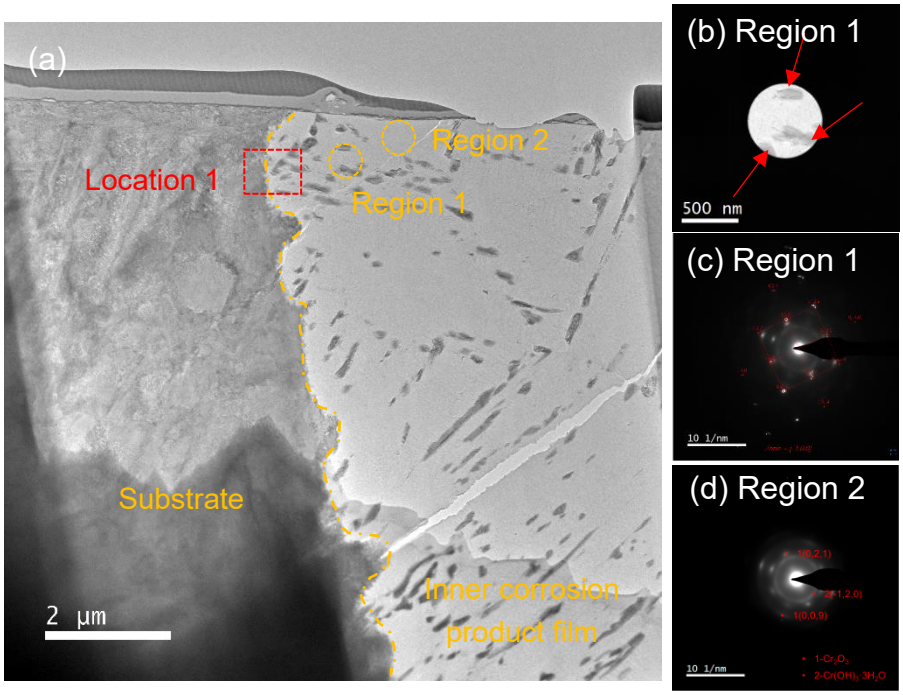

Figure 6-10. (a) TEM images of corrosion product film formed on S13Cr MSS in formation brine under 200°C and 5.2 MPa CO_2 for 168 hours, (b) selected region 1 for electron diffraction pattern analysis and (c) the corresponding electron diffraction patterns.

Figure 6-11 provides high-angle annular dark-field (HAADF) images of the metal/corrosion products interface region marked in Figure 6-10 and related EDS mapping. It can be clearly seen in the Fe distribution mapping that the dark area in the HAADF, i.e. the corrosion product, has a low Fe content. A gray region between the metal matrix (light area) and the corrosion scale (dark area) with a medium Fe content compared to the matrix and a medium O content compared to the corrosion product in the dark area can be distinguished. In contrast, Ni and Cr in this region show the same lining compared to matrix, suggesting a preferential dissolution of Fe during corrosion. Besides, the Ni content in the corrosion scale was slightly reduced compared to the Ni content in the matrix, while the uncorroded austenite shows a significantly higher Ni lining than the matrix and Fe preferential dissolution area. It is notable that Ni enrichment can be observed at the Fe preferential dissolution are/corrosion scale interface. A similar observation was reported by Yue et al. [135], suggesting that the Ni enrichment layer at the

material interface limits the dissolution rate of the metal. However, this Ni barrier was not observed around the undissolved austenite. Furthermore, there is no significant change in the contrast in the corrosion scale, Fe preferential dissolution area and the matrix in terms of Cr, implying that during the growth of the corrosion scale towards the metal matrix, Cr in the metal is mainly taken part in the formation of the corrosion products rather than diffusing and dissolving into the solution as in the case of Fe.

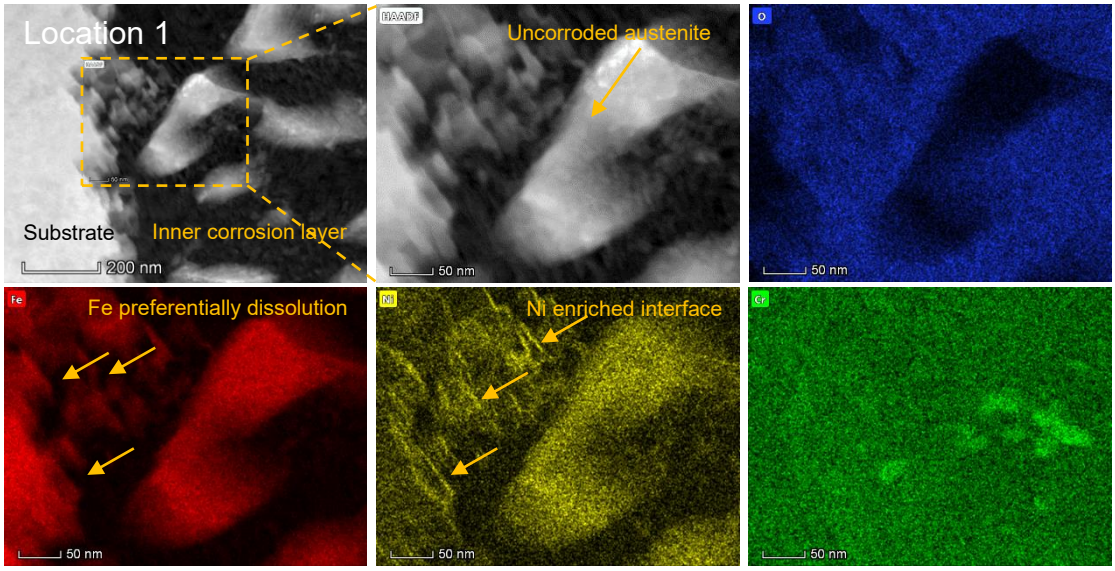

Figure 6-11. HAADF images of metal/corrosion products interface and related EDS mapping of O, Fe, Mo, Ni and Cr.

6.3. Film formation and morphology observation at 200°C with pCO_2 of 0.27 MPa

6.3.1. Overall observation of the surface morphology at 200°C with pCO_2 of 0.27 MPa

Figure 6-12 illustrates the top-view and cross-section of the corrosion product evolution for S13Cr MSS exposed in simulated formation brine at 200°C, pCO_2 of 0.27 MPa during various immersion times. The steel surfaces appeared to be locally covered by crystalline precipitates during the corrosion process as shown in Figure 6-12(a), (c), (e) and (g). Precipitates were characterized by two different shapes according to the top-view observation: cubic

precipitates and flattened precipitates. These two different shapes of precipitates show a great difference not only in quantity but also in size during the corrosion process. Furthermore, both the cubic precipitates and flattened precipitates show a significant growth in size but minimal increase in quantity with increasing immersion time. The nucleation of cubic precipitates and flattened precipitates mainly happened in the first 5 hours. Compared to the flattened precipitates, the number of cubic precipitates was as much as several orders of magnitude higher, indicating a faster nucleation kinetic process. However, greater size and higher growth rate of flattened precipitates compared to those of cubic precipitates can be clearly observed since 20 h indicative of a faster growth kinetic process of flattened precipitates.

Besides the precipitates, areas without precipitates covered show a slight change in morphology over 7 days of exposure as shown in the local magnification in backscattered electron imaging in Figure 6-12(a)-(d). The darker areas in local magnification of Figure 6-12(a) represent preferential corrosion in the darker area during the first 5 h of immersion. Non-uniform corrosion product layer is evident in the cross-section image of the sample after 5 h of immersion provided in Figure 6-12(b), confirming the preferential corrosion at 5 h.

Furthermore, a uniform corrosion scale can be observed after 20 h of exposure as shown in Figure 6-12(d), (e) and (g). In contrast to corrosion product film formed at 5.2 MPa p_{CO2}, where uncorroded austenite particles were only observed after 7 days, visible white particles in the corrosion product film can be observed after 20 h of exposure at 0.27 MPa p_{CO2} as marked in Figure 6-12(d). The corrosion product films formed after 20-168 h of immersion at 0.27 MPa p_{CO2} exhibited a single-layer structure, distinct from the bilayer structure observed at 5.2 MPa p_{CO2}. The uncorroded austenite distributed throughout the entire corrosion product film, rather than being confined to the inner layer.

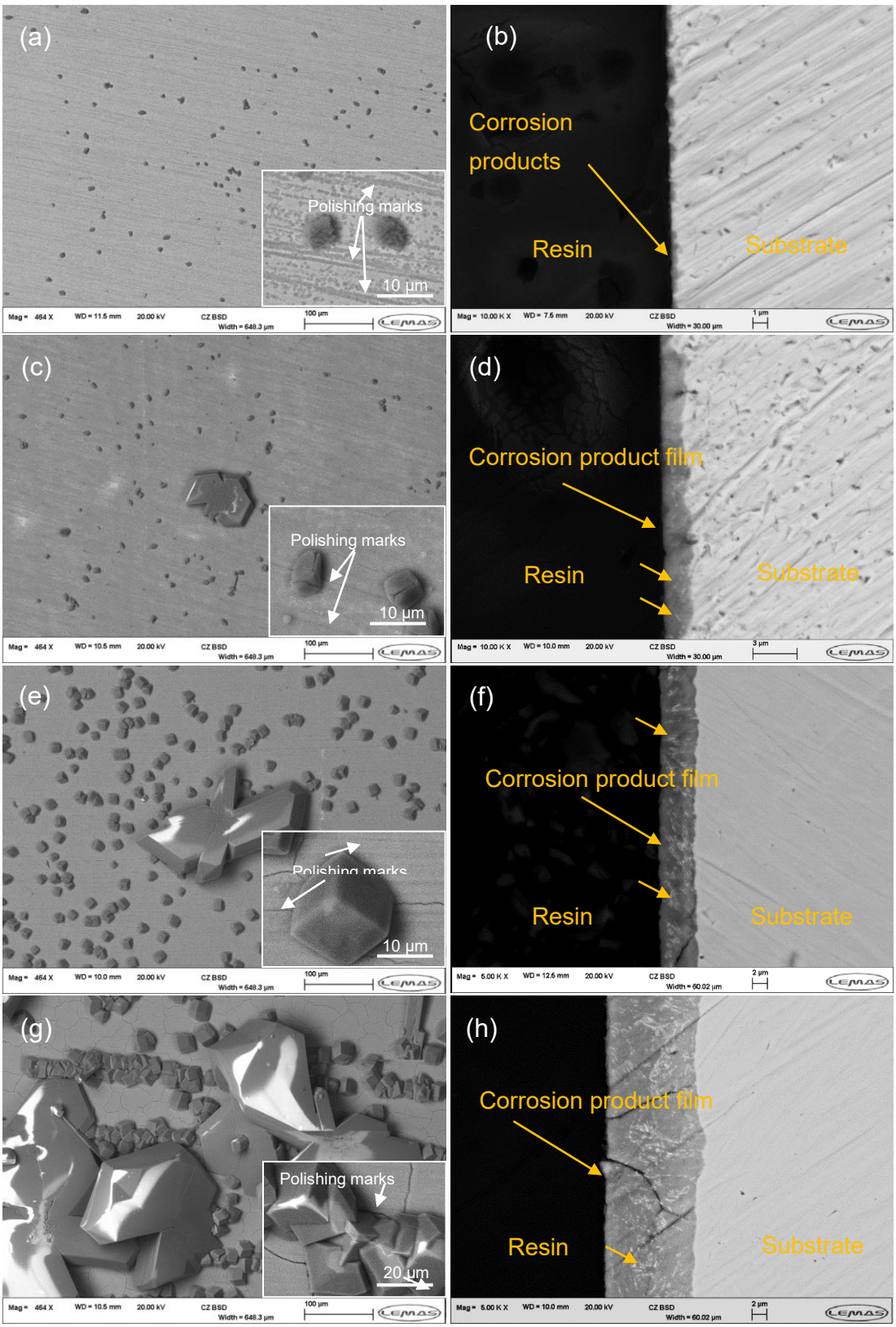

Figure 6-12. Surface and cross-sectional morphologies of corrosion product film on S13Cr MSS under 200°C and 0.27 MPa CO_2 for (a)(b) 5, (c)(d) 20, (e)(f) 48 and (g)(h) 168 hours.

The XRD patterns for corrosion products formed on S13Cr MSS at various immersion times are presented in Figure 6-13. In the first 5 h, only peaks belonging to the S13Cr MSS matrix can be observed. Then precipitate with a strong diffraction peak at 25.54°, which is the characteristic peak of the anhydrite ($CaSO_4$), was evident since 20 h. Peaks belonging to calcite and aragonite can be observed from 20 h and 48 h, respectively, with intensity became stronger with increasing immersion time. This indicates the precipitation of precipitates continues to occur during the corrosion process.

In addition, as the corrosion time increased, the intensity of the martensite peak gradually decreased, while the intensity of the austenite peak gradually increased. This indicates that the white particles preserved in the corrosion product film after corrosion are uncorroded austenite particles. As the corrosion time increased, the increasingly thick corrosion product film led to a decreasing effective penetration depth of X-ray into the metal substrate due to X-ray absorption by corrosion products, resulting in a smaller signal strength from the S13Cr MSS substrate, and thus the peak intensity of martensite became lower. Moreover, given the significantly lower X-ray mass absorption coefficient of corrosion products compared to the metal substrate, the effective XRD sampling depth (encompassing both the corrosion film and underlying base metal) increased with increased thickness of corrosion product film. Concurrently, the uncorroded austenite within the corrosion product film combined with the austenite within the S13Cr MSS substrate enhanced the overall austenite phase fraction within the XRD detection depth range, leading to an enhancement of the austenite peak intensity as corrosion time increased.

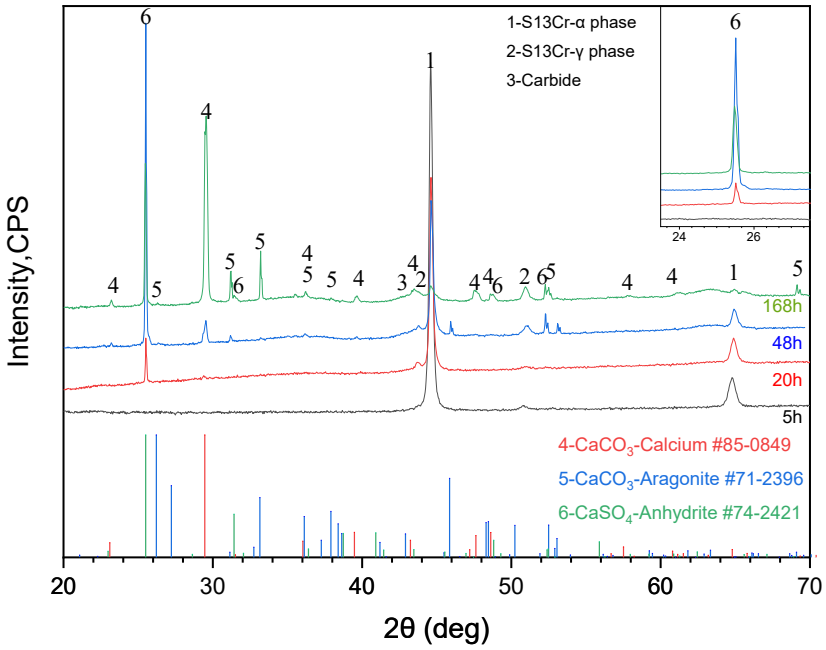

Figure 6-13. XRD patterns of S13Cr MSS specimens exposed at 200°C and 0.27 MPa CO_2 for 5, 20, 48 and 168 h.

Referring to the differentiation of corrosion stages under high p_{CO2} condition, the formation process of the Cr-rich corrosion product layer under 0.27 MPa CO_2 can be divided into two stages:

Based on the above observations, the corrosion process of S13Cr MSS at 200°C and 0.27 MPa CO_2 can be divided into two stages:

1. Early stage: characterised by a non-uniform corrosion product film formed on the surface;
2. Final stage: characterised by the formation of a uniform corrosion product film containing uncorroded austenite.

A more detailed analysis of these two stages is provided in the subsequent sections.

6.3.2. Early stage of the corrosion scales formation and evolution during long-term corrosion at 200°C with pCO_2 of 0.27 MPa

Figure 6-14(a) and (b) provide the typical top-view images of S13Cr MSS exposed to CO_2-saturated formation brine at 200°C with CO_2 partial pressure of 0.27 MPa during the early stage of corrosion.

Beyond the cubic precipitates, the most distinctive surface characteristic is the formation of dual-tone corrosion features (dark and light regions), which similar to the observation at 5.2 MPa p_{CO2}. However, unlike the randomly distributed dark regions at 5.2 MPa p_{CO2}, specimens corroded at 0.27 MPa p_{CO2} exhibit an organized pattern where dark regions primarily align linearly, with sporadic dark spots distributed between these lines. Cross-sectional image (Figure 6-14(c)) shows the discontinuous distribution of corrosion products on the sample surface, revealing a non-uniform corrosion occurring in the early stage of corrosion at 0.27 MPa p_{CO2}.

It is worth noting that the distribution pattern of the linear dark regions is consistent with the grinding marks introduced during the sample preparation process. Since no other grinding scratches were visible outside these dark regions, it is reasonably for us to conclude that at 0.27 MPa p_{CO2}, corrosion preferentially initiates at the locations of the surface scratches.

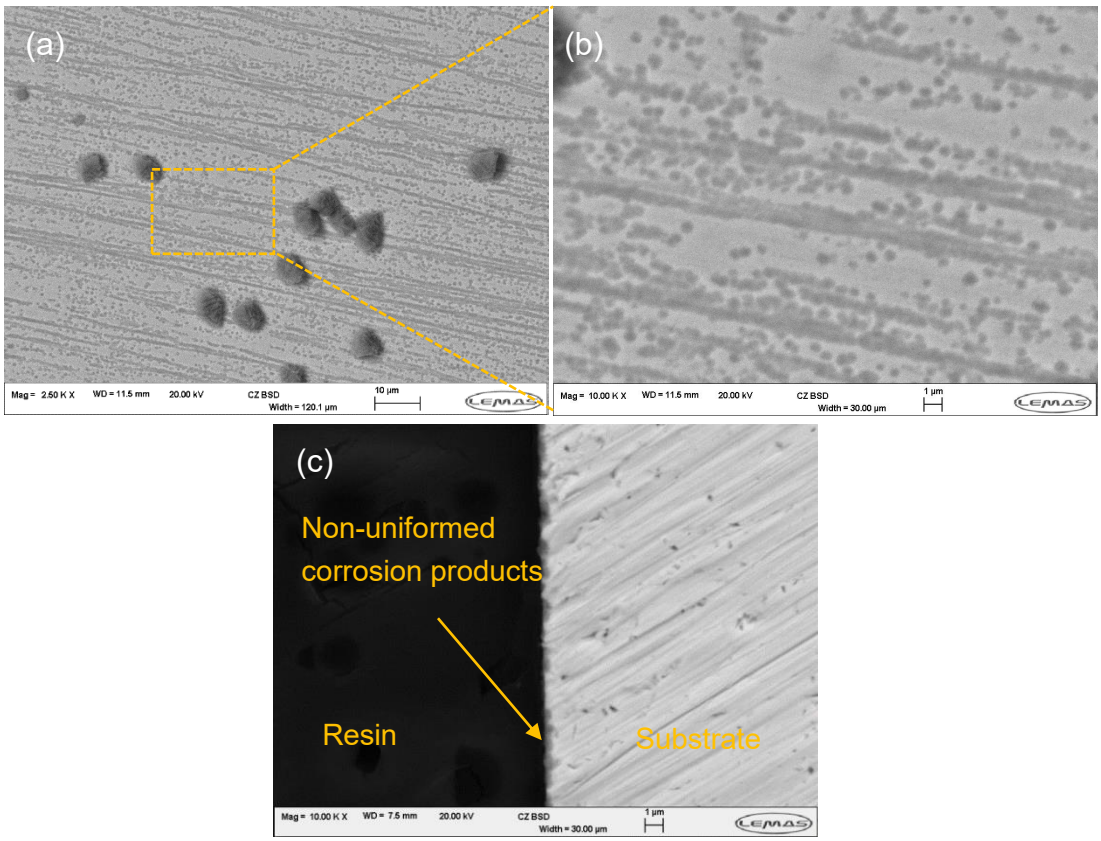

Figure 6-14. (a)(b) Surface and (c) cross-sectional morphologies of corrosion product film on S13Cr MSS under 200°C and 0.27 MPa CO_2 for 5hours.

To understand the chemistry of the corrosion products on S13Cr MSS at 200°C and 0.27 MPa CO_2 for 5 hours, EDS line scanning was performed on the surface of S13Cr MSS as shown in Figure 6-15. Figure 6-15(a) shows the region designated for EDS line scanning, encompassing both light and dark regions within the scanned line. The line scan results in Figure 6-15(b) reveal that the dark region has higher content of O element compared to the light region, confirming that the dark region experiences more significant corrosion compared to the light region at the early stage of corrosion. It is noteworthy that the distribution of Cr, Ni and Mo element follow a similar trend to that of O element, while Fe demonstrated an inverse trend. This distinct behaviour provides direct evidence for the preferential dissolution of Fe at the preferentially corroded sites during the initial stage of non-uniform corrosion.

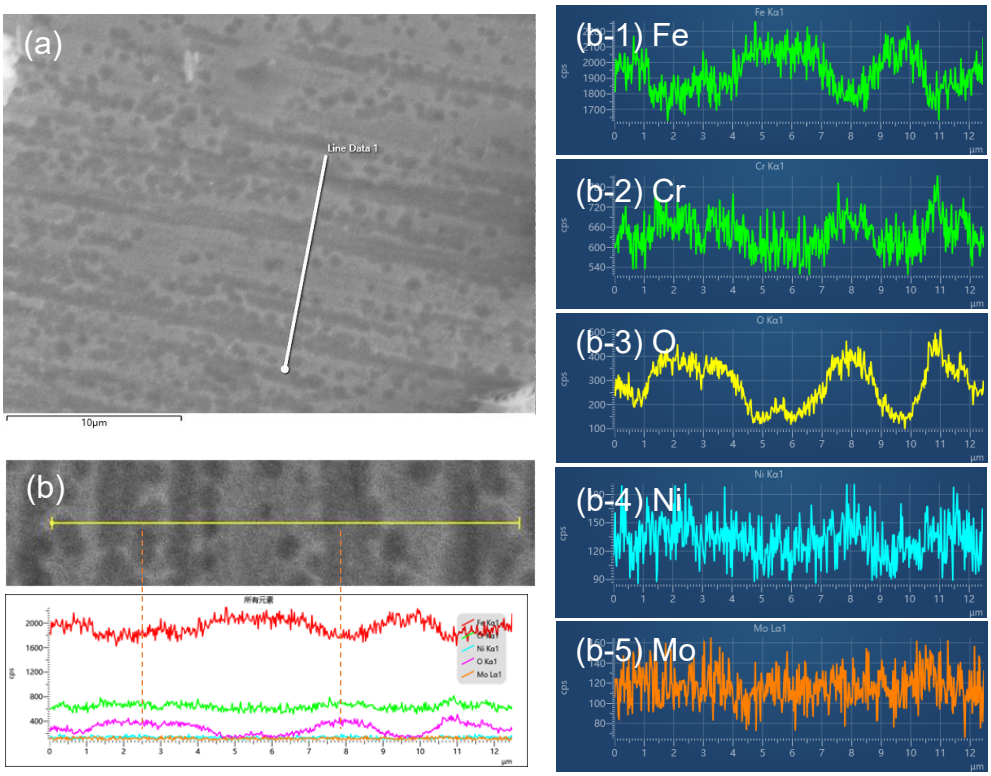

Figure 6-15. (a) SEM image of selected area used for EDS line scanning obtained from S13Cr MSS exposure to formation brine under 200°C and 0.27 MPa CO_2 for 5 hours and (b) EDS line scanning results of the selected position.

To further understand the distribution and chemical composition of the corrosion products on sample surface during the early stage, Raman spectroscopy as well as EDS were used for point composition analysis of different areas on the specimen's surface. As shown in Figure 6-16(b), Raman spectral analysis of the cube presents a strong signal from carbonate ions (CO_3^{2-}) and a relatively weak signal from sulfate ions (SO_4^{2-}) . The EDS result of the cube indicates that it mainly contains C, O, and Ca elements, along with trace amounts of S, Mg, and Fe elements. Based on the combined results of EDS and Raman spectroscopy, we conclude that the cubic precipitate is a co-precipitation product of carbonate and small amounts of sulfate, the cations are dominated by Ca^{2+} with trace amounts of Mg^{2+} and Fe^{2+}.

Figure 6-16(b) presents Raman spectra from both light and dark regions, revealing characteristic peaks corresponding to the corrosion products (Cr_2O_3 (~552 cm^{-1}) and spinal (~696 cm^{-1})/ $Cr(OH)_3$ (~717 cm^{-1})). The line-scan Raman analysis in Figure 6-17

demonstrates significantly higher peak intensities in dark region compared to light region, corroborating our previous conclusion that dark region is the preferential corrosion site during the early stage of corrosion. It is worth noting that the EDS results obtained from both the light and dark regions show very high content of Fe. Since the thickness of the corrosion products is too thin, which is smaller than the detection depth of the EDS (about 1 μm), the high Fe signal in the EDS results may partly came from the substrate underneath the corrosion products rather than completely from the corrosion products.

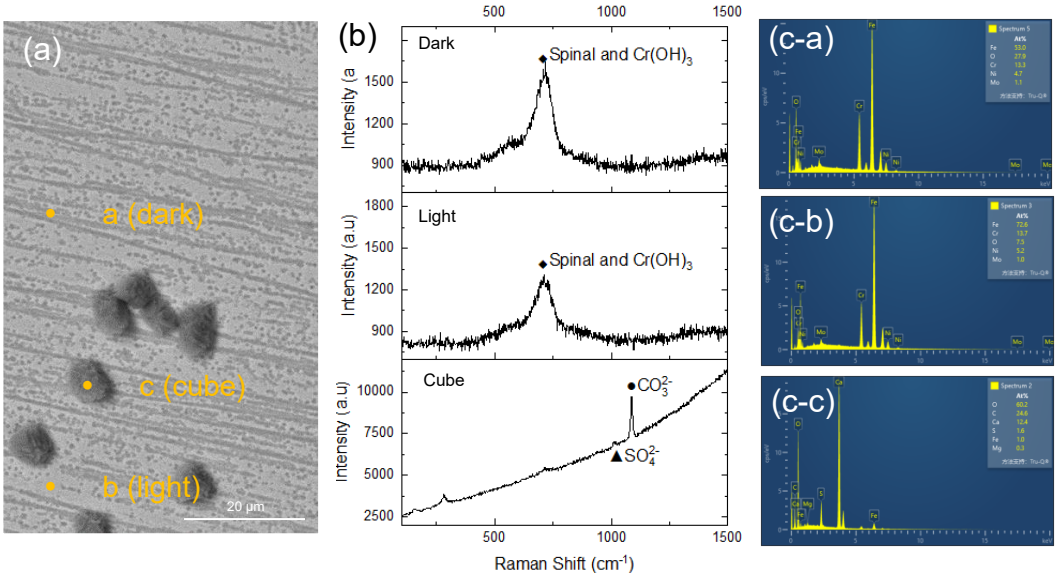

Figure 6-16. Raman spectroscopy and EDS point identify results of S13Cr MSS specimen exposed at 200°C and 0.27 MPa CO_2 for 5 hours: (a) SEM image of S13Cr MSS specimen immersed for 5 hours, (b) Raman spectra for selected point, (c) EDS point identify results for selected point.

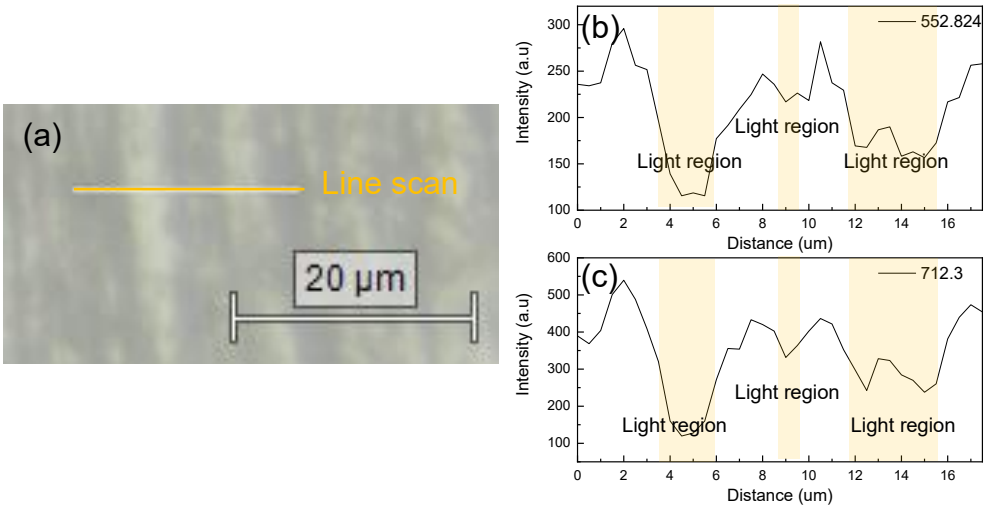

Figure 6-17. Raman spectroscopy line scanning of S13Cr MSS specimen exposed at 200°C and 0.27 MPa CO_2 for 5 hours: (a) schematic diagram of scanning area and (b), (c) line scanning results at 552 cm^{-1} and 712 cm^{-1}.

6.3.3. Final stage of the corrosion scales formation and evolution during a long-term corrosion at 200°C with pCO_2 of 0.27 MPa

As previously illustrated in Figure 6-18, the corrosion product film formed at 0.27 MPa p_{CO2} maintained a single-layer structure during a 168 h test after completely cover the sample surface. The uncorroded austenite distributed throughout the entire corrosion product film, rather than being confined to the inner layer. Here, the corrosion product film generated after 168 hours of corrosion was analysed.

As shown in Figure 6-18(a), two distinct precipitate morphologies are observed on the specimen surface: cubic and flattened structures (their phase identification will be discussed subsequently). In precipitate-free region as shown in Figure 6-18(b), parallel scratches are clearly visible, similar to the observation on the sample surface at 5.2 MPa p_{CO2}. These scratches are believed to be left from the grind process during sample preparation, implying the inward growth of the corrosion product film.

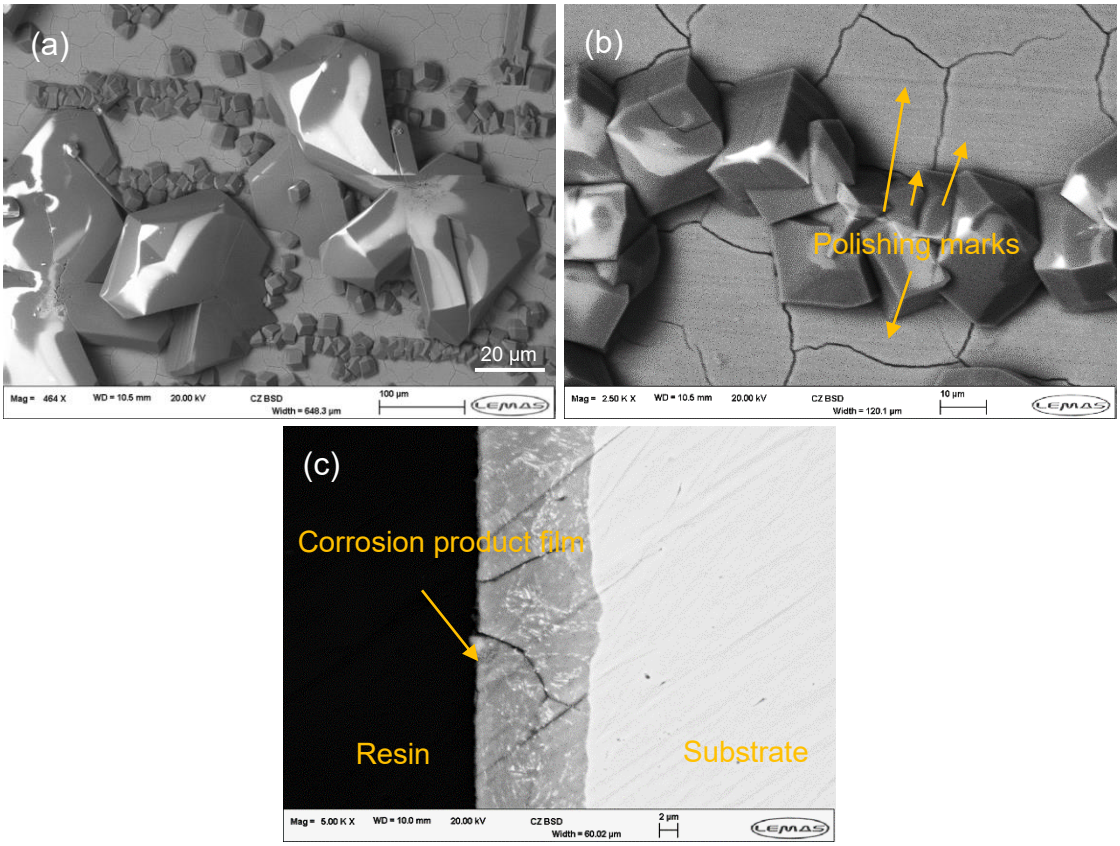

Figure 6-18. (a)(b) Surface and (c) cross-sectional morphologies of corrosion product film on S13Cr MSS under 200°C and 0.27 MPa CO_2 for 168 hours.

FIBs-SEM and TEM were employed for further characterization of the corrosion product film. The cross-section of the corrosion product film prepared by FIBs is shown in Figure 6-19(a). Notice that no uncorroded austenite particles were observed in the cross-section prepared by FIBs, which appears inconsistent with our previous SEM observations where such particles were found throughout the corrosion product film. This discrepancy could be due to the distribution characteristics of austenite within the martensitic matrix. In S13Cr MSS, austenite particles primarily distribute along the martensitic lath boundaries, while the randomly selected FIBs cross-section may have coincidentally avoided intersection with these boundaries, leading to the abandon of uncorroded austenite in the cross-section image. Therefore, this observation is not contradictory to previous cross-sectional observations.

The selected area marked in Figure 6-19(a) was used to prepare the TEM sample, the TEM sample is shown in Figure 6-19(b). The electron diffraction pattern for the selected region 1 of the corrosion products is shown in Figure 6-19(d). The broadening of the diffraction spots and rings indicates that the corrosion products are nanocrystalline and amorphous. Phase identification indicates that the corrosion product phases are spinel ($FeCr_2O_4$) and $Cr(OH)_3$.

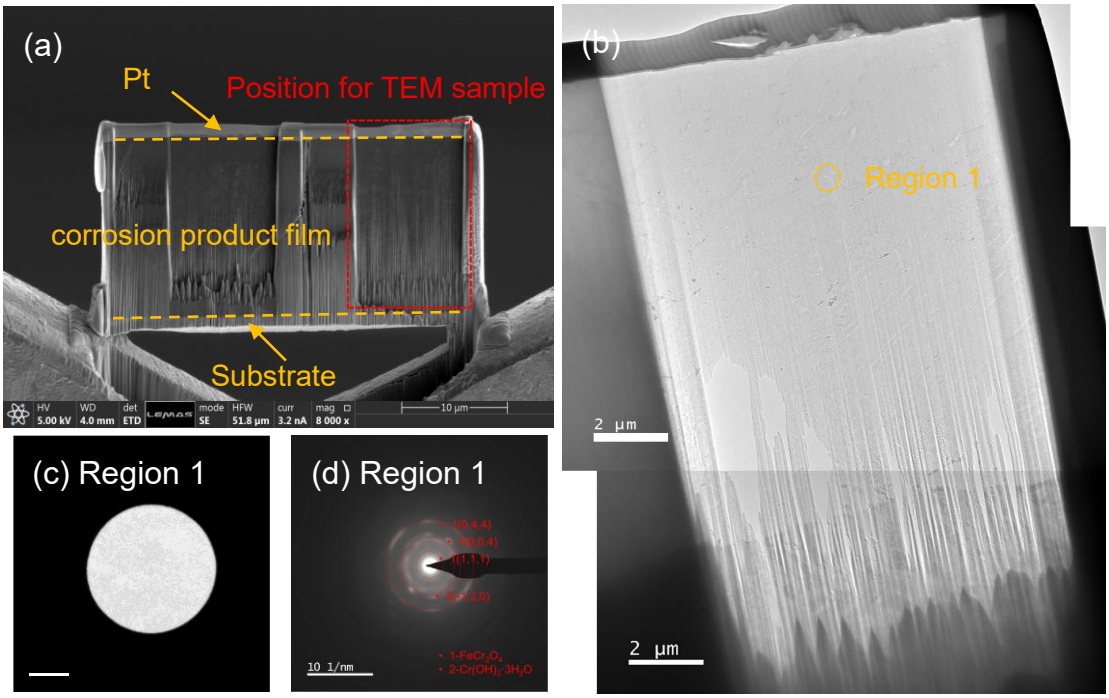

Figure 6-19. (a) SEM image of selected area used for TEM sample preparation, (b) TEM image of corrosion product film formed on S13Cr MSS in formation brine under 200°C and 0.27 MPa CO_2 for 168 hours, (c) selected region for electron diffraction pattern analysis and (d) the corresponding electron diffraction pattern.

To further understand the chemistry of the corrosion products and precipitates on S13Cr MSS surface locally, Raman spectroscopy and EDS were employed. As presented in Figure 6-20, a band at 1085 cm^{-1} which is assigned to both calcite and aragonite can be observed for both big crystal and small cube, but they have significant differences in lattice modes below 400 cm^{-1}. The small cube is confirmed to contain calcite with the characteristic peak observed at 282 cm^{-1}, in the meantime, the big crystal is confirmed

to be aragonite with the characteristic peaks observed at 152, 179 and 205 cm^{-1} [160]. Besides, a characteristic peak of $CaSO_4$ (anhydrite) at 1017 cm^{-1} confirmed that small cube is a mixture of calcite and anhydrite. EDS results confirmed the presence of S in the small cube. Notably, the cubic precipitates contained calcite ($CaCO_3$) and anhydrite ($CaSO_4$) phases rather than forming a solid solution, this phase separation is clearly demonstrated by the distinct diffraction peaks for both phases in the XRD results provide before. It is also worth noting that there is a slight difference in the cation ions between the big crystal and small cube. In contrast to the big crystal which only contained Ca ions as cation ions, the small cube contained traces of Mg ions from the formation brine and Fe ions from the dissolved S13Cr MSS. The precipitation processes and the differences in precipitation processes under different CO_2 pressure conditions will be discussed in detail in the following discussion section.

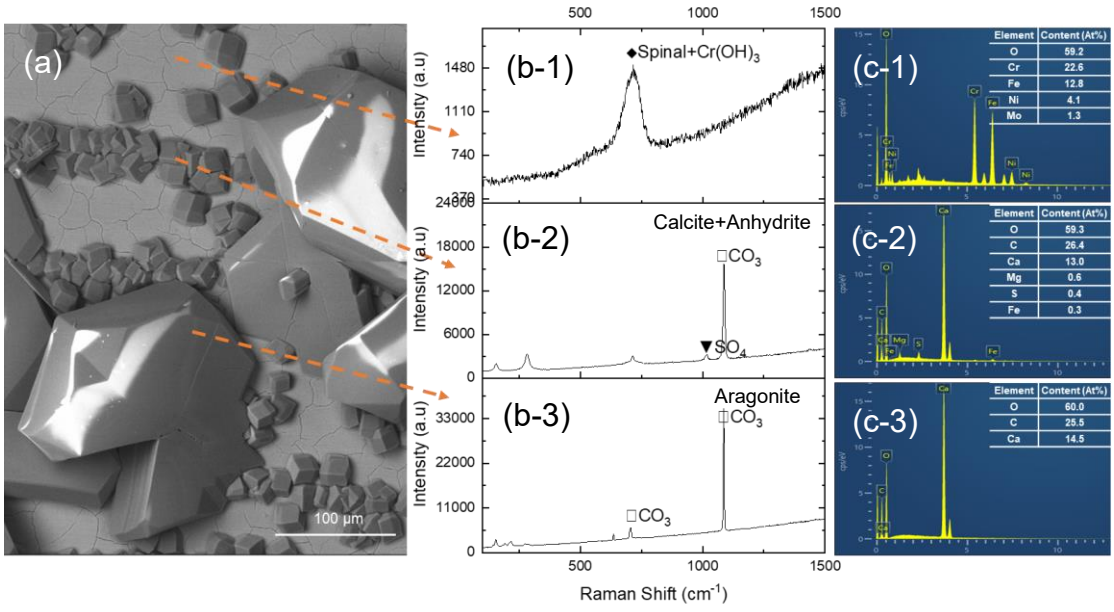

Figure 6-20. (b) Raman spectra and (c) EDS point identify results of S13Cr MSS specimens exposed at 200°C and 0.27 MPa CO_2 for 168 h.

Raman analysis of precipitate-free corrosion product region identified spinel and $Cr(OH)_3$, which is consistent with TEM characterization. EDS quantification reveals significant Fe content

in the corrosion products, suggesting a high proportion of spinel in the corrosion products.

Compared to the corrosion products generated under high CO_2 pressure condition, the Fe content in the products formed under low CO_2 pressure significantly increased, and the composition shifted from $Cr(OH)_3$ and Cr_2O_3 at high CO_2 pressure condition to $Cr(OH)_3$ and spinel at low CO_2 pressure condition. The thermodynamic discussion for this transition will be systematically analysed in the discussion section.

6.4. The comparisons of corrosion behaviour of S13Cr at 200°C with various pCO_2

Figure 6-21 shows the general and localized corrosion rates of S13Cr MSS at different immersion times in the formation brine at 200°C and 0.27 or 5.2 MPa p_{CO2}. For sample tested at 5.2 MPa p_{CO2}, it can be seen that the general corrosion rates were recorded as 1.70 mm/year and 1.37 mm/year after 5 hours and 20 hours respectively, then dropped to a rate of 1.04 mm/year over 7 days exposure. The reduction in corrosion rates can be contributed to the formation of the corrosion scales on the surface, suggesting that the corrosion scales can protect the surface from corrosion. A similar trend was recorded on the corrosion rates of the sample tested at 0.27 MPa p_{CO2}, compared to corrosion rates recorded at 5.2 MPa p_{CO2}, corrosion rates of S13Cr MSS tested at 0.27 MPa p_{CO2} were slightly lower at each test period. The general corrosion rates of S13Cr MSS at 0.27 MPa and 5.2 MPa of CO_2 are at a high level after 168h according to NACE standard RP0775-05 [156].

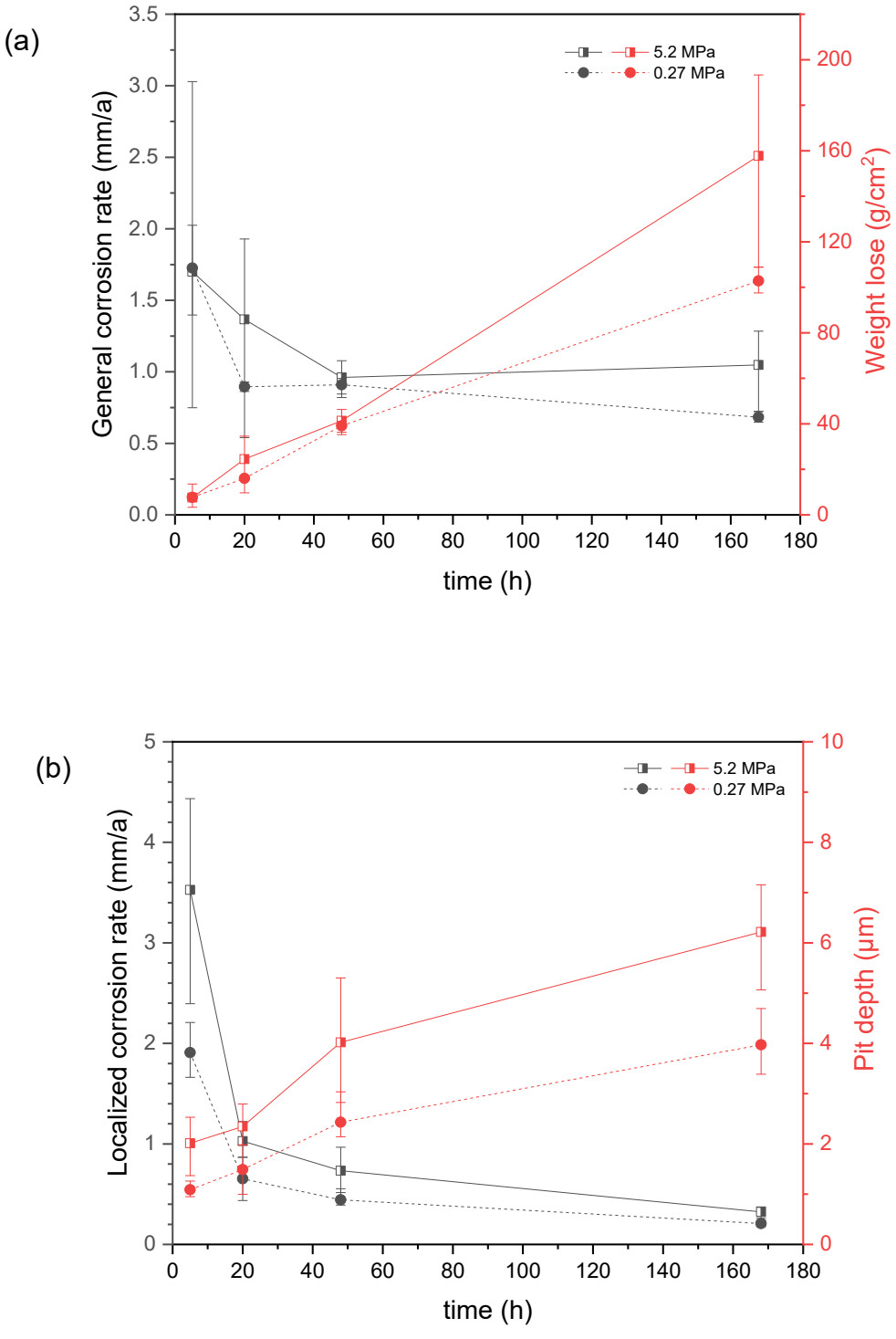

Figure 6-21. General corrosion rate (a) and localized corrosion rate (b) of S13Cr MSS specimens exposed at 200°C, 0.27 MPa and 5.2 MPa CO_2.

As illustrated in Figure 6-21(b), the pit depth of the sample tested at 5.2 MPa p_{CO2} continually increased with increasing immersion time, however, the growth rate of the pit slowed down with immersion time, which corresponds to a decrease in localized corrosion rate from 2.27 mm/y after 5 hours to 0.37 mm/y after 168 hours. As compared, the localized corrosion rates of S13Cr MSS tested at 0.27 MPa p_{CO2} were significantly lower at each test period, recorded as 1.90 mm/y in the first 5 h and rapidly decreased to 0.65 mm/y after 20 h, finally gradually decreased to 0.21 mm/y after 168 h. The localized corrosion rates of S13Cr MSS at both 0.27 MPa and 5.2 MPa of CO_2 are at a low level after 168h according to NACE standard RP0775-05 [156].

In order to further understand the localized corrosion behaviour between samples tested at 0.27 MPa and 5.2 MPa CO_2. 2D profilometry of corroded S13Cr MSS after removing the corrosion products was observed by using NPFLEX 3D optical profilometer. As shown in Figure 6-22(a), (c), (e) and (g), bumps, marked by white circle, can be observed on samples tested at 0.27 MPa, which are consistent with aragonite in the distribution and size, implying the local protective effect of aragonite. Moreover, it is obvious that the density of pits is significantly higher at 5.2 MPa CO_2 than that obtained at 0.27 MPa CO_2 as shown in Figure 6-22(g) and (h), indicating a higher pitting corrosion risk at a higher CO_2 partial pressure condition.

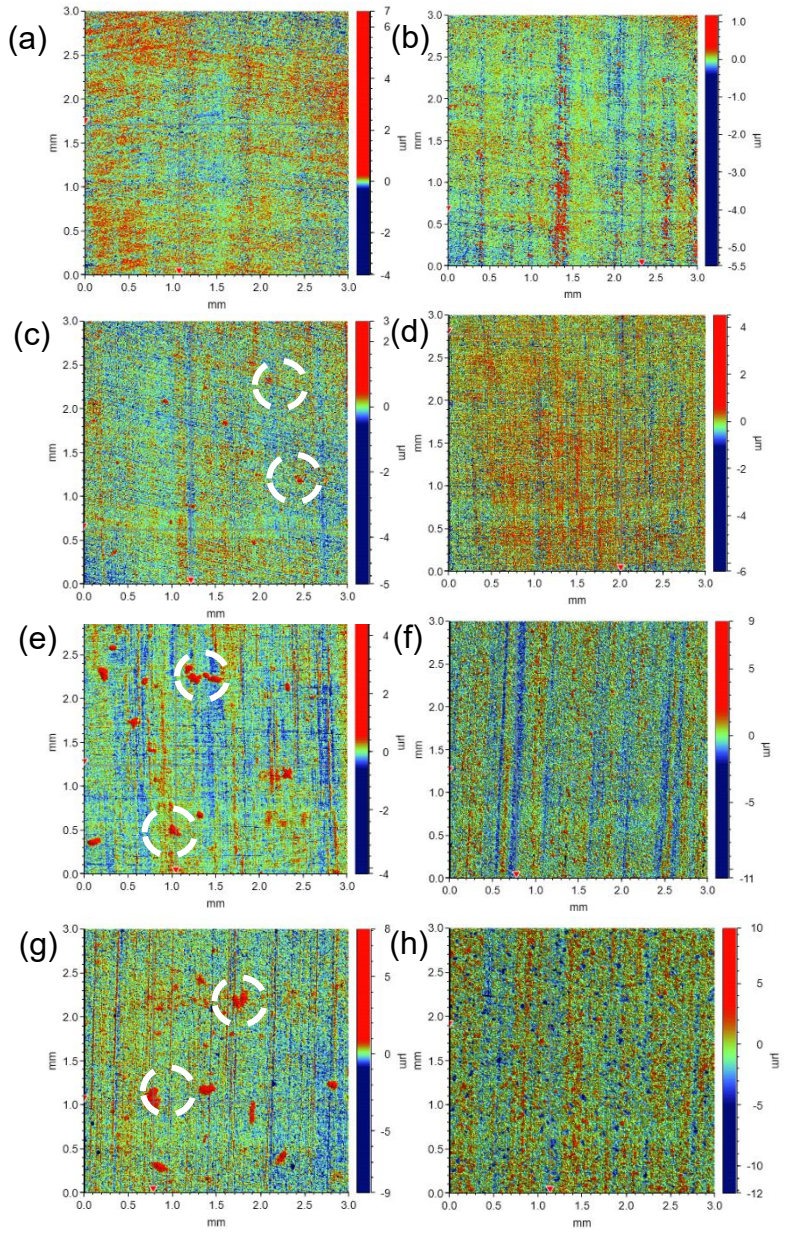

Figure 6-22. 2D profilometry of corroded S13Cr MSS at 200°C, 0.27 MPa (a)(c)(e)(g) and 5.2 MPa CO_2 (b)(d)(f)(h) after removing the corrosion products.

6.5. The comparisons of electrochemical behaviour of S13Cr at 200°C with various pCO_2

6.5.1. OCP measurements

Figure 6-23 demonstrates the OCP variation of the S13Cr MSS during the 168 h immersion experiment. It can be seen that at two

different partial pressures of CO_2, the OCP undergone a similar change: at the beginning of corrosion, the OCP decreased rapidly; after reaching the lowest point, the OCP raised rapidly for a duration; afterward, the OCP continued to rise but at a gradually slowing rate, eventually reaching a stable value. The decrease and subsequent increase of OCP is most likely related to the dissolution of the air-formed passive film and then the formation of the corrosion product film.

At the initial stage of corrosion, the potential dropped rapidly, which usually indicates that the air-formed native passive film on the sample surface begins to gradually degradation, and corrosion starts to occur on the sample surface. This change in OCP corresponds to the non-uniform corrosion observed on the sample surface at the early stage during the immersion test.

Subsequently, the corrosion potential raised rapidly. Increasing corrosion potentials typically indicate either a disproportionate retardation of the anodic reaction or an enhancement of the cathodic reaction. Considering our observations of the corrosion morphology on the sample surface, we can infer that this change is due to the formation of corrosion products, which suppresses the anodic reaction, leading to an increase in potential until it eventually stabilizes.

It should be noted that the OCP under high pressure condition was always higher than the OCP under low pressure condition. This observed positive shift in OCP likely correlates with the enhanced cathodic reaction under high CO_2 pressure, and will be discussed through polarisation test in the next section.

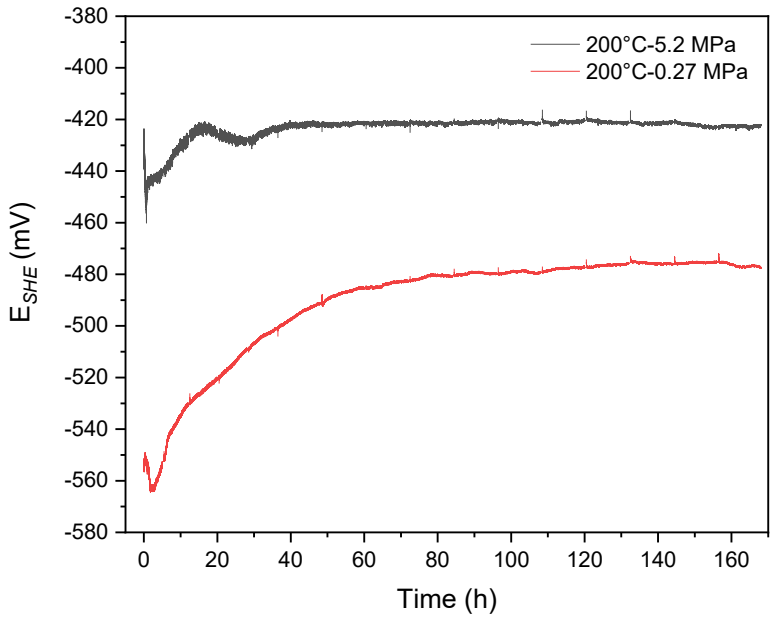

Figure 6-23. OCP of S13Cr MSS as a function time tested at 200°C and 0.27/5.2 MPa of CO_2.

6.5.2.Potentiodynamic polarisation measurements

The cyclic potentiodynamic polarisation curves of S13 MSS tested in simulated formation brine at 200°C and 0.27/5.2 MPa of CO_2 after exposure for 168 hours are shown in Figure 6-24. It is obvious that as the potential increase during the anodic polarisation, the current density shows a stable region at both 0.27 and 5.2 MPa of CO_2, shows a qualitative sign of passivity. However, those observed current densities in the current stabilization region were too high to be considered as the samples being in the true passive state. The terms pseudo-passive is typically used to describe such observation [161]. This current plateau is usually associated to the mass transfer controlled anode reaction due to the blocking effect of the corrosion scale. Noting that the current density in the current stable region at 5.2 MPa p_{CO2} was lower than that at 0.27 MPa p_{CO2}, implying that the corrosion product film formed at a higher p_{CO2} provide a stronger blocking effect to the mass transfer process.

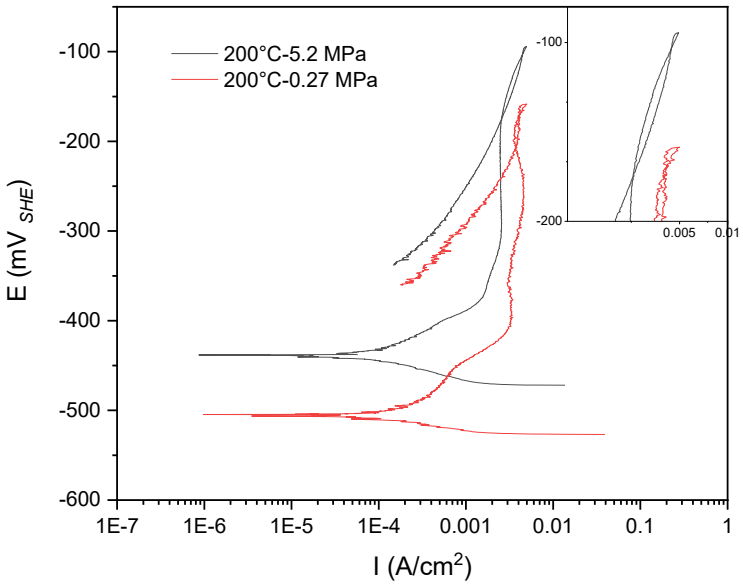

Figure 6-24. Cyclic potentiodynamic polarisation curves of S13Cr MSS tested at 200°C and 0.27/5.2 MPa of CO_2 after exposure for 168 hours.

Cathodic polarisation measurements were conducted at varying CO_2 partial pressures to compare the cathodic reaction kinetics under different CO_2 partial pressure conditions (as shown in Figure 6-25). In the test system, the cathodic reaction was mainly hydrogen evolution. Increased CO_2 pressure enhances CO_2 dissolution in formation brine and subsequent carbonic acid formation, carbonic acid then dissociates to generate H^+ ions, leading to an increase in H^+ ions concentration in the formation brine which could accelerate the cathodic reaction rate. This change is clearly demonstrated in the Tafel regions (BC and B′C′) of the cathodic polarisation curves, where a higher cathodic current density was observed under a higher CO_2 partial pressure. As the potential further scanned toward the negative direction, the cathodic curves entered a mass transfer controlled region (CD and C′D′). At this region, the increase of current density became suppressed with decreasing potential, the cathodic reaction was under mass transfer control. Generally, for bare metal, higher CO_2 partial pressure usually corresponds to higher cathodic current density in the mass transfer controlled region. However, in this study, the cathodic current density obtained at higher CO_2 partial pressure condition exhibited a lower value. This

is usually associated with the hindrance to mass transfer process induced by the corrosion product film, implying that the blocking effect of the corrosion product film to cathodic reaction outweighs the promoting effect of increased H^+ ion concentration to cathodic reaction under high CO_2 partial pressure. The stronger blocking effect on mass transfer process under high CO_2 partial pressure may be attributed to the formation of a thicker corrosion product film under high CO_2 partial pressure. Meanwhile, the evolution of the film composition under different partial pressures might also affect the blocking effect induced by the corrosion product film. As the potential further decreased, a secondary linearly increasing current range appeared at more negative potentials (DE and D′E′), this current change is generally attributed to the reduction of water.[22]

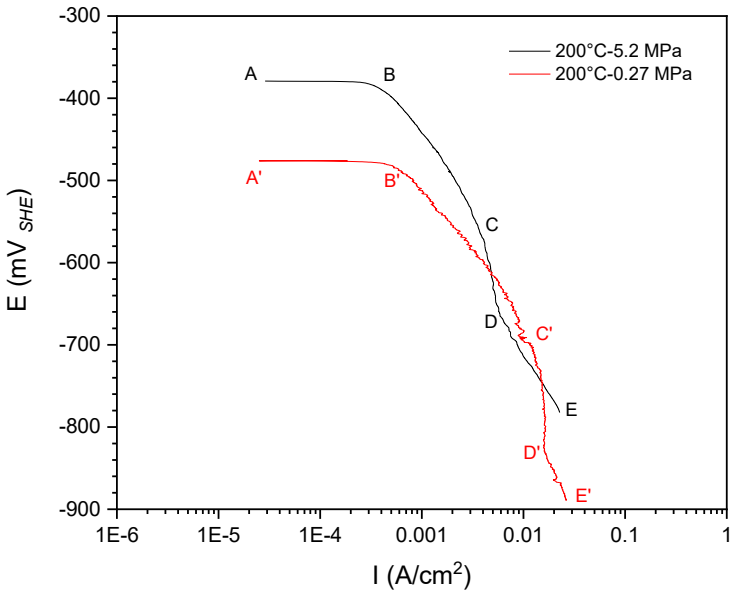

Figure 6-25. Cathodic polarisation curves of S13Cr MSS tested at 200°C and 0.27/5.2 MPa of CO_2 after exposure for 168 hours.

The combined effects of (1) cathodic polarisation curve shifting to higher current densities (rightward shift) and (2) anodic polarisation curve shifting to lower current densities (leftward shift) under elevated CO_2 pressure condition collectively result in an increase in the corrosion potential.

6.5.3. EIS measurements

Figure 6-26 and Figure 6-27 show the Nyquist and Bode plots of S13Cr MSS at different corrosion stages in CO_2-saturated formation brine at 200 °C and 5.2 MPa/0.27 MPa of CO_2. It is clearly that all the Nyquist plots obtained at different corrosion stages show capacitor characteristic.

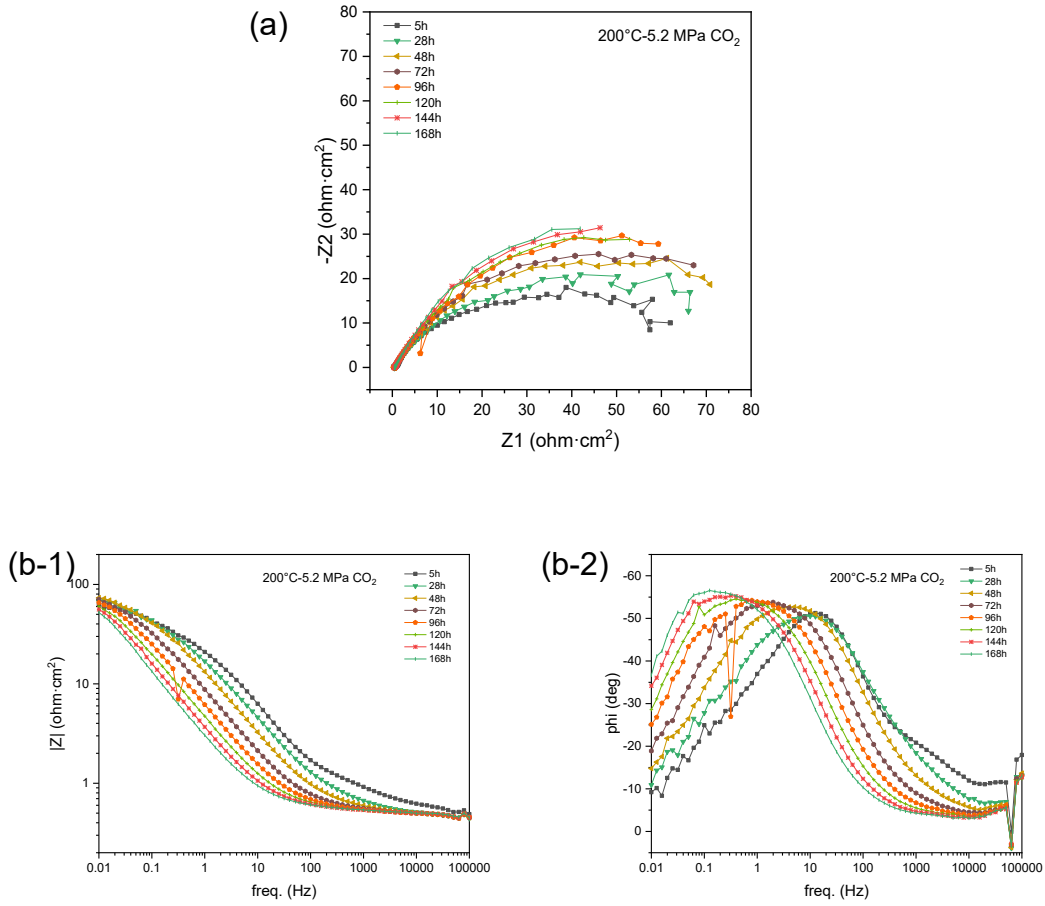

Figure 6-26. (a) Nyquist and (b) Bode plots of S13Cr MSS after various immersion times in CO_2-saturated formation brine at 200°C and 5.2 MPa of CO_2.

As displayed in the Nyquist plots, the radius of the semicircle increased with exposure time. In most cases, a larger arc diameter in the Nyquist plot typically corresponds to a higher |Z| in the Bode plot. However, in our EIS results, the |Z| decreased over time. Meanwhile, the Nyquist plot reveals that the semi-circle became increasingly incomplete as the testing duration extends. This phenomenon could be due to the non-ideal capacitive behaviour of

the electrode during the corrosion process, which might relate to the change in surface roughness, surface chemical inhomogeneity, or porous electrode. Due to corrosion, the specimen surface gradually deviated from the ideal state (e.g., due to the increased surface roughness), the value of n then deviated from 1, and the semi-circle in the Nyquist plot became increasingly incomplete.

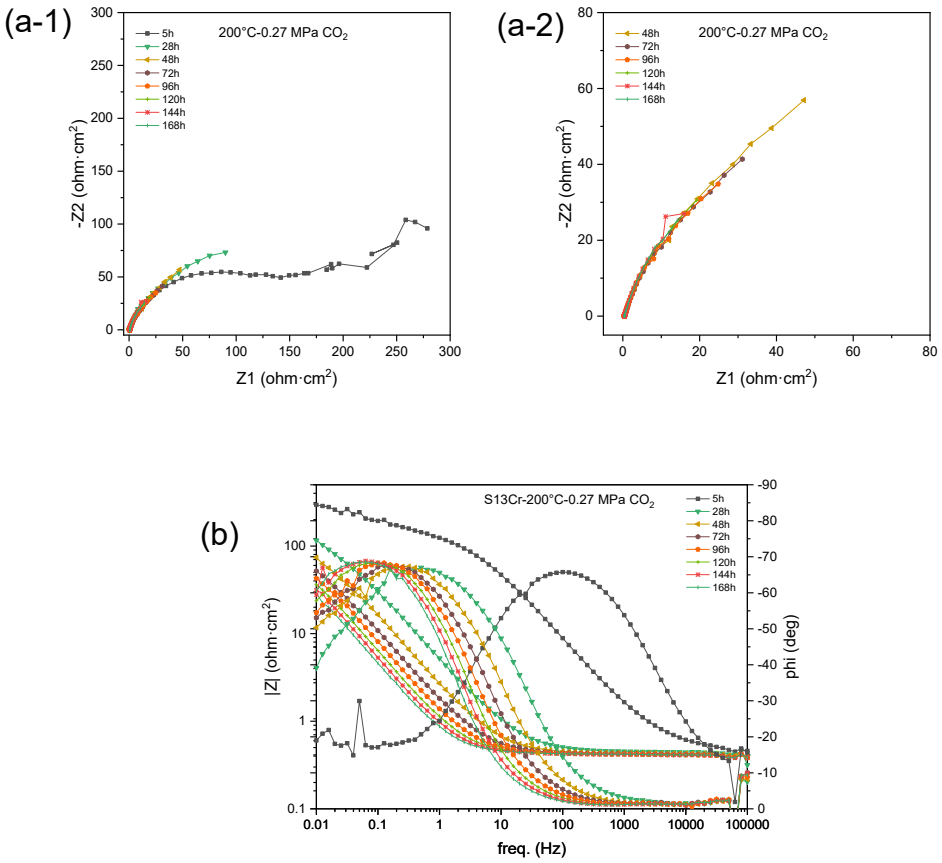

Figure 6-27. (a) Nyquist and (b) Bode plots of S13Cr MSS after various immersion times in CO_2-saturated formation brine at 200°C and 0.27 MPa of CO_2.

Comparative analysis of the Nyquist plots under both pressure conditions is shown in Figure 6-28. The arcs under both conditions were incomplete, and it is clear that the arcs under low pressure were more incomplete, but the arc radiuses were larger, indicating a greater corrosion resistance at low pressure condition.

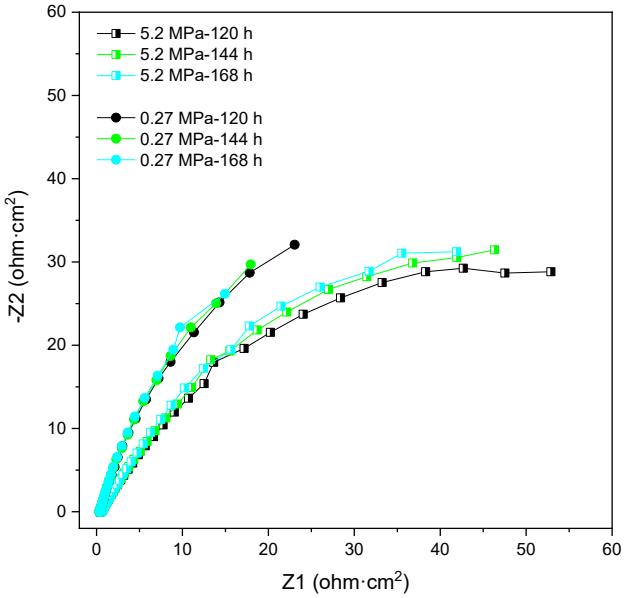

Figure 6-28. Nyquist plots of S13Cr MSS after various immersion times in CO_2-saturated formation brine at 200°C and 5.2/0.27 MPa of CO_2.

The Bode plots in Figure 6-26 and Figure 6-27 present quite broad peaks, this could be the superposition of two peaks which corresponds to a low high frequency time constant and a high frequency time constant. Therefore, an electrical equivalent circuit as provide in Figure 6-29 was proposed to model the electrolyte/sample interface. In all EIS spectra, the maximum phase angle modulus is lower than 90°, indicating a deviation from ideal capacitor behaviour. Thus, constant phase element (CPE) was used in the electrical equivalent circuit in place of a capacitor to compensate for non-homogeneity in the system. In the equivalent circuit, R_s is the solution resistance, CPE_f represents the capacitance related to the corrosion scale, R_f is the resistance of the corrosion scale. CPE_{dl} and R_{ct} can be attributed to a charge transfer process in which CPE_{dl} is the capacitance of the electrical double layer and R_{ct} represent the charge transfer resistance.

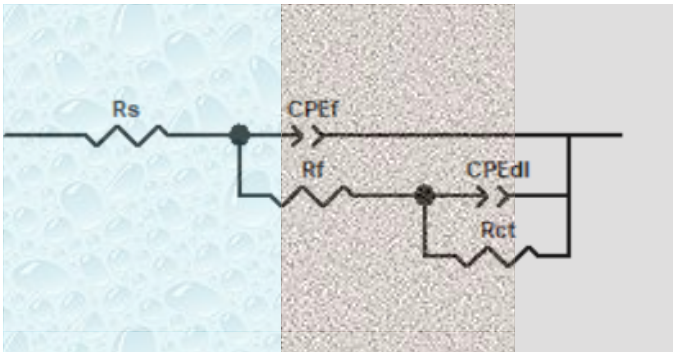

Figure 6-29. The equivalent circuit diagram used to fit the EIS experimental data.

The fitting results are summarized in Table 6-2. To facilitate direct comparison of the R_{ct} and R_f, these parameters are graphically presented in Figure 6-30.

The fitting results reveal that R_{ct} was significantly higher than R_f during a 168-hour corrosion monitoring at both 0.27 and 5.2 MPa of CO_2. This dominance of R_{ct} indicates that charge transfer is the rate-determining step in the corrosion process, and had a crucial effect on corrosion process. Therefore, the corrosion behaviour of S13Cr steel at 200°C under both pressure conditions can be classified as charge-transfer controlled process.

In the middle and late stages of corrosion, the R_f of the corrosion product film formed under high CO_2 partial pressure is consistently higher than that under low CO_2 partial pressure. This implies that the corrosion product film formed under high pressure are more protective. This is consistent with the results obtained from potentiodynamic polarisation measurements as the corrosion product film formed under high CO_2 partial pressure provided a stronger blocking effect. However, since the corrosion of S13Cr MSS in CO_2-containing formation water at 200°C is controlled by charge transfer process, the influence of the corrosion product film on corrosion through affecting the mass transfer process is insignificant.

Table 6-2. EIS spectra fitting data of the EECs for S13Cr MSS after various immersion times in CO_2-saturated formation brine at 200°C and 5.2/0.27 MPa of CO_2.

CO_2 pressure/Mpa	Time/h	Rs/Ω·cm^2	CPEf-T/ Ω^{-1}·s^{-n}·cm$^{-2(1-n)}$	CPEf-n	Rf/Ω·cm^2	CPEdl-T/ Ω^{-1}·s^{-n}·cm$^{-2(1-n)}$	CPEdl-n	Rct/Ω·cm^2
5.2	5	0.448	0.014	0.537	1.971	0.0007	0.999	66.25
	20	0.378	0.014	0.548	0.692	0.0026	0.796	78.60
	48	0.445	0.020	0.607	0.638	0.0024	0.867	87.91
	72	0.454	0.024	0.615	0.272	0.0095	0.781	89.63
	96	0.443	0.019	0.609	0.135	0.0297	0.717	99.29
	120	0.454	0.009	0.695	0.100	0.0547	0.690	97.42
	144	0.495	0.036	0.711	0.180	0.0453	0.692	105.60
	168	0.504	0.043	0.722	0.192	0.0579	0.699	113.10
0.27	5	0.516	0.001	0.801	123.653	0.012	0.388	1116.17
	20	0.474	0.010	0.918	0.728	0.728	0.668	227.06
	48	0.440	0.022	0.946	0.372	0.372	0.701	217.48
	72	0.423	0.053	0.944	0.268	0.268	0.718	157.99
	96	0.419	0.087	0.921	0.257	0.257	0.742	124.49
	120	0.416	0.137	0.874	0.163	0.163	0.761	125.79
	144	0.409	0.047	0.849	0.018	0.018	0.829	119.28
	168	0.411	0.036	0.915	0.016	0.016	0.826	117.21

The primary impact of CO_2 partial pressure variation on the corrosion process is the alteration of the charge transfer resistance. The R_{ct} under high CO_2 partial pressure was significantly lower than that under low CO_2 partial pressure, resulting in a higher corrosion rate under high CO_2 partial pressure. The higher R_{ct} under high CO_2 partial pressure is likely because the increase in CO_2 partial pressure leads to a decrease in solution pH, which promotes the anodic dissolution of the metal. At the same time, higher CO_2 partial pressure accelerates the cathodic reaction process. Ultimately, those change due to the high CO_2 partial pressure lead to a higher corrosion rate under high CO_2 partial pressure.

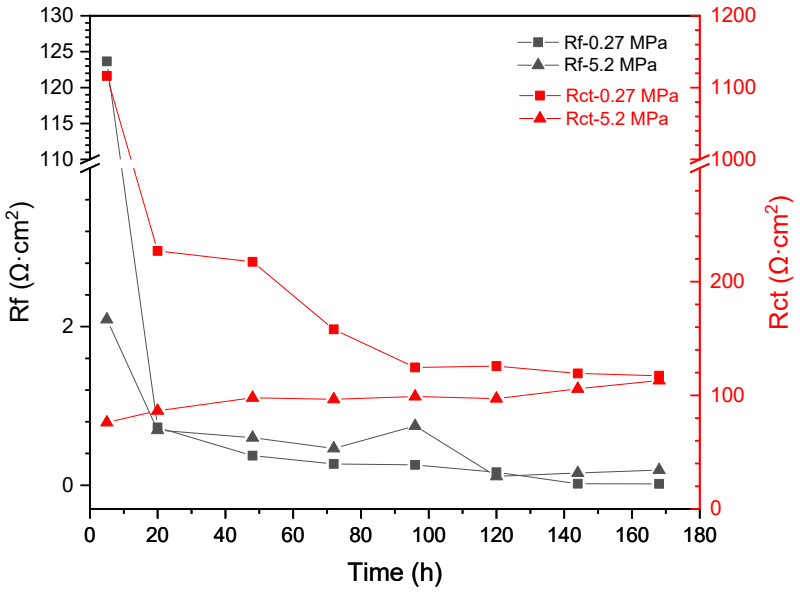

Figure 6-30. R_{ct} and R_f of S13Cr MSS after various immersion times in CO_2-saturated formation brine at 200°C and 5.2/0.27 MPa of CO_2.

6.6. Conclusion

1. At 5.2 MPa of CO_2, based on the surface morphology and the structure of the corrosion product film, the corrosion process can be divided into three stages: a). Early stage: characterised by a non-uniform corrosion product film formed on the surface; b). Middle stage: characterised by the formation of a fully covered single-layer corrosion product film; c). Final stage: characterised by the formation of a double-layer corrosion product film, consisting of an outer corrosion product layer and an inner corrosion product layer containing uncorroded austenite particles.
2. At 0.27 MPa of CO_2, based on the surface morphology and the structure of the corrosion product film, the corrosion process can be divided into two stages: a). Early stage: characterised by a non-uniform corrosion product film formed on the surface; b). Final stage: characterised by the formation of a fully covered single-layer corrosion product film containing uncorroded austenite particles.

3. Compared to the corrosion products generated under high CO_2 pressure condition, the Fe content in the corrosion products formed under low CO_2 pressure significantly increased, and the composition shifted from $Cr(OH)_3$ and Cr_2O_3 at high CO_2 pressure condition to $Cr(OH)_3$ and spinel at low CO_2 pressure condition.
4. At 0.27 MPa, two types of $CaCO_3$ crystals precipitated on the specimen surface: one is small and abundant calcite, and the other is large and sparse aragonite. For the small calcite particles, the cations were doped with Mg^{2+} ions from the solution and Fe^{2+} ions released by the corrosion process, the anions were doped with SO_4^{2-}. XRD and Raman analyses confirmed that these particles were a mixture formed by the co-precipitation of calcite and anhydrite. In contrast, the aragonite is a pure $CaCO_3$ crystal, containing no anionic or cationic impurities.
5. Potentiodynamic polarisation measurements and EIS tests indicate that the corrosion products formed under high pressure provide stronger protective properties. However, since R_{ct} is significantly higher than R_f, the corrosion of S13Cr MSS in CO_2-saturated formation brine at 200°C is controlled by charge transfer process. Consequently, the significantly lower R_{ct} under high CO_2 pressure led to a higher corrosion rate.

7. Chapter 7 Formation/evolution of corrosion product film formed on S13Cr MSS in aggressive HTHP downhole environments: effect of temperature

7.1. Introduction

Building upon the previous investigation of S13Cr MSS corrosion behaviour at 200°C under 0.27 MPa and 5.2 MPa of CO_2, the non-uniform corrosion during the initial exposure and degradation of the air-formed native passive film were observed. However, this process occurred too rapidly for effective electrochemical monitoring. To address this limitation, lower test temperatures were selected to slow down the initial corrosion kinetics. At the same time, we aimed to compare the corrosion behaviour of S13Cr MSS across different temperatures. Additionally, to minimize the influence of precipitates on surface observations, we maintained high CO_2 partial pressure throughout the experiments of this chapter.

In this chapter, as outlined in Table 7-1, comparative studies were conducted at 160°C, 180°C and 200°C were chosen for comparative studies, the CO_2 partial pressure was set at 3.2 MPa at room temperature. Investigation was conducted through systematic experiments with varying exposure times through immersion test and electrochemical measurement combined with surface characterization using SEM, EDS, TEM, Raman spectroscopy, etc..

Table 7-1. Test matrix for the immersion tests.

Temperature (°C)	P_{CO2} at 25°C (MPa)	Calculated P_{CO2} at test temperature (MPa)	Solution	Immersion time (hours)
160	3.2	4.6	Formation brine	5/20/48/168/168*5
180		4.9		
200		5.2		

7.2. Effect of temperature on the long-term corrosion behaviour of S13Cr MSS and thermodynamic consistency assessment

It can be predicted that lower temperatures reduce corrosion kinetics, leading to the decreased corrosion rates and slower corrosion product growth. Consequently, the minor corrosion extent and sparse corrosion products at a lower temperature may complicate the analysis of corrosion behaviour and corrosion products. Hence, within our experimental capabilities, we conducted immersion tests on S13Cr MSS in CO_2-saturated formation water across the 160-200°C temperature range for as long as possible to obtain more comprehensive corrosion data. Therefore, five-week immersion experiments were performed at 160°C, 180°C and 200°C, followed by analysis of the corrosion products.

Figure 7-1 presents the surface and cross-sectional images of corrosion product films formed on S13Cr MSS specimens immersed for 5 weeks at 160°C, 180°C and 200°C. All specimens developed fully covering corrosion product film with measurable thickness. Surface morphology revealed minimal differences across three temperatures. Grinding marks remaining visible from top-view images, suggesting inward growth of corrosion products at both 160°C, 180°C and 200°C. Cross-sectional images show a rapid decrease in film thickness with decreasing temperature: ~85 μm at 200°C, ~12 μm at 180°C, and ~3.5 μm at 160°C.

At 200°C, film delamination, which is the characteristic of the final corrosion stage described in the previous chapter, persisted after 5 weeks of immersion, the corrosion product film separating into an inner layer containing uncorroded austenite particles and an outer particle-free layer. A similar delamination pattern was observed at 180°C (demarcated by yellow dashed line), indicating a similar corrosion process. At 160°C, however, no distinct delamination was evident. But this does not necessarily indicate a different corrosion mechanism from higher temperatures, the corrosion process during the 5^{th} week at 160°C may remain at the middle stage due to the slower corrosion kinetic.

Notably, the corrosion products/metal interface at 160°C exhibited significant irregularity, which could be caused by preferential corrosion at localized hotspots resulting from the compositional variation or metallic defects. Additionally, uncorroded particles observed within the corrosion product film formed at 160°C were significantly larger than previously identified uncorroded austenite particles. Therefore, these uncorroded particles are not considered as the uncorroded austenite particles, but potentially as metal protrusions originating from the irregular corrosion products/metal interface.

Figure 7-2, Figure 7-3 and Figure 7-4 present the EDS elemental mapping results of the corrosion product films formed at 160°C, 180°C and 200°C. EDS mapping clearly reveals the stratified structure of the corrosion product films formed at 180°C and 200°C, with the most significant distinction being the distribution of Fe. The inner layer exhibits higher Fe content due to the presence of numerous uncorroded austenite particles, whereas the outer layer shows Fe depletion. The elemental maps further demonstrate pronounced enrichment of Cr, Ni, and Mo elements, along with Fe depletion throughout the corrosion product films. These observations corroborate that the formation corrosion product films on S13Cr MSS in high-temperature environments primarily involves the preferential dissolution of Fe into the solution and reaction of Cr, Mo, and Ni with corrosive media to form corrosion products.

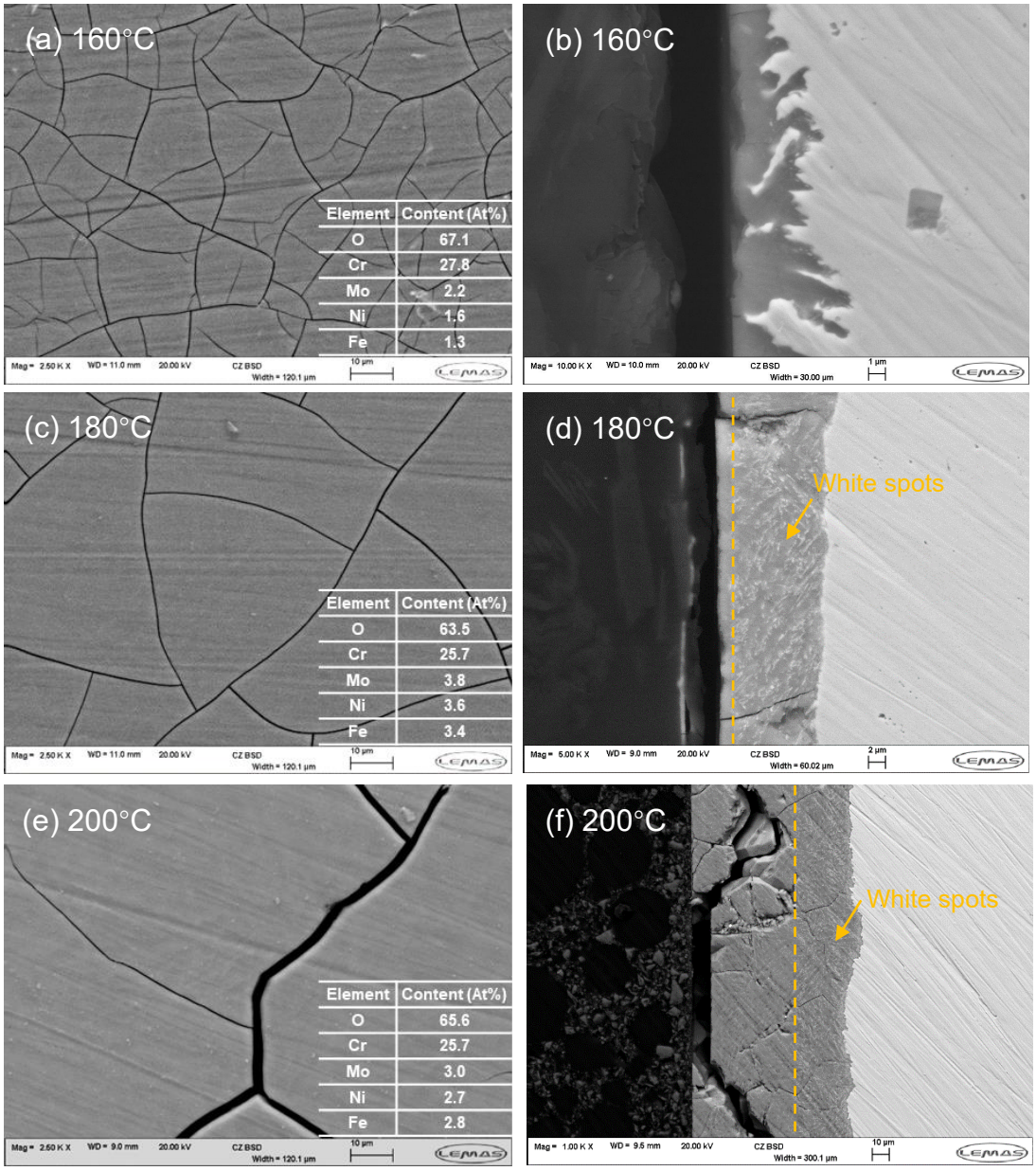

Figure 7-1. Top-view and cross-section morphologies of corrosion product film on S13Cr MSS at (a)(b) 160°C, (c)(d) 180°C and (e)(f) 200°C after 5 weeks of immersion.

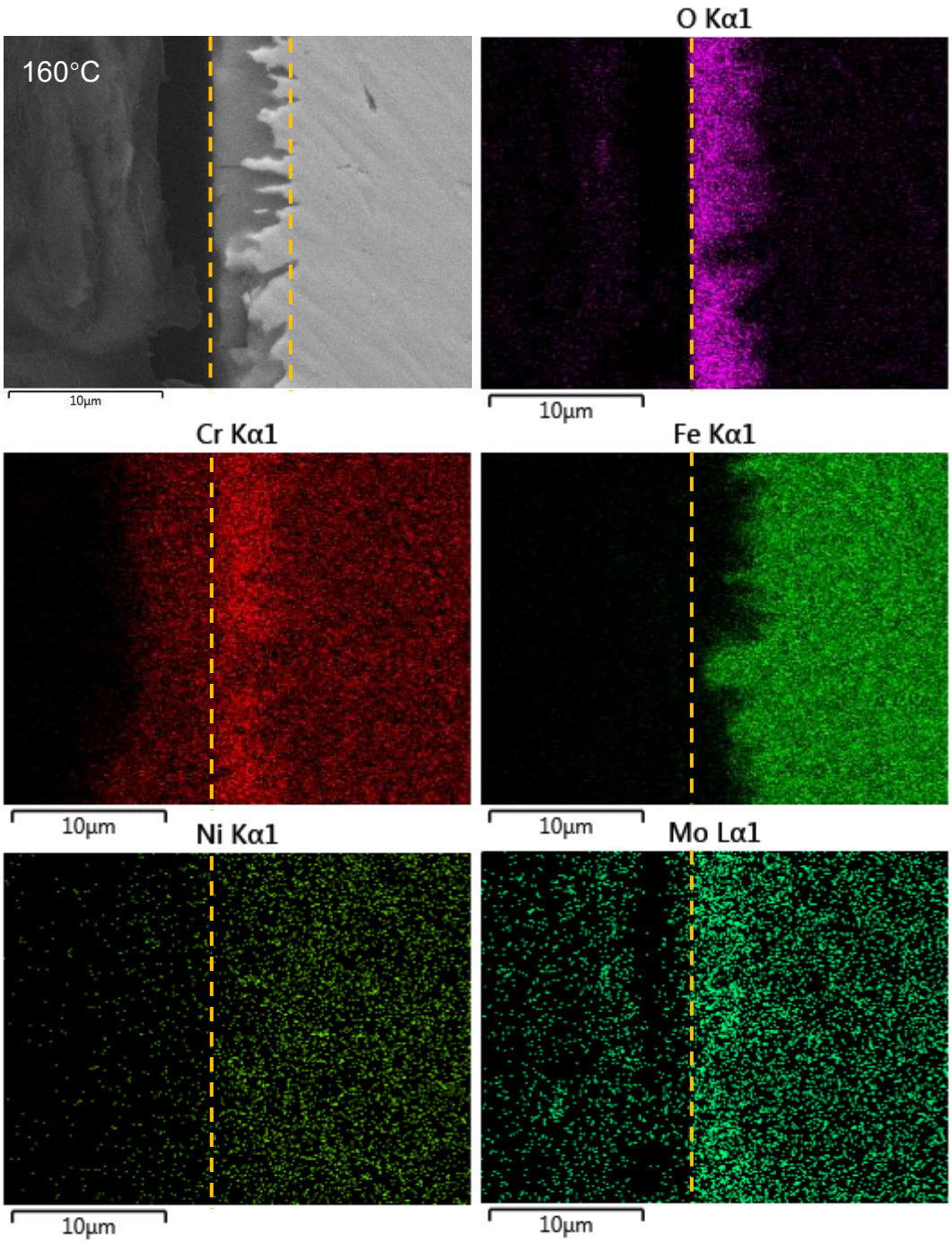

Figure 7-2. Cross-section morphology of corrosion product film on S13Cr MSS at 160°C after 5 weeks of immersion and related EDS mapping of O, Cr, Fe, Ni and Mo.

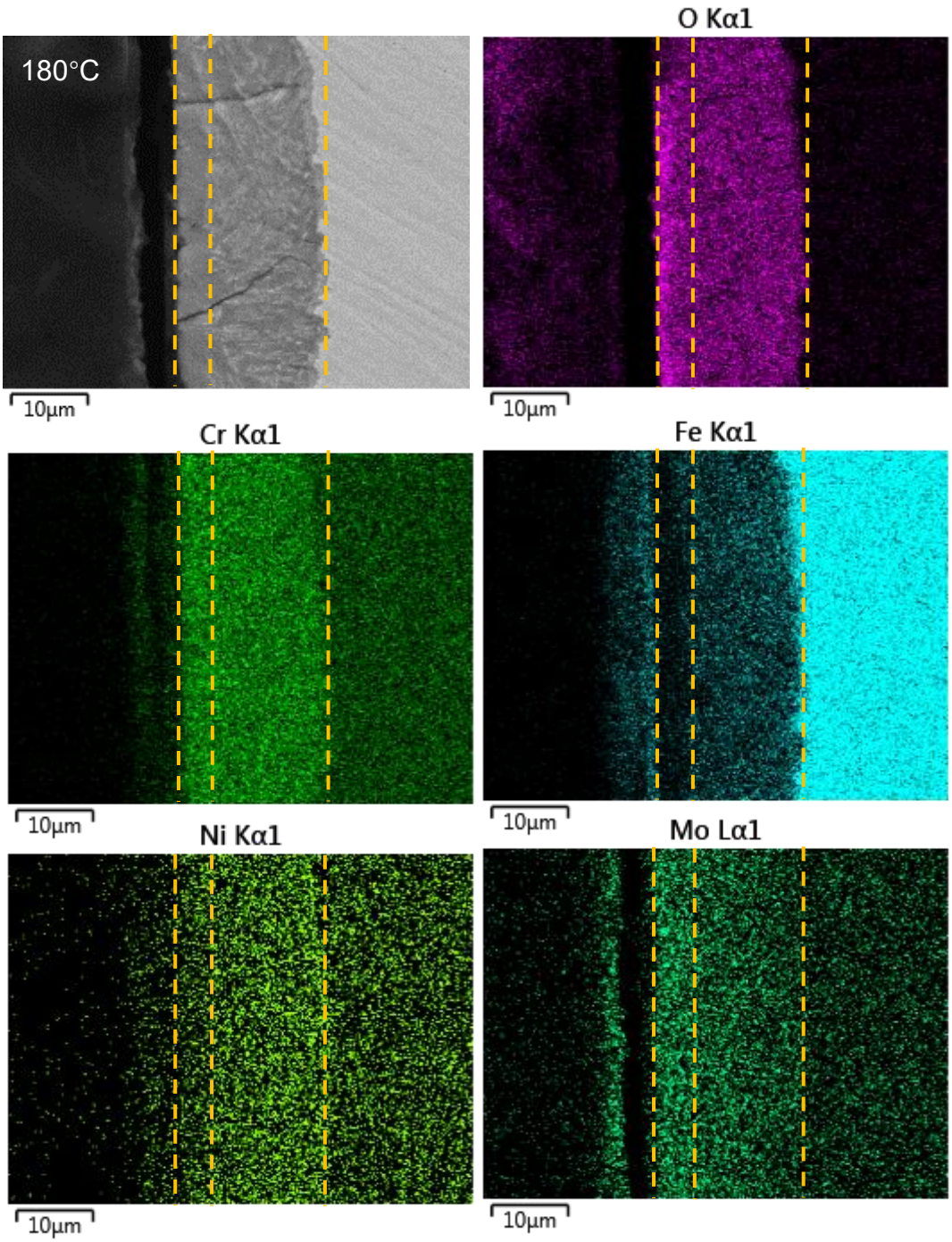

Figure 7-3. Cross-section morphology of corrosion product film on S13Cr MSS at 180°C after 5 weeks of immersion and related EDS mapping of O, Cr, Fe, Ni and Mo.

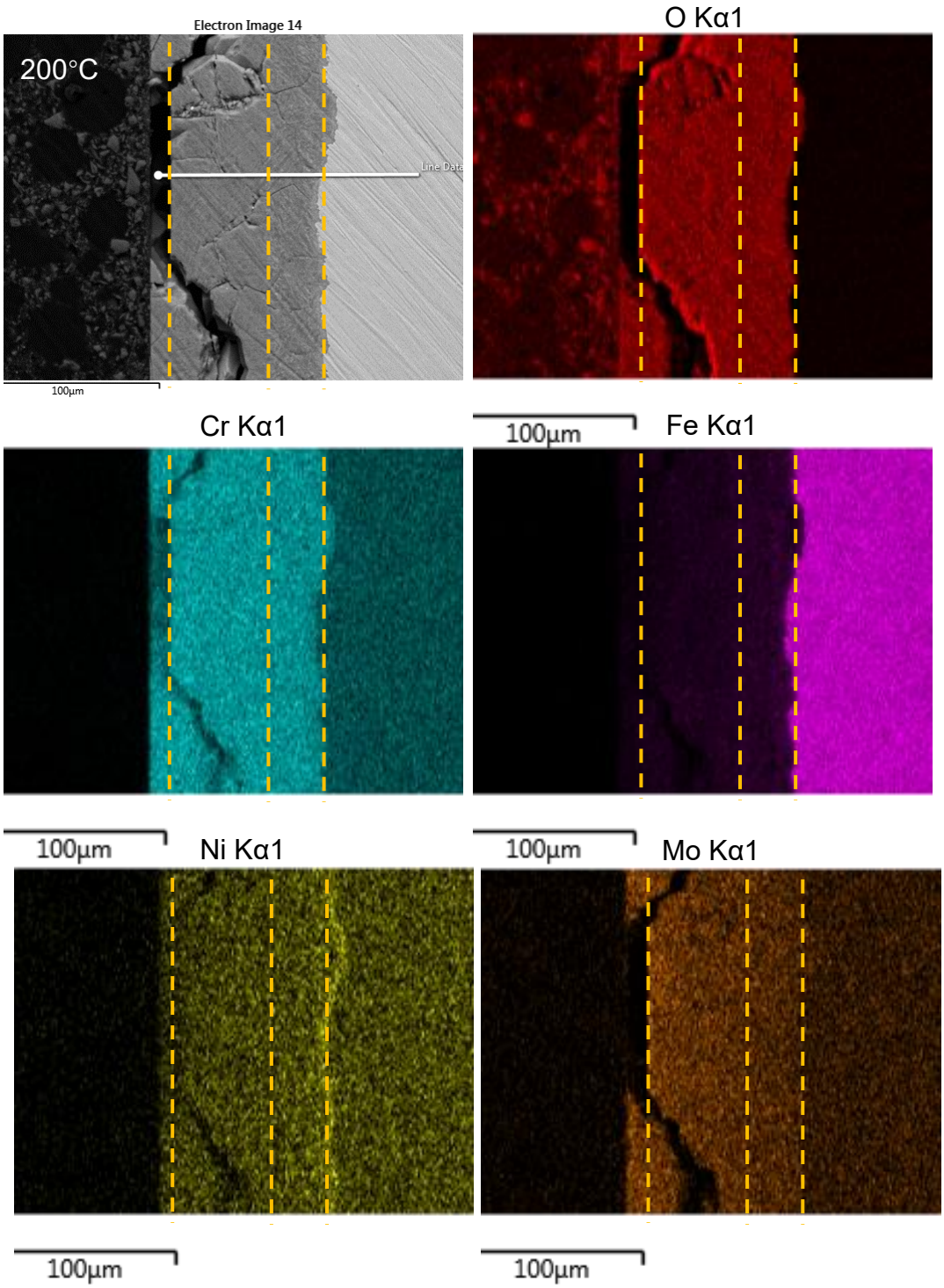

Figure 7-4. Cross-section morphology of corrosion product film on S13Cr MSS at 200°C after 5 weeks of immersion and related EDS mapping of O, Cr, Fe, Ni and Mo.

EDS point analysis of the corrosion products' chemical composition (as provide in Figure 7-1) revealed similar elemental constituents across all three temperatures, predominantly comprising O and Cr with minor amounts of Fe, Ni, and Mo. Raman spectroscopy was employed to further characterize the chemical composition of corrosion products formed at 160°C, 180°C and 200°C. The characteristic spectra obtained are presented in Figure 7-5. The Raman spectra obtained from corrosion products formed at 160°C, 180°C and 200°C revealing characteristic peaks corresponding to Cr_2O_3 (~552-cm^{-1}) and $Cr(OH)_3$ (~717 cm^{-1}), revealing a similar composition of the corrosion products formed at 160°C, 180°C and 200°C.

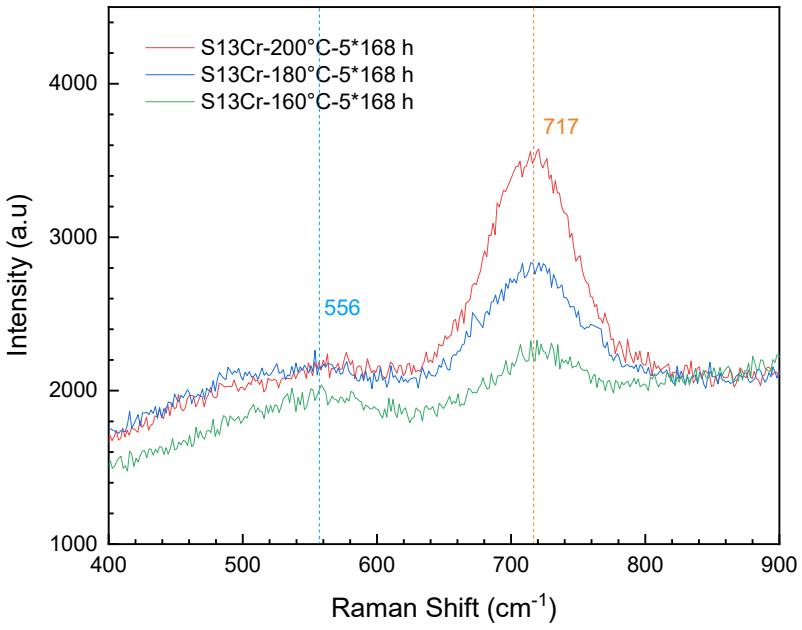

Figure 7-5. Raman spectra of corrosion product film on S13Cr MSS at 160°C, 180°C and 200°C for 5 weeks.

The above findings, combined with the Pourbaix diagram calculations presented in Chapter 9 (discussion part), suggests a consistent corrosion mechanism operates throughout the 160-200°C temperature range.

General corrosion rates of S13Cr MSS at 160°C, 180°C and 200°C for 5 weeks are provided in Figure 7-6, the corrosion level was marked in the graph according to NACE standard RP0775. The

general corrosion rate shows a tendency to increase with temperature and was 0.037 mm/y at 160°C, which is identified as moderate level according to NACE standard RP0775-05 [156]. As the corrosion temperature increased, the general corrosion rate reached 0.130 mm/y and 0.877 mm/y at 180°C and 200°C, which are identified as high level and severe level respectively.

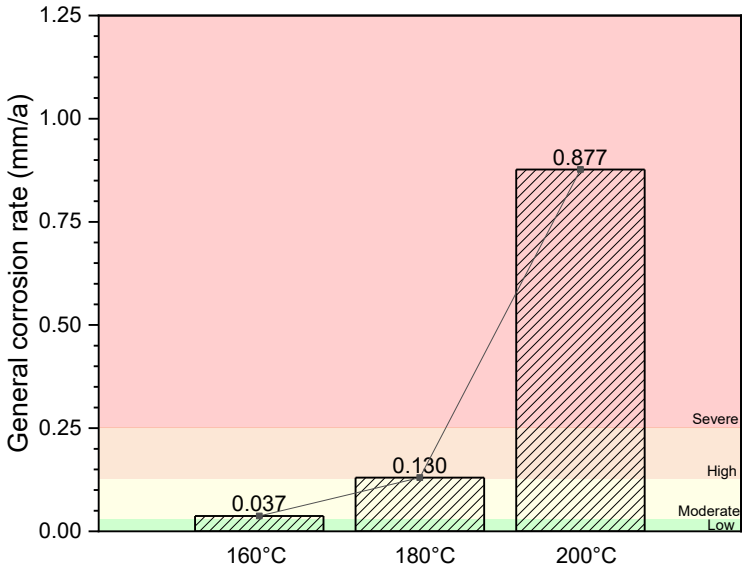

Figure 7-6. General corrosion rates of S13Cr MSS at 160°C, 180°C and 200°C for 5 weeks.

Within the tested temperature range, the corrosion rate of S13Cr MSS exhibits exponential growth with increasing temperature, which aligns with the temperature dependence predicted by the Arrhenius law for a consistent corrosion mechanism. However, since the measured corrosion rates involve non-negligible contributions from different corrosion stages, the activation energy calculated from Arrhenius plot would lack practical significance. We therefore refrain from further discussion of activation energy in this context. However, this finding still carries important implications for the application of S13Cr MSS. At 160°C, the S13Cr MSS shows a moderate corrosion rating, indicating suitability for long-term service; but temperatures exceeding 180°C require careful evaluation before deployment. Moreover, the dramatic increase in corrosion rate of

S13Cr MSS across 160-200°C necessitates substantial temperature control margins in high temperature applications to mitigate the risk of severe corrosion rate fluctuation caused by minor temperature variation.

7.3. Formation and evolution of the corrosion product film at different temperatures

This part focuses on characterizing the temperature-dependent formation and evolution of corrosion product films over time across different test temperatures (160°C, 180°C, and 200°C) and apply our previously established corrosion stage classification to analyse the observed corrosion processes at each temperature condition.

7.3.1. Formation and evolution of the corrosion product film at 200°C

Since detailed analyses of the corrosion behaviour of S13Cr MSS at 200°C and the composition and structure of the corrosion product films have been conducted previously, we focus here on providing a brief review of the corrosion process and film evolution at 200°C. This summary serves as a critical reference for comparative analysis with the newly presented results obtained at 180°C and 160°C in subsequent sections.

Figure 7-7 provides the top-view and cross-section images of S13Cr MSS immersed in CO_2-saturated simulated formation brine at 200°C for various immersion times. Significant preferential corrosion happened in the first 5 h as shown in Figure 7-7(a)(b). After that, a uniform corrosion product layer can be observed after 20 h of exposure. As the corrosion period continued to increase, double-layer corrosion product film (uncorroded austenite particles-containing inner layer and austenite particle free outer layer) was observed after both 168 hours and 5 weeks of corrosion.

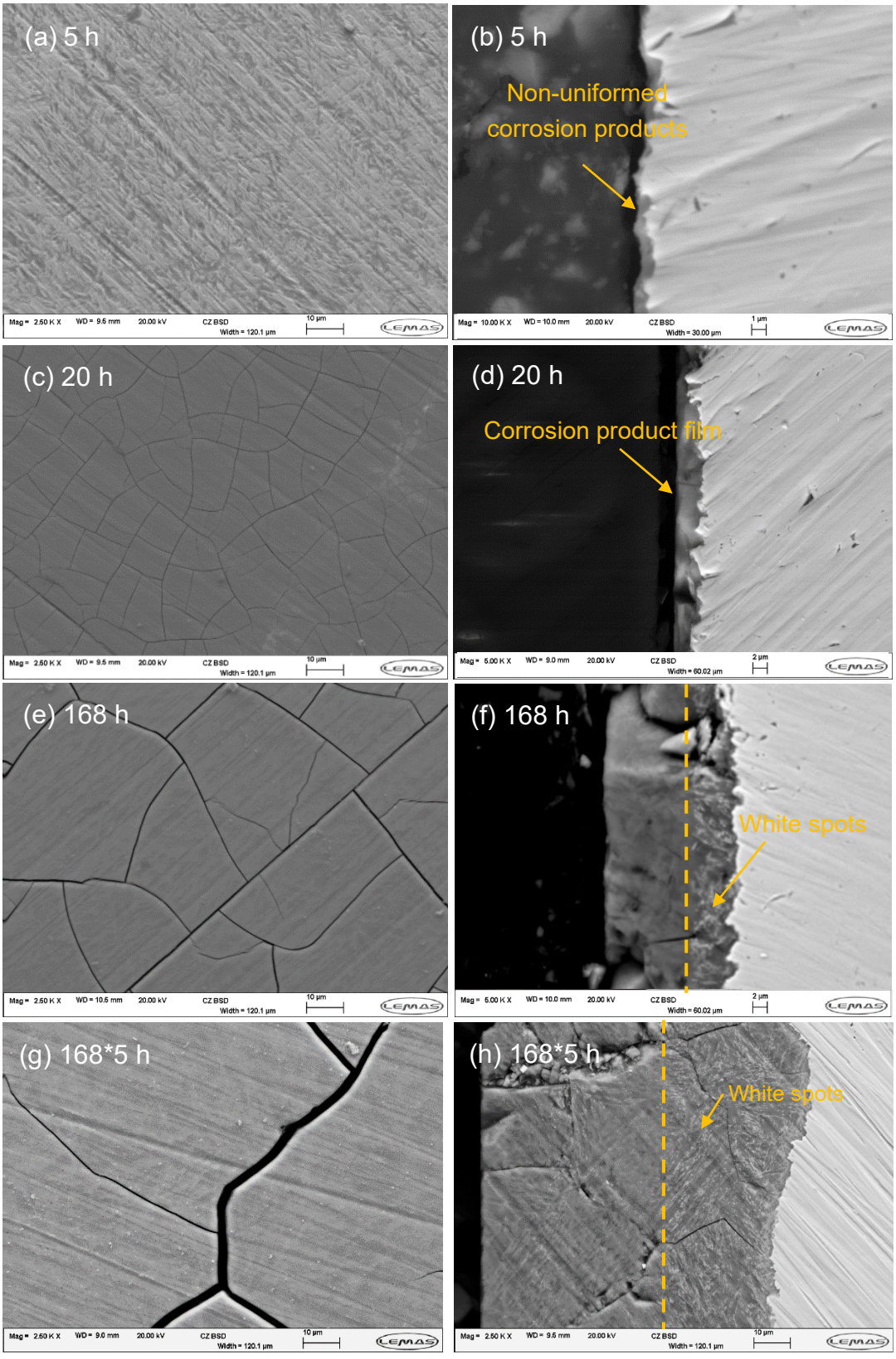

Figure 7-7. Top-view and cross-section morphologies of corrosion product film on S13Cr MSS at 200°C for (a)(b) 5, (c)(d) 48, (e)(f) 168 and (g)(h) 168*5 hours.

Based on the observations, the corrosion process of S13Cr MSS can be divided into three stages:

1. Early stage: characterised by a non-uniform corrosion product film formed on the surface;
2. Middle stage: characterised by the formation of a uniform single-layer corrosion product film
3. Final stage: characterised by the formation of a double-layer corrosion product film which including a uniform outer layer and an inner layer containing white spots.

Notice that the cross-sectional analysis of specimen after 5 weeks of exposure (Figure 7-7(h)) revealed trace amounts of residual metallic particles within the outer corrosion product layer. However, their population density was markedly lower than that observed in the inner layer. Therefore, it is believed that the above-mentioned division of inner and outer layers remains applied.

In addition, it is important to note that at the final stage of corrosion, as shown in Figure 7-7(f) and (h), the thickness of both the inner and outer layers of the corrosion product film increased as corrosion progressed. The interface between the inner and outer layers moved towards the metal substrate with the increase in corrosion time. This interface movement indicates that the uncorroded austenite particles retained in the inner layer will undergo corrosion as corrosion continues, rather than permanent retention in the corrosion product film.

This phenomenon may be related to the diffusion of the corrosive species (e.g., H^+, HCO_3^-) within the corrosion product film. During the corrosion process, the corrosive species continues to diffuse from corrosion product/solution interface towards the corrosion product/metal interface, establishing a concentration gradient along the corrosion product film where the concentration of the corrosive species continuously decreases from the corrosion product/solution interface to the corrosion product/metal interface. As corrosion progresses, corrosion species continued diffuse toward corrosion product/metal interface, when the local environment at the interface between the inner and outer layers reaches a critical concentration of the corrosive species, the corrosion of uncorroded austenite

particles will be trigger, causing the inward movement of the outer layer/inner layer interface.

Previous analysis indicates the corrosion products formed at 200°C were in an amorphous state and were mainly Cr_2O_3 and $Cr(OH)_3$. The types of corrosion products did not change significantly with increasing immersion time.

7.3.2. Formation and evolution of the corrosion product film at 180°C

Figure 7-8 provides the top-view images of S13Cr MSS immersed in CO_2-saturated simulated formation brine at 180°C for various immersion times. Slightly corrosion marks on the surface of the S13Cr MSS after 5 hours of corrosion were visible. After 20 hours of corrosion, as shown in Figure 7-8(b), there are slight corrosion marks on the entire surface with obvious corrosion marks (as indicated by the dark areas marked with yellow arrows in Figure 7-8(b)) in localized areas, which evidences the preferential corrosion at the early stage of corrosion.

As the exposure duration time increased to 48 hours, distinct alternating dark (preferential corrosion areas) and light (uncorroded or slightly corroded areas) zones observed across the entire specimen surface as shown in Figure 7-8(c), indicating a significant preferential corrosion happened after 48 hours of corrosion. The cross-section image (Figure 7-8(d)) reveals a highly irregular corrosion product/metal substrate interface with non-uniform thickness distribution of corrosion product film. Obvious localized corrosion penetration into the metal substrate alternates with regions of minimal corrosion products coverage demonstrates significant non-uniform corrosion occurred during a 48-hour of corrosion.

It can be inferred that the specimens observed at 5 h and 20 h were both in the initial stage of corrosion. For the 48 h corroded specimen, although clear distinction of light/dark areas were visible in the top-view image, the cross-sectional analysis reveals that the light regions were also covered by an observable but thin layer of corrosion products. This indicates the formation of a complete

covered corrosion product film over the entire specimen surface. Furthermore, in the magnified top-view image, arrows highlight crack that traverse both the dark and light zones. As noted earlier, Cracks resulted from dehydration of the corrosion product film upon exposure to air after testing. The presence of the crack across both dark and light zones provides additional evidence that a continuous corrosion product film had already formed on the specimen surface after 48 hours of exposure. Therefore, we conclude that the corrosion state of specimen at 48 h was just transitioned from the early stage to the middle stage.

After that, a uniform corrosion product layer formed on sample surface as the exposure duration increased to 168 h, the specimen had already entered the middle corrosion stage. After 5 weeks of exposure, as previously reported, the corrosion process progressed to its final stage, characterized by a double-layer corrosion product film, uncorroded austenite particles reversed within the inner layer of the corrosion product film as shown in Figure 7-8(h).

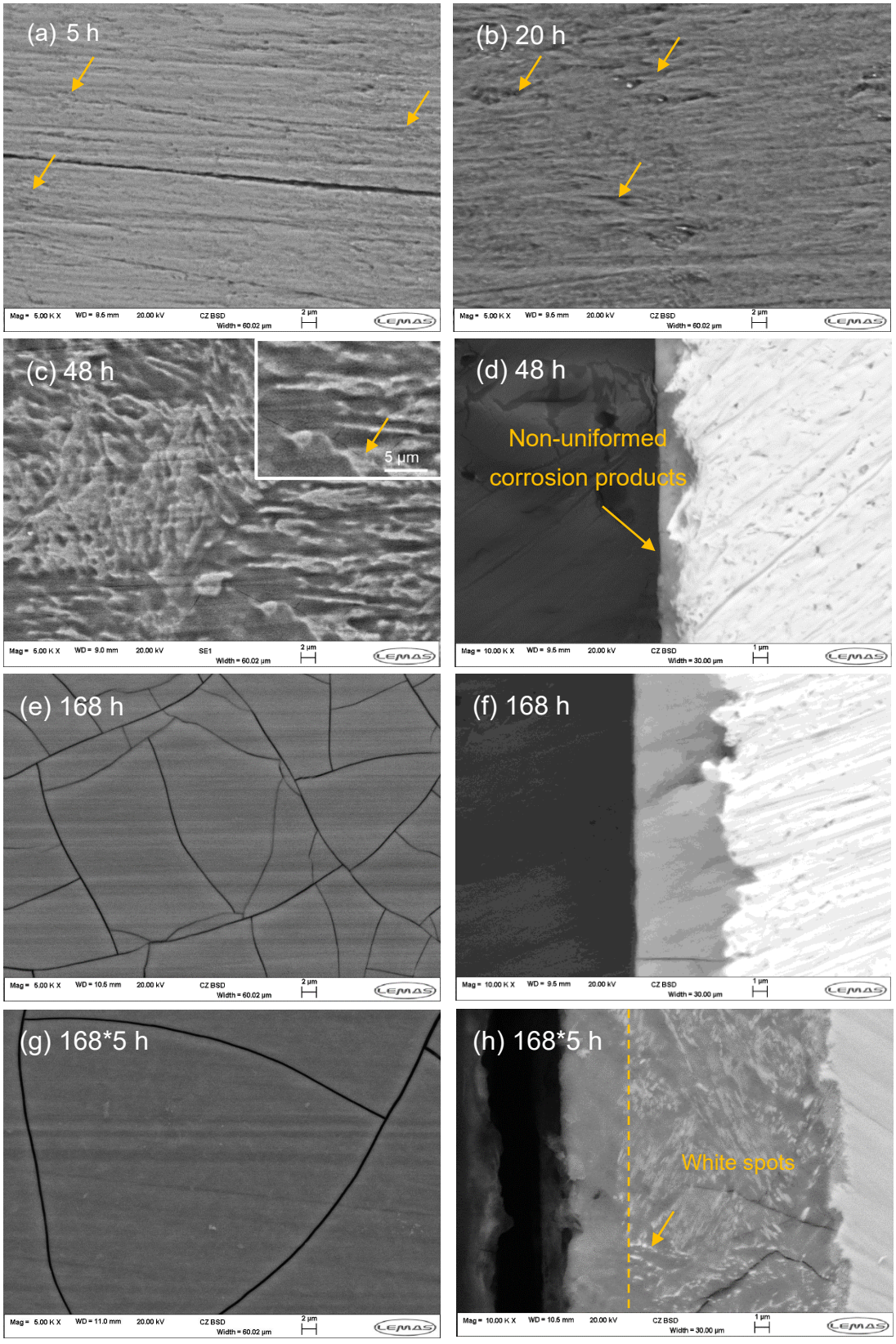

Figure 7-8. Top-view and cross-section morphologies of corrosion product film on S13Cr MSS at 180°C for (a) 5, (b) 20, (c)(d) 48, (e)(f) 168 and (g)(h) 168*5 hours.

XRD analysis was performed on the corroded specimen surface. As shown in Figure 7-9, the corrosion products exhibited poor crystallinity, as evidenced by the absence of distinct characteristic diffraction peaks. Only two broad hump peaks located at approximately 35° and 64° were observed, which are typical of amorphous phases. As the corrosion duration increased, the diffraction peak intensity corresponding to the martensitic matrix gradually decreased, whereas the austenite peak intensity showed noticeable enhancement after 5 weeks of exposure. This observation is consistent with the cross-sectional morphological analysis. The attenuation coefficient of corrosion products for X-rays is typically lower than that of the metallic matrix. With increasing corrosion product film thickness, the proportion of X-rays penetrating to the underlying metal matrix decreased, resulting in the observed reduction in martensite peak intensity. Meantime, the enrichment of uncorroded austenite within the inner corrosion product layer accounts for the enhanced austenite diffraction peaks.

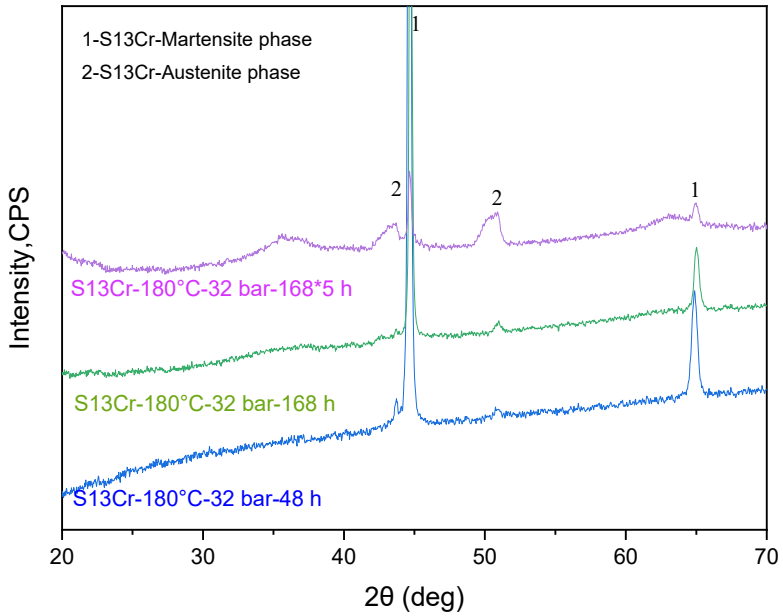

Figure 7-9. XRD patterns of corrosion products on S13Cr MSS at 180°C for 48, 168 and 168*5 hours.

As shown in Figure 7-10, the Raman spectra of both the light and dark regions on the 48 h corroded specimen exhibited similar

characteristic peaks at 717 and 556 cm^{-1}, with no significant difference in peak intensities. This indicates that the chemical composition of the corrosion products in these two regions was essentially identical, further confirming the formation of significant amount corrosion products in the light region.

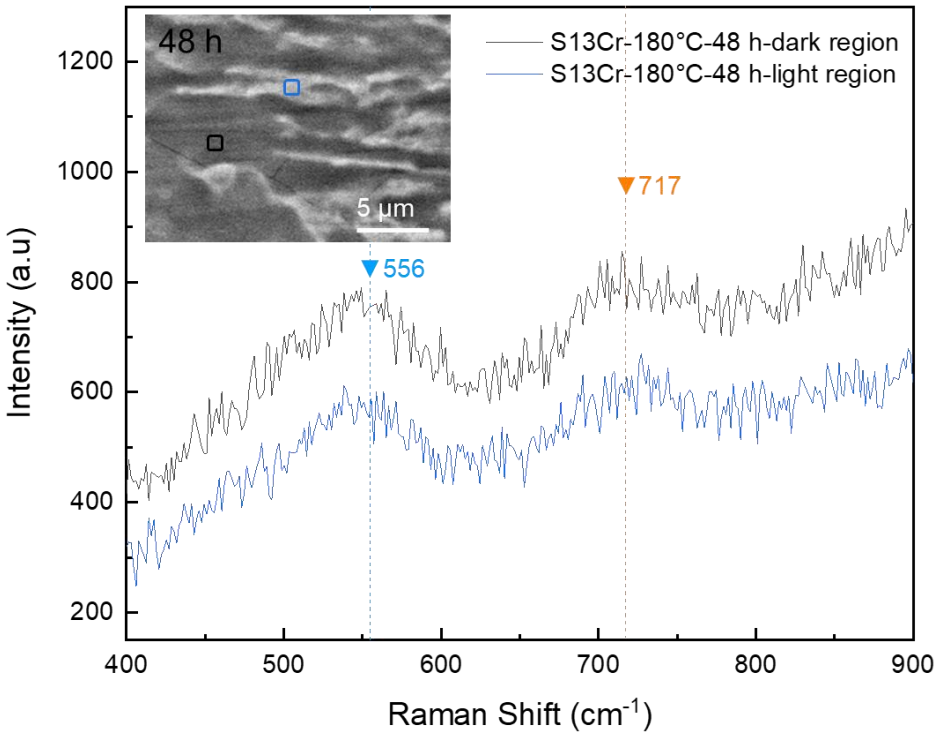

Figure 7-10. Raman spectra of corrosion products at dark and light regions on S13Cr MSS at 180°C for 48 hours.

Raman spectroscopy of specimens corroded for varying durations, as shown in Figure 7-11, revealed that the corrosion products consist mainly of $Cr(OH)_3$ and Cr_2O_3 with a primary peak located at 717 cm^{-1} and a secondary peak located at 556 cm^{-1}.

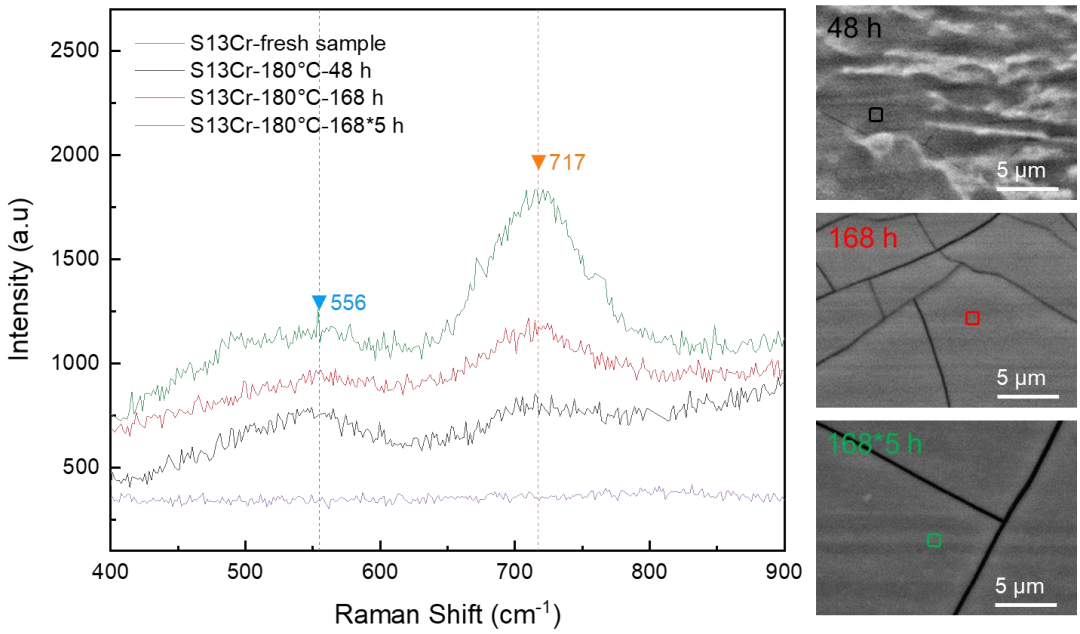

Figure 7-11. Raman spectra of corrosion product film on S13Cr MSS at 180°C for 48, 168 and 168*5 hours.

The morphological evolution and chemical composition of corrosion product films on S13Cr steel exhibited identical characteristics at both 180°C and 200°C. This consistency confirms thermodynamically equivalent corrosion behaviour at these temperatures. However, significant differences in corrosion progression rates were observed. At 200°C, the corrosion process has entered the middle stage after 20 h, and has reached the final stage after 168 h. On the contrary, at 180°C for 48 h, the corrosion process of S13Cr MSS was in the transition phase from the initial stage of corrosion to the middle stage of corrosion. At 168 h, S13Cr MSS was in the middle stage of corrosion, and after 5 weeks, it has reached the final stage of corrosion. From the corrosion kinetic perspective, the corrosion kinetic of S13Cr at 180°C was markedly slower than that at 200°C.

7.3.3. Formation and evolution of the corrosion product film at 160°C

Figure 7-12 indicates the top-view and cross-sectional images of S13Cr MSS immersed in CO_2-saturated simulated formation brine

at 160°C for various immersion times. After 5 hours of exposure, localized corrosion initiation with slight trace was observed on the specimen surface (indicated by arrows in Figure 7-12(a)), demonstrating the initial degradation of the native passive film and the onset of localized metal matrix corrosion. With extended exposure period to 20 hours, the area of the slightly visible corrosion marks on the sample surface began to expand and became more discernible (as indicated by the arrow in Figure 7-12(b), with the edge of the corrosion mark demarcated by yellow dashed line). Furthermore, when the corrosion time increased to 48 hours, these localized corrosion marks became even more pronounced and covered a larger area of the sample surface. This process of change indicates the progressive degradation of the air-formed native passive film which gradually losing its protective capability over the metal substrate, leading to corrosion of the metal substrate.

As the exposure duration increased to 168 hours, the specimen surface exhibited distinct alternating dark and light regions with high contrast (Figure 7-12(d)), indicating preferential corrosion attack in the dark regions. Cross-sectional image (Figure 7-12(e)) confirms the formation of a non-uniform corrosion product film on the S13Cr MSS surface, demonstrating significant preferential corrosion after 168 hours of immersion in CO_2-saturated simulated formation brine at 160°C. Notice that certain areas showed minimal corrosion attack which characterized by either thin corrosion product layer or nearly bare metal surface. Refer the observations at 180°C and 200°C, it can be concluded that S13Cr at 160°C after 168 hours of exposure had reached the terminal phase of initial corrosion stage and was approaching the imminent transition to middle stage of corrosion to form a fully covered uniform single-layer corrosion product film.

After 5 weeks of corrosion at 160°C, top-view image (Figure 7-12(f)) revealed a fully covered corrosion product film, which was further confirmed by cross-sectional analysis, showing a fully covered corrosion product film with an average thickness of ~3.5 μm. These observations demonstrate that the S13Cr MSS has progressed into the middle stage of corrosion after 5 weeks of corrosion in CO_2-saturated simulated formation brine at 160°C.

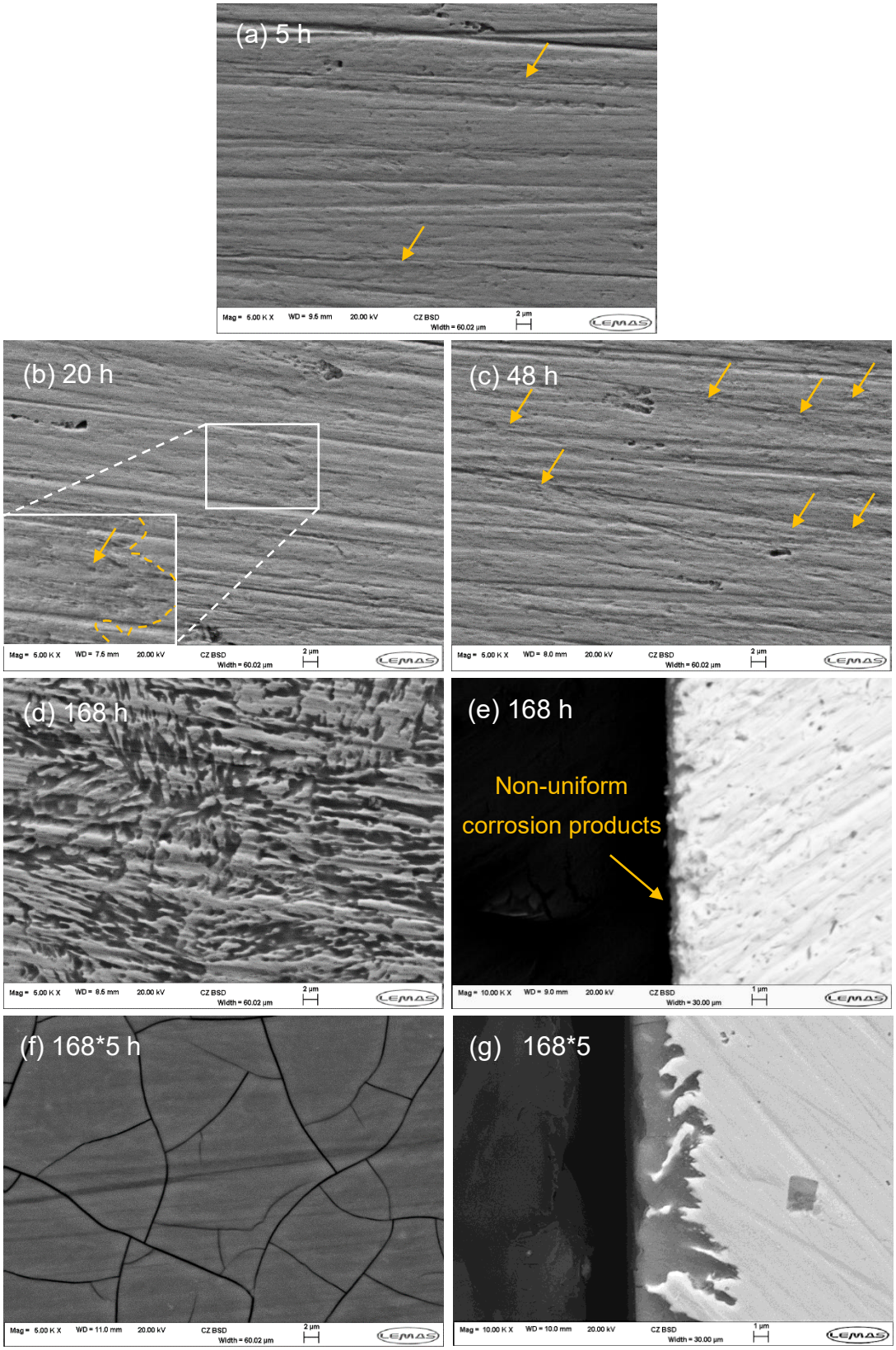

Figure 7-12. Top-view morphologies of corrosion product film on S13Cr MSS at 160°C for (a) 5, (b) 20, (c) 48 (d)(e) 168 and (f)(g) 168*5 hours.

XRD analysis was performed on the corroded specimen surface. As shown in Figure 7-13, XRD analysis revealed only martensitic and austenitic peaks from the metallic substrate being detected. Despite a continuous corrosion product film with ~3.5 μm thick formed after 5 weeks of exposure, no discernible diffraction peaks attributable to corrosion products were observed. This indicates that the corrosion products possess poor crystallinity.

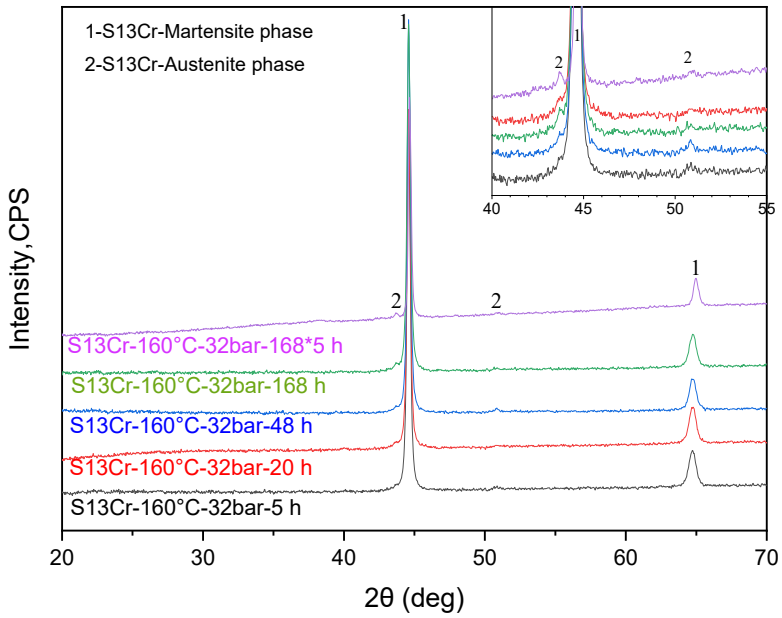

Figure 7-13. XRD patterns of corrosion products on S13Cr MSS at 160°C for 5, 20, 48, 168 and 168*5 hours.

Raman spectroscopy of specimens corroded for varying durations, as shown in Figure 7-14, revealed that the corrosion products consist mainly of $Cr(OH)_3$ and Cr_2O_3 with peaks located at 717 and 556 cm^{-1}. Furthermore, the slower corrosion kinetic at 160°C enabled more detailed observation of the corrosion product evolution during the initial corrosion stage. As shown in in Figure 7-14, the characteristic peak of $Cr(OH)_3$ at 717 cm^{-1} was significantly less pronounced compared to the Cr_2O_3 peak at 556 cm^{-1} during the early corrosion stage. This relative intensity relationship persisted until 48 h of exposure. Notably, stronger $Cr(OH)_3$ peak appeared after 168 h in the preferentially corroded region. Then with prolonged corrosion up to 5 weeks, the $Cr(OH)_3$ peak intensity

continued to increase and becoming the dominant spectral feature. This kind of composition change in the corrosion products will be further discussed in the following discussion part.

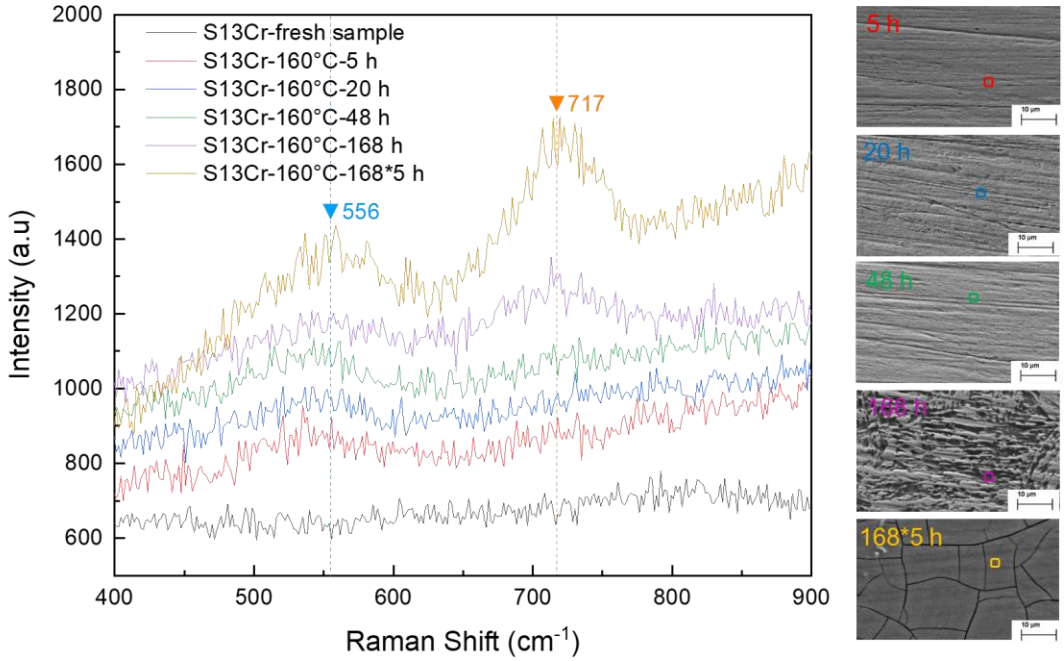

Figure 7-14. Raman spectra of corrosion products on S13Cr MSS at 160°C for 5, 20, 48, 168 and 168*5 hours.

7.4. Electrochemical behaviour of S13Cr MSS at different temperatures

To further investigate the corrosion behaviour of S13Cr MSS and the evolution of its surface corrosion product film during the corrosion process, in-situ electrochemical characterization was employed for real-time monitoring.

7.4.1. OCP measurements

Figure 7-15 presents the OCP evolution of S13Cr MSS with time at different temperatures.

At 200°C, the OCP of S13Cr exhibits a characteristic three-stage evolution: from rapid decline to rapid rise then to stabilization. Immediately after corrosion initiation, the OCP dropped rapidly,

which for stainless steels typically corresponds to the degradation of the native passive film. Once the sample lose the protection form native passive film, the anodic reaction accelerates, leading to a decrease in the OCP. The subsequent rapid rise in OCP indicates the formation of a protective corrosion product film on the surface, which hinders further dissolution of the metallic substrate, resulting in an increase in the OCP. After this rapid rise, the potential stabilized after around 16 h, indicating that the corrosion the corrosion of S13Cr MSS has reached a steady state.

A similar trend of OCP change was also observed at 180°C. However, due to slower corrosion kinetic, the process was significantly delayed. As shown in Figure 7-15, after an initial rapid decrease, the OCP reached its minimum within 5-12 h, then began to rise quickly till 48 h, and finally entered the next stage in which the OCP slow and steady raised.

As for the OCP measured at 160°C, due to its relatively slower corrosion kinetic, the sample immersed for 168 h was still in the early stage of corrosion. Therefore, in a 168-hour monitoring, we only observed a continuous decrease in potential after corrosion began, which declined to the bottom at around 30 h, and then started to gradual rise.

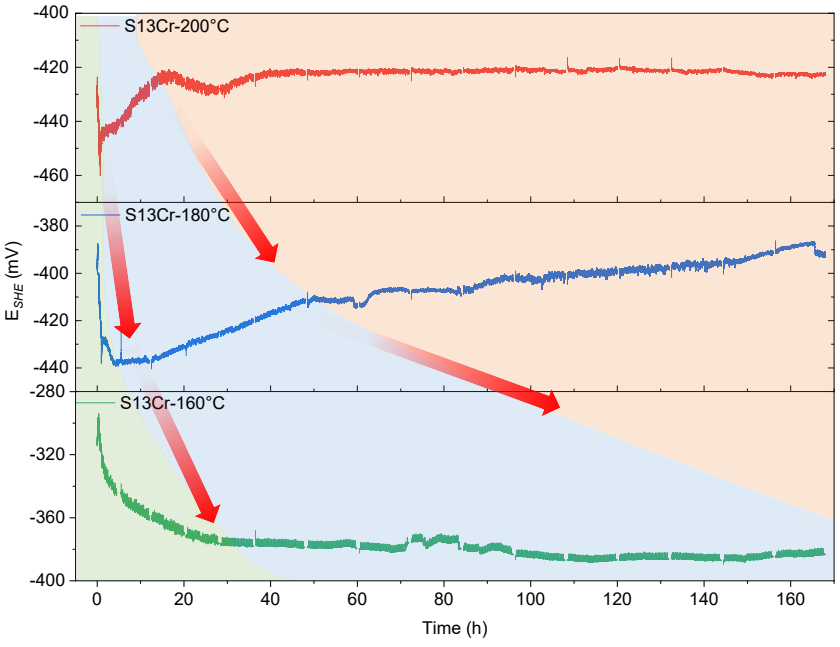

Figure 7-15. OCP of S13Cr MSS as a function time tested at 160°C, 180°C and 200°C.

Combining previous surface morphological observations, the key transition points in the OCP can be correlated with specific stages of the corrosion process.

The initial continuous decrease in OCP, reaching its minimum at ~16 h (180°C) and ~30 h (160°C), corresponds to the gradual degradation of the native passive film and the expansion of localized slightly corrosion areas. Surface morphology analysis (Figure 7-12(a)-(c)) at 160°C showed that from 5 to 20 h, localized slightly corrosion marks appeared and progressively expanded. This confirms that the OCP decline represents the loss of protective properties in the native passive film and the expansion of localized slightly corrosion areas.

Subsequent OCP increase aligns with the occurrence of significant preferential corrosion, characterized by distinct alternating dark (preferentially corroded) and light (uncorroded or slightly corroded) zones across the surface, as shown in Figure 7-8(b) (180°C/20 h). This stage ended by the formation of a continuous corrosion product film, as shown in Figure 7-8(c)(d) (180°C/48 h).

It should be noted that the differences in surface morphology between the end of passive film degradation stage and the start of non-uniform corrosion stage were relatively subtle. Therefore, it is quite difficult to distinguish these two phases only based on surface morphologies, as we previously mistakenly classified 160°C/48 h as part of the passive film degradation stage. Clearly, identify these two stages using OCP is more accurate, which has been confirmed the subsequent EIS test results.

The subsequent OCP stabilization marks the corrosion process enter the middle corrosion stage defined by morphological analysis. Notably, according to the surface morphology at 200°C as shown in Figure 7-7, the corrosion process was in the middle stage characterized by a uniform single layer of corrosion product film and was in the final stage at 168h which characterized by a double layer corrosion product film (a austenite-free outer layer and an austenite-containing inner layer). But the OCP obtained at 200°C remained stable between 20-168 h despite significant microstructural evolution in the corrosion product film happened during this period. This electrochemical stability suggests that the

middle and final stage corrosion, while morphologically distinct, are thermodynamically and mechanistically consistent from an electrochemical perspective.

7.4.2. Potentiodynamic polarisation measurements

To investigate the electrochemical behaviour of S13Cr MSS at different corrosion stages under 160°C, potentiodynamic polarisation tests were conducted during both the OCP declining (20 h) and rising (168 h) periods, as shown in Figure 7-16. The two polarisation curves exhibit critical differences, reflecting the evolution of surface film.

At 20 h, corresponding to the degradation stage of the native passive film, the polarisation curve displays a distinct passive region. This indicates that despite ongoing passive film degradation, the residual air-formed passive film still provides effective protection within a certain potential range, thereby suppressing the anodic dissolution of substrate and leading to a stable current density. Film breakdown occurs at approximately -65 mV.

After 168 h of exposure, localized preferential corrosion has led to the formation of corrosion products in certain areas. Two notable changes are observed in the polarisation curve. Firstly, the pitting potential (E_{pit}, also known as the breakdown potential of the surface film) at 168 h was slightly higher than that of the 20 h specimen. This indicates that the corrosion products exhibit greater stability than the native passive film at 160°C in CO_2 saturated formation brine. Secondly, an active dissolution peak appeared at 168 h as marked by red arrow, suggesting insufficient protectiveness of the corrosion products at this stage.

The appearance of the active dissolution peak is typically regarded as the result of the competition between two opposing kinetic processes within the system: metal dissolution and protective film formation. Prior to the peak potential, which is known as primary passivation potential, anodic dissolution dominates, and the current density increases with the forward shift of potential. However, when the potential reaches a critical value, the reaction between the metal and the corrosive medium initiates the formation of a protective corrosion product film/passive film. This film acts as an effective

barrier, hindering the metal dissolution, thereby causing the current density to decrease even as the potential continues to rise. The transition of the metal surface from active to passive state results in the maximum anodic dissolution rate, forming the active dissolution peak.

The absence of the active dissolution peak in the anodic polarisation curve at 20 h implies that the active to passive transition did not occur. This observation implies the happening of one of the following two situations: (i) the dissolution kinetics are dominated by external factors, thereby preventing the system from entering a pronounced active dissolution stage; (ii) the film-forming kinetics are significantly suppressed, impeding the development of a continuous and protective layer. Consequently, the classical active to passive transition is absent [162, 163].

In the present case, after 20 h of corrosion, the sample was in the native passive film degradation stage, the metal surface still retained its air-formed native passive film. Thus, at the initiation of anodic polarisation, the specimen was already in a passive state. The anodic dissolution was suppressed with the forward shift of potential, resulting in no transition from activation to passivation, and consequently, no anodic dissolution peak appears.

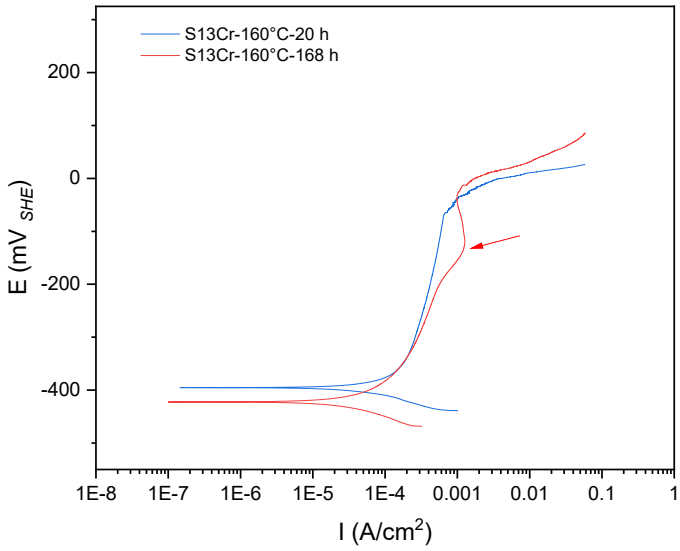

Figure 7-16. Potentiodynamic polarisation curves of S13Cr MSS at 160°C after 20 h and 168 h of immersion.

Potential dynamic polarisation scanning at 180°C across different exposure durations revealed similar trends as shown in Figure 7-18. At 5 h, which is at the native passive film degradation stage, no active dissolution peak was detected in the polarisation curve. However, in subsequent stages, at 48 h (during the transition stage from localized preferential corrosion to formation of uniform single-layer corrosion product film, OCP shifted from rapid rise to slow and steady rise) and 168 h (uniform single-layer corrosion product film formation stage), distinct active dissolution peaks were observed, indicating that the corrosion product film formed in simulated downhole environment provide less protection compared to the native air-formed passive film under HTHP downhole environment. Furthermore, the passive region of the curve obtained at 168 h exhibited a significantly higher current density than that obtained at 5 h, indicating that the native air-formed passive provides better blocking effect that the corrosion product film.

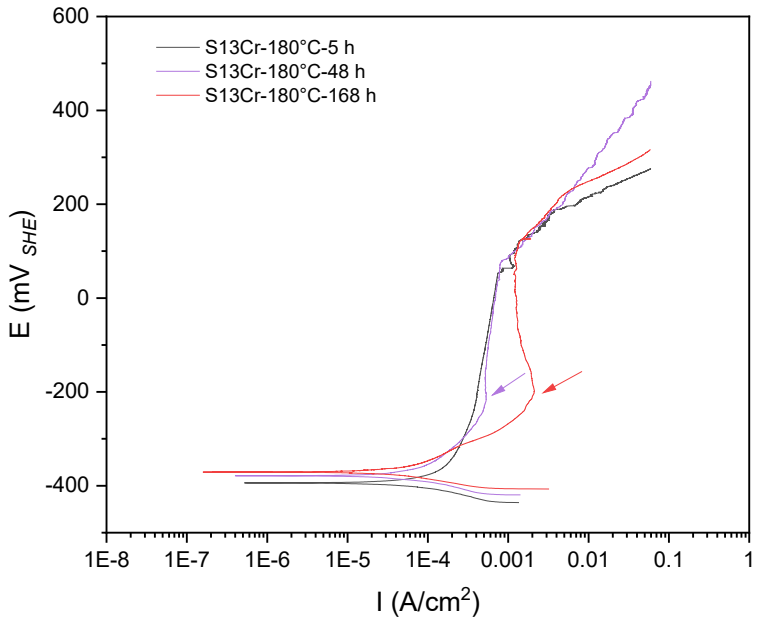

Figure 7-17. Potentiodynamic polarisation curves of S13Cr MSS at 180°C after 5 h, 48 h and 168 h of immersion.

Similar trend was also observed at 200°C. Given the rapid progression of the initial corrosion stage at this temperature (characterized by a sharp decline in the OCP, corresponding to the

degradation of the native passive film), potential dynamic polarisation scanning was performed immediately after the test temperature reached 200°C to ensure the entire polarisation scanning was performed during this stage. The polarisation curve obtained at 0 h, as shown in Figure 7-18, exhibited no active dissolution peak. As the potential was scanned in the anodic direction, the electrode transitioned directly into the passive region without undergoing the active to passive transition, indicating that even at 200°C, the degrading native air-formed passive film still provided a measurable level of protection by suppressing active dissolution on the metal surface.

In contrast, after the formation of a fully covered corrosion product film, whether a single-layer film (20 h) or a double-layer film (48 h and 168 h), distinct active dissolution peaks can be observed in the potential dynamic polarisation curves. Moreover, both the passive current density and the peak current density of the active dissolution peak increased with prolonged immersion time, suggesting a gradual decline in the protection of the corrosion product film. This conclusion was further supported by subsequent EIS analysis.

Furthermore, compared to the native air-formed passive film, the corrosion product film formed on the specimen surface resulted in a higher passive current density and a higher breakdown potential in the polarisation curves under HTHP downhole environment. This suggests that although the native air-formed passive film exhibits a better blocking effect and thus better protection under the test condition, the corrosion product film possesses greater thermodynamic stability.

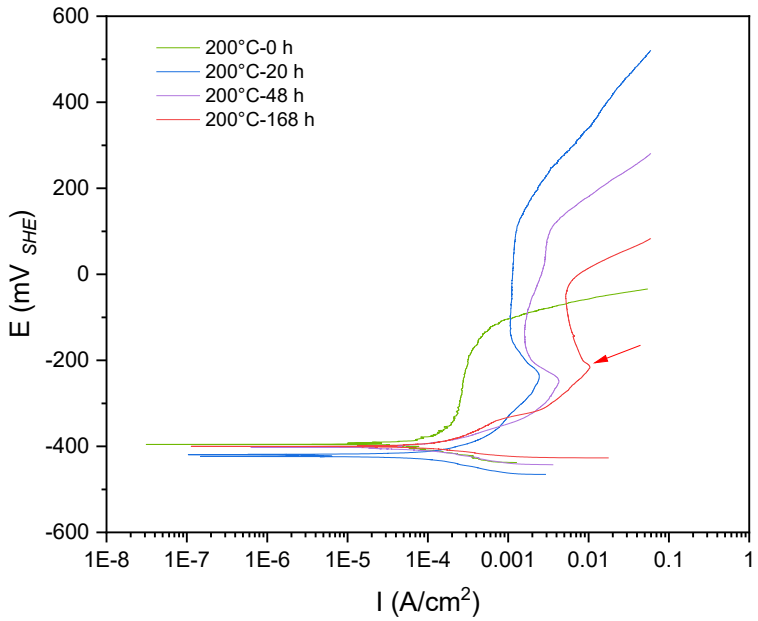

Figure 7-18. Potentiodynamic polarisation curves of S13Cr MSS at 200°C after 0 h, 20 h ,48 h and 168 h of immersion.

The cathodic polarisation curves obtained at all three temperatures exhibit similar shape, indicating a consistent cathodic reaction mechanism and demonstrating thermodynamic similarity across the tested conditions, no new cathodic reactions were introduced by the change in temperature. As temperature increased, the cathodic polarisation curve shifted toward higher current density, reflecting an acceleration of the cathodic reaction kinetic with higher temperature.

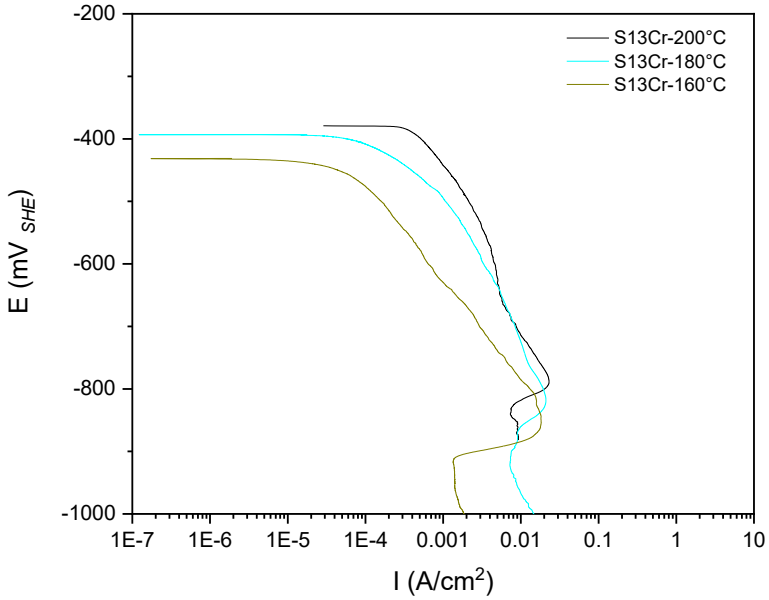

Figure 7-19. Cathodic polarisation curves of S13Cr MSS at 160°C, 180°C and 200°C after 168 h of immersion.

7.4.3. EIS measurements

The EIS of S13Cr MSS in simulated formation brine at 160°C during a 168 h immersion test are shown in Figure 7-20. Prior to 36 h, the Nyquist curve consisted of a capacitive semi-circle in the high-frequency domain and a finite diffusional curve in the low-frequency domain. The latter displayed as a straight line with an arched tail, but the line's slope deviated from the ideal 45° which is believed to be attributable to surface roughness and non-ideal electrode geometry. After 48 h, as shown in Figure 7-20 (c) and (d), besides the capacitive semi-circle in the high-frequency domain and the finite diffusional tail in the low-frequency domain, a capacitive loop gradually appears in the middle-frequency domain in the Nyquist plots, corresponding to a peak occurred in the middle-frequency domain in the Bode plots. It is worth noting that the above shift in EIS pattern is correlated with the change in OCP: during the OCP rapid decline stage, Nyquist curve consisted of a capacitive semi-circle in the high-frequency domain and a finite diffusional tail in the low-frequency domain; After that, Nyquist curve consisted of a capacitive semi-circle in the high-frequency domain, a capacitive

semi-circle in the mid-frequency domain and a finite diffusional tail in the low-frequency domain.

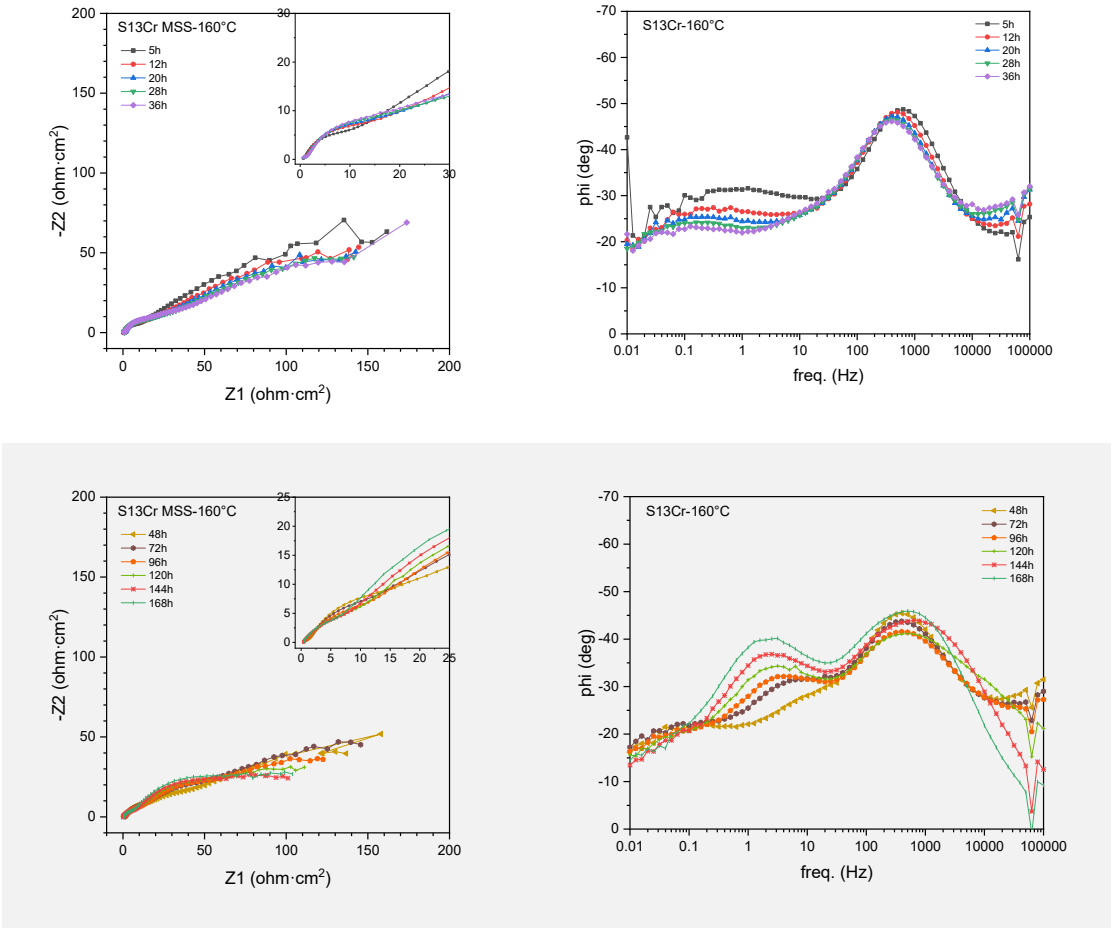

Figure 7-20. Electrochemical impedance spectroscopy of S13Cr MSS at different times in formation brine at 160°C.

The high-frequency capacitive semi-circle, which is believed to be associated with the impedance of corrosion products,[164] is observed to increase in radius with the immersion time in the first 36 hours and progressively decrease after that. The mid-frequency arc is usually associated with the charge transfer resistance and double layer capacitance[164], and its radius increased with immersion time since it has been identified. The characteristics of finite diffusion with transmission boundary in the low-frequency domain indicates that the diffusion of the corrosive species to the scale/substrate interface is constrained, implying the corrosion process is controlled by mass transfer process. The corresponding variations in equivalent circuit elements will be discussed in detail in the subsequent analysis of fitting results.

The EIS obtained at 180°C are presented in Figure 7-21. The spectrum after 5 h of exposure displays a high-frequency capacitive loop coupled with a low-frequency finite diffusional tail. After 12 h, a mid-frequency capacitive arc emerged, the radius of which progressively increased with immersion time. Correspondingly, the Bode plots shows a growing phase angle for the peaks located at the mid-frequency range, indicating more ideal capacitive behaviour which usually reflects a higher electrode surface homogeneity. After 48 h, the low-frequency diffusional feature disappeared and the mid-frequency capacitive arc continued to expand.

This evolution process, similar to that observed at 160°C, correlates with the change in OCP. During the initial period while the OCP rapid drop, the Nyquist plots exhibited a high-frequency capacitive arc coupled with a low-frequency finite diffusional tail. Subsequently, in the OCP rising stage, a mid-frequency capacitive arc emerged in addition to the high-frequency arc and low-frequency finite diffusional tail. Finally, when the OCP stabilized, the diffusional feature disappeared. The disappearance of diffusional characteristic and the emergence of a mid-frequency capacitive loop imply that the controlling process of the corrosion reaction gradually shifted from diffusion control to charge transfer control during a 168 h of immersion at 180°C.

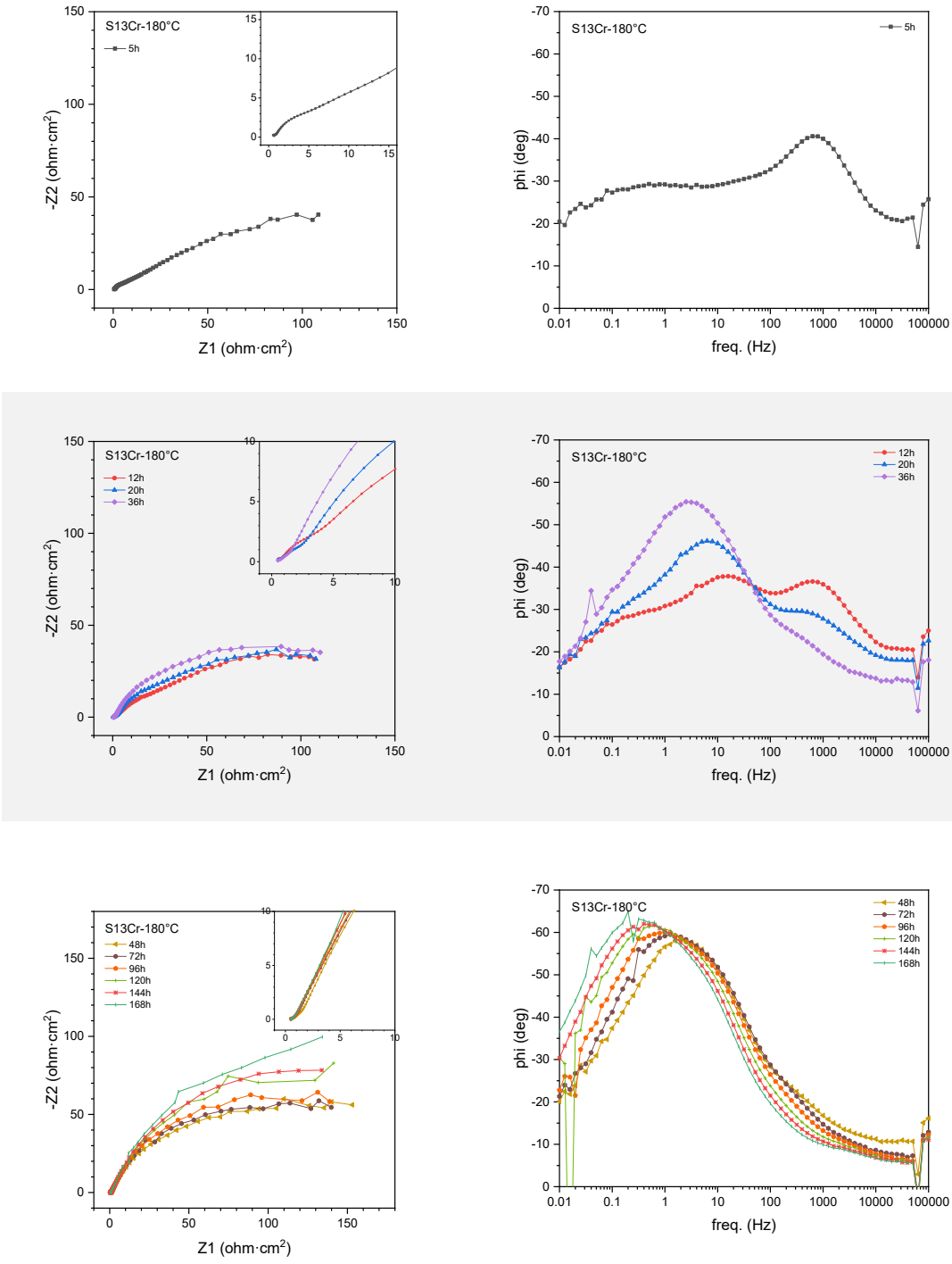

Figure 7-21. Electrochemical impedance spectroscopy of S13Cr MSS at different times in formation brine at 180°C.

Figure 7-22 shows the Nyquist and Bode plots of S13Cr MSS in CO_2-saturated formation brine at 200 °C. It is clearly that all the Nyquist plots obtained at during 168 hours of immersion show

capacitor characteristic with no significant diffusional characteristics. The radius of the semicircle increased with exposure time.

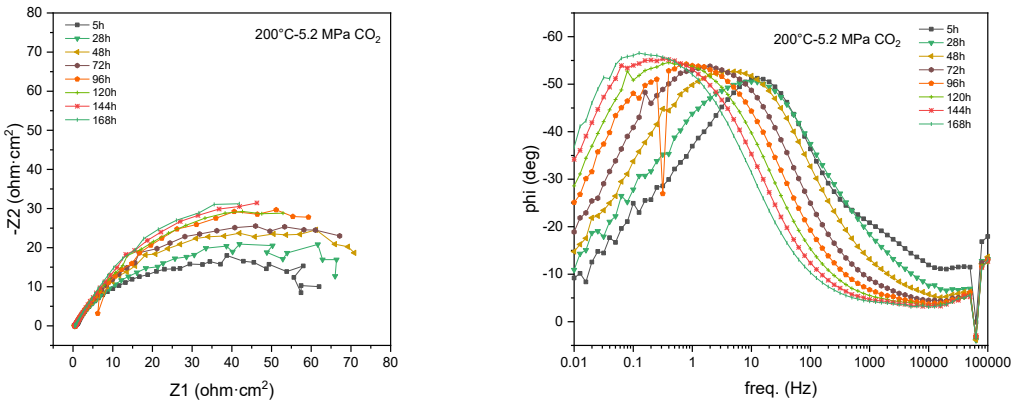

Figure 7-22. Electrochemical impedance spectroscopy of S13Cr MSS at different times in formation brine at 200°C.

The EIS results were fitted into the equivalent electrical circuits (EECs) shown in Figure 7-23. In the equivalent circuits, R_s is the solution resistance, CPE_f and R_f are the constant phase element and resistance of corrosion scale, CPE_{dl} is the constant phase element representing double layer capacitance, R_{ct} is the charge transfer resistance, W_s is the impedance of finite diffusion.

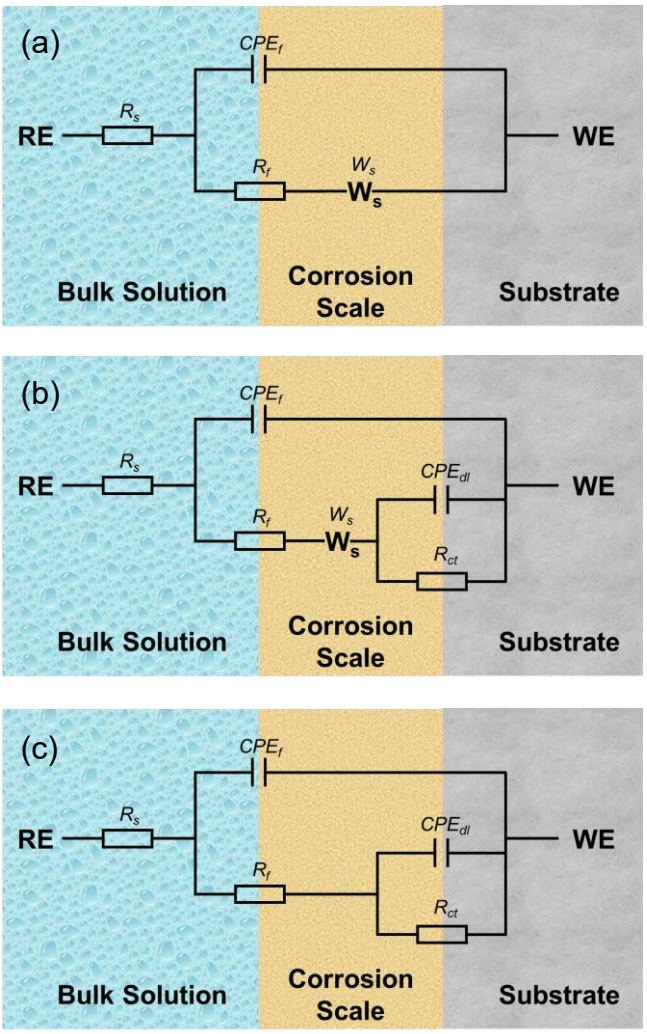

Figure 7-23. EECs utilized for fitting the EIS results of S13Cr MSS at different times in formation brine at 160°C, 180°C and 200°C.

Constant phase element (CPE) is used here as a substitute for the ideal capacitance C to describe the capacitive response that deviates from the ideal state (due to surface roughness, porous structure or relaxation process distribution, etc.). The impedance of CPE can be expressed with the following expression:

$$Z_{CPE} = \frac{1}{Y_0(j\omega)^n} \tag{7-1}$$

Where Y_0 is the magnitude of the CPE. n $(0 < n \leq 1)$ is the deviation parameter which quantifies the non-ideality degree. For an ideal capacitor C, n = 1.

The diffusional impedance is commonly referred to as the Warburg impedance, and can be classified into the following 3 types according to the boundary conditions [165]:

i) Infinite Warburg (IW) impedance

When the length of the diffusion zone can be considered as infinite, IW impedance will be adopted to describe the diffusion impedance, whose real and imaginary components are equal. IW impedance is characterised by a straight line that having a 45° angle from the abscissa in the Nyquist plot as shown by the black line in Figure 7-24(b).

ii) Finite-length Warburg (FLW) impedance

FLW, also known as Warburg-short, is used to describe the impedance of the diffusion of which the diffusion length is finite and the unloaded boundary is a transmissive boundary (or unblocked boundary) where ions are free to penetrate the unloaded boundary. The boundary condition of the unloaded boundary can be described as $C = C_B$ (C_B is the charge carrier concentration outside the boundary) as shown in Figure 7-24(a)-ii. FLW impedance is characterised by a 45° straight line in the high-frequency region and transition to a semicircle in the low-frequency region in the Nyquist plot as shown by the blue line in Figure 7-24(b).

iii) Finite-space Warburg (FSW) impedance

FSW, also known as Warburg-open, is used to describe the impedance of the diffusion of which the diffusion length is finite and the unloaded boundary is a reflective boundary (or blocked boundary) where ions cannot penetrate the unloaded boundary. The boundary condition of the unloaded boundary can be described as $\partial C/\partial x = 0$ as shown in Figure 7-24(a)-iii. FSW impedance is characterised by a 45° straight line in the high-frequency region and transition to a vertical straight line in the low-frequency region in the Nyquist plot as shown by the red line in Figure 7-24(b).

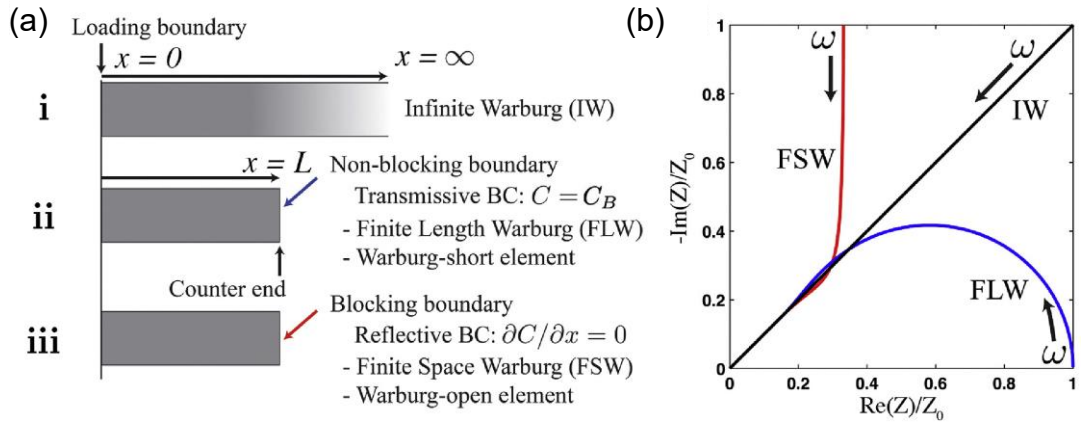

Figure 7-24. Illustration of the three types of Warburg impedance. (a) The domains for diffusion and boundary conditions and (b) Nyquist plot for: (i) the infinite Warburg, (ii) finite-length Warburg, and (iii) finite-space Warburg impedance [165].

In this study, based on the obtained EIS results in low-frequency region illustrated in Figure 7-20 and Figure 7-21 in conjunction with the state of the electrode surface, it is proposed to introduce a FLW element into the EEC for the EIS data fitting.

The Nyquist plots for the three types of diffusion displays in Figure 7-24(b) are calculated based on the ideal diffusion conditions of one-dimensional diffusion. However, in practical scenarios, deviations in Nernst plots emerge due to non-ideal diffusion behaviour (due to non-uniform diffusion and the existence of multiple transport pathways, etc.). To address this, the fractal FLW (also known as generalized FLW) element was applied to describe the finite-length diffusion behaviour under non-ideal conditions. The fractal-FLW is a phenomenological expression, in analogy with the parallel combination of a resistance and a CPE or ZARC (i.e. CPE//R) element [166]. The impedance of fractal FLW can be described with the following expression:

$$Z_{f.FLW}(\omega) = \frac{R_W}{(j\omega T)^n} \tanh(j\omega T)^n, n \leq 0.5 \qquad (7\text{-}2)$$

Where R_w is the diffusion resistance, T is the characteristic time constant and n is the fractal exponential coefficient. For the FLW under ideal diffusion condition, the parameter factor n is 0.5. R_w and T can be expressed by the following equation:

$$R_W = \frac{RTL}{z^2F^2CSD} \tag{7-3}$$

$$T = \frac{L^2}{D} \tag{7-4}$$

where R is the ideal gas constant (8.314 J/(mol·K)), T is the absolute temperature, z is the number of electrons involved in the electrochemical reaction, F is the Faraday constant (96485 C/mol), C is the bulk concentration of ions, S is the electrode surface area, L is the effective ion diffusion thickness, and D is the effective ion diffusion coefficient.

The parameters related to the electrochemical impedance of the oxide film that were obtained from the fitting are listed in Table 7-2.

Table 7-2. EIS spectra fitting data of the EECs for S13Cr MSS in CO_2-saturated formation brine at 160°C, 180°C and 200°C after various immersion times.

Temperature/ °C	Time/ h	Rs/ $\Omega \cdot cm^2$	CPEf-T/ $\Omega^{-1} \cdot s^{-n} \cdot cm^{-2(1-n)}$	CPEf-n	Rf/ $\Omega \cdot cm^2$	Ws-R/ $\Omega \cdot cm^2$	Ws-T/ s	Ws-P	CPEdl-T/ $\Omega^{-1} \cdot s^{-n} \cdot cm^{-2(1-n)}$	CPEdl-n	Rct/ $\Omega \cdot cm^2$
200	5	0.448	0.014	0.537	1.971				0.0007	0.999	66.25
	12	0.425	0.015	0.6117	1.112				0.0015	0.9469	76.44
	20	0.378	0.014	0.548	0.692				0.0026	0.796	78.60
	36	0.301	0.017	0.483	0.392				0.0010	0.902	85.61
	48	0.445	0.020	0.607	0.638				0.0024	0.867	87.91
	72	0.454	0.024	0.615	0.272				0.0095	0.781	89.63
	96	0.443	0.019	0.609	0.135				0.0297	0.717	99.29
	120	0.454	0.009	0.695	0.100				0.0547	0.690	97.42
	144	0.495	0.036	0.711	0.180				0.0453	0.692	105.60
	168	0.504	0.043	0.722	0.192				0.0579	0.699	113.10
180	5	1.087	0.000158	0.863	1.787	205.092	36.450	0.325			
	12	0.687	0.002389	0.591	6.930	167.373	15.870	0.339	0.002528	1.000	35.567
	20	0.622	0.008393	0.496	8.957	84.450	6.682	0.444	0.000650	1.000	111.251

	28	0.676	0.008747	0.529	3.448	76.814	8.037	0.444	0.001400	1.000	125.529
	36	0.694	0.008917	0.568	2.005	67.545	11.930	0.432	0.002042	1.000	131.714
	48	0.683	0.011198	0.609	2.785				0.001879	0.953	199.137
	72	0.594	0.012158	0.655	1.901				0.003362	0.875	184.934
	96	0.562	0.010916	0.679	0.990				0.008039	0.789	193.410
	120	0.538	0.007464	0.710	0.537				0.015405	0.751	231.283
	144	0.547	0.006873	0.735	0.461				0.020237	0.747	237.697
	168	0.542	0.007105	0.740	0.406				0.024335	0.749	293.207
	5	1.019	0.000275	0.797	10.117	254.266	14.820	0.377			
	12	1.392	0.000237	0.810	13.469	232.962	19.550	0.351			
	20	1.571	0.000248	0.801	14.248	251.593	33.930	0.327			
	28	1.798	0.000210	0.818	13.500	269.690	51.380	0.307			
160	36	1.736	0.000276	0.779	15.493	266.712	53.660	0.296			
	48	1.684	0.000309	0.768	16.943	236.475	44.250	0.301	0.005946	1.000	6.787
	72	1.465	0.000399	0.750	14.332	247.394	45.480	0.318	0.005205	0.913	18.142
	96	1.148	0.000801	0.677	17.814	177.299	40.020	0.339	0.005313	0.840	32.062
	120	0.703	0.001414	0.627	18.310	138.586	40.100	0.349	0.005132	0.817	43.095

144	0.472	0.001476	0.655	14.775	99.950	36.110	0.373	0.005675	0.769	56.725
168	0.505	0.001167	0.724	10.186	102.775	35.680	0.380	0.006846	0.773	60.497

To better illustrate the evolution of key electrochemical parameters, the variations in film resistance (R_f), Warburg diffusion resistance (W_s-R), charge transfer resistance (R_{ct}) and calculate polarisation resistance (R_p) with immersion time are plotted in Figure 7-25 to Figure 7-28.

Figure 7-25 presents the evolution of R_f with immersion time at different temperatures. A clear decrease in R_f was observed with increasing temperature. During the transition from the native air-formed passive film to the corrosion product film, Rf exhibits an initial significant increase followed by a sharp decrease, as shown for 160°C (0-168 h) and 180°C (0-48 h). The initial rise in R_f is likely due to a thickening response of the native passive film prior to its breakdown. At this early corrosion stage, oxidants in the environment react with the metal substrate, forming additional oxides on the existing passive film and leading to temporary thickening, which could cause the increase in R_f. Meantime, thermodynamically unstable components in the native passive film (typically Fe-oxides/hydroxides) preferentially dissolve, which could cause the decrease in R_f. The observed increase and subsequent decrease in Rf can therefore be attributed to the competition between film thickening and dissolution of unstable phases: the initial immersion period is dominated by thickening of the passive film, leading to an increase in R_f, while the following stage is dominated by the dissolution of thermodynamically unstable components, causing a decrease in $R4_f$. It is noteworthy that during the native passive film degradation stage, Rf differs considerably between 160°C and 180°C, with higher temperature resulting in lower R_f, implying reduced protective capacity of the native passive film at elevated temperatures. Increased temperature not only diminishes the thermodynamic stability of the native passive film but also markedly accelerates ionic migration rates through the defects within the passive film, thereby lowering its resistance.

After a fully covered corrosion product film formed on the specimen surface (after 48 h at 180°C and throughout the test at 200°C), R_f stabilized at a relatively low value. The significantly lower Rf in this stage indicates that the native passive film offers superior protection compare to the corrosion product film formed in the CO_2-saturated

formation brine. During this period, R_f at 180°C consistently exceeds that at 200°C, indicating better protectiveness of the film formed at the lower temperature. Furthermore, cross-sectional analysis shows that the corrosion product film thickens over time, yet the fitted film resistance decreases slightly, especially during the early period since a fully covered corrosion product film formed. This suggests that although the corrosion product film grows thicker, changes in its properties (such as a reduction in compactness) may lead to a decrease in the overall film resistance.

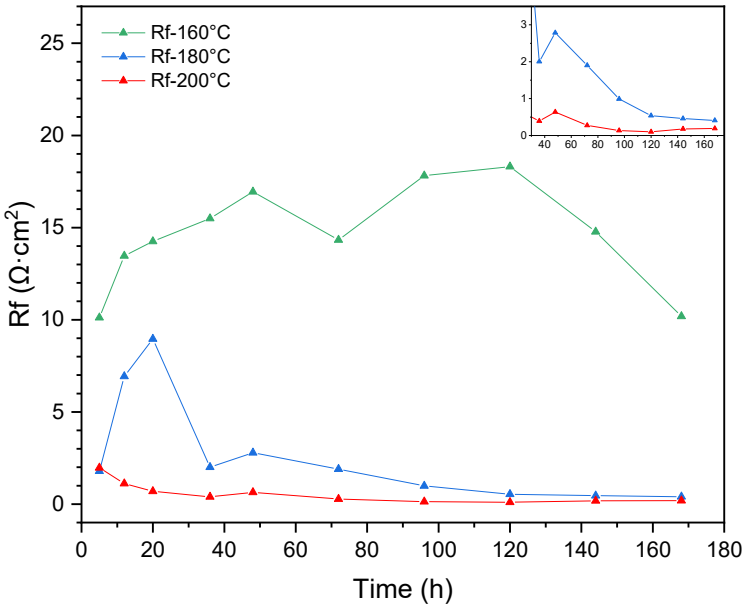

Figure 7-25. R_f of S13Cr MSS in CO_2-saturated formation brine at 160°C, 180°C and 200°C after various immersion times.

The Warburg resistance (W_s-R), as shown in Figure 7-26, progressively decreased with ongoing corrosion, corresponding to the degradation process of the native passive film. The presence of this native passive film necessitates that corrosive species diffuse through its micropores or defects to reach the film/metal interface and react with metal substrate, resulting in the observed diffusional impedance in the EIS results.

After 48 h at 180°C and throughout the 5-168 h period at 200°C, a corrosion product film formed on the S13Cr MSS surface. This newly formed corrosion product film is likely to be looser and more

porous than the native passive film, thus, the diffusion resistance for corrosive species diffuse through the film significantly reduced, which explains the absence of diffusional features in the EIS data at these periods.

The continuous decrease in W_s-R indicates a decreased blocking effect as the native passive film degrades. Moreover, the more rapid decline of W_s-R at 180°C compared to 160°C suggests an accelerated degradation rate of the passive film at elevated temperature.

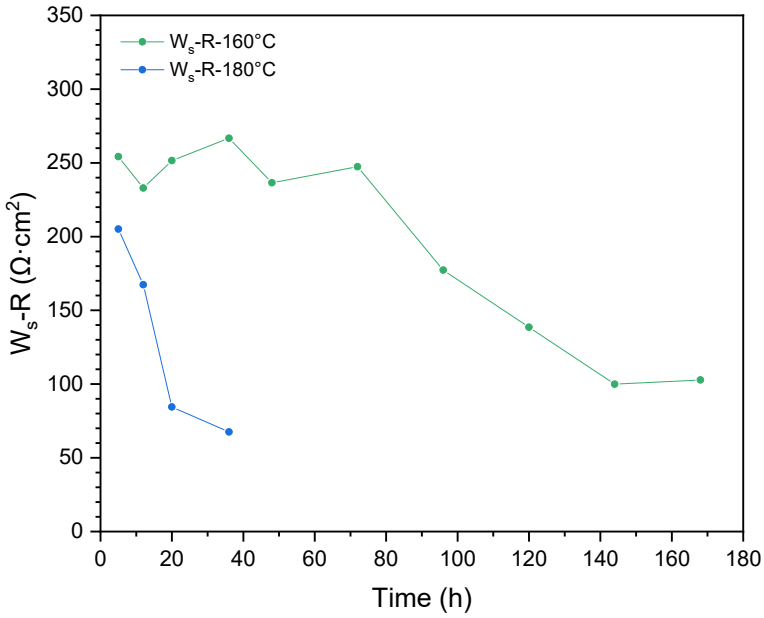

Figure 7-26. Ws-R of S13Cr MSS in CO_2-saturated formation brine at 160°C, 180°C and 200°C after various immersion times.

Figure 7-27 illustrates the variation in R_{ct} across different temperatures. After the formation of a continuous corrosion product film (during 48-168 h at 180°C and 5-168 h at 200°C), R_{ct} increased gradually with exposure time. During this stage, the corrosion process became charge transfer controlled, and the EEC no longer includes a Warburg element, although diffusion may still exert a minor influence. As the corrosion progressed, the corrosion product layer became thicker, the extended diffusion path hindered the transport of reactants and products, thereby increasing the charge

transfer resistance. Notably, at 200°C, the transition of corrosion product film from a single layer to a double-layer (comprising an inner layer with uncorroded austenite particles and an outer layer without austenite particles) film structure from 48 h to 168 h did not cause an abrupt change in R_{ct}. This suggests that the structural evolution of the corrosion product film may not related to a fundamental change of the corrosion mechanism. A more detailed discussion of the mechanism associated with this transition will be provided in the discussion section. Furthermore, during the stage when a fully covered corrosion product film formed, R_{ct} at 200°C was significantly lower than that at 180°C. From a kinetic perspective, elevated temperature accelerates the speed of charge transfer, resulting in a lower R_{ct}, which is consistent with the phenomenon we observed.

However, prior to the formation of a fully covered corrosion product film (48-168 h at 160°C and 12-36 h at 180°C), R_{ct} remained relatively low. Moreover, R_{ct} values obtained throughout the entire test period at 160°C were substantially lower than those at 180°C and 200°C, which contradicts with the general understanding that increase in temperature would accelerate the kinetics of charge transfer process and leads to a lower R_{ct}. This unusual phenomenon occurred during the OCP rising stage, based on the surface morphology observations, is associated with localized preferential corrosion. The degradation of the native passive film led to the exposure of active sites where localized corrosion occurs.

These active sites had lost the protection of the native passive film and had not yet generated sufficient corrosion product to provide protection, and expose the bare metal to the corrosive environment, resulting in a very low local Rct. The very low local R_{ct} depresses the measured R_{ct} for the entire test surface. Additionally, the gradual increase in tested R_{ct} during this period may be attributed to the gradually formation of corrosion products at active sites, which progressively suppresses corrosion and increases charge transfer resistance.

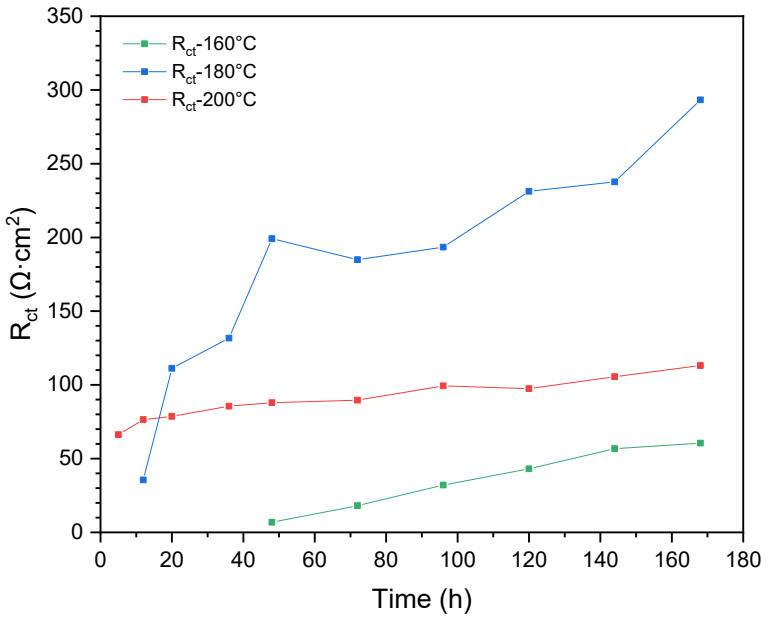

Figure 7-27. R_{ct} of S13Cr MSS in CO_2-saturated formation brine at 160°C, 180°C and 200°C after various immersion times.

The polarization resistance, which exhibits an inverse relationship with corrosion rate, was calculated using Equation (7-5)(7-5, with the results presented in Figure 7-28.

$$R_p = R_f + W_s\text{-}R + R_{ct} \quad (7\text{-}5)$$

At 160°C, Rp decreased progressively throughout a 168-hour test, indicating a continuous increase in the corrosion rate. This period is characterized by the degradation of the passive film and the following development of localized preferential corrosion. The diffusion resistance (W_s-R) constituted the dominant component of R_p during this period. As the passive film deteriorated, its ability to hinder the diffusion of corrosive species weakened, thereby accelerating corrosion.

At 180°C, R_p underwent a slight decline and then increased after 72 h, revealing a transition in corrosion rate from an initial increase to a subsequent decrease. This change results from the competing effects of decreasing W_s-R due to the degradation of native passive film and increasing R_{ct} caused by the thickening corrosion product film.

At 200°C, R_p showed a gradual increase, suggesting a steadily decreasing corrosion rate during the 168 h observation period. This phenomenon is attributed to the extremely rapid completion of the native passive film degradation stage at this temperature, meaning that only the subsequent period of fully covered corrosion product film formation stage was captured. During this stage, R_{ct} served as the primary contributor to R_p. The continuous thickening of the corrosion product film increasingly suppressed charge transfer, leading to the observed rise in R_{ct} and ultimately leading to a decrease in the corrosion rate. Furthermore, a strong correlation was observed between the R_p and the corrosion rate obtained from weight loss measurements in Chapter 6 at 200°C. The R_p values exhibit a gradual increase with prolonged immersion time, while the corresponding corrosion rate shows a progressive decrease. This consistent inverse relationship enhances confidence in the reliability of the electrochemical data.

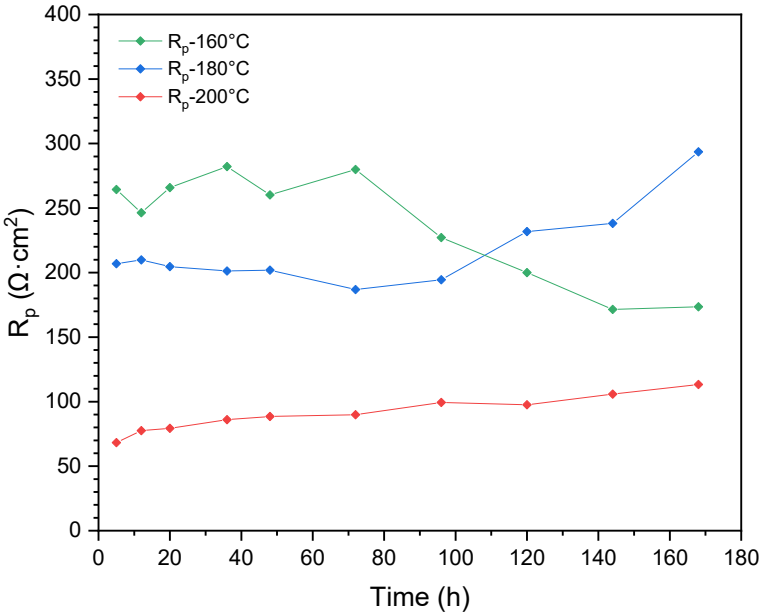

Figure 7-28. R_p of S13Cr MSS in CO_2-saturated formation brine at 160°C, 180°C and 200°C after various immersion times.

7.5. Conclusion

This chapter systematically investigated the corrosion behaviour of S13Cr MSS in CO_2-saturated formation water across 160-200°C through immersion tests coupled with electrochemical monitoring. The following conclusions are drawn:

1. The corrosion evolution of S13Cr MSS demonstrated similar stage transition across the temperature range of 160-200°C, as validated by both immersion experiments and electrochemical measurements. Lower temperature significantly prolonging the duration of each corrosion stage due to reduced reaction kinetics. However, from a thermodynamic perspective, the corrosion mechanism remains consistent across the temperature range of 160-200°C. This mechanistic similarity is further evidenced by the comparable chemical composition of the corrosion products, which consist primarily of chromium oxides and hydroxides at all three test temperatures.
2. Electrochemical techniques, particularly OCP monitoring, provide superior resolution for identifying stage transitions compared to immersion tests. Based on OCP evolution, the corrosion process can be categorized into three distinct stages:
   a) Native passive film degradation stage: The main feature of this stage is the degradation of the native passive film, characterized by continuous OCP drop, dominated by diffusion process.
   b) Localized preferential corrosion stage: The main feature of this stage is that obvious local corrosion occurred on the sample surface, marked by sustained OCP rise. The corrosion is controlled by both diffusion and charge transfer during this stage.
   c) General corrosion stage: A complete covering corrosion product film forms on the surface during this stage, identified by OCP stabilization, and controlled by charge transfer. This stage can be subdivided into two stages according to the cross-sectional morphology of the corrosion product film: single-layer film stage and double-layer film stage. Despite their structural differences, these two stages exhibited no significant electrochemical distinction.

3. The native passive film provided an initial excellent protection, but its thermodynamic instability at high temperatures led to its rapid degradation; the subsequent formed corrosion product film, although able to persist stably, could not match the protective performance of the native passive film.

8. Chapter 8 Effect of austenite on the corrosion behaviour of S13Cr MSS under HTHP downhole environment

8.1. Introduction

Reversed austenite usually nucleated around the Cr-rich carbides, which are distributed along the martensite laths boundaries. Reversed austenite has higher contents of Ni and Mo, but a similar content of Cr in comparison with the martensitic matrix. The presence of reversed austenite reduces the extent of Cr depletion and enhances the stability of passive film, thereby, during the corrosion process, reversed austenite can improve the pitting resistance of S13Cr MSS [114]. But Ni-partitioning resulting from austenite reversion process is reported to led to an increase in the susceptibility of the alloy to pitting corrosion [111]. At the same time, austenite, which acts as a ductile strengthening phase in martensitic stainless steel, can improve the toughness but reduce the strength of the material. Moreover, austenite as a hydrogen trapping site can hinder the hydrogen diffusion process, which allows it to increase the HE resistance of the material [122, 126]. Therefore, the austenite content in the S13Cr MSS can be adjusted according to the application environment to achieve the optimal combination of corrosion resistance, mechanical properties and hydrogen embrittlement resistance.

However, the above observations were predominantly derived from S13Cr MSS in its passive state. As a stainless steel, the corrosion resistance of S13Cr MSS primarily relies on its protective passive film, and thus it is typically maintained in a passive state under its primary service conditions. Consequently, it is understandable that most existing research has focused on the corrosion and fracture behaviour of S13Cr MSS in this passive condition. In contrast, our previous findings demonstrate that after the degradation of the passive film under HTHP downhole environments, the S13Cr MSS ultimately maintains an active dissolution state, which differs

significantly from the scenarios explored in the majority of prior studies.

Our previous observations revealed significant different corrosion behaviour between austenite particles and martensitic matrix during the later stage of corrosion process, the martensite substrate continuously corrosion while the austenite particles remain within the inner layer of the corrosion product film. The different corrosion behaviour between austenite particles and the martensitic matrix suggest possible galvanic corrosion between these two phases. Increased austenite content may potentially enhance such galvanic interaction, thereby accelerating corrosion of the martensitic matrix. Moreover, when the austenite fraction reaches a substantial level, it remains unclear whether these preserved austenite regions could form a continuous protective barrier that mitigates further corrosion of the martensitic matrix.

To address these questions, this chapter systematically investigates the effect of austenite content on the corrosion behaviour of S13Cr MSS at 200°C with 5.2 MPa of CO_2. The findings aim to provide corrosion-perspective insights for optimizing the austenite content in S13Cr MSS materials used under HTHP downhole environments. Investigation was conducted through systematic experiments with varying exposure times through immersion test combined with surface characterization using SEM, EDS, and Raman spectroscopy.

8.2. Preparation of S13Cr MSS with different austenite content

8.2.1. Microstructure of S13Cr MSS used in previous study

The S13Cr MSS-110 ksi material used in the prior corrosion tests was manufactured via the processing route illustrated in Figure 8-1. The raw stock was first hot-rolled to shape, followed by a heat treatment consisting of solid solution treatment (1020 °C/30 min) and tempering (620 °C/60 min). The chemical composition of the used S13Cr MSS previously provided in Table 4-1, which is

characterized by 0.01% C, 12.6 % Cr, along with 5.1 % Ni and 1.6 % Mo.

Figure 8-1. Treatment process of S13Cr MSS-110 ksi.

Figure 8-2 presents the XRD pattern of the S13Cr MSS-110 ksi. Distinct martensitic diffraction peak (α(110)) and austenitic diffraction peaks (γ(111) and γ(200)) are evident. The austenite content was evaluated using the following equation[167]:

$$V_\gamma = \frac{1.4I_\gamma}{I_{\alpha\prime}+1.4I_\gamma} \quad (8\text{-}1)$$

Where V_γ are the volume fraction of reversed austenite, I_α and I_γ are the integrated intensities of α(110) and γ(111) peak, respectively. The calculated austenite content is 4.13% for the S13Cr MSS-110 ksi used in this study.

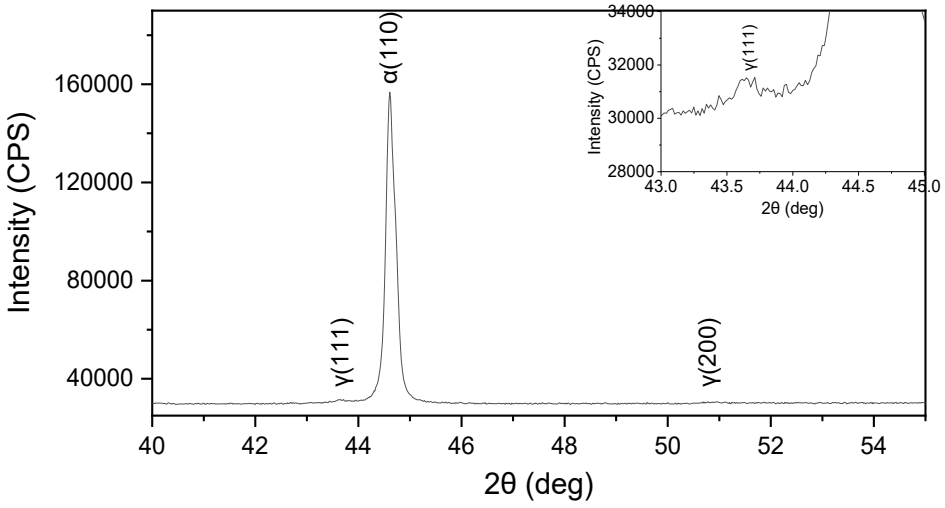

Figure 8-2. XRD pattern of S13Cr MSS.

The microstructure of S13Cr MSS-110 ksi obtained by EBSD are shown in Figure 8-3, green lines show grain boundary between 15° and 45° which coincides with most of the original austenite grain boundaries. The martensite structure is a lath martensite structure with no significant reversed austenite and inclusion inside.

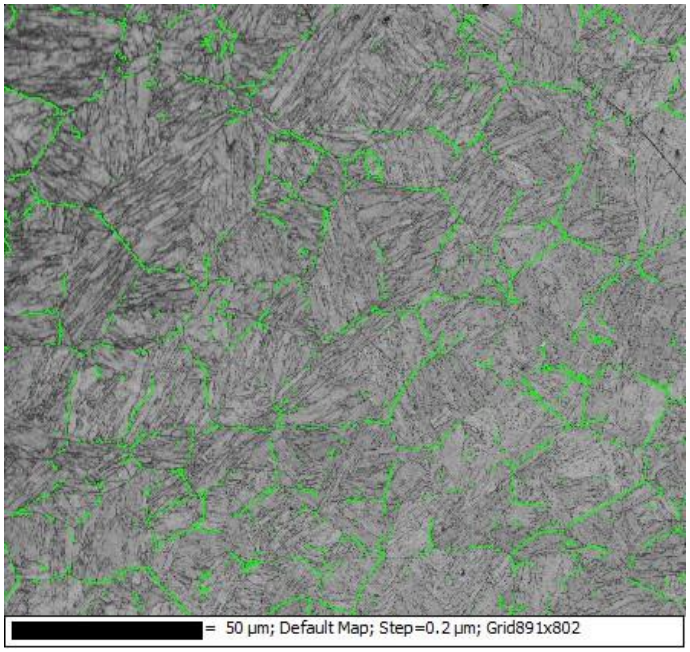

Figure 8-3. Microstructure of S13Cr MSS after heat treatment with green lines show grain boundary between 15° and 45°.

In order to further understand the organization and structure of the S13Cr MSS, EBSD was used for orientation and phase analysis.

Crystallographic orientation results obtained by EBSD as Figure 8-4 indicated that the material has no obvious preferred orientation.

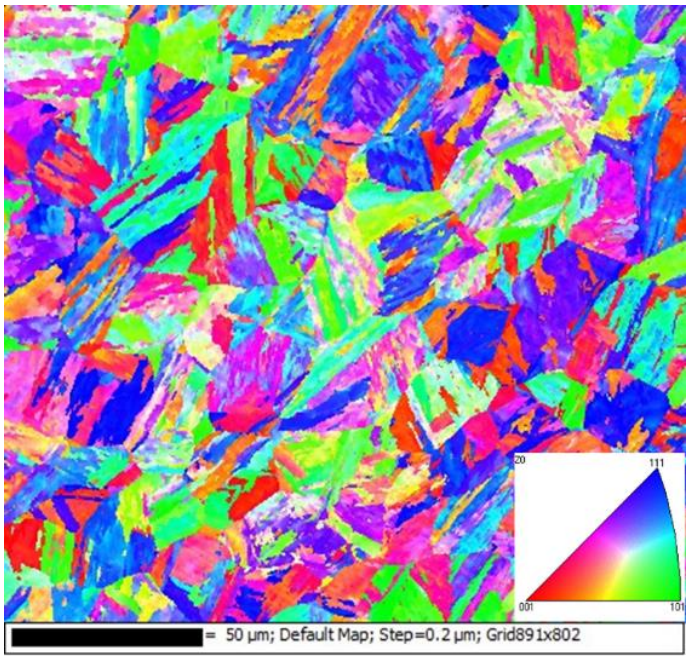

Figure 8-4. The crystallographic orientation of S13Cr MSS after heat treatment.

To further understand the distribution of austenite in S13Cr MSS, SEM was used to investigate the etched sample. As shown in Figure 8-5, reversed austenite finely distributed along the martensitic slat boundaries and ex-austenitic grain boundaries.

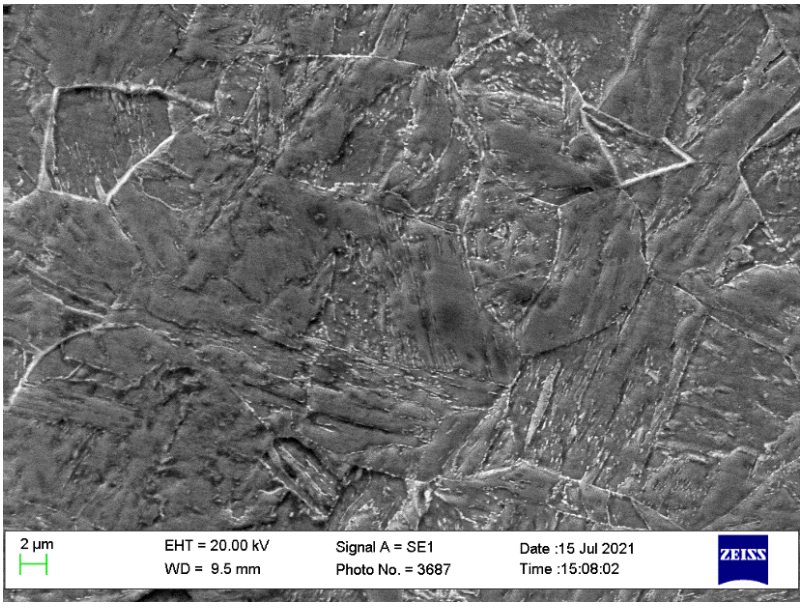

Figure 8-5. Crystallographic orientation (a) and phase distribution (b) of S13Cr MSS after heat treatment.

8.2.2. Heat treatment of S13Cr MSS

Phase diagram calculation was performed for S13Cr MSS based on the chemical composition of the main elements in used S13Cr MSS to provide data support for subsequent heat treatment from a thermodynamic perspective. The calculated phase diagram is shown is Figure 8-6. Based on the phase diagram, the temperature range for austenite formation is notably wide. To achieve a substantial content of reversed austenite, tempering temperatures above 600°C were selected.

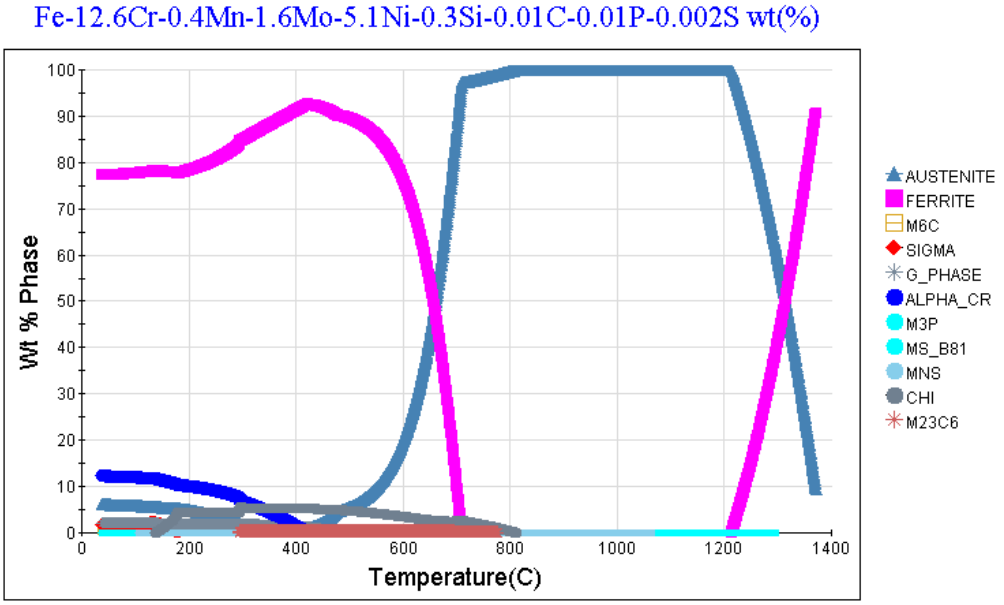

Figure 8-6. Phase diagram of S13Cr MSS used in this study.

Typically, the microstructure of quenched martensitic stainless steel consists of supersaturated lath martensite, sometimes containing a small amount of retained austenite. This martensite is supersaturated with carbon and alloying elements, exhibits high internal stress, and remains in a metastable state. When the quenched martensite is heated to the tempering temperature, austenite-stabilizing elements (e.g., Ni, Mn, N) diffuse and enrich at specific locations such as lath boundaries and prior austenite grain boundaries. Simultaneously, carbon diffuses from the martensite matrix toward these regions. Once the local chemical composition and crystal structure meet the thermodynamic conditions (i.e., the tempering temperature is above the Ms point), martensite (BCC) transforms in-situ into austenite (FCC) through a combined shear

and diffusion mechanism, forming reverted austenite [92, 100, 101, 104].

Upon subsequent cooling to room temperature, when the temperature drops below the Ms point, a portion of it may transform back into martensite. The extent of this transformation depends on the chemical stability of the reverted austenite (higher content of austenite-stabilizing elements enhances the reverted austenite stability) and the cooling rate. The more stable the austenite and the slower the cooling, the less reverted austenite transforms back into martensite. This transformation occurs via a shear-type transformation without element diffusion, during the transformation the chemical composition remains unchanged [92, 100, 101, 104].

The volume fraction of reverted austenite is typically controlled by adjusting the tempering temperature and holding time. The influence of tempering temperature on reverted austenite content follows a non-monotonic trend: it initially increases, reaches a maximum, and subsequently decreases with further temperature increase, indicating that higher temperatures do not necessarily produce higher austenite content. Meanwhile, extending the holding time promotes the austenite content approach toward thermodynamic equilibrium at tempering temperature. However, as indicated by the phase diagram, prolonged holding time also facilitates precipitation of carbides ($M_{23}C_6$). Therefore, the holding time should not be too long either to avoid excessive carbide formation [79, 99].

In order to increase the reversed austenite and obtain martensitic stainless steel with different austenite content, double tempering was applied.

The double tempering treatment is commonly employed to achieve a high volume fraction of reverted austenite. In this procedure, the first tempering step is conducted at a relatively high temperature to facilitate substantial formation of reverted austenite at tempering temperature. During subsequent cooling, part of the reversed austenite undergoes a shear transformation back to martensite while retaining its chemical composition. The second tempering step is then performed at a lower temperature, allowing the martensite formed during cooling of the first tempering process to revert again to austenite. Since the elemental diffusion required the formation of

reversed austenite has already completed during the first tempering process, the driving force required for reversed austenite formation is significantly reduced. Consequently, the reversion to austenite can be accomplished at a lower temperature. Moreover, the lower tempering temperature makes it easier for the reversed austenite to be preserved during the following cooling process. Thus, the double tempering treatment ultimately enables us to achieve a higher reversed austenite content compared to single tempering treatment.

In this study, two different heat treatment strategies were applied to obtain reversed austenite:

1. Variable first tempering temperature: The first tempering temperature was systematically varied while maintaining a fixed holding time;

2. Variable first tempering duration: The holding time of the first tempering was adjusted while maintaining a fixed tempering temperature.

In both strategies, the second tempering parameters were fixed at 620°C for 1 h to ensure consistent secondary phase transformation process. Prior to tempering treatments, the material was homogenized at 1020 °C for 30 min to establish a consistent initial grain structure.

Different heat treatments according to strategy 1 were carried out according to Table 8-1.

Table 8-1. Austenite contents of S13Cr MSSs with different first tempering temperatures

Sample No.	Solid solution -water quench	Tempering 1 -air cooling	Tempering 2 -air cooling	Austenite content vol.%
1	1020°C/30min	635°C/1h	620°C/1h	1.11%
2	1020°C/30min	650°C/1h	620°C/1h	6.93%
3	1020°C/30min	665°C/1h	620°C/1h	10.17%
4	1020°C/30min	680°C/1h	620°C/1h	10.13%

The XRD results for obtained samples are shown in Figure 8-7, calculated austenite contents according to the XRD results are provided in Table 8-1. As the first tempering temperature increase

from 635°C to 650°C, the austenite content shows a significant increase. But there was no significant change in austenite content with further increases in the first tempering temperature.

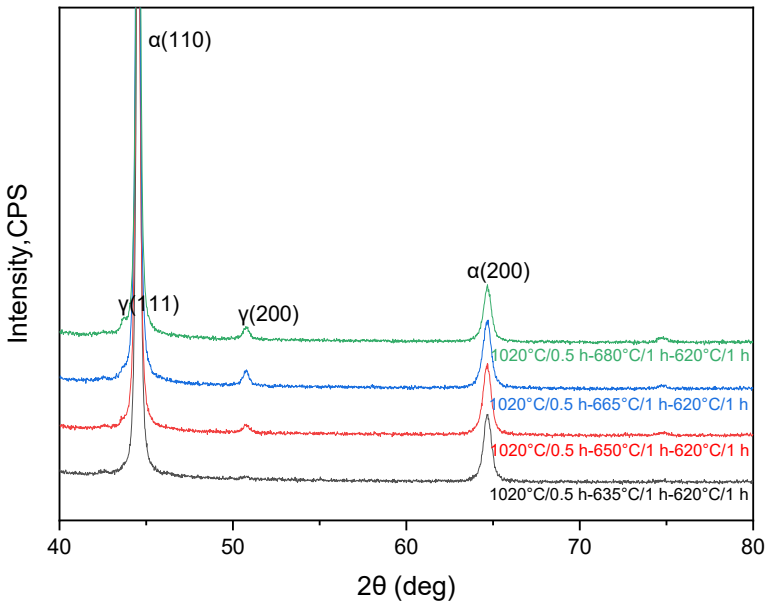

Figure 8-7. XRD patterns of the S13Cr MSS with different first tempering temperatures.

The maximum austenite content of 10.17% achieved thus far falls below the requirement for our subsequent corrosion tests. Therefore, we employed strategy 2 to obtain materials with different austenite contents suitable for the planned corrosion experiments. Different heat treatment steps according to strategy 2 were carried out as shown in Table 8-2. The XRD results are shown in Figure 8-8, calculated austenite contents according to the XRD results are provided in Table 8-2. As the first tempering temperature period increase from 0 h to 2 h, the austenite content shows a significant increase from 4.13% to 17.77%.

Table 8-2. Austenite contents of S13Cr MSSs with different first tempering holding times

Sample No.	Solid solution -water quench	Tempering 1 -air cooling	Tempering 2 -air cooling	Austenite content wt%
1	1020°C/30min	-	620°C/1h	4.13%
2	1020°C/30min	650°C/1h	620°C/1h	6.93%
3	1020°C/30min	650°C/2h	620°C/1h	17.77%

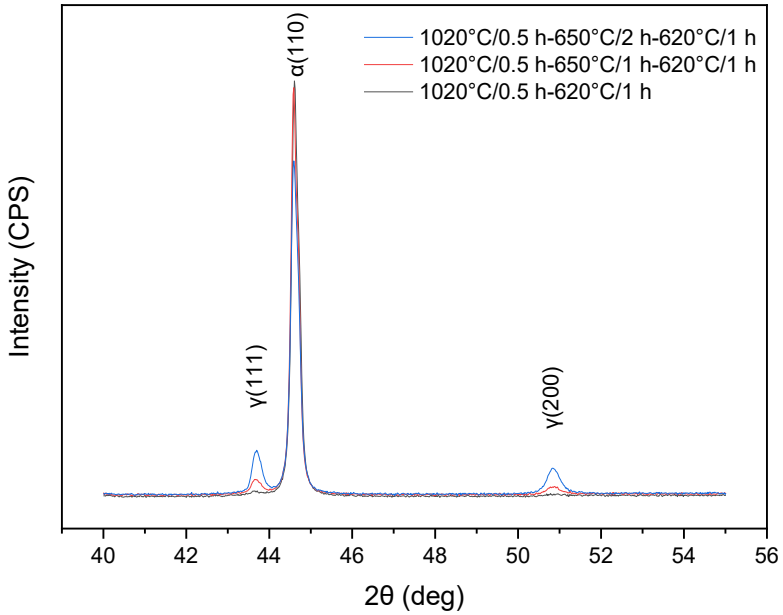

Figure 8-8. XRD patterns of the S13Cr MSS with different first tempering periods.

Consequently, four materials specified in Table 8-3 were selected for subsequent corrosion test to investigate the influence of austenite content on the corrosion behaviour of S13Cr MSS in arduous CO_2-containing environment.

Table 8-3. Austenite contents of S13Cr MSSs used in the following study

Sample No.	Solid solution -water quench	Tempering 1 -air cooling	Tempering 2 -air cooling	Austenite content wt%
M	1020°C/30min	-	-	0%
A1	1020°C/30min	-	620°C/1h	4.13%
A2	1020°C/30min	650°C/1h	620°C/1h	6.93%
A3	1020°C/30min	650°C/2h	620°C/1h	17.77%

8.3. Corrosion behaviour of S13Cr MSSs with different austenite contents at 200°C

8.3.1. Corrosion behaviour of S13Cr MSS with 0% austenite content (S13Cr MSS-M) at 200°C

Figure 8-9 provides the typical top-view and cross-section images of S13Cr MSS-M exposed to CO_2-saturated formation brine at 200°C with CO_2 partial pressure of 5.2 MPa at different immersion times.

After 5 h of corrosion, as shown in Figure 8-9(a) and (b), densely distributed speckled corrosion traces appeared on the specimen surface, primarily distributed along polishing marks introduced during sample preparation. Cross-sectional analysis revealed no significant corrosion product film at this stage.

When the exposure time increased to 20 h (Figure 8-9(c) and (d)), large speckled corrosion areas became visible. Higher magnification images show crack, which is believed to result from dehydration of corrosion product, distributed outside the speckled zones, indicating that even seemingly uncorroded area was covered by a thin corrosion product film, suggesting a complete surface coverage of the corrosion product film had been achieved. The corresponding cross-section image (Figure 8-9(d)) reveals an extremely thin (< 0.5 μm) continuous corrosion product film. Additionally, several approximately semicircular corrosion pits with

depths up to 2 μm were observed, corresponding to the speckled regions in the surface morphology. This indicates significant pitting corrosion at this stage, with a relatively high pit density observed across the surface.

EDS line scan analysis across the pitting regions (as shown in Figure 8-10) shows that, compared to the surrounding areas, the pits contain lower Fe content and higher concentrations of O, Cr, Ni, and Mo. Simultaneously, Cl enrichment was detected within these pitted regions.

After 48 hours, a uniform corrosion product film had formed on the specimen surface, with the original polishing marks remaining visible. This observation, consistent with our previous findings, indicates inward growth of the corrosion products toward the substrate. With prolonged exposure, the corrosion product film continued to thicken, while its composition remained stable: mainly contain Cr and O, and also contains minor amounts of Fe, Ni, and Mo. This chemical component is consistent with the corrosion product formed on S13Cr MSS-A1 under same test conditions as described in the previous chapter.

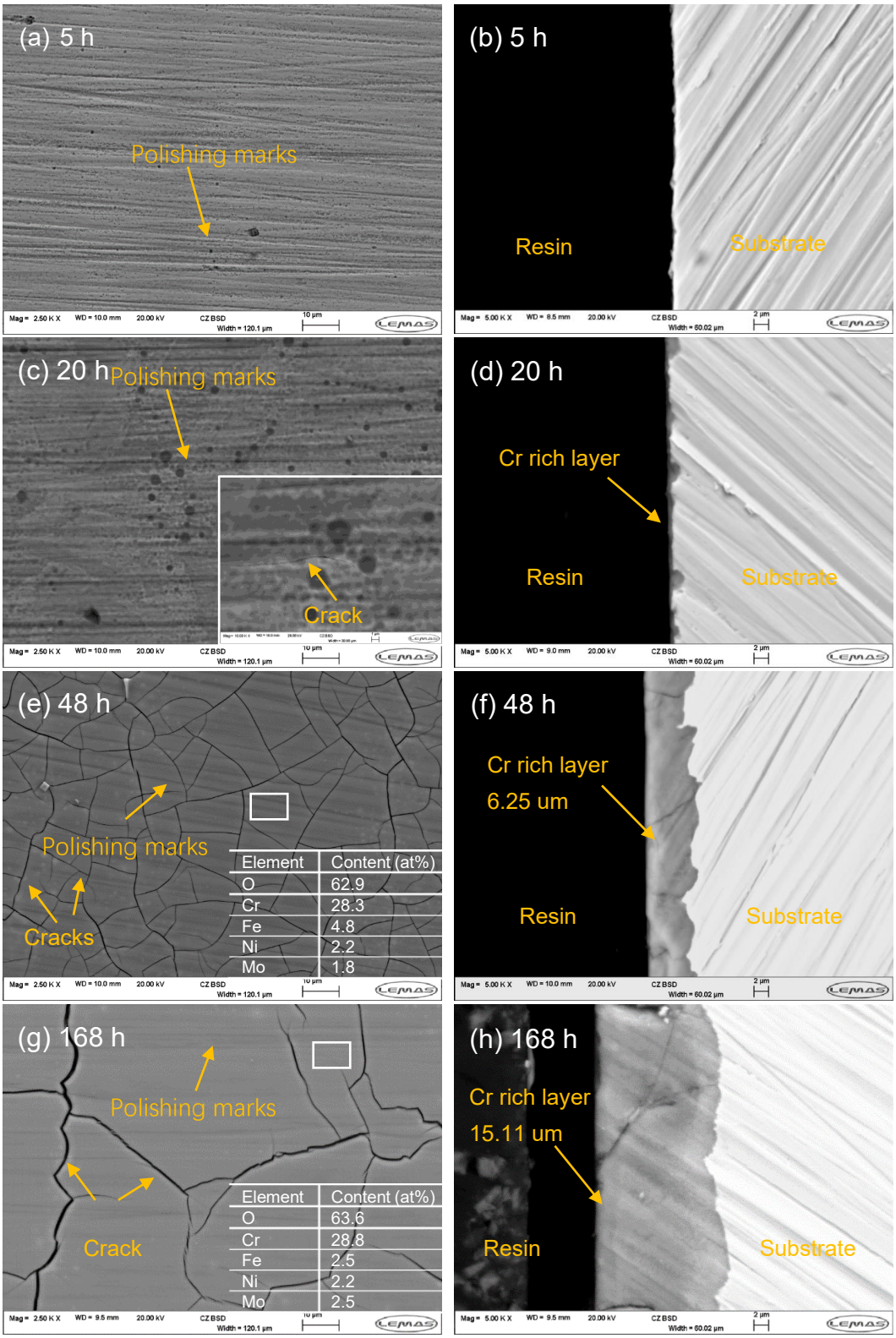

Figure 8-9. Surface and cross-sectional morphologies of corrosion product film on S13Cr MSS-M under 200°C and 5.2 MPa CO_2 for (a)(b) 5, (c)(d) 20, (e)(f) 48 and (g)(h) 168 hours.

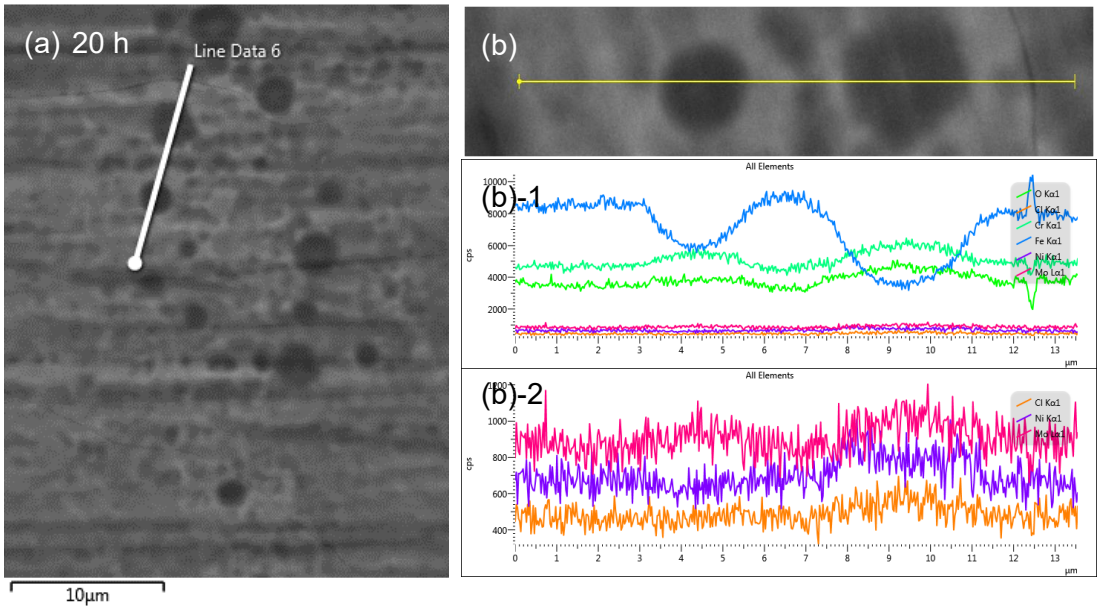

Figure 8-10. (a) SEM image of selected area used for EDS line scanning obtained from S13Cr MSS-M exposure to formation brine under 200°C and 5.2 MPa CO_2 for 20 hours and (b) EDS line scanning results of the selected position.

The corrosion process observed here is similar to corrosion behaviour of S13Cr MSS-A1 described in previous chapters. Both materials follow a same process: initial degradation of the native passive film, followed by selective corrosion in localized areas, and eventual form a fully covered corrosion product film.

However, a distinct difference occurred during the localized corrosion stage. S13Cr MSS-A1 exhibited irregular corrosion morphology, while S13Cr MSS-M demonstrated regular circular pitting morphology.

8.3.2. Corrosion behaviour of S13Cr MSS with 4.1% austenite content (S13Cr MSS-A1) at 200°C

Figure 8-11 provides the typical top-view and cross-section images of S13Cr MSS-A1 exposed to CO_2-saturated formation brine at 200°C with CO_2 partial pressure of 5.2 MPa at different immersion times. As previously described, S13Cr-MSS-A1 and S13Cr-MSS-M exhibit distinct corrosion morphologies during the non-uniform corrosion stage. S13Cr-MSS-A1 exhibited irregular corrosion morphology, while S13Cr MSS-M demonstrated regular circular

pitting morphology. Meantime, after 5 hours of exposure, the cross-sectional analysis reveals detectable corrosion products on S13Cr-MSS-A1 as shown in Figure 8-11(b), but none on S13Cr-MSS-M. This indicates faster initial degradation of the native passive film on S13Cr-MSS-A1, leading to more severe corrosion during the early stage of corrosion. This accelerated initial corrosion on S13Cr-MSS-A1 is likely attributable to its austenite. The presence of austenite phase can disrupt the homogeneity of the passive film, creating local hot points where the native passive film is more susceptible to breakdown, leading to preferential dissolution at these locations.

Furthermore, in later stage of corrosion, the corrosion product film formed on S13Cr-MSS-A1 is thicker than that on S13Cr-MSS-M at equivalent exposure times. This suggests a persistently higher corrosion rate throughout the exposure for S13Cr-MSS-A1 than S13Cr-MSS-M, implying that the introduction of small amount of austenite accelerate the corrosion of S13Cr MSS across all corrosion stages under HTHP downhole environment.

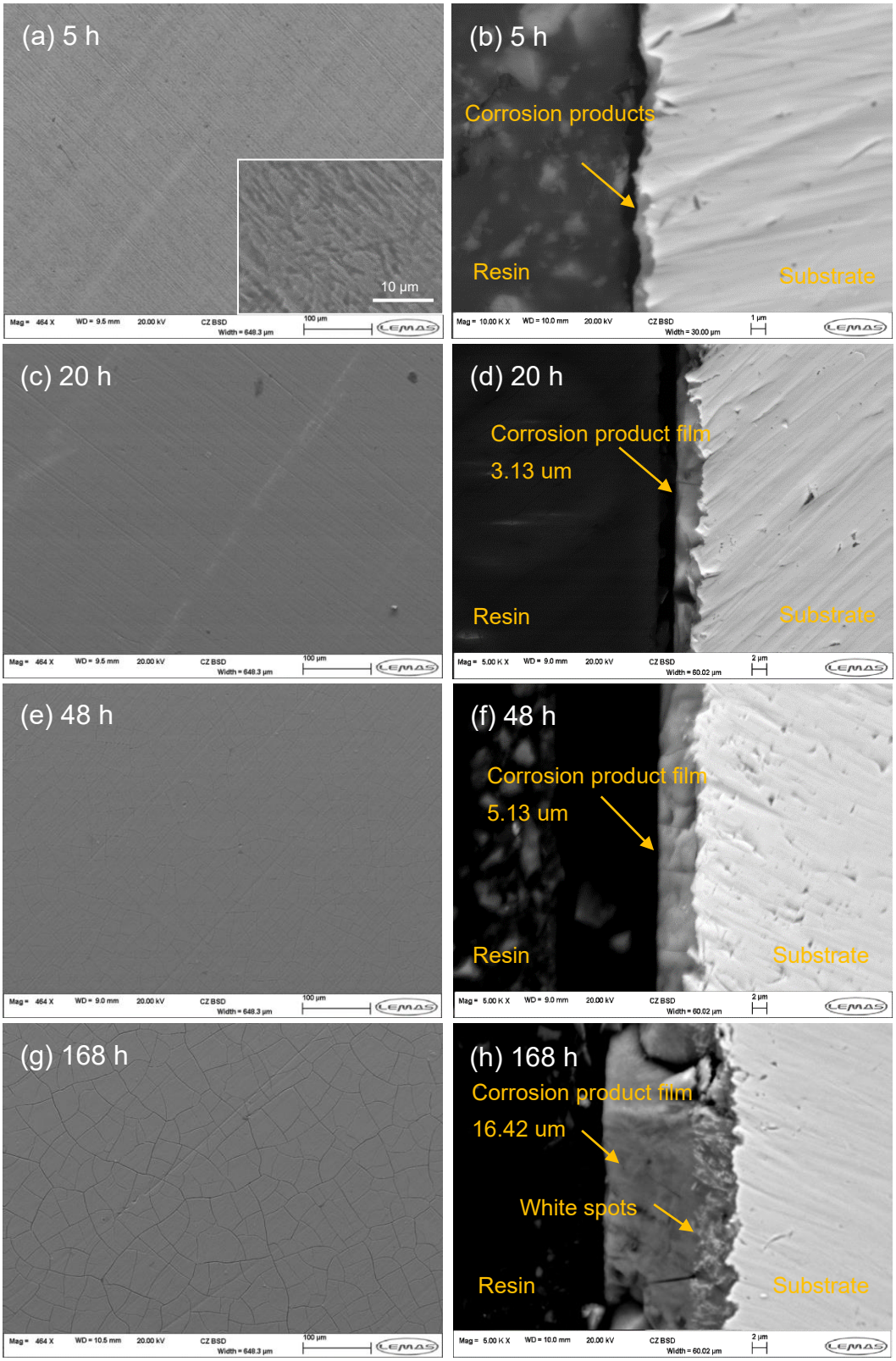

Figure 8-11. Surface and cross-sectional morphologies of corrosion product film on S13Cr MSS-A1 under 200°C and 5.2 MPa CO_2 for (a)(b) 5, (c)(d) 20, (e)(f) 48 and (g)(h) 168 hours.

8.3.3. Corrosion behaviour of S13Cr MSS with 6.9% austenite content (S13Cr MSS-A2) at 200°C

The typical top-view and cross-section images of S13Cr MSS-A2 exposed to CO_2-saturated formation brine at 200°C with CO_2 partial pressure of 5.2 MPa at different immersion times are shown in Figure 8-12.

With the austenite content increased to 6.9%, more pronounced localized corrosion was observed on the specimen surface after 5 h of exposure and uncorroded austenite particles were clearly visible, as shown in Figure 8-12(a). Notably, the preferentially corroded darker regions are predominantly distributed around these uncorroded austenite particles. Within the martensite laths, lightly corroded matrix areas (corresponding to the large light regions in Figure 8-12(a)) were also evident. Cracks induced by dehydration of the corrosion products, indicated by yellow arrows, confirm the formation of a continuous corrosion product film on the specimen surface, which is further supported by the cross-sectional image as shown in Figure 8-12(b).

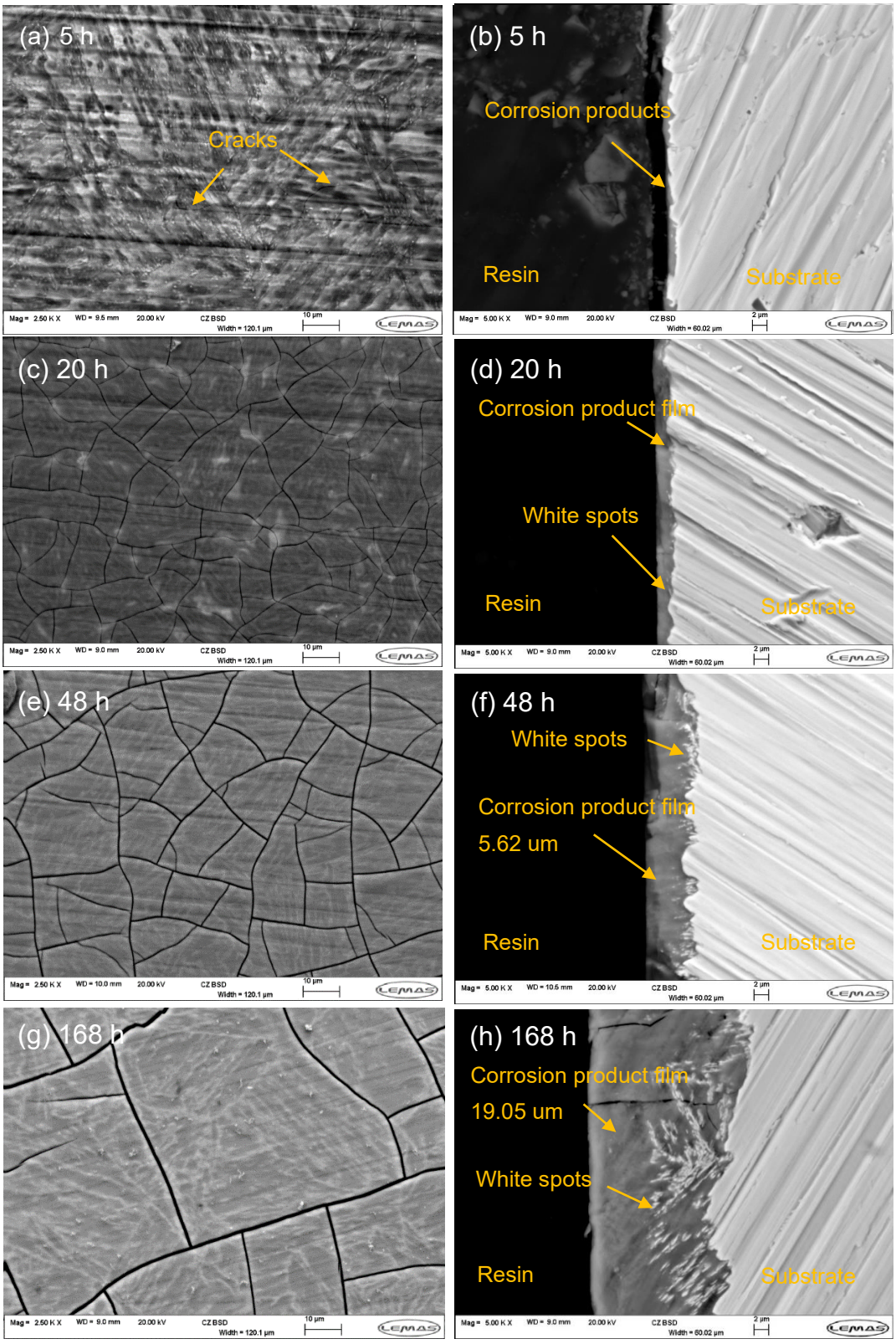

Figure 8-12. Surface and cross-sectional morphologies of corrosion product film on S13Cr MSS-A2 under 200°C and 5.2 MPa CO_2 for (a)(b) 5, (c)(d) 20, (e)(f) 48 and (g)(h) 168 hours.

As shown in Figure 8-13, EDS analysis of the S13Cr MSS-A2 specimen surface after 5 h of corrosion reveals that the light-toned regions exhibit higher Fe content and lower concentrations of O, Cr, and Mo compared to the darker zones. These results confirm that preferential corrosion occurred in the dark regions, leading to the observed higher oxygen content. Meantime, the preferential dissolution of Fe during corrosion process resulted in lower Fe content detected in the dark regions.

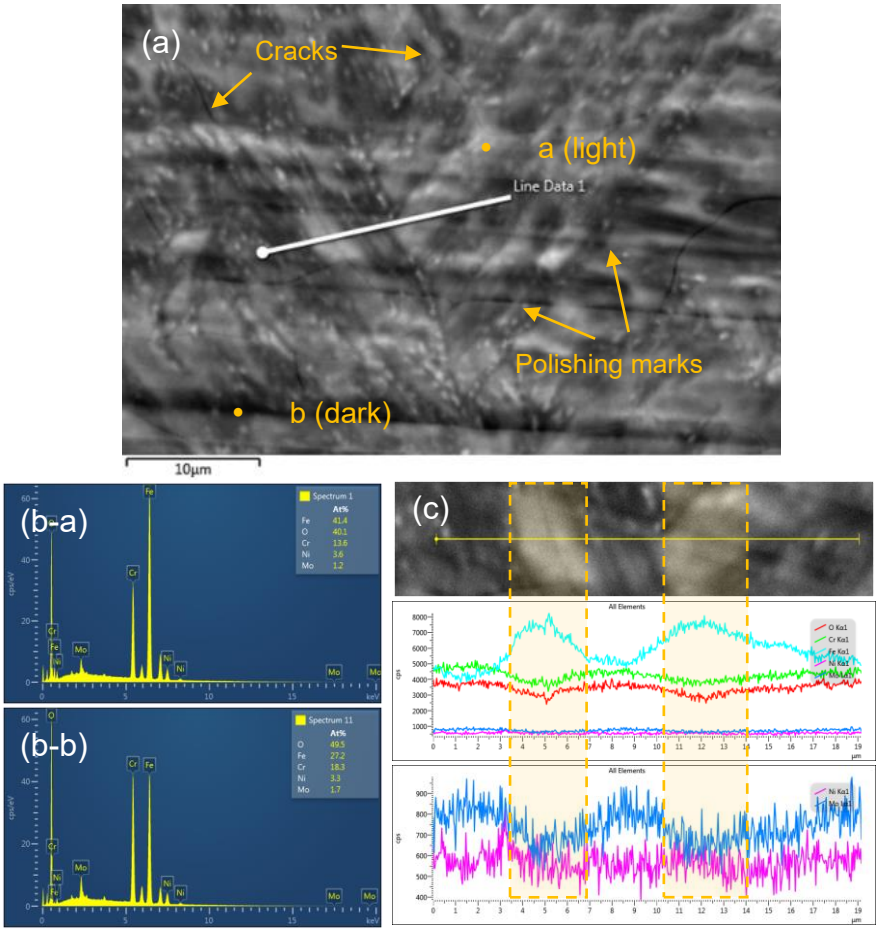

Figure 8-13. (a) Surface morphology, (b) EDS point identify and (c) EDS line scanning results of corrosion product film on S13Cr MSS-A2 under 200°C and 5.2 MPa CO_2 for 5 hours.

During the subsequent corrosion period from 20 to 168 hours (Figure 8-12(c)-(h)), a corrosion product film with measurable thickness developed on the specimen surface, with film thickness increasing progressively with immersion time. Notably, as the austenite content rose from 4.1% to 6.9%, the corrosion product film thickness increased correspondingly across all corrosion periods,

indicating increased corrosion rate in S13Cr MSS with higher austenite content. Throughout this period, uncorroded austenite particles were consistently observed within the inner layer of the corrosion product film.

A distinct light pattern became apparent on the film surface (as shown in Figure 8-12(c), (e), (g)), though cross-sectional analysis did not reveal corresponding uncorroded metal particles in the near-surface region of the corrosion product film. The distribution of this light pattern coincided with that of the reversed austenite, suggesting its formation is related to the corrosion behaviour of reversed austenite. EDS analysis (Figure 8-14) revealed no substantial compositional differences between light and dark regions via point analysis, both regions exhibited high oxygen content exceeding 60%, indicating complete oxidation of metallic elements. However, line scanning revealed subtle compositional variations between those two regions: the light region showed higher Fe, Mo, and Ni content alongside lower O and Cr concentrations compared to the dark regions. These compositional differences are likely to be inherited from the compositional variations between the martensitic matrix and reversed austenite particles, resulting in a surface pattern after corrosion which mirrors the reversed austenite distribution.

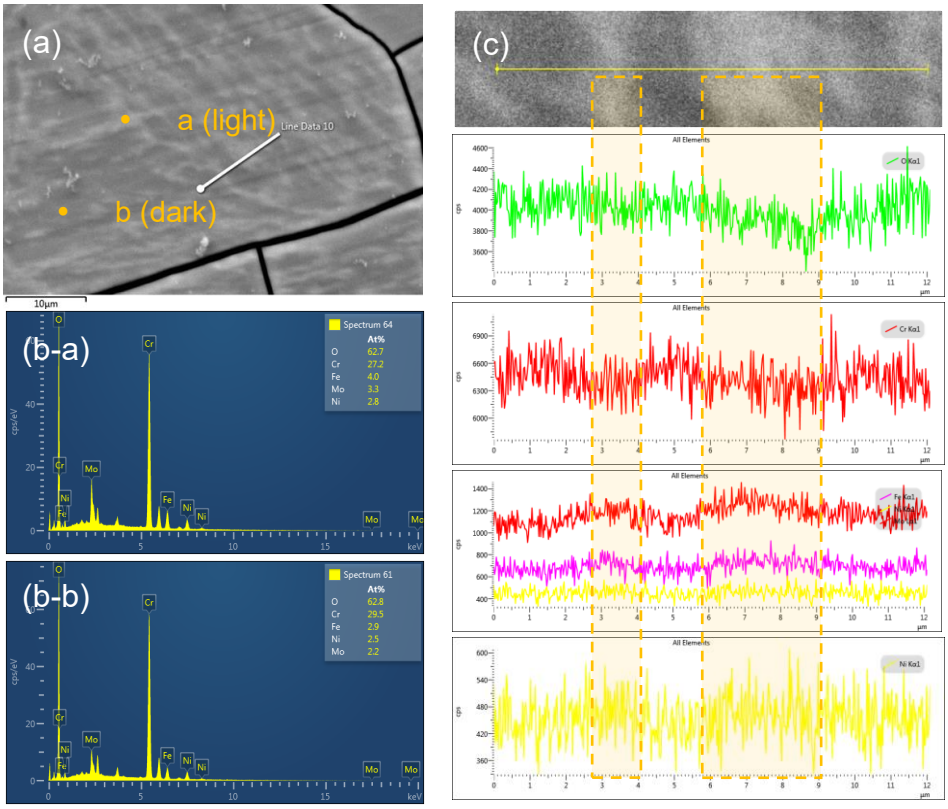

Figure 8-14. (a) Surface morphology, (b) EDS point identify and (c) EDS line scanning results of corrosion product film on S13Cr MSS-A2 under 200°C and 5.2 MPa CO_2 for 168 hours.

8.3.4. Corrosion behaviour of S13Cr MSS with 17.8% austenite content (S13Cr MSS-A3) at 200°C

As the austenite content was further increased to 17.8%, the surface morphology after different corrosion periods is shown in Figure 8-15. The corrosion behaviour of S13Cr MSS-A3 is similar to that of S13Cr MSS-A2 as described before. S13Cr MSS-A3 suffered significant non-uniform corrosion during 5 h of corrosion, which is further confirmed by EDS line scanning results in Figure 8-16. Cross-sectional image reveals uncorroded austenite particles maintained within the corrosion products at this early corrosion stage.

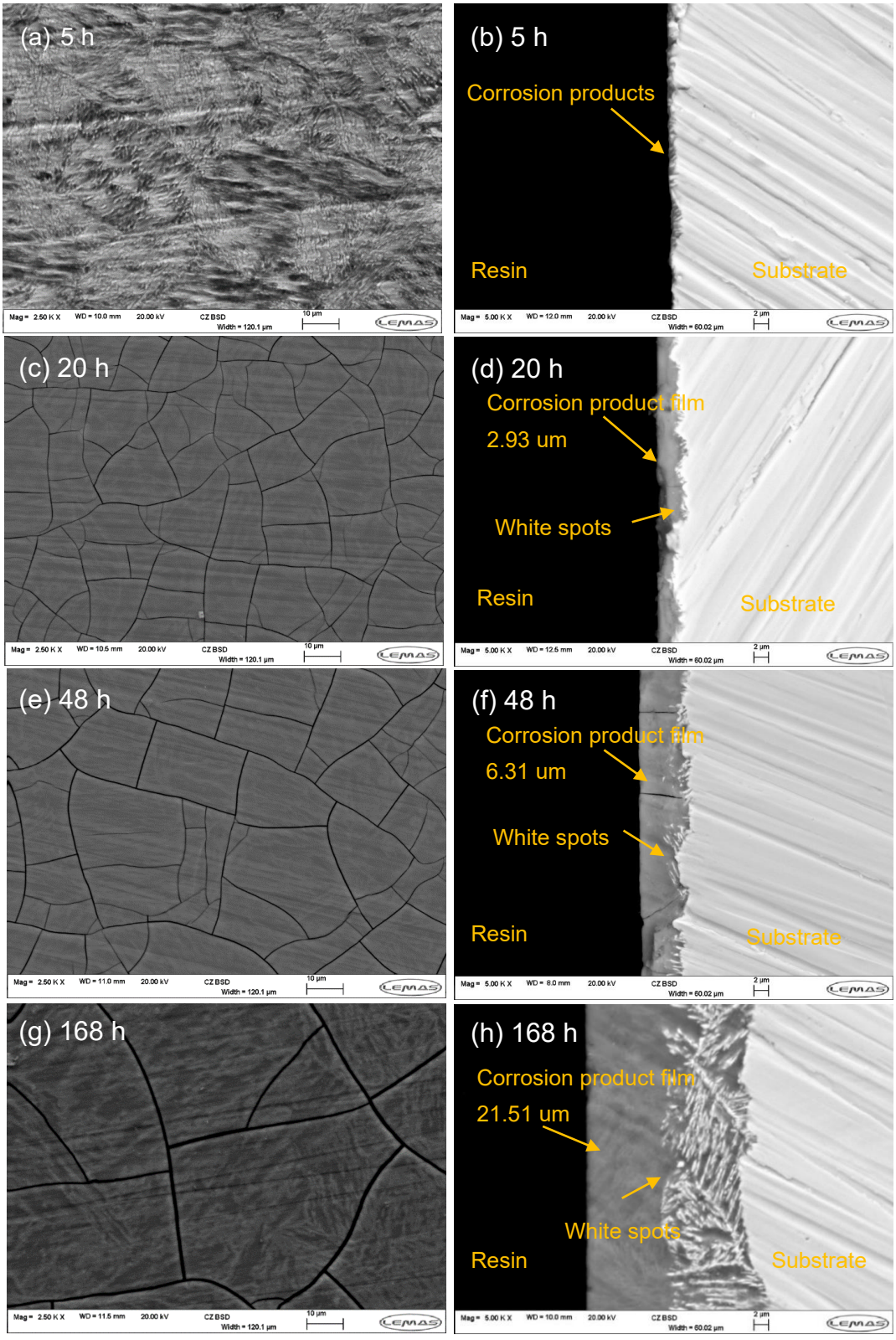

Figure 8-15. Surface and cross-sectional morphologies of corrosion product film on S13Cr MSS-A3 under 200°C and 5.2 MPa CO_2 for (a)(b) 5, (c)(d) 20, (e)(f) 48 and (g)(h) 168 hours.

As corrosion progresses, the corrosion product film thickens gradually, with uncorroded austenite particles consistently present in the inner layer. Notably, the corrosion product film is thicker than that formed on S13Cr MSS-A2 after equivalent exposure durations, indicating that even at 17.8% austenite content, the austenite phase fails to form an effective barrier against corrosion progression. On the contrary, the increased austenite content appears to accelerate corrosion of the martensitic matrix.

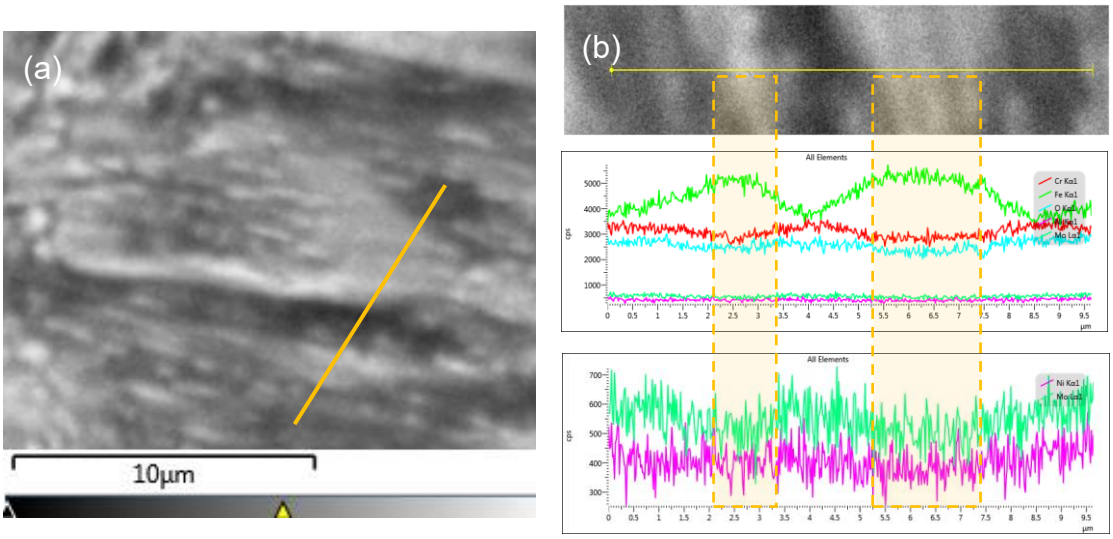

Figure 8-16. (a) Surface morphology, (b) EDS line scanning results of corrosion product film on S13Cr MSS-A3 under 200°C and 5.2 MPa CO_2 for 5 hours.

As shown in Figure 8-15(g), a light pattern consistent with the reversed austenite distribution was also observed on the corrosion product film surface. Both cross-sectional analysis (Figure 8-15(h)) and corresponding EDS results (Figure 8-17) confirm that this pattern does not involve uncorroded metal particles. It is therefore suggested that the pattern likely results from compositional differences between the martensitic matrix and reversed austenite particles, which become visually manifested after corrosion, reproducing the original reversed austenite distribution.

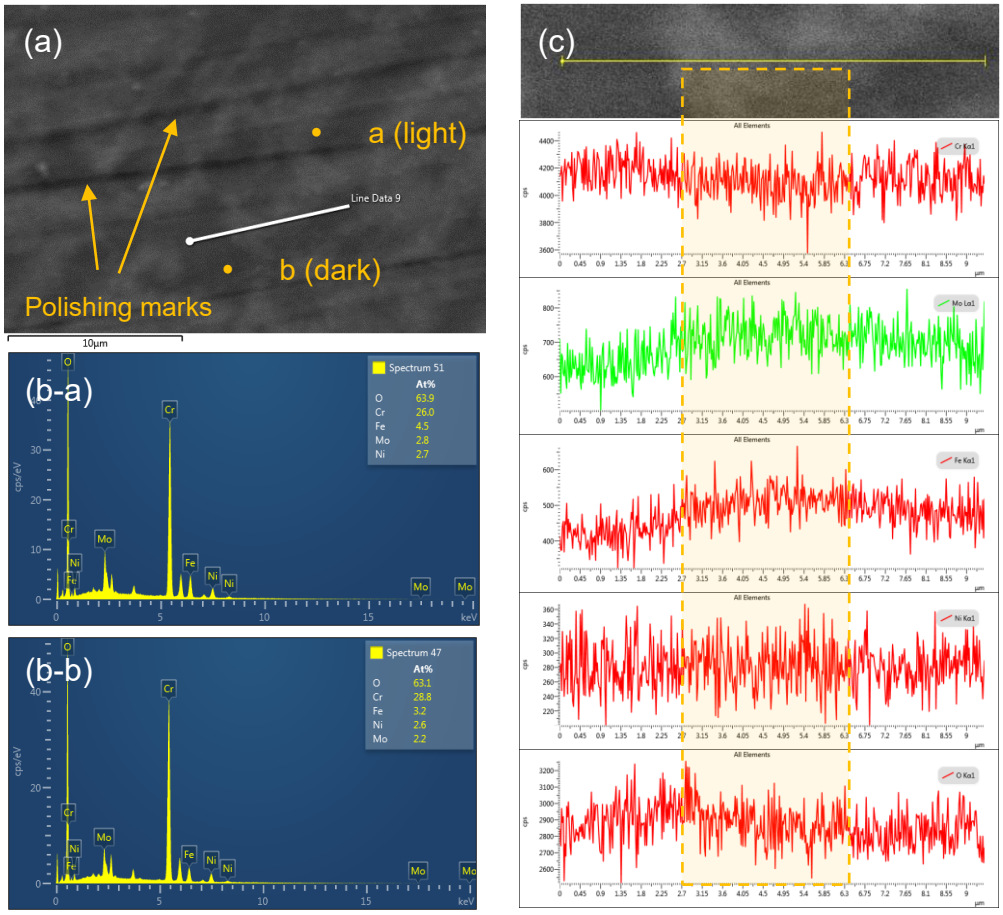

Figure 8-17. (a) Surface morphology, (b) EDS point identify and (c) EDS line scanning results of corrosion product scale on S13Cr MSS-A3 under 200°C and 5.2 MPa CO_2 for 168 hours.

8.3.5. Comparisons of corrosion behaviour of S13Cr MSS with various austenite contents at 200°C

To investigate whether variations in austenite content influence the types of corrosion products formed, the corrosion product films on S13Cr MSS with different austenite levels after 168 h of exposure in HTHP downhole environment were analysed. XRD results (Figure 8-18) showed no distinct crystalline peaks related to corrosion products, but exhibited broad hump peaks near 35° and 63°, indicating the amorphous nature of the corrosion products. Therefore, Raman spectroscopy was employed for further phase identification.

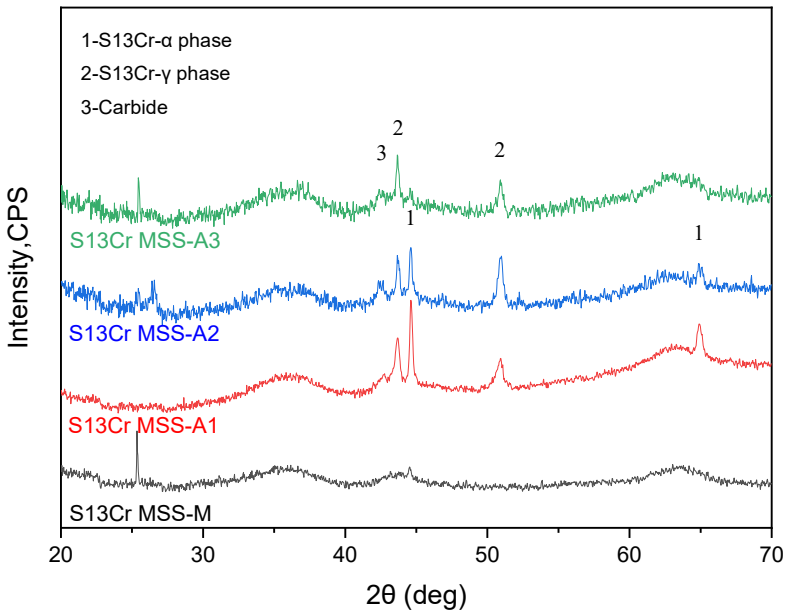

Figure 8-18. XRD patterns of S13Cr MSS specimens with various austenite contents exposed at 200°C and 5.2 MPa CO_2 for 168 h.

As shown in Figure 8-19, the Raman spectra of corrosion products formed on S13Cr MSS with varying austenite contents displayed consistent characteristic peaks at 717 cm-^{1} and 556 cm^{-1}, indicating that the corrosion products are composed mainly of $Cr(OH)_3$ and Cr_2O_3, regardless of austenite content. This suggests that changes in austenite content do not thermodynamically alter the composition of the corrosion products.

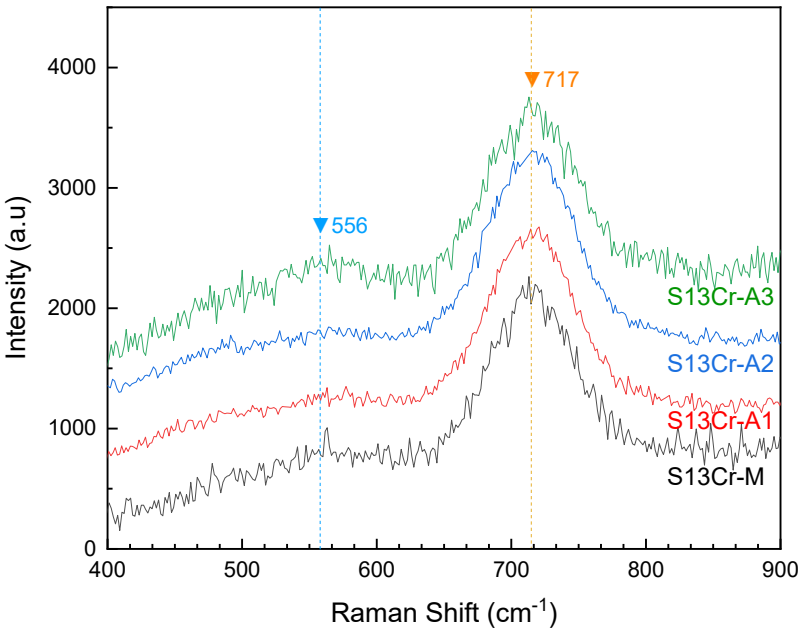

Figure 8-19. Raman spectra of S13Cr MSS specimens with various austenite contents exposed at 200°C and 5.2 MPa CO_2 for 168 h.

The general corrosion rates of S13Cr MSS with different austenite contents are compared in Figure 8-20. The introduction of austenite into S13Cr MSS led to an increase in general corrosion rate. Then the general corrosion rate continued to rise with following increase in austenite content. Increasing the austenite content from 0% to 17.8% resulted in a 35% increase in the general corrosion rate of the S13Cr MSS. This implies that, from a corrosion perspective, excessive austenite is not advisable for S13Cr MSS used under HTHP downhole environments.

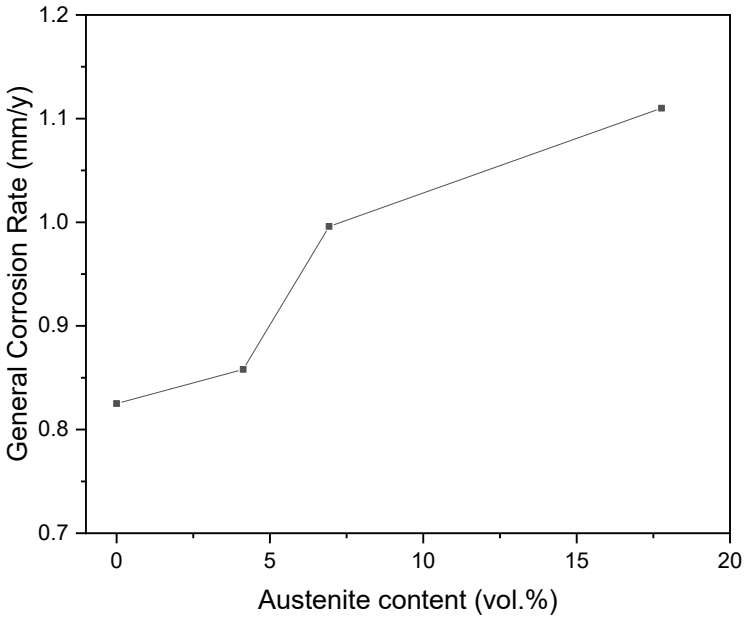

Figure 8-20. General corrosion rates of S13Cr MSS specimens with various austenite contents exposed at 200°C and 5.2 MPa CO_2 for 168 h.

8.4. Conclusion

1. The austenite content in S13Cr MSS can be adjusted by different tempering treatments. Double tempering treatment can greatly in the reversed austenite content of the material. The reversed austenite content can reach 17.77% by double tempering treatment at 650°C for 2 h and then at 620°C for 1 h.
2. Austenite plays a critical role in the initial non-uniform corrosion stage. Increased austenite content accelerates the degradation of the native passive film and promotes severe localized attack during early exposure. The regions surrounding reversed austenite particles are particularly susceptible to preferential corrosion.
3. A substantial increase in general corrosion rate was observed with increase austenite content in S13Cr MSS. Specifically, increasing the austenite content from 0% to 17.8% resulted in a 35% increase in general corrosion rate, demonstrating that even 17.8% austenite fails to form an effective barrier against corrosion progression.

4. Variations in austenite content did not significantly change the composition and structure of the corrosion products.

9. Chapter 9 Overall discussion

9.1. Introduction

The preceding chapters (Chapters 5-8) systematically elucidated the corrosion evolution behaviour of S13Cr MSS under HTHP downhole environments. The experimental results primarily identified the dominant failure mode under this extreme condition, confirming general corrosion as the principal characteristic. Building on this foundation, the influence of environmental factors was investigated. CO_2 partial pressure was shown to significantly affect both scaling behaviour and localized attack. By reducing temperature to decelerate reaction kinetics, the initial corrosion stage was examined in greater detail, providing deeper insight into early-stage corrosion mechanism. Finally, based on the observed corrosion behaviour, a strategy for modulating corrosion rate by adjusting reversed austenite content was proposed and experimentally validated. This involved producing S13Cr MSS with varying reversed austenite contents through different heat treatments, followed by corrosion testing to evaluate its impact.

This chapter provides a theoretical synthesis and comprehensive analysis of these findings, offering a detailed interpretation of the specific corrosion behaviour observed. The discussion is structured into the following six sections:

1. Identification and comparison of failure modes: Establishing the primary failure risks under HTHP downhole environments based on immersion tests and SSRT, and differentiating these from failure modes reported in conventional environments.
2. Establishment of the corrosion evolution model: Proposing a "native passive film degradation → non-uniform corrosion → uniform film formation" three-stage evolution model for S13Cr MSS based on corrosion product analysis and in-situ electrochemical measurements.
3. Effect of temperature on corrosion of S13Cr MSS: Verifying the universality of the proposed corrosion mechanism within the 160-200°C range and analysing the kinetic variations induced by temperature changes.

4. Effect of CO_2 partial pressure on corrosion of S13Cr MSS: Discussing the impact of CO_2 partial pressure on scaling tendencies and corrosion thermodynamics.
5. Effect of microstructure on corrosion of S13Cr MSS: Discussing the specific role of reversed austenite throughout the corrosion evolution process.
6. Implications for engineering applications: Proposing optimizations for laboratory assessment strategies and predicting safety windows for field service based on experimental observations.

9.2. Failure Mode of S13Cr MSS under HTHP downhole environment

In the HTHP formation water environment (200°C, 5.2 MPa CO_2), the general corrosion rate of S13Cr MSS reached 1.04 mm/y after 7 days of immersion, while the pitting rate was 0.37 mm/y. Potentiodynamic polarisation results confirmed that S13Cr MSS exhibits active dissolution in the steady state within this environment, signifying a complete loss of the passivity typical of stainless steels. Consequently, conventional evaluation criteria for stainless steels are inapplicable at this situation. Therefore, the corrosion rates of S13Cr MSS were qualitatively evaluated referencing the NACE standard RP0775-Qualitative Categorization of Carbon Steel Corrosion Rates for Oil Production Systems [156]. As outlined in Chapter 5, according to NACE standard SP0775, the general corrosion rate of S13Cr MSS is classified as severe level among the four categories (low, moderate, high and severe), while the pitting rate reaches the high level. Although both indicate high corrosion activity, the pitting rate was significantly lower than the general corrosion rate, indicating that uniform corrosion is the dominant morphology under HTHP downhole environment.

Furthermore, the SSRT test results show that the loss of ductility (based on ER and RAR) of S13Cr MSS in the HTHP CO_2-saturated formation brine without pre-corrosion was slightly less than 20% while the loss of ductility with pre-corrosion was slightly higher than 20%. Meanwhile S13Cr MSS did not fracture and no cracks were

observed after a 15 days FPB constant load test with an applied stress of 90% of the yield strength. In other words, despite demonstrating obvious SCC susceptibility in the accelerated fracture test, the S13Cr MSS remains capable of withstanding the constant load test without failure.

S13Cr MSS exhibits unsatisfactory general corrosion rate, localized corrosion rate, and SCC susceptibility in HTHP downhole environment. Among these, its general corrosion is classified as severe level, represents the most critical failure mode for this material during downhole service.

9.2.1. General corrosion behaviour of S13Cr MSS under HTHP downhole environment

Under the HTHP downhole environment, after rapidly undergoing the stages of passive film degradation and non-uniform corrosion, S13Cr MSS finally enters a steady-state general corrosion stage characterized by the formation of a fully-covered corrosion product film. Potentiodynamic polarisation results indicate that in the steady-state corrosion stage, S13Cr MSS was in an active dissolution state rather than a passive state. Although pseudo-passivation characteristics appear in the high-potential region, the extremely high passive current density confirms the corrosion product film failed to provide excellent corrosion resistance EIS fitting results further reveal that the corrosion kinetics at this stage are dominated by the charge transfer resistance (R_{ct}), indicating a charge transfer controlled process. The R_{ct} obtained under HTHP conditions was very low (< 300 $\Omega \cdot cm^2$), implying minimal resistance to corrosion and a consequently high corrosion rate. Under the HTHP downhole environment, the severe general corrosion exhibited by S13Cr MSS leads to a drastic reduction in the effective load-bearing cross-section of the downhole tubing, thereby severely limiting the service life of the tubing.

9.2.2. Localized corrosion behaviour of S13Cr MSS under HTHP downhole environment

The pitting morphology of S13Cr MSS obtained in HTHP formation brine can be charactered as typical elliptical shape pits. Generally,

the propagation of the localized corrosion in stainless steels at the passive state relies on the "large cathode with small anode" occluded cell structure.[168] However, S13Cr MSS exhibited active dissolution state under HTHP conditions, it’s relative low charge transfer resistance implies that the entire metal surface possesses high electrochemical activity. Since neither the interior nor the exterior of the elliptical pits is in a passive state, and their geometric characteristics offer less hindrance to the outward diffusion of intra-pit species, it is relatively more difficult to form or maintain the occluded cell.[169] Consequently, the propagation of the elliptical shape pits formed in HTHP formation water is slower compared to the narrow-deep, subsurface, or vertical shape pits commonly observed at the passive state.

Pitting perforation can lead to the loss of control over the wellbore pressure system and the leakage of completion fluid from the tubing-casing annulus into the tubing, thereby exacerbating the service environment of the tubing. It is noteworthy that as corrosion proceeds, as the pitting depth of S13Cr MSS increased, the radius/depth ratio decreased, the pits become steeper during development. This results in an increasing degree of stress concentration at the pit location as corrosion progress, leading to a degradation in both the static strength and fatigue strength of the tubing.

9.2.3. SCC behaviour of S13Cr MSS under HTHP downhole environment

Based on previous experimental observations, the failure of S13Cr MSS in HTHP formation brine experienced a "pitting-crack initiation-fracture" process. Cracks originate from the bottom of pits and exhibits typical quasi-cleavage characteristics during the initial propagation stage, followed by a rapid transition to ductile dimple rupture. The stress-strain curves indicate that the introduction of the corrosive environment did not significantly alter the elastic deformation stage and the work-hardening stage of S13Cr MSS, the ultimate tensile strength (UTS) did not show a significant decline either. However, the necking stage was significantly shortened. This suggests that the bulk properties of the

S13Cr MSS remain intact, but the stress concentration induced by pitting accelerates the necking process.

The initial quasi-cleavage features imply the presence of local embrittlement. This phenomenon can be generally attributed to either hydrogen embrittlement caused by a rapid cathodic hydrogen evolution reaction, or SCC induced by anodic dissolution under HTHP condition. The former hydrogen embrittlement mechanism could be attributed to the fast cathodic hydrogen evolution reaction at elevated temperature as the cathodic reaction on the metal surface is confirmed to be hydrogen evolution reaction by the Pourbaix diagram calculated in Section 9.4. Given that S13Cr MSS is in an active dissolution state without protection from a dense passive film, hydrogen atoms generated through the cathodic reaction can more easily permeate into the metal matrix, thereby inducing quasi-crack propagation. As for the latter anodic dissolution induced SCC mechanism, under the test condition of this study, the high local stress at pit sites leads to a high anodic dissolution rate [170], ultimately resulting in cleavage fracture via the slip-dissolution mechanism. In the present work, crack initiation is typically observed at pits. Under applied stress, due to stress concentration at pits, pits act as anode compare to the surrounding matrix and predominantly undergoes anodic dissolution rather than the cathodic reaction. Therefore, the quasi-cleavage fracture behaviour observed in the SSRT tests in this study is considered to be dominated by the anodic dissolution mechanism. A study conducted under a similar condition (180 °C, CO_2-saturated formation brine) by Qi et al. [151] also confirmed this through SSRT tests with applied cathodic and anodic polarization on 13Cr MSS, confirming that the SCC mechanism in a HTHP CO_2-saturated formation brine is dominated by the anodic process.

SSRT results obtained after 7 days of pre-corrosion indicate that the losses in ER and RAR for S13Cr MSS exceeded 20%. The fracture features observed in the SSRT after 7 days pre-corrosion were consistent with those of non-pre-corroded specimens, indicating that the fracture mechanism did not undergo a fundamental change due to pre-corrosion. The elastic deformation and work-hardening stages of the stress-strain curves showed no obvious changes after

pre-corrosion, but the UTS decreased by approximately 10 MPa. The primary impact of pre-corrosion was the significant advancement and shortening of the necking stage. This can be attributed to the steeper of the pit geometry as corrosion progressed which increased the degree of stress concentration at the pit sites, resulting in a significant decline in macroscopic ductility.

Our experimental results demonstrate that while the bulk mechanical properties (e.g., yield strength, ultimate tensile strength) of S13Cr MSS did not show obvious degradation under the HTHP downhole environment, the material's damage tolerance and plastic reserve had significantly deteriorated. Consequently, the impact resistance, dynamic load-bearing capacity, and fatigue life of the S13Cr MSS tubing during service may be significantly compromised.

9.3. Three-stage corrosion evolution mechanism of S13Cr MSS under HTHP downhole environments

In this subsection, based on the analysis of the composition and morphology of the corrosion product films on the corroded specimens described in the preceding chapters, combined with in-situ electrochemical monitoring (OCP, EIS, Potentiodynamic polarisation), typical corrosion process model for S13Cr MSS in the HTHP formation brine was established. The model divides the corrosion process into three consecutive but distinguishable stages, including: (I) Degradation of the native passive film; (II) Non-uniform corrosion; and (III) Uniform corrosion. The schematic diagram of this process is shown in Figure 9-1.

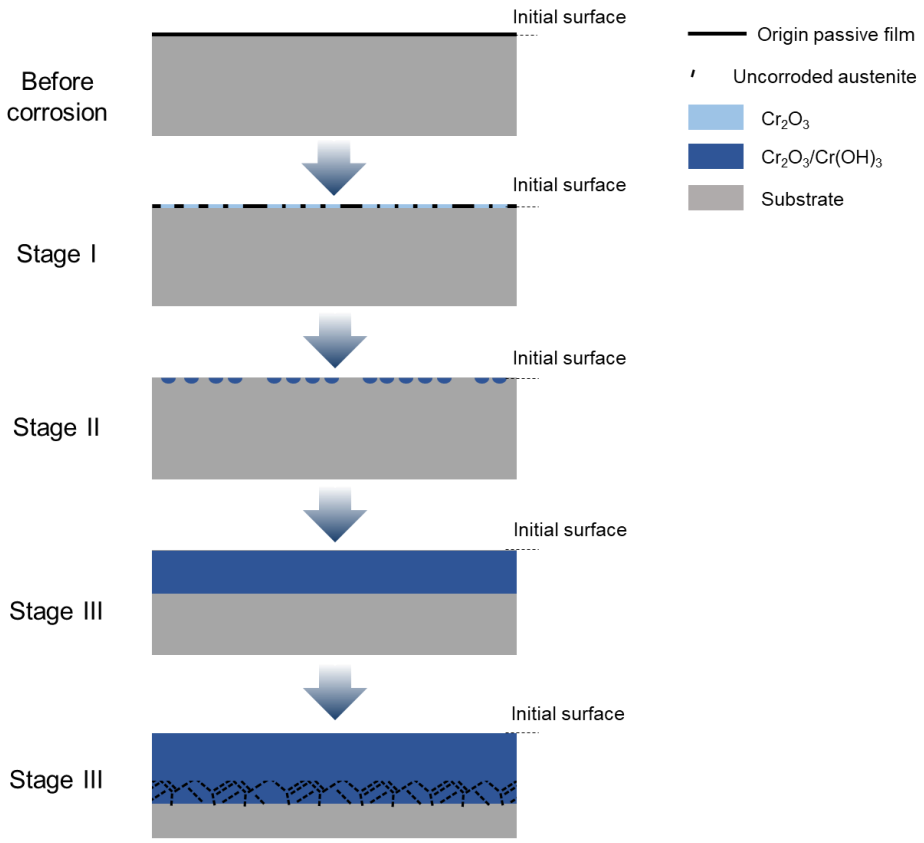

Figure 9-1. The schematic diagram for the typical corrosion process of S13Cr MSS under HTHP downhole environments.

In subsequent discussions, this model will be extended to analyse the effects of temperature, CO_2 partial pressure, and variations in reversed austenite content on the corrosion behaviour of S13Cr MSS in HTHP downhole environments.

9.3.1. Stage I: Degradation of native passive film

In the initial stage of corrosion, degradation of the native passive film occurs, which involves the thermodynamic instability and selective dissolution of iron oxides within the native film, as well as the growth of chromium oxide. During this stage, the surface morphological changes on the material surface are not significant, making it difficult to observe variations based on surface morphology alone; however, the electrochemical response in this stage exhibits distinct characteristics.

The OCP of S13Cr MSS drops rapidly during this stage. The potentiodynamic polarisation curve displays no active dissolution peak, transitioning directly into the passive region with the positive

shift of potential. This indicates that during this stage, the degrading native passive film still provides a relatively good protection. The Nyquist curves exhibit a high-frequency capacitive semi-circle, which is believed to be associated with the impedance of corrosion products, and a low-frequency finite diffusional tail. During this stage, the corrosion resistance mainly comes from Warburg resistance (W_s-R), and the corrosion process is controlled by diffusion process.

The composition of the native passive film formed on stainless steel in air at room temperature consists of Fe oxides, Cr oxides, and Fe-Cr oxides [171]. According to the calculated Pourbaix diagram for the HTHP downhole environment (as shown in Figure 9-2), Fe oxides are unstable in this environment, thus the Fe oxides in the native passive film tend to undergo dissolution after immersed in HTHP formation brine.

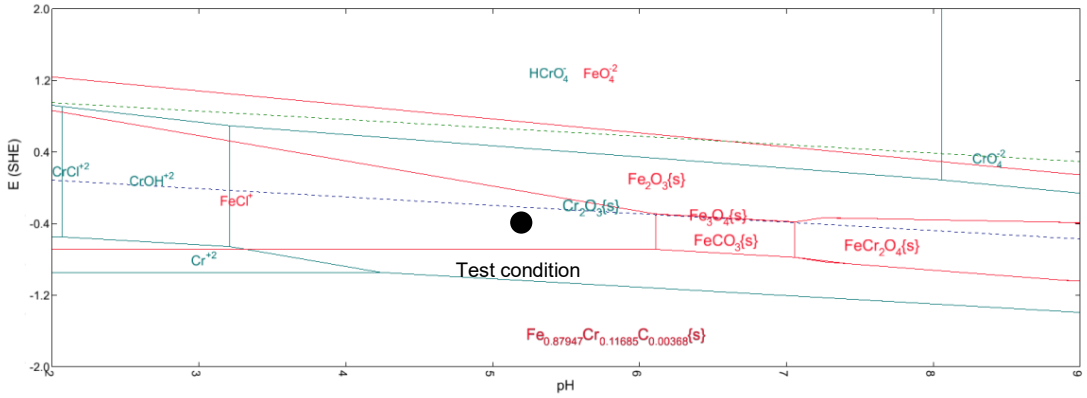

Figure 9-2. Pourbaix diagram for S13Cr MSS at 200°C and 5.2 MPa bar CO_2.

Concurrently, according to the Pourbaix diagram, Cr_2O_3 is thermodynamically stable in this environment. In the Raman spectra results for Stage I, it was observed that as the corrosion time increased, a Cr_2O_3 peak appeared in the Raman spectra and the intensity of the Cr_2O_3 peak increased slightly with the progression of corrosion during this stage. This suggests that the growth of corrosion product Cr_2O_3 occurred during this stage through the following anodic electrochemical reaction:

$$2Cr + 3H_2O \rightleftharpoons Cr_2O_3 + 6H^+ + 6e^- \quad (9\text{-}1)$$

In summary, Stage I, the degradation of the native passive film, is a process where the thermodynamic instability and selective dissolution of Fe oxides proceed synchronously with the growth of Cr oxide. During this process, the native passive film is still able to provide a certain degree of protection.

9.3.2. Stage II: Non-uniform corrosion

As the failure of the native passive film intensifies and it loses its original protective capability, corrosion process enters Stage II, where localized corrosion occurs on the specimen surface. This stage can be clearly identified from the significant localized corrosion morphology. During this stage, localized corrosion preferentially occurs at the martensite matrix surrounding the reversed austenite (this phenomenon is particularly significant in Chapter 8). This phenomenon is related to the micro-galvanic couple formed between the austenite and martensite. Numerous studies have shown that the reversed austenite and the martensite matrix in martensitic stainless steels possess different corrosion potentials [109, 112, 119, 132, 172]. Typically, reversed austenite has a more positive potential, acting as the cathode, while the martensite matrix has a more negative potential, acting as the anode, thus forming a corrosion micro-galvanic couple [132, 172]. Under these circumstances, the corrosion rate of the anodic part near the interface of two phases is the fastest [173], resulting in a macroscopically localized corrosion morphology around reversed austenite.

According to the Raman spectra results, the composition of the surface film transforms from Cr_2O_3 in Stage I to Cr_2O_3 and $Cr(OH)_3$ in Stage II. Based on the previously calculated Pourbaix diagram for solid (as shown in Figure 9-2) and the Pourbaix diagram for aqueous under HTHP downhole environment (as shown in Figure 9-3), Cr_2O_3 and $Cr(OH)_3$ are stable corrosion products at the test condition. $Cr(OH)_3$ can be deposited to form as the amorphous during a precipitation process in the aqueous phase [16]:

$$Cr^{3+} + 3H_2O \rightleftharpoons Cr(OH)_3 + 3H^+ \quad (9\text{-}2)$$

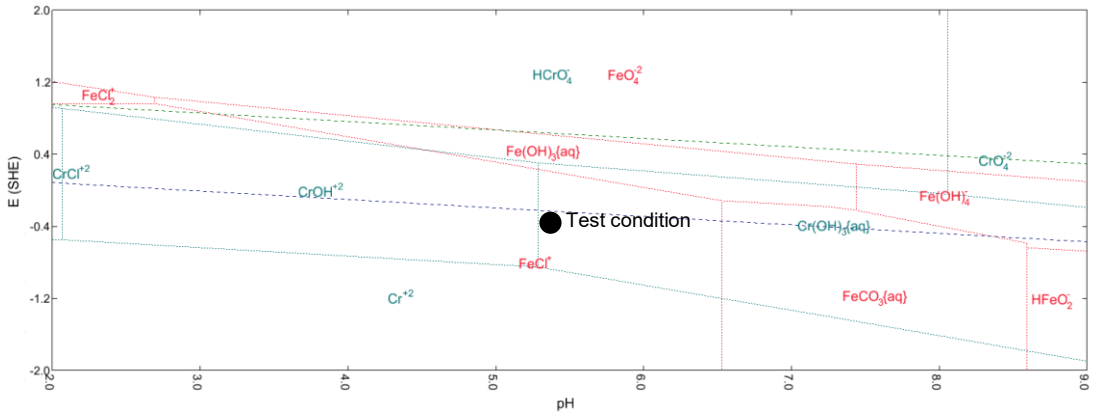

Figure 9-3. Pourbaix diagram for aqueous at 200°C and 5.2 MPa bar CO_2.

The precipitation of $Cr(OH)_3$ is driving by supersaturation, which is controlled by the concentrations of the aqueous species at the material/solution interface. As the native passive film loses its protectiveness, the corrosion of the metal matrix led to the accumulation of Cr^{3+} near the metal surface, and $Cr(OH)_3$ began to deposit when it reached a certain supersaturation level.

The electrochemical response at this stage shows significant differences from that in stage I. OCP begins to rise at Stage II after reaching a trough at Stage I. The potentiodynamic polarisation curve begins to show an active dissolution peak at this stage, indicating that the specimen has essentially lost the protection of the native passive film and the matrix begin to suffer active dissolution. EIS at this stage exhibits a high-frequency capacitive semi-circle, a low-frequency finite diffusional tail, and a mid-frequency capacitive arc which is believed to be associated with the charge transfer process. The corrosion process in this stage is dominated by both W_s-R and R_{ct}, indicating the corrosion process is under mixed control of diffusion and charge transfer.

9.3.3. Stage III: Uniform corrosion

At the final stage, uniform corrosion occurs on the specimen surface, characterized by the formation of a completely covered corrosion product film. The OCP transitions from the rapid increase at Stage II to a slow increase or gradual stabilization at Stage III. The anodic branch of the potentiodynamic polarisation curve exhibits an active

dissolution peak, implying the poor protective capability of the corrosion product film. The diffusion tail in the EIS Nyquist plots disappears, the corrosion process is controlled by charge transfer. The disappearance of the diffusion tail suggests that the inhibitory effect of the corrosion product film on diffusion is significantly weaker than that of the native passive film.

This stage can be further divided into two sub-stages based on the morphological characteristics of corrosion product film. The first involves the formation of a uniform corrosion product film without obvious uncorroded austenite particles within the film. As corrosion progresses further, an inner corrosion product layer containing uncorroded austenite appears on the inner side of the film. However, since there is no significant difference in the electrochemical response between these two sub-stages, the corrosion mechanism is considered to be identical. Consequently, these two sub-stages are classified into the same corrosion stage.

At this stage, Raman spectra results of the product film reveals that the primary change is the significant enhancement and dominance of the $Cr(OH)_3$ peak, indicating that the composition of the corrosion product film has shifted from being Cr_2O_3-dominated in Stage I to $Cr(OH)_3$-dominated. It is important to highlight that, based on the uncorroded austenite retained within the corrosion product film and the machining scratches consistently preserved on the specimen surface, it can be inferred that the growth direction of the corrosion products is from the metal/film interface inward toward the metal matrix. The poor protective capability of the corrosion product film implies that it is porous. Since the precipitated film is loose and porous, and the diffusion coefficient of ions in the liquid phase within the micropores is extremely high at high temperature, the corrosion product film no longer acts as an effective diffusion barrier, leading to the disappearance of diffusion characteristics in the EIS. At this stage, the corrosive medium diffuse through the micropores within the porous corrosion product film to the metal/film interface, causing active dissolution of the metal matrix and the release of metal cations. Near the metal/film interface, the concentration of Cr^{3+} rises rapidly; local accumulation causes the ionic product to exceed the

solubility product of $Cr(OH)_3$, leading to the precipitation of Cr^{3+} in the form of $Cr(OH)_3$.

9.4. Temperature dependence of the corrosion process

9.4.1. Verification of thermodynamic consistency at different temperatures

According to the observation provide in Chapter 7, in the temperature range of 160°C to 200°C, the evolution of corrosion product film morphology and composition shows high similarity. Also, the electrochemical response characteristics are similar in all corrosion stages at these three temperatures. Those evidences imply the consistency of the thermodynamic mechanisms in each stage.

Figure 9-4 provides the Pourbaix diagrams calculated at the three test temperatures. It can be seen that at each temperature, although the increase in temperature changes the potential and pH values, the stable corrosion product composition is consistent at all three temperatures. S13Cr MSS remains in the same thermodynamic stability region of Cr_2O_3.

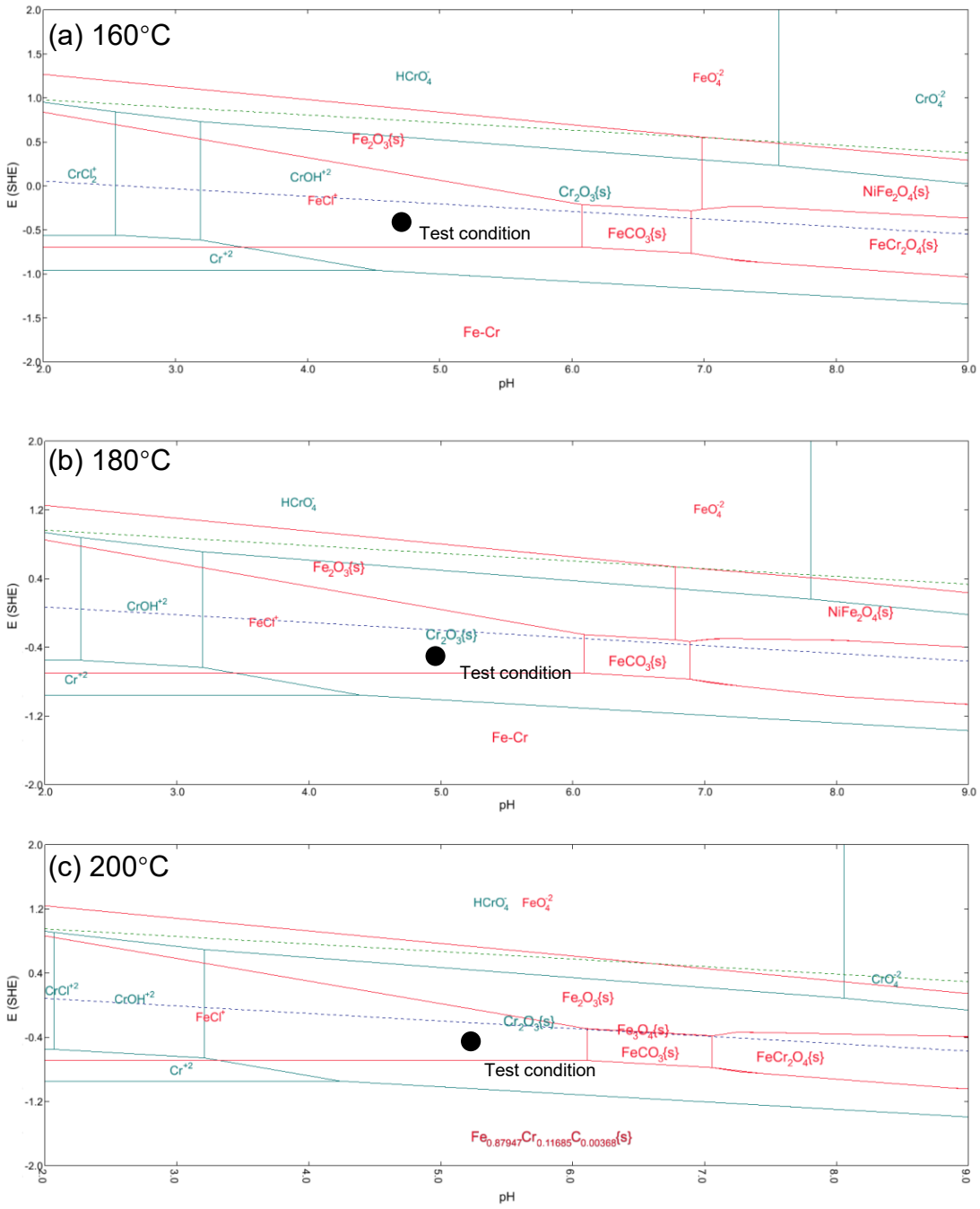

Figure 9-4. Pourbaix diagram for S13Cr MSS at (a) 160°C, (b) 180°C and (c) 200°C.

The Pourbaix diagram provided indicates that Cr_2O_3 is the stable product formed via solid-state reaction. At the same time, in the aqueous phase within the micropores of the corrosion product film near the film/metal interface, when the concentration of Cr^{3+} accumulates to a certain level, $Cr(OH)_3$ can be deposited to form via precipitation.

This thermodynamic consistency confirms the universality of the corrosion mechanism in the range of 160-200°C. The effect of temperature is not to change the corrosion mechanism, but to affect the corrosion kinetics. The increase in temperature accelerates the corrosion kinetic process, leading to the acceleration of all corrosion stages. This means we are justified in using a more detailed initial corrosion process observed at low temperature (160°C) to analyse the transient details missing at high temperature due to the excessively fast corrosion process. Also, we can refer the steady-state corrosion process observed at 200°C to predict the evolution of corrosion process at 160°C.

9.4.2. Temperature dependent native passive film degradation process

At all three test temperatures, we observed the complete first stage through in-situ electrochemical tests, and the time consumed in this stage decreased with increasing temperature. This change can be attributed to the following three reasons:

1) First, according to the previously provided Pourbaix diagrams at three temperatures, iron oxides are thermodynamically unstable at these three temperatures. Therefore, the first stage involves the selective dissolution of Fe oxides at all three temperatures. Increasing temperature intensifies the thermal vibration amplitude of ions within the oxide lattice, lowering the activation energy required for metal cations (Fe^{2+} and Fe^{3+}) to overcome the lattice binding energy and enter the solution, thereby accelerating the degradation of the native passive film [174].
2) Second, high temperature promotes the dissolution and hydrolysis of CO_2, leading to an increase in H^+ concentration in formation brine. According to the oxide dissolution mechanism below [175, 176], the reaction rate is positively correlated with the H^+ concentration:

$$Fe_2O_3 + 6H^+ \rightleftharpoons 2Fe^{3+} + 3H_2O \quad (9\text{-}3)$$

$$Fe_3O_4 + 8H^+ \rightleftharpoons Fe^{2+} + 2Fe^{3+} + 4H_2O \quad (9\text{-}4)$$

The higher the temperature, the higher the solution H^+ concentration, and the faster the iron oxides dissolution rate.

Therefore, high temperature not only provides thermal activation energy but also further accelerates film degradation by changing the interface chemical environment.

3) Thirdly, according to reports, there is a significant difference in thermal expansion coefficients (α) between the native passive film and the stainless steel matrix ($\alpha_{metal} > \alpha_{film}$) [177]. During the process of rising from room temperature to the downhole temperature, the matrix expands more than the native passive film. This causes the passive film to bear biaxial tensile stress, which induces the initiation of micro-cracks and the growth of point defect density, thereby accelerating the degradation of the passive film. The higher the temperature, the greater the tensile stress on the native passive film, and the stronger the effect in promoting its degradation.

Define the time required for the OCP corresponding to the first stage to drop from the initial value to the lowest point as t_I (i.e., the first stage duration). The ln(t_I) vs. 1/Temp curve is plotted as shown in the Figure 9-5. It can be seen that the experimental points fit the linear relationship well, which follows the Arrhenius relationship.

The following form of the Arrhenius equation with respect to time is used to fit the experimental points:

$$\frac{1}{t_I} = A \cdot exp\left(-\frac{E}{RT}\right) \tag{9-5}$$

where A is a pre-exponential factor, E is the activation energy required for the degradation of the native passive film, R is the molar gas constant.

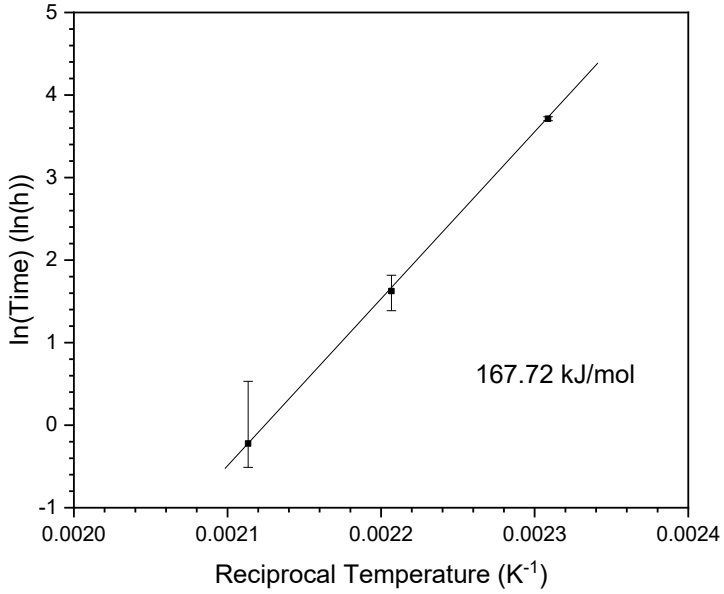

Figure 9-5. ln(t_I) vs. 1/Temp curve of S13Cr MSS under HTHP downhole environments.

Based on the Arrhenius equation fitting, the activation energy E for the degradation of the native passive film was calculated to be 167.72 kJ/mol. This energy magnitude usually corresponds to the energy required for chemical bond breaking (>100 kJ/mol).

The linear relationship between $\ln(t_I)$ vs. 1/T indicates that the degradation mechanism of the native passive film is stable under HTHP downhole environments within the temperature range of 160 to 200°C. Also, this implies that the time required for the degradation of the native passive film at other temperatures can be predicted by the Arrhenius equation. In addition, the high activation energy implies a significant energy barrier for the degradation of the passive film.

9.4.3. Confirmation of medium transport mode in corrosion product films at different temperatures

According to the EDS results of the corrosion product films obtained at three temperatures, Fe hardly participates in the film formation. The corrosion product film consists mainly of $Cr(OH)_3$ mixed with Cr_2O_3. Here, we calculate the Pilling-Bedworth Ratio (PBR) of the $Cr(OH)_3/Cr_2O_3$ film relative to the matrix using the following equation

(assuming that all Fe undergoes selective dissolution and all Cr participates in forming the corrosion product film):

$$PBR = \frac{V_{film}}{V_{metal}} = \frac{\frac{m_{film}}{\rho_{film}}}{\frac{m_{metal}}{\rho_{film}}} = \frac{w_{Cr} \cdot M_{film} \cdot \rho_{metal}}{n \cdot M_{Cr} \cdot \rho_{film}} \quad (9\text{-}6)$$

where V_{film} is the volume of the generated corrosion product, V_{metal} is the volume of the consumed S13Cr MSS metal, m_{film} is the mass of the generated corrosion product, m_{metal} is the mass of the consumed S13Cr MSS metal; M_{film} is the molar mass of the generated corrosion product (where the molar mass of Cr_2O_3 is 152.00 g/mol and $Cr(OH)_3$ is 103.03 g/mol); M_{Cr} is the molar mass of Cr (52.00 g/mol); ρ_{film} is the density of the generated corrosion product (where the density of Cr_2O_3 is 5.22 g/cm^3 and $Cr(OH)_3$ is 2.90 g/cm^3); ρ_{metal} is the density of S13Cr metal (7.75 g/cm^3); w_{Cr} is the mass fraction of Cr in S13Cr MSS (13%); n is the number of metal atoms contained in one corrosion product molecule (where n = 2 for Cr_2O_3 and n = 1 for $Cr(OH)_3$).

The PBR is defined as the ratio of the volume of corrosion product to the volume of metal consumed. When PBR < 1, the film volume less that consumed metal volume, the corrosion product film provides poor protection; when 1 < PBR < 2.5, the volume of the generated product is slightly larger than the volume of consumed metal, the corrosion product film provides excellent protection; when PBR > 2.5, the film volume >> consumed metal volume, the corrosion product film is prone to peeling, blistering, or spalling, thereby failing to provide adequate protection.

The calculated PBR for Cr_2O_3 is 0.28, and the PBR for $Cr(OH)_3$ is 0.69. Therefore, even if all Cr participates in forming the corrosion product film, the PBR of the $Cr(OH)_3$/ Cr_2O_3 film is significantly less than 1. The generated corrosion product is insufficient to compensate for the volume loss caused by the massive dissolution of Fe. Therefore, the corrosion product film inevitably forms pores, the corrosive medium can propagate through the liquid phase within the microscopic pores of the loose and porous corrosion product film.

Figure 9-6 compares the cyclic potentiodynamic polarisation curves of S13Cr MSS at different temperatures. The curves obtained at

160°C, 180°C, and 200°C all exhibit a stable current density region, referred to as pseudo-passive region, as the potential increases in the noble direction during the anodic scan. This behaviour is attributed to the mass transfer barrier effect provided by the corrosion product film.

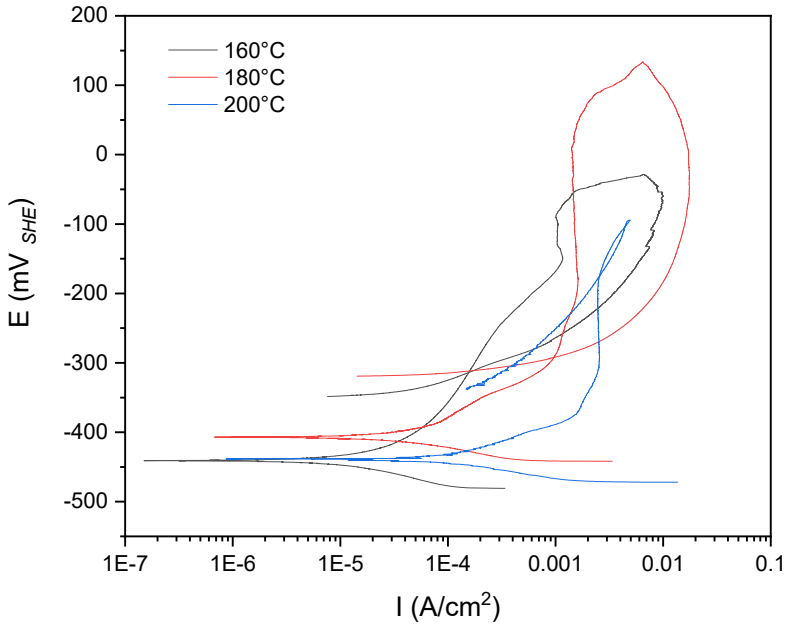

Figure 9-6. Cyclic potentiodynamic polarisation curves of S13Cr MSS at 160°C, 180°C and 200°C.

The activation energy of the corrosion scale growth in the pseudo-passive region can be obtained according to the Arrhenius plot:

$$I_p = A \cdot exp\left(-\frac{E}{RT}\right) \quad (9\text{-}7)$$

where A is a pre-exponential factor, E is the activation energy, R is the molar gas constant, and Ip is the passive current density.

In this study, the activation energy value for the corrosion scale growth on S13Cr MSS in CO_2-saturated formation brine in the pseudo-passive region is 36.89 kJ/mol, as shown in Figure 9-7. This value falls within the activation energy region for liquid phase diffusion (the activation energy for liquid phase diffusion generally lies below a value of 41.84 kJ/mol according to the report issued by Robertson [40]).

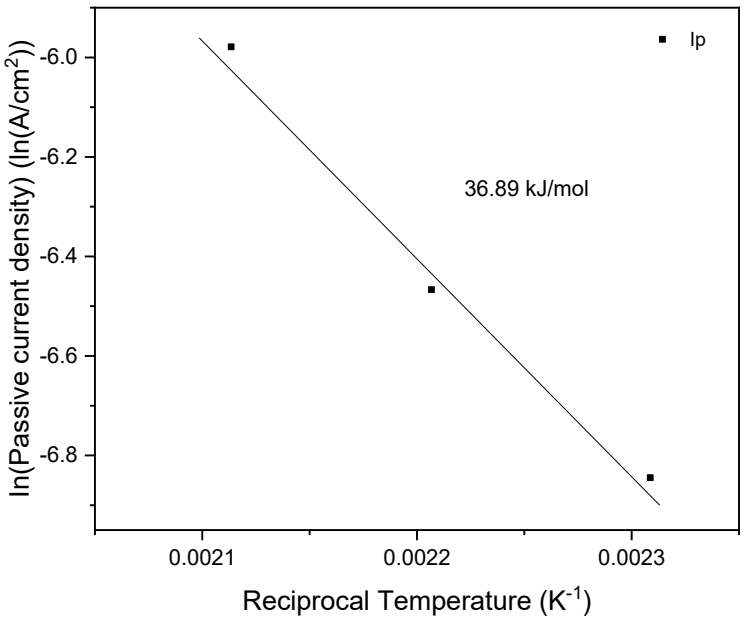

Figure 9-7. Arrhenius plot of the passive current density obtained from the potential dynamic polarisation curves of S13Cr MSS immersed in CO_2-saturated formation brine.

This further confirms that the corrosion product film generated in the third stage of corrosion in the HTHP formation brine environment is a loose and porous film, and the corrosive medium propagates through the liquid phase within the micropores. Also, the diffusion coefficient (D) of ions in the liquid phase is extremely high, leading to a very rapid diffusion process. Therefore, after the corrosion product film forms, material diffusion is no longer the bottleneck of the reaction, and the diffusion feature in the Nyquist plots of EIS disappears.

9.5. Effect of CO_2 partial pressure on precipitation and corrosion behaviour

Based on the observations in Chapter 6, the change in CO_2 partial pressure altered the chemical equilibrium of the HTHP formation brine. This significantly affected the thermodynamic tendency of mineral scaling and the types of thermodynamically stable corrosion products. As shown in the schematic diagram in Figure 9-8, dual-

phase carbonate precipitates formed at 0.27 MPa of CO_2 partial pressure, and Fe-containing spinel appeared in the corrosion products.

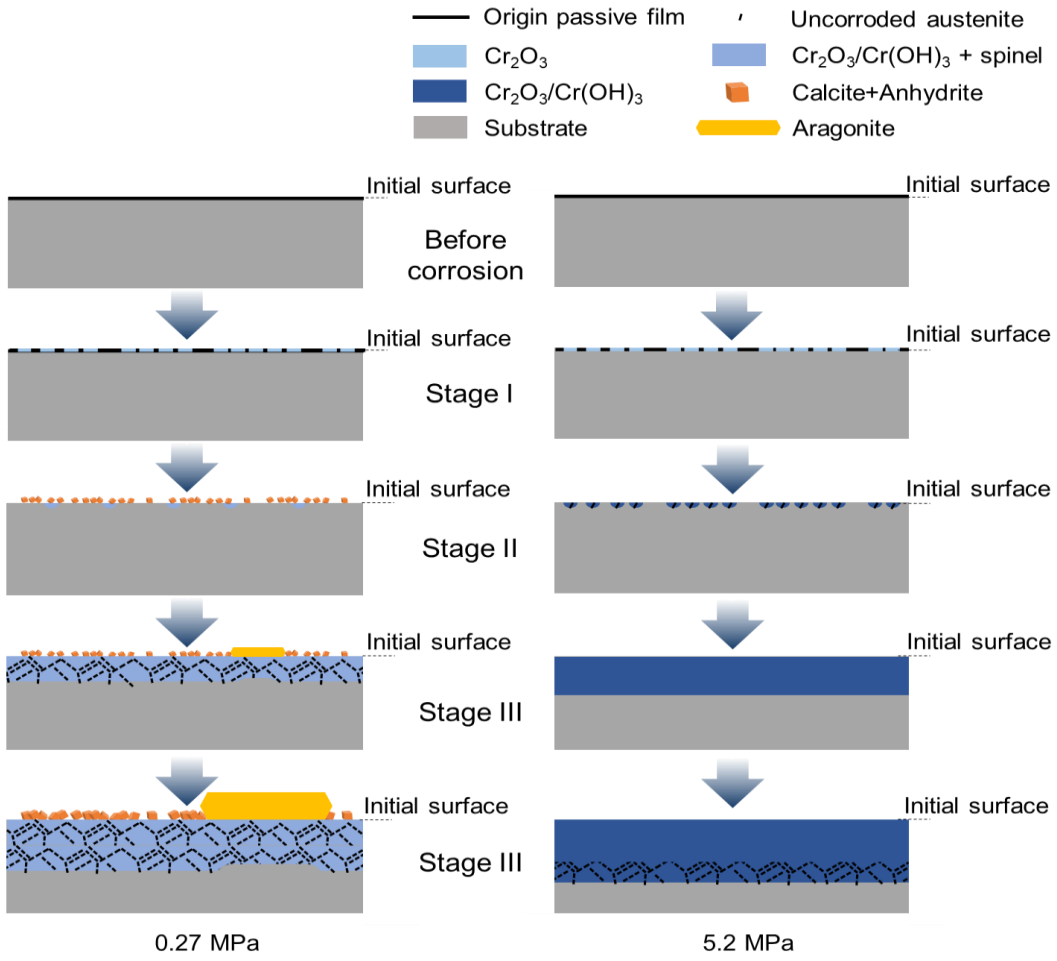

Figure 9-8. The schematic diagram for corrosion process of S13Cr MSS at 200°C and various CO_2 partial pressure.

The change in CO_2 partial pressure also significantly altered the surface morphology of localized corrosion in the second stage, as shown in Figure 9-9. At the low CO_2 partial pressure of 0.27 MPa, localized corrosion preferentially occurred at the scratches produced during specimen preparation. However, at the high CO_2 partial pressure of 5.2 MPa, localized corrosion preferentially occurred at the martensite matrix surrounding the reversed austenite. The detail will be discussed in the following sections.

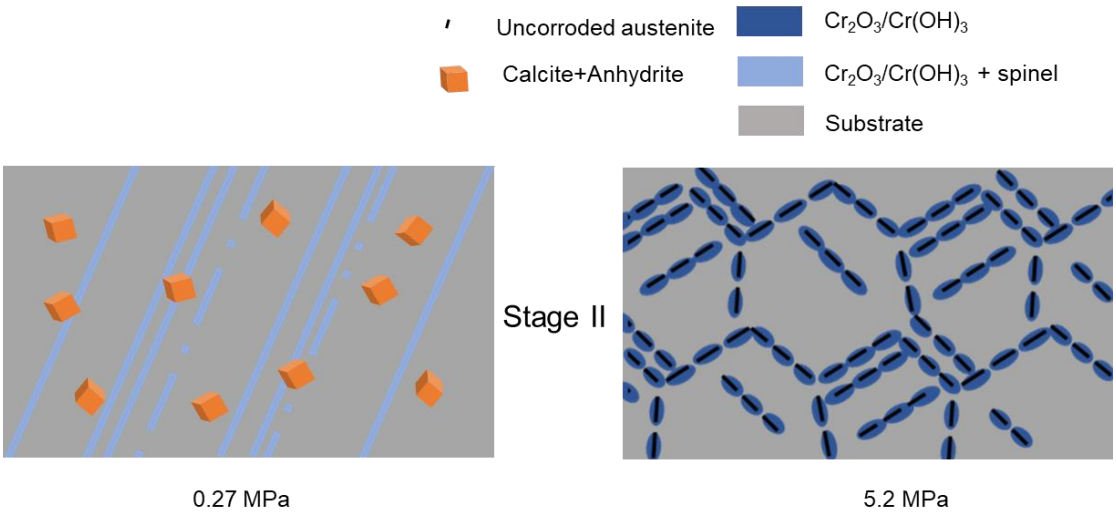

Figure 9-9. The schematic diagram for Stage II of corrosion process of S13Cr MSS at 200°C and various CO_2 partial pressure from the top view.

In addition, the change in CO_2 partial pressure altered the corrosion behaviour of the austenite in the Stage III of the corrosion process, as shown in Figure 9-8. At the low CO_2 partial pressure of 0.27 MPa, the corrosion product film contained uncorroded austenite particles, and the product film did not appear stratified during 7 days of immersion. However, at the high CO_2 partial pressure of 5.2 MPa, based on its typical morphological characteristics, the Stage III can be further subdivided into two sub-stages. First, a uniform corrosion product film without uncorroded austenite particles formed. As corrosion progressed further, an inner corrosion product layer containing uncorroded austenite particles appeared on the inner side of the corrosion product film. These differences in corrosion and scaling behaviour caused by the change in CO_2 partial pressure will be discussed in the following sections.

9.5.1. Deposition of precipitates at different CO_2 partial pressure

Based on the experimental observations in Chapter 6, no obvious precipitates (such as carbonates) were observed on the specimen surface under high CO_2 partial pressure, whereas two types of carbonates deposited under low CO_2 partial pressure. Under low CO_2 partial pressure, XRD results showed that the $CaSO_4$

(anhydrite) signal was distinct during the initial stage of precipitation. Then, as precipitation continued, the carbonate signal gradually emerged. Localized Raman analysis of the cube-shaped precipitates from the early stage revealed signals from both sulfate and carbonate (calcite). Also, EDS composition confirmed that the cube-shaped precipitates contained S, and the cations were predominantly Ca, containing trace amounts of Mg and Fe. These results collectively indicate that calcite ($CaCO_3$) and anhydrite ($CaSO_4$) co-precipitate as a mixture rather than a solid solution to form the cube-shaped precipitate. The large and flat crystal was confirmed to be aragonite based on localized Raman analysis results. Also, the presence of aragonite was verified by XRD results. EDS showed that its cation was Ca, without other impurity ions such as Fe and Mg.

9.5.1.1. Deposition trends of precipitates at different CO_2 partial pressure

As illustrated before, one of the most significant differences in corrosion behaviour between 0.27 and 5.2 MPa p_{CO_2} is the precipitation behaviour of the precipitates. $CaSO_4$ (anhydrite) and $CaCO_3$ (calcite and aragonite) deposited on sample surface as an outer corrosion scale at 0.27 MPa p_{CO_2} while no precipitates deposited at 5.2 MPa p_{CO_2}.

In aqueous environments containing CO_2, CO_2 is dissolved in brine to form H_2CO_3, H_2CO_3 is further decomposed to generate HCO_3^-, CO_3^{2-} and H^+. The sequence of equilibrium reactions that are associated with the presence of CO_2 in H_2O are as follows [21]:

$$CO_{2(g)} \rightarrow CO_{2(aq)} \quad (9\text{-}8)$$

$$CO_{2(aq)} + H_2O \rightarrow H_2CO_3 \quad (9\text{-}9)$$

$$H_2CO_3 \rightarrow HCO_3^- + H^+ \quad (9\text{-}10)$$

$$HCO_3^- \rightarrow CO_3^- + H^+ \quad (9\text{-}11)$$

In this study, with the increase of CO_2 partial pressure, reaction 9-8, 9-9 and 9-10 drived to the right, the concentration of H_2CO_3, HCO_3^- and H^+ in brine increased. The simulated formation brine used in this study contains buffer HCO_3^- before the injection of CO_2, the amount

of HCO_3^- introduced by buffer was several orders of magnitude higher than the amount of HCO_3^- generated by the injection of CO_2 through reaction 9-10, in this case, the concentration of HCO_3^- can be regard as a constant. Hence, reaction 9-11 drived to the left as the concentration of H^+ increased according to reaction 9-10, resulting a decrease in the concentration of CO_3^{2-}.

The solubility of anhydrite intend to increase with decreasing pH [178], thus, $CaSO_4$ (anhydrite) is easier to deposit at 0.27 MPa p_{CO_2} than at 5.2 MPa p_{CO_2}. As for $CaCO_3$, the concentration of CO_3^{2-} in tested formation brine increased with decreasing CO_2 partial pressure as discussed previously, resulting in a higher supersaturation of $CaCO_3$ (SR_{CaCO_3}) as the following equation:

$$SR_{CaCO_3} = \frac{[Ca^{2+}][CO_3^{2-}]}{K_{sp}} \quad (9\text{-}12)$$

Where K_{sp} represents the solubility product associated with $CaCO_3$ which only determined by temperature and ionic strength, $[Ca^{2+}]$ and $[CO_3^{2-}]$ are the concentration of Ca^{2+} and CO_3^{2-}, respectively. Meanwhile, a higher pH promotes the deposition of $CaCO_3$ [179], a lower SR_{CaCO_3} is required for the nucleation of $CaCO_3$. Hence, compared to the condition of 5.2 MPa p_{CO_2}, 0.27 MPa p_{CO_2} provide a higher solution pH, higher concentrations of CO_3^{2-} result in an easier precipitation of significant amount of precipitates.

9.5.1.2. Evolution of precipitates at P_{CO_2} of 0.27 MPa

Carbonates and sulphates containing Ca^{2+} and Mg^{2+} ions are the most common precipitates in oil and gas applications which usually generate by the dissolution of rock and precipitate in an appropriate condition [180, 181]. Besides, $FeCO_3$, as a corrosion product, is also a common precipitate during oil and gas extraction and transportation [182]. Those precipitates tend to deposit when concentration of ions in solution exceeds the solubility limit (solubility product, K_{sp}) of the precipitates, significantly depending on their supersaturation (SR) degrees in brine, temperature, brine pH, impurity ions and etc.

At 200°C, the K_{sp} of calcite is 5.11×10^{-12}, while that of aragonite is 5.93×10^{-12} [183]. Under the same conditions, the supersaturation of

calcite is higher than that of aragonite. Therefore, in an ideal state, the nucleation and growth rate of calcite should be greater than that of aragonite.

It was reported by Ghazal [178,184] and Kangbi [185] that anhydrite is the most stable phase of $CaSO_4$ at 200°C among anhydrite, gypsum and hemihydrate. And anhydrite has been observed to be the only precipitation form of $CaSO_4$ at 200°C after sufficient reaction time.[186] In the meantime, calcite is reported to be able to co-precipitate with anhydrite via an epitactic relationship (i.e., $(104)_{Cal}//(200)_{Anh}$) [186, 187]. This phenomenon was confirmed during the immersion test under 200°C and 0.27 MPa CO_2, a large number of cubic with multiple steps at the boundary/surface co-precipitated/nucleated within the first 20 h, and localized Raman spectra confirmed the mixture of calcite and anhydrite within a single cubic.

The lattice matching between calcite and the anhydrite at specific crystal planes (i.e., $(104)_{Cal}//(200)_{Anh}$) has been claimed to promote a strong adhesion between both phases and reduce the energy required in heterogeneous nucleation of calcite and anhydrite on each other with a specific orientation relationship [187]. Therefore, the nucleation of calcite and the anhydrite will be accelerated thermodynamically and kinetically [188]. As a result, in the HTHP underground environment, the nucleation rate of calcite during the initial stage of precipitation is higher than aragonite.

The Fe^{2+} concentration raised rapidly as corrosion proceeded. But the introduction of high concentration Ca^{2+} ions significantly reduced and delayed the precipitation of $FeCO_3$, $CaCO_3$ precipitation was favoured in this situation [189-192]. Meanwhile, Mg^{2+} and Fe^{2+} ions can easily co-precipitate with Ca^{2+} ions to form a Mg^{2+} and Fe^{2+} ions containing calcite as magnesite ($MgCO_3$), siderite ($FeCO_3$), and calcite ($CaCO_3$) share the same crystal structure [193-195]. This was confirmed by EDS as provided before.

It was reported that the impurity ions effect the growth rate of $CaCO_3$ by either blocking propagation of the kink (kink blocking), or straining the local crystal lattice, and hence increasing the mineral solubility if the impurity ions incorporated into the growing mineral (incorporation inhibition) [196]. Compared to calcite, aragonite is

less inclusive of impurities than calcite [197]. This is confirmed by EDS results as shown before, the cations of aragonite are almost free of impurity ions such as Mg^{2+} ions and Fe^{2+} ions. Thus, the growth of aragonite is inhibited by kink blocking while that of calcite is inhibited by both kink blocking and incorporation inhibition, resulting in a faster growth rate of aragonite compare to calcite, ultimately leading to a larger size of aragonite.

9.5.2. Evolution of the corrosion products at different CO_2 partial pressure

Figure 9-10 compares the Raman spectra of corrosion products formed at 200°C under 0.27 MPa and 5.2 MPa CO_2 conditions. Under the high CO_2 partial pressure (5.2 MPa), the main characteristic peak of the corrosion products is located at 717 cm^{-1}, which corresponds to $Cr(OH)_3$. However, when the partial pressure decreases to 0.27 MPa, this characteristic peak shifts to 711 cm^{-1}. This shift implies a change in the composition of the corrosion products. In HTHP environments, this change is usually associated with the formation of spinel ($FeCr_2O_4$) [140]. EDS point analysis results show that under high CO_2 partial pressure, the corrosion product contains only a small amount of Fe, and the cations are predominantly Cr. However, under low CO_2 partial pressure, significant Fe content was detected in the corrosion products, and the Fe/Cr atomic ratio is close to 1:2. This agrees well with the chemical stoichiometry of $FeCr_2O_4$. TEM selected area electron diffraction patterns finally confirmed that the corrosion products formed under low CO_2 partial pressure consist of spinel ($FeCr_2O_4$) and $Cr(OH)_3$.

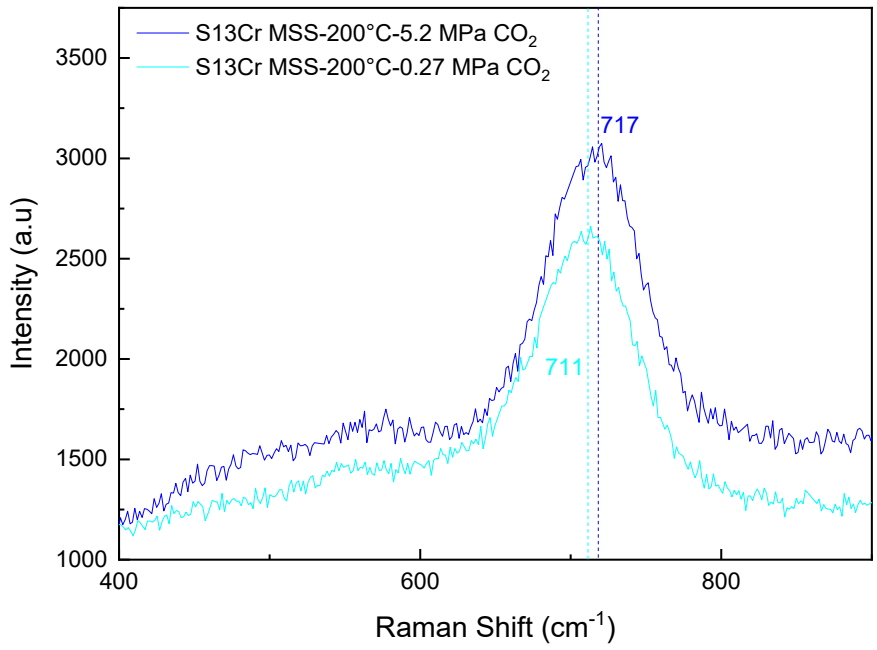

Figure 9-10. Raman spectroscopy of S13Cr MSS specimen exposed at 200°C and 0.27/5.2 MPa CO_2.

Based on the solution chemistry parameters, Pourbaix diagrams under different CO_2 partial pressures were constructed as shown in the Figure 9-11. The comparison results clearly explain the change in corrosion product composition. At low CO_2 partial pressure, due to the expansion of the $FeCr_2O_4$ stability region and the increase in solution pH, the stable corrosion products are identified as $FeCr_2O_4$ and Cr_2O_3. However, at high CO_2 partial pressure, the thermodynamically stable products are Cr_2O_3, and there are no thermodynamically stable Fe products. This explains the change in corrosion product composition caused by the variation in CO_2 partial pressure from a thermodynamic perspective. In addition to the solid-state reaction products provide by the Pourbaix diagram, $Cr(OH)_3$ is also formed via a dissolution-precipitation mechanism.

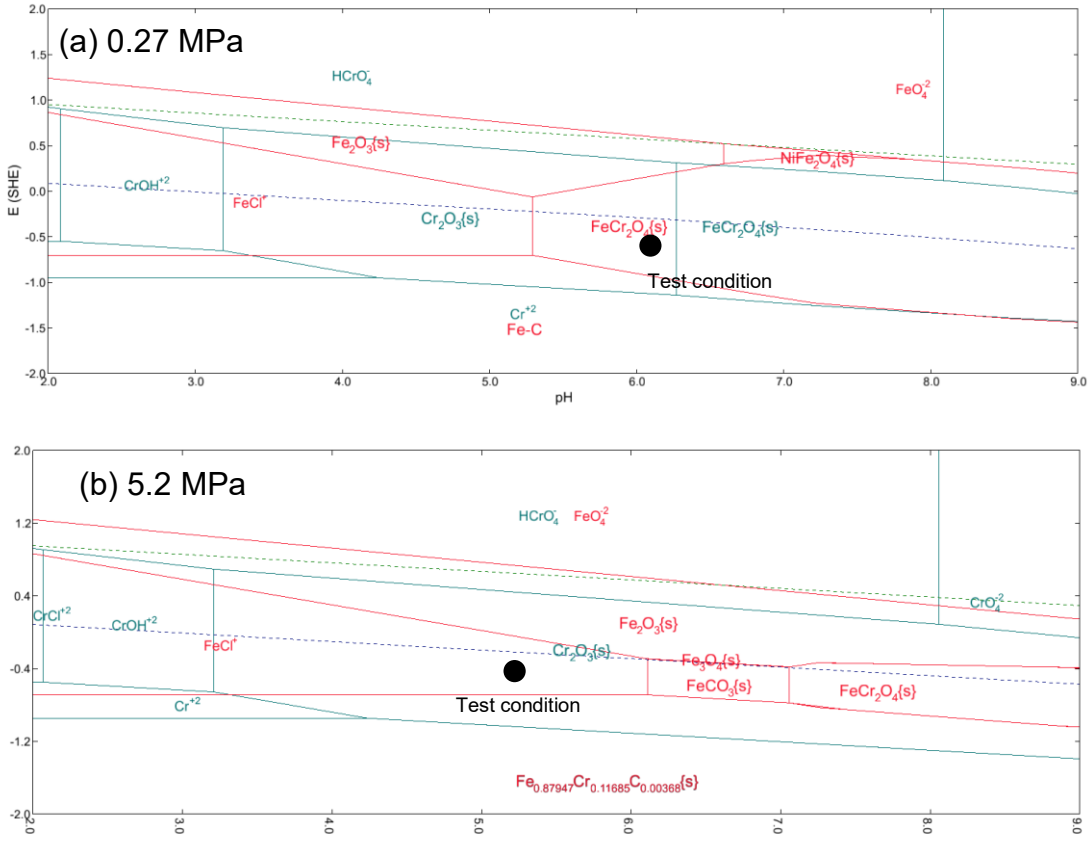

Figure 9-11. Pourbaix diagram for S13Cr MSS at 200°C with (a) 0.27 and (b) 5.2 MPa of CO_2.

It is generally believed that, compared to the loose and porous $Cr(OH)_3$-dominated corrosion product film at high pressure, the $FeCr_2O_4$-rich corrosion product film formed at low CO_2 partial pressure possesses superior compactness and barrier properties, thereby providing a better physical shielding effect [140]. At the same time, the decrease in CO_2 partial pressure leads to a significant reduction in the H^+ concentration in the solution, which kinetically inhibits the rate of the cathodic hydrogen evolution reaction. The combined effect of the improved film barrier properties and the reduced electrochemical reaction activity results in a lower corrosion rate for S13Cr MSS in the low-pressure environment.

9.5.3. Effect of CO_2 partial pressure on the localized preferential corrosion during the Stage II of corrosion process

In the stage II of corrosion process of S13Cr MSS under HTHP downhole environments, localized corrosion occurs on the S13Cr

MSS surface. According to experimental observations, as the CO_2 partial pressure rises from 0.27 MPa to 5.2 MPa, the location of localized corrosion shifted from the scratches produced during specimen preparation to the martensite matrix surrounding the reversed austenite, as shown in Figure 9-9.

In the low CO_2 partial pressure environment, the corrosivity of the bulk solution is relatively weak. A semi-enclosed occluded region forms inside the scratch. Mass transfer inside the scratch is restricted to a certain extent, which causes the local pH increase due to the consumption of H^+ ions by the cathodic reaction and local accumulation of Cl^- ions inside the scratch [198-201]. A macro-cell is then established: the anode inside the scratch vs. the cathode on the flat area outside the scratch. This process is similar to that of crevice corrosion and accelerates the corrosion at inside the scratch. When this morphology induced galvanic effect is greater than the galvanic effect formed between martensite matrix and reversed austenite, the local acidification inside the scratch dominates the occurrence of localized corrosion under low CO_2 partial pressure, forming a preferential corrosion zone distributed along the scratches.

However, in the high CO_2 partial pressure environment, the pH value of the bulk solution is lower, and the corrosivity of the bulk solution is stronger. This severe macro-environment leads to a change in the control mechanism of the localized corrosion. Since the bulk solution itself already possesses stronger corrosivity (higher H^+ concentration), the H^+ concentration difference caused by occlusion effect inside the scratch is weaken and can be negligible compared to the huge bulk concentration, thus the entire sample surface (inside and outside the scratch) is in a severe corrosion environment. Besides, the changes in the corrosive environment are believed to affect the strength of the microstructure related galvanic effect [198], a lower solution pH is reported to enhance the galvanic effect caused by differences between phases [202]. Therefore, the intrinsic electrochemical difference between the martensite matrix and reversed austenite dominates the occurrence of localized corrosion, forming a preferential corrosion zone surrounding the reversed austenite in the high CO_2 partial pressure environment.

9.5.4. Effect of CO_2 partial pressure on the corrosion behaviour of reversed austenite during the Stage III of corrosion process

In the stage III of the corrosion process of S13Cr MSS under HTHP downhole environment, the corrosion product film formed at the low CO_2 partial pressure of 0.27 MPa contains uncorroded austenite particles, and the corrosion product film did not stratify. And throughout a 7-day immersion experiment, no stratification of the corrosion product film was observed. The uncorroded austenite is distributed throughout the entire corrosion product film.

However, at the high CO_2 partial pressure of 5.2 MPa, based on its typical morphological characteristics, the stage III can be further divided into two sub-stages. In the early stage III, a uniform corrosion product film without uncorroded reversed austenite particles formed. In the later stage III, as corrosion progressed further, an inner corrosion product layer containing uncorroded austenite particles appeared on the inner side of the corrosion product film. At the same time, it was noted that the interface between the inner and outer layers moved toward the metal matrix as corrosion progressed. The uncorroded austenite on the outer side undergoes corrosion as the corrosion progressed, leading to the movement of the interface between the inner and outer corrosion product films toward the metal matrix direction.

At low CO_2 partial pressure, due to the better protective capability of the $FeCr_2O_4$-rich corrosion product film and the lower H^+ concentration in the solution, the corrosion of both the martensite matrix and the reversed austenite is inhibited compared to the high CO_2 partial pressure condition. The martensite matrix acts as the anode and dissolves preferentially, while the austenite cathode, which is more corrosion-resistant than the matrix, is preserved. As the corrosion of the martensite matrix proceeds, the corrosion product film/matrix interface moves toward the metal matrix direction. The uncorroded reversed austenite particles are retained in-situ in the corrosion product film like inert markers. Since the environment at low CO_2 partial pressure is mild, even if the reversed austenite is retained in the porous film and immersed for a long time, it resists

environmental corrosion due to its superior intrinsic corrosion resistance and remains in the corrosion product film.

However, at high CO_2 partial pressure, due to the poorer protective capability of the corrosion product film, higher H^+ concentration in the solution, the driving force for the corrosion of both the martensite matrix and reversed austenite increases. Therefore, when the martensite matrix exists around it, the reversed austenite acts as a cathode and does not corrode first. But after the surrounding martensite matrix is corroded away, the reversed austenite also undergoes corrosion. This leads to the formation of a corrosion product film without uncorroded reversed austenite in the early stage III of corrosion process.

Concentration gradients of corrosive species (such as H^+) and metal ions generated by corrosion exist within the porous corrosion product film. H^+ transfers from the solution to the solution/film interface and then to the metal/film interface, and its concentration gradually decreases during this transfer process. Conversely, metal ions are released from the film/metal interface and diffuse toward the solution/film interface, and their concentration gradually decreases during this process. As corrosion proceeds, the corrosion product film thickens, and the local chemical environment in the porous film changes. The thickened porous film hinders the inward diffusion of H^+ and the outward diffusion of metal ions. Corrosion leads to an increase in metal ion (e.g., Fe^{2+}, Cr^{3+}) concentration at the film/metal interface and consumes the H^+ at the interface. This change in the local chemical environment reduces the corrosion driving force. Therefore, when the corrosion product film thickens to a certain extent, the above inhibitory effect increases the stability of the reversed austenite, allowing the reversed austenite to be temporarily retained in the corrosion product film. But this retention is temporary. As corrosion proceeds further, the film/metal interface moves toward the metal direction. The uncorroded austenite becomes farther away from the film/metal interface. The metal ion concentration around the uncorroded austenite gradually decreases, and the H^+ concentration gradually increases. The local chemical environment change leads to an increase in its corrosion driving force. Therefore, the uncorroded reversed austenite is activated and

undergoes corrosion. This results in the observed movement of the interface between the inner and outer corrosion product films toward the metal matrix direction. In summary, the formation of the double-layer corrosion product film structure and the movement of its interface under high CO_2 partial pressure condition are essentially the result of the response of the reversed austenite particles to the changes in the local chemical environment.

9.6. The role of reverted austenite in corrosion evolution under HTHP downhole environments

9.6.1. The difference in corrosion tendencies between martensite and austenite

Work function (WF) is a fundamental electronic property of a metallic surface and is becoming increasingly useful in predicting corrosion tendency as it is able to distinguish the corrosion potential or electrochemical nobility of different phases [203]. The phase with lower WF possesses lower corrosion potential and is more easily corroded because of their more unstable electronic states [204].

The WF (φ) of metallic material is theoretically proportional to one-six power of the average density of free electrons in a metal lattice (n) according to the following equation [205]:

$$\varphi = \frac{7.8\alpha}{\mathrm{a}_0} n^{\frac{1}{6}} \tag{9-13}$$

where α is an empirical constant and a_0 is the Bohr radius.

Assuming that all the elements of austenite and martensite phases are identical and considering only the effect of structure on the WF. The $\varphi_\gamma/\varphi_\alpha$ can be estimated as the ratio of the atomic packing density of austenite to that of martensite phase:

$$\frac{\varphi_\gamma}{\varphi_\alpha} = \left(\frac{n_\gamma}{n_\alpha}\right)^{\frac{1}{6}} = \left(\frac{4}{a_\gamma^3} \Big/ \frac{2}{a_\alpha^3}\right)^{\frac{1}{6}} = 2^{\frac{1}{6}} \left(\frac{a_\gamma}{a_\alpha}\right)^{\frac{1}{2}} \tag{9-14}$$

where the a_γ and a_α are the lattice constants of austenite and martensite phases, and in this study, they were calculated to be

2.871 Å and 3.592 Å, respectively, based on the tested XRD results. Therefore, the $\varphi_\gamma/\varphi_\alpha$ calculated to be 1.004.

From the aspect of compositions effect, the variation of the work function due to compositional changes deviates from linearity but still fellows a monotonic trend.[206] The ranking of the work function of the alloying elements involved in this study follows the order of Ni>Mo>Fe>Cr with 5.15 eV for Ni and 4.6 eV for Mo, 4.5 eV for Cr while 4.5 eV for Fe. Therefore, an increase in the content of Mo and Ni in the alloy, which have significantly higher work functions than Fe and Cr, leads to an increase in the work function of the alloy. Hence, the difference in composition between martensite and reversed austenite also leads to a higher work function for reversed austenite than for martensite in this study. Eventually, it can be concluded that the reversed austenite is more novel than martensite due to a combination of differences in their crystal structures and composition.

9.6.2. The role of reverted austenite in stability of the native passive film under HTHP downhole environments

After 5 hours of immersion, the reversed austenite-containing S13Cr MSS already exhibited dehydration cracks crossing dark and light regions, indicating that it had formed a fully covered corrosion product film and entered stage III of corrosion process. In contrast, the pure martensitic S13Cr MSS showed only slight, scattered spot-like corrosion traces, indicating it was still in the transition period from Stage I to Stage II. Even after 20 hours, clear localized preferential corrosion areas were still visible on the pure martensitic S13Cr MSS surface, and the cross-section confirmed that only an extremely thin corrosion product film had formed. This indicates that the entry of pure martensite into stage III was delayed by several times compared to the reversed austenite-containing S13Cr MSS.

This difference is attributed to the homogeneity of the element distribution in pure martensitic S13Cr MSS. Since the chemical composition of pure martensitic S13Cr MSS is more uniform, the native passive film on pure martensitic S13Cr MSS has lower defect density, leading to a slower degradation rate under HTHP downhole environment.

For the reversed austenite-containing S13Cr MSS, during the formation of reversed austenite, corrosion-resistant elements (Cr, Mo, Ni) tend to enrich in the austenite phase, leading to the formation of a depletion zone in the adjacent martensite matrix and at the phase boundaries [80, 92, 107, 111]. This microscopic chemical segregation significantly reduces the protective capability of the passive film covering the phase boundaries, thereby accelerating its degradation speed under HTHP downhole environment [172].

9.6.3. The role of reversed austenite in the non-uniform corrosion behaviour during the Stage II of corrosion process

In the stage II of corrosion process, S13Cr MSS with and without reversed austenite exhibits distinct differences in corrosion behaviour. As shown in Figure 9-12, the localized corrosion morphology of pure martensitic S13Cr MSS presents scattered semi-circular pits. However, for the reversed austenite-containing S13Cr MSS, localized corrosion occurs on the martensite matrix surrounding the reversed austenite.

Due to its uniform composition distribution, localized corrosion in pure martensitic S13Cr MSS occurs at randomly distributed surface defects (e.g., inclusions). However, after reversed austenite is introduced into S13Cr MSS, a micro-galvanic couple is formed between the martensite matrix and the reversed austenite. This leads to the preferential corrosion of the anodic martensite matrix surrounding the cathodic reversed austenite.

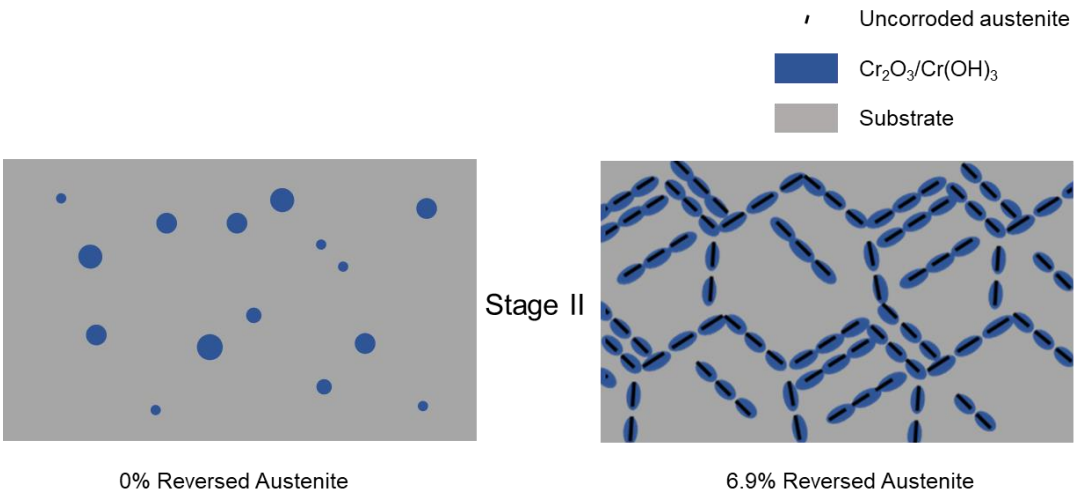

Figure 9-12. The schematic diagram for Stage II of corrosion process of S13Cr MSS specimens with/without reversed austenite exposed at 200°C and 5.2 MPa CO_2 from the top view.

9.6.4. The role of reversed austenite in the steady-state corrosion behaviour of S13Cr MSS under HTHP downhole environments

After entering the stage III, it was observed that the corrosion rate of S13Cr MSS increased with the increasing austenite content. The S13Cr MSS without reversed austenite exhibited the best corrosion resistance.

As the austenite content increases, the cathodic area increases, thereby promoting the corrosion of the martensite matrix and leading to an increase in the corrosion rate of S13Cr MSS. At the same time, the increase in austenite content increases the tortuosity of the diffusion path for the corrosive medium, resulting in a longer diffusion path [207, 208]. This creates blocking effect against the diffusion of the corrosive medium, thereby inhibiting the corrosion of the martensite matrix.

However, according to our experimental results, the accelerated corrosion caused by galvanic effect completely masks the inhibitory effect on corrosion due to the blocking effect caused by the increasing austenite content. The pure martensitic S13Cr MSS

exhibited the best corrosion resistance because it lacks the acceleration of matrix corrosion caused by the galvanic effect.

9.7. Engineering implications and optimization strategies for S13Cr MSS application

9.7.1. Establishment of native passive film degradation time-temperature map

Based on the electrochemical data obtained in Chapter 7, the native passive film degradation time-temperature map was constructed to describing the relationship between temperature and the life of the native passive film, as shown in Figure 9-13.

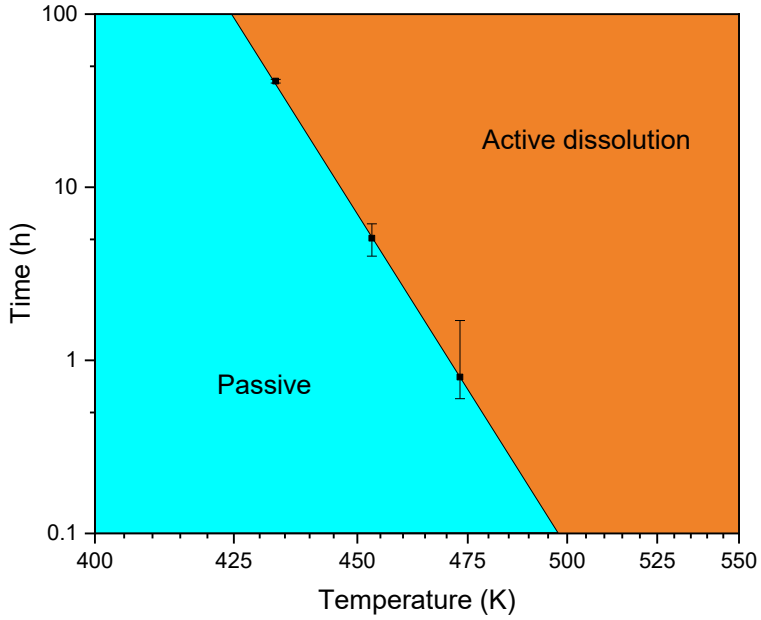

Figure 9-13. Native passive film degradation time-temperature map of S13Cr MSS under HTHP downhole environments.

By plotting the Arrhenius relationship of ln(t_I) vs. 1/T, this diagram establishes the "passive - active dissolution" boundary for S13Cr under HTHP downhole environments. This map allows for the prediction of the time required for the degradation of the native passive film under specific temperature conditions. Also, it enables the determination of the surface state (passive state or active

dissolution state) of in-service S13Cr MSS based on service time and temperature. Furthermore, for long-term service condition, the native passive film degradation time-temperature map can be used to determine the predominant surface state of the material during its service cycle, thereby guiding the targeted selection of corrosion evaluation methods and specimen surface pre-treatment methods during material selection and assessment. At the same time, for critical components that must maintain a passive state, the corresponding maximum allowable service temperature can be reverse-derived from the native passive film degradation time-temperature map based on the engineering design life.

In addition, this native passive film degradation time-temperature map based on Arrhenius kinetics holds the potential to be generalized for the life prediction of other stainless steels.

9.7.2. Service risk management recommendations

9.7.2.1. Catastrophic consequences caused by temperature fluctuations

For tubing in the passive state, brief temperature fluctuations (such as steam injection) may cause the material to prematurely transition from stage I to stage II. The critical risk lies in the fact that the degradation of the native passive film is irreversible. When the temperature returns to normal (decreases), the destroyed passive film cannot self-heal in the HTHP downhole environment. The material irreversibly enters the active dissolution state. Therefore, field monitoring should focus not only on the average temperature but also strictly control the peak temperature. Once an overheating event occurs, the state of the material's native passive film should be assessed based on the native passive film degradation time-temperature map, the remaining service life prediction should be revised, and corrosion protection strategies should be adjusted in a timely manner.

For materials already in the active dissolution state, the increase in steady-state corrosion rate caused by temperature rise is non-linear. Our experimental results indicate that a temperature increase from 160°C to 200°C causes an increase in corrosion rate by orders of

magnitude. Therefore, even brief temperature increases can cause rapid consumption of the corrosion allowance and require focused attention.

9.7.2.2. Depassivation induced by mechanical/chemical damage

Downhole operations (such as acidizing and milling) may cause damage to the native passive film on the tubing surface, artificially causing parts or the whole of the tubing to enter the active dissolution state prematurely, leading to the failure of life assessments based on the "passive state" assumption. Brief operating conditions that cause severe damage to the native passive film can significantly affect the corrosion rate of the material throughout its entire service life. Therefore, for downhole operations which could cause the damage of the native passive film, "surface damage + corrosion" coupled testing can be introduced in laboratory assessments, or life verification can be performed directly based on the active dissolution rate to confirm the applicability of the material under the severe conditions.

9.7.3. Optimization of laboratory assessment process based on corrosion evolution stages

9.7.3.1. Determine of the duration for immersion test

Traditional fixed-duration (e.g., 7 days/30 days) immersion test assessments may bring the risk of misjudgement because they fail to distinguish between the "native passive film protection period" and the "steady-state corrosion period." For long-term service where the native passive film degradation time-temperature map confirms that the material is primarily in the active dissolution state during the service cycle, short-term corrosion immersion experiments mainly characterize the corrosion rate under the protection of the native passive film. This will lead to a severe underestimation of long-term service risks. To obtain effective long-term corrosion rates, the effective duration of immersion experiments should be calculated starting from the moment the OCP stabilizes. Alternatively, the native passive film on the specimen surface should be artificially

removed before the corrosion experiment to force the material into the steady-state corrosion stage. This allows to obtain the intrinsic corrosion rate of the material in HTHP downhole environments, providing more reliable conservative data for long-cycle material selection.

9.7.3.2. Timing for electrochemical characterization

Consider the case where the native passive film failure time (predictable via the native passive film degradation time-temperature map) is very short, and the material is primarily in the steady-state corrosion stage under the active dissolution state throughout the entire service life. At this time, electrochemical testing performed in the early stage (Stage I) measures the performance of S13Cr MSS under the protection of the native passive film, which does not represent the actual service behaviour and may lead to the misconception that the material possesses excellent corrosion resistance throughout the entire service life. Therefore, it is suggested to combine OCP monitoring and perform electrochemical testing only after confirming that the material has entered the steady-state corrosion stage. Only then, the measured results can represent the true service behaviour of the material under the HTHP downhole environment. Alternatively, the native passive film on the specimen surface can be removed via cathodic polarisation or other methods before conducting the experimental testing, thereby obtaining more authentic electrochemical data of the material in HTHP environment.

9.7.4. Recommendations for material modification

9.7.4.1. Modification of passive film

The degradation of the native passive film initiates with the selective dissolution of iron oxides. Surface treatment techniques (such as high temperature oxidation, anodic polarisation, physical/chemical/electrochemical coating, etc.) can be employed to modulate the composition of the native passive film, making it rich in Cr_2O_3. This enhances the thermodynamic stability of the native passive film under HTHP downhole environments, thereby inhibiting

its degradation and achieving the goal of improving the corrosion resistance of S13Cr MSS.

9.7.4.2. Recommendations for adjustment of reversed austenite content

Although the presence of austenite has a significant improvement effect on the toughness and hydrogen embrittlement resistance of S13Cr MSS, the introduction of austenite also causes deterioration in some respects. First, the introduction of austenite reduces the strength of martensitic stainless steel. Second, our experiments also indicate that the introduction of austenite accelerates the degradation of the native passive film, and the galvanic effect generated with the martensite matrix increases the steady-state corrosion rate of S13Cr MSS under HTHP downhole environments. Therefore, during the material design process, the mechanical properties, hydrogen embrittlement resistance, and corrosion resistance should be comprehensively considered based on application requirements. The goal is to balance various properties and achieve the optimal match between mechanical performance and corrosion resistance.

10. Chapter 10 Conclusions and future work

10.1. Conclusions

The conclusions from the project have been broken down into the key observations from each of the results chapters, using the analysis in the discussions from Chapter 9.

10.1.1. Conclusions from Chapter 5 - Corrosion and SCC risk assessment.

HTHP immersion test and SSRT combined with SEM surface observation were applied to general understanding of the corrosion and cracking behaviour of S13Cr MSS and to assess the risk of corrosion and SCC in the formation brine at 200°C with 5.2 MPa CO_2. The main conclusions which can be drawn from this study are:

- The general corrosion rate of S13Cr MSS in a simulated downhole environment was 1.04 mm/year while the pitting rate was 0.37 mm/y with the pit depth of 7.11 μm over 7 days exposure. according to NACE standard SP0775, the general corrosion rate of S13Cr MSS is classified as severe level among the four categories (low, moderate, high and severe), while the pitting rate reaches the high level.
- The SSRT results show that the loss of ductility (based on ER and RAR) of S13Cr MSS in the HTHP CO_2-saturated formation brine without pre-corrosion was slightly less than 20% while the results obtained after 7 days of pre-corrosion indicate that the losses in ER and RAR for S13Cr MSS exceeded 20%. Both the SCC susceptibility of S13Cr MSS in the HTHP CO_2-saturated formation brine without and without pre-corrosion can be classified as Class 4 (on a scale from Class 1 to Class 4) according to the NACE standard TM0198 due to the existence of secondary crack. However, S13Cr MSS passed the 15-day FPB test with a load of 90% of the yield strength.
- The fracture mechanism did not undergo a fundamental change due to pre-corrosion. Cracks initiated at pits and propagate in a quasi-cleavage fracture mode, but eventually ruptured following

the micro void coalescence mechanism. The morphology of the pits became steeper during the corrosion process as the R/D ratio decreasing from 7.28 to 1.15 between 5h and 168h of exposure. The steeper shape as corrosion progressed increased the degree of stress concentration at the pits site, resulting in a significant decline in macroscopic ductility (significant advance and shortening of the necking stage).

10.1.2. Conclusions from Chapter 6 - Effect of CO_2 partial pressure

HTHP immersion test combined with surface analysis technologies and HTHP electrochemical measurements (OCP, EIS and potentiodynamic polarisation) were applied to evaluate the corrosion behaviour of S13Cr MSS in the formation brine at 200°C with 0.27/5.2 MPa CO_2. The main conclusions which can be drawn from this study are:

- The corrosion process obtained at 200°C can be divided into three stages: a). Early stage: degradation of native passive film; b). Middle stage: non-uniform corrosion characterized by the formation of a incompletely covered corrosion product film on the specimen surface; c). Final stage: uniform corrosion characterized by the formation of a completely covered corrosion product film.
- The increase in CO_2 partial pressure led the composition of corrosion products shifted from $Cr(OH)_3$ and $FeCr_2O_4$ at low CO_2 pressure to $Cr(OH)_3$ and Cr_2O_3 at high CO_2 pressure. The corrosion product film formed under high CO_2 partial pressure had a higher R_f and provided stronger blocking effect. However, since R_{ct} is significantly higher than R_f, the corrosion of S13Cr MSS in CO_2-saturated formation brine at 200°C is controlled by charge transfer process. Consequently, the significantly lower R_{ct} under high CO_2 pressure led to a higher corrosion rate (1.04 mm/y and 0.68 mm/y at 5.2 MPa and 0.27 MPa of CO_2 after 7 days of exposure, respectively).
- During the middle corrosion stage, preferential corrosion initiated at scratch sites under low CO_2 partial pressure. As the CO_2 partial pressure increased, the preferential corrosion sites became the martensite matrix surrounding austenite particles.

- During the final corrosion stage, austenite particles acted as cathodic, forming galvanic couples with the martensite matrix. Under low CO_2 partial pressure, uncorroded austenite particles retained within the corrosion product film throughout the entire final corrosion stage. In contrast, under high CO_2 partial pressure, austenite particles were only observed in the inner layer of the corrosion product film during the latter phase of the final corrosion stage.
- At 0.27 MPa of CO_2, two types of $CaCO_3$ crystals precipitated on the specimen surface while no precipitate can be observed at 5.2 MPa of CO_2 due to a higher H^+ concentration and lower CO_3^{2-} concentration at 5.2 MPa of CO_2. As for the precipitates obtained at 0.27 MPa of CO_2, one is small and abundant crystal which is a mixture formed by the co-precipitation of calcite and anhydrite (the cations were doped with Mg^{2+} ions and Fe^{2+} ions), and the other is large and sparse aragonite (pure $CaCO_3$).

10.1.3. Conclusions from Chapter 7 - Effect of temperature

This chapter systematically investigated the corrosion behaviour of S13Cr MSS in CO_2-saturated formation brine across 160-200°C through immersion test coupled with electrochemical monitoring. The main conclusions which can be drawn from this study are:

- The corrosion behaviour of S13Cr MSS in CO_2-saturated formation brine undergone a distinct stage transition. This transition was found to be consistent across the temperature range of 160-200°C. From a thermodynamic perspective, the corrosion mechanism remains consistent across the temperature range of 160-200°C. But lower temperature significantly prolonging the duration of each corrosion stage due to reduced reaction kinetics.
- Electrochemical techniques, particularly OCP monitoring, provide superior resolution for identifying stage transitions compared to immersion tests. Based on OCP evolution, the corrosion process can be categorized into three distinct stages:
  a) Early stage: The degradation of the native passive film process, characterized by continuous OCP drop, dominated by diffusion-controlled corrosion.

b) Middle stage: The preferential localized corrosion process, marked by sustained OCP rise. The corrosion is controlled by both diffusion and charge transfer during this stage.
c) Final stage: A complete covering corrosion product film forms on the surface during this stage, identified by OCP stabilization, and controlled by charge transfer process. This stage can be subdivided into two stages according to the cross-sectional morphology of the corrosion product film: single-layer film stage and double-layer film stage. Despite their structural differences, these two stages exhibited no significant electrochemical distinction.

- The activation energy value for the corrosion scale growth on S13Cr MSS in CO_2-saturated formation brine in the pseudo-passive region of potentialdynamic polarisation curve is 36.89 kJ/mol. This value falls within the activation energy region for liquid phase diffusion, implying that the corrosion product film generated in the final stage of corrosion in the HTHP formation brine is a loose and porous film, and the corrosive medium propagates through the liquid phase within the micropores.
- The degradation mechanism of the native passive film is stable under HTHP downhole environments within the temperature range of 160-200°C. The degradation time of the native passive film (t_l) exhibits Arrhenius relationship with temperature (T), as confirmed by the linear relationship between $\ln(t_l)$ and 1/T. The high activation energy (167.72 kJ/mol) implies a significant energy barrier for the degradation of the native passive film.

10.1.4. Conclusions from Chapter 9 - The role of austenite on corrosion

S13Cr MSS with varying austenite contents (0% to 17.77%) were produced through different heat treatment processes, and their corrosion behaviour were investigated via immersion test. The main conclusions which can be drawn from this study are:

- The fully martensitic S13Cr MSS exhibited slower degradation of the native passive film due to its more homogeneous elemental distribution.
- During the middle corrosion stage, localized preferential corrosion on the fully martensitic S13Cr MSS occurred as

randomly distributed pitting. In contrast, for specimens containing reversed austenite, localized preferential corrosion initiated in the martensitic matrix surrounding the austenite particles.

- The increase in austenite content from 0% to 17.8% raised the overall corrosion rate by approximately 35% (from 0.83 mm/y to 1.11 mm/y), which is attributed to the galvanic effect between austenite particles and martensite matrix. However, the change in austenite content did not significantly change the structure and composition of the corrosion product film.

10.2. Recommendations for future work

This research project lays the foundation for a series of subsequent studies aimed at further consolidating the understanding proposed in the current work.

10.2.1. Observation of the native passive film degradation process

Understanding the degradation process of the native passive film is crucial for comprehending the corrosion of S13Cr MSS in HTHP environments. However, direct observation of this quick process remains a challenge due to the extreme test conditions. Establishing an oxygen-free environment for sample collection and transfer after the immersion test to strictly control the oxygen content during these processes to enable the quasi-in-situ analysis of the native passive film. This will allow the observation of the degradation process of native passive film and the initial formation of the corrosion products at different locations on the specimen surface (e.g., the martensite matrix surrounding austenite, the austenite and scratch), and will help to deepen the understanding of the degradation and transformation process of the native passive film under HTHP downhole environments.

10.2.2. Numerical simulation of galvanic corrosion behaviour at the steady-state corrosion stage

Establishing a numerical model for steady-state corrosion at the late stage of corrosion to simulate the galvanic corrosion behaviour between the austenite and the martensite matrix under different corrosion environments (such as temperature, CO_2 partial pressure, pH, etc.). To predict the corrosion rate of S13Cr MSS at the steady-state corrosion stage in different corrosion environments based on this model. By altering the content, shape, and distribution characteristics of the austenite particles to further understand the role of austenite in the corrosion process of S13Cr MSS under HTHP downhole environments based on numerical model.

10.2.3. Corrosion evolution under full lifecycle conditions

During the oil and gas exploitation process, the corrosion environments that tubing faces are not only formation brine but may also be the alternating impact of operating conditions such as acidizing operations (acidizing fluid) and flowback (returned acidizing fluid). The corrosion behaviour of S13Cr MSS in acidizing fluids and returned acidizing fluids, as well as the evolution of the corrosion product film under the alternating working conditions of " acidizing fluid-returned acidizing fluid-formation brine" within a single operation cycle, deserve equal attention.

10.2.4. Material optimization based on microstructural control

10.2.4.1. Construction of an austenitic network

Austenite has been proved to be able to retain in the corrosion product film at the steady-state corrosion stage under HTHP downhole environments. The strategy of forming a continuous network of a more corrosion-resistant second phase to improve the corrosion resistance of materials has been used in Mg alloys and Al alloys. Therefore, forming a continuous austenitic network that act as an effective barrier to hinder the corrosion is a potentially effective material modification strategy. This hypothesis remains to be confirmed by subsequent heat treatment strategy adjustment combining with corrosion evaluation.

10.2.4.2. Grain boundary engineering and segregation control

Pure martensitic S13Cr MSS, due to its homogeneous chemical composition, has been confirmed to exhibit better corrosion resistance than reversed austenite-containing S13Cr MSS in terms of both native passive film degradation speed and steady-state corrosion rate. However, pure martensitic stainless steel lacks sufficient toughness and resistance to hydrogen embrittlement. Therefore, optimizing mechanical properties of S13Cr MSS by introducing austenite is necessary. It is able to apply grain boundary engineering and segregation control to eliminate the Cr depletion zone at the phase boundaries and promote the homogenization of the material composition while forming austenite. This aims to weaken the galvanic effect caused by phase differences, thereby achieving an excellent corrosion resistance of S13Cr MSS while introduce austenite.

10.2.4.3. Data-driven material optimization

The composition and morphology of austenite obtained through different heat treatment processes, as well as the size of the elemental depletion zone around it, will affect the austenite-martensite galvanic effect, thereby influencing the corrosion rate of S13Cr MSS. In the meantime, they will also affect the mechanical properties and hydrogen embrittlement resistance of S13Cr MSS.

A further study could obtain austenite with different volume fractions, compositions, sizes, shapes and distribution characteristics through small-batch combinations of different heat treatment conditions. By performing quantitative descriptions of the austenite features such as volume fraction, morphology, composition, etc., and obtaining the material's mechanical properties, corrosion rate, and hydrogen embrittlement resistance, a database is constructed. A heat treatment process- microstructure/composition-corrosion performance/mechanical property prediction model can be developed with machine learning based upon this database. Finally, multi-objective optimization can be used to obtain the optimal heat treatment strategy.

11. Chapter 11 Reference

1. Piccolo, E.L., et al., Corrosion and Environmental Cracking Evaluation of High Density Brines for Use in HPHT Fields, in *SPE High Pressure/High Temperature Sour Well Design Applied Technology Workshop*. 2005, Society of Petroleum Engineers: The Woodlands, Texas, USA. p. 12.
2. John David Downs and H. Leth-Olsen, Effect of Environmental Contamination on the Susceptibility of Corrosion Resistant Alloys to Stress Corrosion Cracking in High-Density Completion Brines, in *SPE International Oilfield Corrosion Symposium*. 2006, Society of Petroleum Engineers: Aberdeen, UK. p. 6.
3. Koch, G., et al., NACE international impact report: International measures of prevention, application, and economics of corrosion technologies study, in *NACE Int., Houston, TX, USA, Tech. Rep*. 2016, NACE Int.: Houston, TX, USA.
4. Wang, Z., et al., Status, trends and enlightenment of global oil and gas development in 2021. *Petroleum Exploration and Development*, 2022. **49**(5): p. 1210-1228.
5. IEA, World Energy Outlook 2023, in *IEA, Paris https://www.iea.org/reports/world-energy-outlook-2023, report*. 2023, IEA: Paris.
6. Fridleifsson, I.B., et al. The possible role and contribution of geothermal energy to the mitigation of climate change. in *IPCC scoping meeting on renewable energy sources: Proceedings*. 2008. Intergovernmental Panel on Climate Change.
7. Belani, A. and S. Orr, A Systematic Approach to Hostile Environments. *Journal of Petroleum Technology*, 2008. **60**(07): p. 34-39.
8. Gautam, S., C. Guria, and V.K. Rajak, A state of the art review on the performance of high-pressure and high-temperature drilling fluids: Towards understanding the structure-property relationship of drilling fluid additives. *Journal of Petroleum Science and Engineering*, 2022. **213**: p. 110318.
9. Horne, R., et al., Enhanced geothermal systems for clean firm energy generation. *Nature Reviews Clean Technology*, 2025. **1**(2): p. 148-160.
10. IEA, The Future of Geothermal Energy, in *IEA, Paris https://www.iea.org/reports/the-future-of-geothermal-energy, report*. 2024, IEA: Paris.
11. Penot, C., D. Martelo, and S. Paul, Corrosion and Scaling in Geothermal Heat Exchangers. *Applied Sciences*, 2023. **13**(20): p. 11549.

12. Ueda, M., 2006 FN speller award lecture: development of corrosion-resistance alloys for the oil and gas industry—based on spontaneous passivity mechanism. *Corrosion*, 2006. **62**(10): p. 856-867.
13. Hoshowski, J., et al. The Development of Novel Corrosion Inhibitors for High Temperature Sour Gas Environments. in *CORROSION 2020*. 2020.
14. Sunaba, T., et al. Sour Service Limit of 17% Cr Stainless Steels Grades for OCTG. in *CORROSION 2021*. 2021.
15. S. Nesic, M.N., R. Nyborg and A. Strangeland, A Mechanistic Model for CO2 Corrosion with Protective Iron Carbonate Films, in *CORROSION 2001*. 2001, NACE International: Houston, Texas, USA. p. 28.
16. Zhao, Y., et al., Investigation of the rotation speed on corrosion behavior of HP-13Cr stainless steel in the extremely aggressive oilfield environment by using the rotating cage test. *Corrosion Science*, 2018. **145**: p. 307-319.
17. Zhao, Y., et al., Pourbaix diagram for HP-13Cr stainless steel in the aggressive oilfield environment characterized by high temperature, high CO2 partial pressure and high salinity. *Electrochimica Acta*, 2019. **293**: p. 116-127.
18. Xu, J., X. Wu, and E.-H. Han, The evolution of electrochemical behaviour and oxide film properties of 304 stainless steel in high temperature aqueous environment. *Electrochimica Acta*, 2012. **71**: p. 219-226.
19. Kuang, W., et al., Effect of alternately changing the dissolved Ni ion concentration on the oxidation of 304 stainless steel in oxygenated high temperature water. *Corrosion Science*, 2011. **53**(8): p. 2582-2591.
20. Zhang, H., Y.L. Zhao, and Z.D. Jiang, Effects of temperature on the corrosion behavior of 13Cr martensitic stainless steel during exposure to CO2 and Cl− environment. *Materials Letters*, 2005. **59**(27): p. 3370-3374.
21. Barker, R., et al., A review of iron carbonate (FeCO3) formation in the oil and gas industry. *Corrosion Science*, 2018. **142**: p. 312-341.
22. Kahyarian, A. and S. Nesic, On the mechanism of carbon dioxide corrosion of mild steel: Experimental investigation and mathematical modeling at elevated pressures and non-ideal solutions. *Corrosion Science*, 2020. **173**: p. 108719.
23. Jones, M., et al., Numerical exploration of a fully mechanistic mathematical model of aqueous CO2 corrosion in steel pipelines. *Corrosion Science*, 2024. **236**: p. 112235.
24. Alsalem, M.M., et al., Modelling of CO2 corrosion and FeCO3 formation in NaCl solutions. *Chemical Engineering Journal*, 2023. **451**: p. 138966.
25. J. O'M. Bockris, J.M., L. Nanis, The Hydrogen Evolution Kinetics and Hydrogen Entry into a-Iron. *Journal of The Electrochemical Society*, 1965. **112**(10): p. 7.

26. N. Pentland, J.O.M.B., E. Sheldon, Hydrogen Evolution Reaction on Copper, Gold, Molybdenum, Palladium, Rhodium, and Iron: Mechanism and Measurement Technique under High Purity Conditions. *Journal of The Electrochemical Society*, 1957. **104**(3): p. 13.
27. M. A. V. Devanathan, Z.S., The Mechanism of Hydrogen Evolution on Iron in Acid Solutions by Determination of Permeation Rates. *Journal of The Electrochemical Society*, 1964. **111**(5): p. 5.
28. Esmailzadeh, S., M. Aliofkhazraei, and H. Sarlak, Interpretation of Cyclic Potentiodynamic Polarization Test Results for Study of Corrosion Behavior of Metals: A Review. *Protection of Metals and Physical Chemistry of Surfaces*, 2018. **54**(5): p. 976-989.
29. Macdonald, D.D., Passivitythe key to our metals-based civilization. *Pure and Applied Chemistry*, 1999. **71**(6): p. 28.
30. Masouri D., Z.M., Mahdi A., Sulfide stress cracking of pipeline-case history Proceedings of the Corrosion 2008, New Orleans, NACE, 2008. Paper No 08480., in *CORROSION 2008*. 2008, NACE International: New Orleans, USA.
31. E., M., Introduction to corrosion science. 2010, New York, USA: Springer Science & Business Media.
32. Chao, C.Y., L.F. Lin, and D.D. Macdonald, A Point Defect Model for Anodic Passive Films: I . Film Growth Kinetics. *Journal of The Electrochemical Society*, 1981. **128**(6): p. 1187.
33. Macdonald, D.D., The history of the Point Defect Model for the passive state: A brief review of film growth aspects. *Electrochimica Acta*, 2011. **56**(4): p. 1761-1772.
34. Li, Y., et al., Point defect model for the corrosion of steels in supercritical water: Part I, film growth kinetics. *Corrosion Science*, 2020. **163**: p. 108280.
35. Verwey, E.J.W., Electrolytic conduction of a solid insulator at high fields The formation of the anodic oxide film on aluminium. *Physica*, 1935. **2**(1): p. 1059-1063.
36. Olsson, C.O.A. and D. Landolt, Passive films on stainless steels—chemistry, structure and growth. *Electrochimica Acta*, 2003. **48**(9): p. 1093-1104.
37. Olsson, C.O.A., D. Hamm, and D. Landolt, Evaluation of Passive Film Growth Models with the Electrochemical Quartz Crystal Microbalance on PVD Deposited Cr. *Journal of The Electrochemical Society*, 2000. **147**(11): p. 4093.
38. Bojinov, M., et al., Conduction Mechanism of the Anodic Film on Fe-Cr Alloys in Sulfate Solutions. *Journal of The Electrochemical Society*, 1999. **146**(9): p. 3238.

39. Bojinov, M., et al., Coupling between ionic defect structure and electronic conduction in passive films on iron, chromium and iron–chromium alloys. *Electrochimica Acta*, 2000. **45**(13): p. 2029-2048.
40. Robertson, J., The mechanism of high temperature aqueous corrosion of steel. *Corrosion Science*, 1989. **29**(11): p. 1275-1291.
41. Castle, J.E. and H.G. Masterson, The role of diffusion in the oxidation of mild steel in high temperature aqueous solutions. *Corrosion Science*, 1966. **6**(3): p. 93-104.
42. ASTM, ASTM F2129-08, Standard Test Method for Conducting Cyclic Potentiodynamic Polarization Measurements to Determine the Corrosion Susceptibility of Small Implant Devices. 2008, ASTM International: West Conshohocken, PA, USA. p. 9.
43. ASTM, ASTM G61-68, Standard Test Method for Conducting Cyclic Potentiodynamic Polarization Measurements for Localized Corrosion Susceptibility of Iron-, Nickel-, or Cobalt-Based Alloys. 2018, ASTM International: West Conshohocken, PA, USA. p. 5.
44. Wang, B., et al., Comparison of corrosion behavior of Al-Mn and Al-Mg alloys in chloride aqueous solution. *Materials and Corrosion*, 2016. **67**(1): p. 51-59.
45. Zhao, J., et al., Effect of surface passivation on corrosion resistance and antibacterial properties of Cu-bearing 316L stainless steel. *Applied Surface Science*, 2016. **386**: p. 371-380.
46. M. Atapour, H.S., M. Esmailzadeh, Pitting corrosion susceptibility of friction stir welded lean duplex stainless steel joints. *The International Journal of Advanced Manufacturing Technology*, 2016. **83**(5-8): p. 8.
47. Khamaj, J.A., Cyclic polarization analysis of corrosion behavior of ceramic coating on 6061 Al/SiCp composite for marine applications. *Protection of Metals and Physical Chemistry of Surfaces*, 2016. **52**(5): p. 886-893.
48. S. Nesic, J.P., S. Olsen, An Electrochemical Model for Prediction of Corrosion of Mild Steel in Aqueous Carbon Dioxide Solutions. *CORROSION*, 1996. **52**(4): p. 15.
49. C. de Waard, U.L., D. E. Milliams, Predictive Model for CO2 Corrosion Engineering in Wet Natural Gas Pipelines. *Corrosion*, 1991. **47**(12): p. 10.
50. A. Ikeda, S.M., M. Ueda, Corrosion Behavior of 9 to 25% Cr Steels in Wet CO2 Environments. *CORROSION*, 1985. **41**(4): p. 8.
51. Li, X., et al., Effect of extremely aggressive environment on the nature of corrosion scales of HP-13Cr stainless steel. *Applied Surface Science*, 2019. **469**: p. 146-161.

52. Yue, X., et al., Evolution and characterization of the film formed on super 13Cr stainless steel in CO2-saturated formation water at high temperature. *Corrosion Science*, 2019: p. 108277.
53. Bing Lei, Y.M., Yin Li, Effect of CO2 on Corrosion Behavior of 13Cr Stainless Steel in High Chlorine Environment, in *The 6th China Corrosion Conference*. 2011, Chinese Society for Corrosion and Protection Yingchuan, Ninxia, China.
54. Yuhua Sun, S.N., A parametric study and modeling on localized CO2 corrosion in horizontal wet gas flow, in *CORROSION 2004*. 2004, NACE International: New Orleans, Louisiana, USA. p. 24.
55. Sven M. Hesjevik, S.O., Marion Seiersten Corrosion at High CO2 Pressure, in *CORROSION 2003*. 2003, NACE International: San Diego, California, USA. p. 12.
56. R. Zhang, M.G.a.W.P.J., Development of a Mechanistic Model for Predicting Corrosion Rate in Multiphase Oil/Water Flows, in *CORROSION 1997*. 1997, NACE International: New Orleans, Louisiana, USA. p. 30.
57. Park, J.J.P., S.I.; Lee, W.J.; Kim, H.P., Effect of bicarbonate ion additives on pitting corrosion of type 316L stainless steel in aqueous 0.5 M sodium chloride solution. *Corrosion*, 1999. **55**(4): p. 9.
58. Xiaozhi Gong, J.X., Yu Zuo, Jingmao Zhao, Jingping Xiong, Effect of pH value on metastable pitting behaviour of stainless steel. *JOURNAL OF BEIJING UNIVERSITY OF CHEMICAL TECHNOLOGY(NATURAL SCIENCE EDITION)*, 2002. **29**(4): p. 4.
59. Chao Ye, N.D., Wenming Wen, Qing Zhao, Li Zhu, Effect of pH on Pitting Corrosion Process of 304 Stainless Steel in 3.5%NaCl Solution. *Journal of Chinese Society for Corrosion and protection*, 2015. **35**(1): p. 5.
60. Sun, H., et al., Effects of pH and dissolved oxygen on electrochemical behavior and oxide films of 304SS in borated and lithiated high temperature water. *Corrosion Science*, 2012. **59**: p. 334-342.
61. Kuang, W., et al., Microstructural characteristics of the oxide scale formed on 304 stainless steel in oxygenated high temperature water. *Corrosion Science*, 2010. **52**(11): p. 3654-3660.
62. Kahyarian, A., M. Singer, and S. Nesic, Modeling of uniform CO2 corrosion of mild steel in gas transportation systems: A review. *Journal of Natural Gas Science and Engineering*, 2016. **29**: p. 530-549.
63. Niu, L.-B. and K. Nakada, Effect of chloride and sulfate ions in simulated boiler water on pitting corrosion behavior of 13Cr steel. *Corrosion Science*, 2015. **96**: p. 171-177.
64. Zhang, B., et al., Unmasking chloride attack on the passive film of metals. *Nat Commun*, 2018. **9**(1): p. 2559.

65. Logan, H.L., Film-Rupture Mechanism of Stress Corrosion. *Journal of Research of the National Bureau of Standards*, 1952. **48**(2): p. 7.
66. Wuyang Chu, L.Q., Jingxu Li, Yanjing Su, et al., Hydrogen embrittlement and stress corrosion-foundation. 2013, Beijing, China: Science Publishing.
67. Sieradzki, K. and R.C. Newman, Brittle behavior of ductile metals during stress-corrosion cracking. *Philosophical Magazine A*, 2006. **51**(1): p. 95-132.
68. Sieradzki K, N.R.C., Stress-corrosion cracking. *Journal of physics and chemistry of solids*, 1987. **48**(11): p. 13.
69. V. S. Raja, T.S., Stress Corrosion Cracking-Theory and Practice. 2011, 80 High Street, Sawston, Cambridge CB22 3H.T, UK: Woodhead Publishing Limited.
70. E. Pugh, J.G., The role of cupric complex ions in the dissolution and stress-corrosion cracking of α-brass in nontarnishing aqueous ammonia. *Metallurgical and Materials Transactions B*, 1971. **2**(11): p. 6.
71. Jarmila, W. and K. Rolf, Damage due to hydrogen embrittlement and stresscorrosion cracking. *Engineering Failure Analysis*, 2000. **7**(6): p. 427-450.
72. Flanagan W F, B.P., Lichter B D.. A theory of transgranular stress-corrosion cracking. *Acta metallurgica et materialia*, 1991. **39**(4): p. 11.
73. A, J.D., A unified mechanism of stress corrosion and corrosion fatigue cracking. *Metallurgical transactions A*, 1985. **16**(6): p. 9.
74. P, L.S., A fractographic study of hydrogen-assisted cracking and liquid-metal embrittlement in nickel. *Journal of Materials science.*, 1986. **21**(2): p. 13.
75. Lynch, S.P., Metallographic contributions to understanding mechanisms of environmentally assisted cracking. *Metallography*, 1989. **23**: p. 24.
76. A, O.R., Hydrogen-the versatile embrittler. *Corrosion*, 1987. **43**(7): p. 8.
77. Lynch, S.P., Progress Towards Understanding Mechanisms Of Hydrogen Embrittlement And Stress Corrosion Cracking, in *CORROSION 2007*. 2007, NACE International: Nashville, Tennessee, USA. p. 55.
78. Song, Y.Y., et al., Formation of the reversed austenite during intercritical tempering in a Fe–13%Cr–4%Ni–Mo martensitic stainless steel. *Materials Letters*, 2010. **64**(13): p. 1411-1414.
79. Zhang, S., et al., Investigation of the evolution of retained austenite in Fe–13%Cr–4%Ni martensitic stainless steel during intercritical tempering. *Materials & Design*, 2015. **84**: p. 385-394.
80. Escobar, J.D., et al., Compositional analysis on the reverted austenite and tempered martensite in a Ti-stabilized supermartensitic stainless

steel: Segregation, partitioning and carbide precipitation. *Materials & Design*, 2018. **140**: p. 95-105.
81. Niessen, F., Austenite reversion in low-carbon martensitic stainless steels – a CALPHAD-assisted review. *Materials Science and Technology*, 2018. **34**(12): p. 1401-1414.
82. Schaeffler, A., Welding dissimilar metals with stainless electrodes. *Iron Age*, 1948. **162**(7): p. 72-79.
83. Tolchard, J.R., et al., On the measurement of austenite in supermartensitic stainless steel by X-ray diffraction. *Materials Characterization*, 2015. **99**: p. 238-242.
84. Zou, D.-n., et al., Influence of Tempering Process on Mechanical Properties of 00Cr13Ni4Mo Supermartensitic Stainless Steel. *Journal of Iron and Steel Research International*, 2010. **17**(8): p. 50-54.
85. Cobb, H.M., The history of stainless steel. 2010: ASM International. 5.
86. Caldwell, E., H. Zhang, and L. Goodman. A selection methodology for 13Cr-Type alloy oil country tubular goods. in *SPE International Oilfield Corrosion Conference and Exhibition*. 2014. OnePetro.
87. Katsumi Masamura, Y asuto Inohara, and Y.u. Minami. Effect of C and N on Corrosion Resistance of High Cr alloys in CO2 and H2S Environments. in *Corrosion 98*. 1998. OnePetro.
88. Monnot, M., et al., Molybdenum effect on the Sulfide Stress Corrosion of a super martensitic stainless steel in sour environment highlighted by Electrochemical Impedance Spectroscopy. *Electrochimica Acta*, 2017. **252**: p. 58-66.
89. Kimura, M., et al., Corrosion resistance of high-strength modified 13% Cr steel. *Corrosion*, 1999. **55**(8): p. 756-761.
90. Tsuchiyama, T., et al., Quenching and partitioning treatment of a low-carbon martensitic stainless steel. *Materials Science and Engineering: A*, 2012. **532**: p. 585-592.
91. Leem, D.-S., et al., Amount of retained austenite at room temperature after reverse transformation of martensite to austenite in an Fe–13% Cr–7% Ni–3% Si martensitic stainless steel. *Scripta materialia*, 2001. **45**(7): p. 767-772.
92. Schnitzer, R., et al., Reverted austenite in PH 13-8 Mo maraging steels. *Materials Chemistry and Physics*, 2010. **122**(1): p. 138-145.
93. Villa, M., F. Niessen, and M.A.J. Somers, In Situ Investigation of the Evolution of Lattice Strain and Stresses in Austenite and Martensite During Quenching and Tempering of Steel. *Metallurgical and Materials Transactions A*, 2018. **49**(1): p. 28-40.
94. Ishida, K., Calculation of the effect of alloying elements on the Ms temperature in steels. *Journal of Alloys and Compounds*, 1995. **220**(1): p. 126-131.

95. Wu, W., et al., The relationship between alloying elements and retained austenite in martensitic stainless steel welds. *Scripta Materialia*, 2000. **42**(11): p. 1071-1076.
96. Tsai, M.C., et al., Phase transformation in AISI 410 stainless steel. *Materials Science and Engineering: A*, 2002. **332**(1): p. 1-10.
97. Bojack, A., et al., In-situ determination of austenite and martensite formation in 13Cr6Ni2Mo supermartensitic stainless steel. *Materials Characterization*, 2012. **71**: p. 77-86.
98. Bojack, A., et al., Austenite Formation from Martensite in a 13Cr6Ni2Mo Supermartensitic Stainless Steel. *Metallurgical and Materials Transactions A*, 2016. **47**(5): p. 1996-2009.
99. Song, Y., et al., The influence of tempering temperature on the reversed austenite formation and tensile properties in Fe–13%Cr–4%Ni–Mo low carbon martensite stainless steels. *Materials Science and Engineering: A*, 2011. **528**(12): p. 4075-4079.
100. Lee, Y.-K., et al., Reverse transformation mechanism of martensite to austenite and amount of retained austenite after reverse transformation in Fe-3Si-13Cr-7Ni (wt-%) martensitic stainless steel. *Materials science and technology*, 2003. **19**(3): p. 393-398.
101. Yuan, W.-h., et al., Microstructure evolution and precipitation behavior of 0Cr16Ni5Mo martensitic stainless steel during tempering process. *Journal of Iron and Steel Research International*, 2016. **23**(4): p. 401-408.
102. Song, Y., et al., Reversed austenite in 0Cr13Ni4Mo martensitic stainless steels. *Materials Chemistry and Physics*, 2014. **143**(2): p. 728-734.
103. Niessen, F., et al., Formation and stabilization of reverted austenite in supermartensitic stainless steel. *Metallurgical Research & Technology*, 2018. **115**(4): p. 402.
104. Park, E.S., et al., Formation of reversed austenite during tempering of 14Cr−7Ni−0.3Nb−0.7Mo−0.03C super martensitic stainless steel. *Metals and Materials International*, 2004. **10**(6): p. 521-525.
105. Song, Y.Y., et al., Reversed austenite in 0Cr13Ni4Mo martensitic stainless steels. *Materials Chemistry and Physics*, 2014. **143**(2): p. 728-734.
106. NAKAGAWA∗, H. and T. MIYAZAKI, Effect of retained austenite on the microstructure and mechanical properties of martensitic precipitation hardening stainless steel. *Journal of Materials science.*, 1991(34): p. 8.
107. Tabatabae, B.A., F. Ashrafizadeh, and A.M. Hassanli, Influence of retained austenite on the mechanical properties of low carbon martensitic stainless steel castings. *ISIJ international*, 2011. **51**(3): p. 471-475.

108. Wang, P., et al., Advantageous Implications of Reversed Austenite for the Tensile Properties of Super 13Cr Martensitic Stainless Steel. *Materials (Basel)*, 2022. **15**(21).
109. Zhao, Y., et al., Clarify the effect of reversed austenite on the pitting corrosion resistance of super 13Cr martensitic stainless steel. *Corrosion Science*, 2023. **213**: p. 110992.
110. Wang, P., et al., Prominent role of reversed austenite on corrosion property of super 13Cr martensitic stainless steel. *Journal of Materials Research and Technology*, 2023. **22**: p. 1753-1767.
111. Carvalho, R.N., et al., Effect of microstructure on the pitting susceptibility of a martensitic-ferritic stainless steel: A corrosion-metallurgical study. *Corrosion Science*, 2022. **202**: p. 110277.
112. Santos, I.G.R., et al., Corrosion resistance of UNS S41426 stainless steel in acid media and its relation to chemical partition and austenite fraction. *Corrosion Science*, 2021. **188**: p. 109519.
113. Mitsuo, K., et al., Effect of Retained Austenite on Corrosion Performance for Modified 13% Cr Steel Pipe. *Corrosion*, 2001. **57**(5): p. 7.
114. Lei, X., et al., Impact of Reversed Austenite on the Pitting Corrosion Behavior of Super 13Cr Martensitic Stainless Steel. *Electrochimica Acta*, 2016. **191**: p. 640-650.
115. Man, C., et al., Beneficial effect of reversed austenite on the intergranular corrosion resistance of martensitic stainless steel. *Corrosion Science*, 2019. **151**: p. 108-121.
116. Zhao, Y., et al., Assessment of the correlation between M23C6 precipitates and pitting corrosion resistance of 0Cr13 martensitic stainless steel. *Corrosion Science*, 2021. **189**: p. 109580.
117. Bonagani, S.K., V. Bathula, and V. Kain, Influence of tempering treatment on microstructure and pitting corrosion of 13 wt.% Cr martensitic stainless steel. *Corrosion Science*, 2018. **131**: p. 340-354.
118. Abbasi-Khazaei, B. and A. Mollaahmadi, Rapid Tempering of Martensitic Stainless Steel AISI420: Microstructure, Mechanical and Corrosion Properties. *Journal of Materials Engineering and Performance*, 2017. **26**(4): p. 1626-1633.
119. Wang, L., et al., The effect of η-Ni3Ti precipitates and reversed austenite on the passive film stability of nickel-rich Custom 465 steel. *Corrosion Science*, 2019. **154**: p. 178-190.
120. Zhao, Y., et al., Influence of microstructure on the corrosion behavior of super 13Cr martensitic stainless steel under heat treatment. *Materials Characterization*, 2021. **175**: p. 111066.
121. Lo, K.H., C.H. Shek, and J.K.L. Lai, Recent developments in stainless steels. *Materials Science and Engineering: R: Reports*, 2009. **65**(4): p. 39-104.

122. He, J., et al., Hydrogen embrittlement behavior of 13Cr-5Ni-2Mo supermartensitic stainless steel. *Corrosion Science*, 2020. **176**: p. 109046.
123. He, J., et al., A novel 13Cr austenitic stainless steel with excellent mechanical properties and high hydrogen embrittlement resistance via heterostructure and TRIP effects. *Materials Science and Engineering: A*, 2020. **793**: p. 139835.
124. Li, X., et al., Effect of aging treatment on hydrogen embrittlement of PH 13-8 Mo martensite stainless steel. *Materials Science and Engineering: A*, 2016. **651**: p. 474-485.
125. Yang, J., et al., Effect of retained austenite on the hydrogen embrittlement of a medium carbon quenching and partitioning steel with refined microstructure. *Materials Science and Engineering: A*, 2016. **665**: p. 76-85.
126. Fan, Y.H., et al., The role of reversed austenite in hydrogen embrittlement fracture of S41500 martensitic stainless steel. *Acta Materialia*, 2017. **139**: p. 188-195.
127. Zhu, X., et al., Hydrogen trapping sites and hydrogen-induced cracking in high strength quenching & partitioning (Q&P) treated steel. *International Journal of Hydrogen Energy*, 2014. **39**(24): p. 13031-13040.
128. Park, Y., et al., Retained austenite as a hydrogen trap in steel welds. *Welding Journal-New York-*, 2002. **81**(2): p. 27-S.
129. Ueda, M., 2006 F.N. Speller Award Lecture: Development of Corrosion-Resistance Alloys for the Oil and Gas Industry—Based on Spontaneous Passivity Mechanism. *Corrosion*, 2006. **62**(10): p. 856-867.
130. Zhu, S.D., et al., Corrosion failure analysis of high strength grade super 13Cr-110 tubing string. *Engineering Failure Analysis*, 2011. **18**(8): p. 2222-2231.
131. Fu, A., et al., Stress corrosion cracking behavior of super 13Cr tubing in phosphate packer fluid of high pressure high temperature gas well. *Engineering Failure Analysis*, 2022. **139**: p. 106478.
132. Wang, L., et al., Enhancing the corrosion resistance of selective laser melted 15-5PH martensite stainless steel via heat treatment. *Corrosion Science*, 2020. **166**: p. 108427.
133. Henderson, J.D., et al., Molybdenum surface enrichment and release during transpassive dissolution of Ni-based alloys. *Corrosion Science*, 2019. **147**: p. 32-40.
134. Jiang, Z., et al., Relationship between Microstructure and Corrosion Behavior of Martensitic High Nitrogen Stainless Steel 30Cr15Mo1N at Different Austenitizing Temperatures. *Materials (Basel, Switzerland)*, 2017. **10**(8): p. 861.

135. Yue, X., et al., Evolution and characterization of the film formed on super 13Cr stainless steel in CO2-saturated formation water at high temperature. *Corrosion Science*, 2020. **163**: p. 108277.
136. Kimura, M., et al. Corrosion Resistance Of Martensitic Stainless Steel OCTG In Hightemperature And High CO2 Environment. in *CORROSION 2004*. 2004.
137. Ishiguro, Y., et al., Enhanced corrosion-resistant stainless steel OCTG of 17Cr for sweet and sour environments. *NACE - International Corrosion Conference Series*, 2013.
138. Moreira, R.M., et al., The effects of temperature and hydrodynamics on the CO2 corrosion of 13Cr and 13Cr5Ni2Mo stainless steels in the presence of free acetic acid. *Corrosion Science*, 2004. **46**(12): p. 2987-3003.
139. Wenting Cai, G.Z., Ailing Wei, The researchment of corrosion resistance of passive film on Super 13Cr and UNS N08028. *Petrochemical Industry Application*, 2011. **30**(2): p. 9.
140. Yue, X., et al., A thermodynamic and kinetic study of the formation and evolution of corrosion product scales on 13Cr stainless steel in a geothermal environment. *Corrosion Science*, 2020. **169**: p. 108640.
141. Yue, X., et al., Influence of a small velocity variation on the evolution of the corrosion products and corrosion behaviour of super 13Cr SS in a geothermal CO2 containing environment. *Corrosion Science*, 2021. **178**: p. 108983.
142. Lei, X.W., et al., Investigation of stress corrosion cracking behavior of super 13Cr tubing by full-scale tubular goods corrosion test system. *Engineering Failure Analysis*, 2015. **50**: p. 62-70.
143. Ji, N., et al., Collapse failure analysis of S13Cr-110 tubing in a high-pressure and high-temperature gas well. *Engineering Failure Analysis*, 2023. **148**: p. 107187.
144. Zhang, Z., et al., Stress corrosion crack evaluation of super 13Cr tubing in high-temperature and high-pressure gas wells. *Engineering Failure Analysis*, 2019. **95**: p. 263-272.
145. Amaya, H., et al. Effect of Chromium and Molybedenum on Corrosion Resistance of Super 13Cr Martenistic Stainless Steel in CO2 Environment. in *CORROSION 98*. 1998.
146. Caldwell, E., H. Zhang, and L. Goodman, A Selection Methodology for 13Cr-Type Alloy Oil Country Tubular Goods, in *SPE International Oilfield Corrosion Conference and Exhibition*. 2014, Society of Petroleum Engineers: Aberdeen, Scotland, UK. p. 15.
147. Morana, R., et al. Environmental Cracking Performance Of Super Martensitic Stainless Steels “13-5-2” (Grades 110Ksi And 125Ksi) For

Tubing Applications In High Chloride Reservoir Fluids Containing H2S/CO2. in *CORROSION 2010*. 2010.
148. Ngomo, V., et al. Environmental Cracking Performance of Super Martensitic Stainless Steels 13Cr In High Chloride Reservoir Fluids Containing H2S/CO2. in *CORROSION 2011*. 2011.
149. Zhao, J.-J., et al., Effect of Cl− Concentration on the SCC Behavior of 13Cr Stainless Steel in High-Pressure CO2 Environment. *Acta Metallurgica Sinica (English Letters)*, 2019. **32**(12): p. 1459-1469.
150. Yue, X., et al., Correlation between electrochemical properties and stress corrosion cracking of super 13Cr under an HTHP CO2 environment. *RSC Advances*, 2018. **8**(43): p. 24679-24689.
151. Qi, W., et al., Insight into the stress corrosion cracking of HP-13Cr stainless steel in the aggressive geothermal environment. *Corrosion Science*, 2021. **190**: p. 109699.
152. Yue, X., et al., The role of Cl- in the formation of the corrosion products and localised corrosion of 15Cr martensite stainless steel under an CO2-containing extreme oilfield condition. *Corrosion Science*, 2022. **194**: p. 109935.
153. G1-03, A., Standard practice for preparing, cleaning, and evaluating corrosion test specimens. ASTM International: West Conshohocken, PA.
154. TM0177, N., Laboratory Testing of Metals for Resistance to Sulfide Stress Cracking and Stress Corrosion Cracking in H2S. 2016, NACE International: Houston, Texas.
155. ASTM, ASTM G1-03, Standard Practice for Preparing, Cleaning, and Evaluating Corrosion Test Specimens. 2003, ASTM International: West Conshohocken, PA, USA. p. 9.
156. Preparation, Installation, Analysis, and Interpretation of Corrosion Coupons in Oilfield Operations. 2005, NACE International.
157. TM0198, N., Slow Strain Rate Test Method for Screening Corrosion-Resistant Alloys (CRAs) for Stress Corrosion Cracking in Sour Oilfield Service. 2020, NACE International: Houston, Texas.
158. Guo, S., et al., Corrosion of alloy steels containing 2% chromium in CO2 environments. *Corrosion Science*, 2012. **63**: p. 246-258.
159. Lee, H.B. and C. Jang, Short communication: “Effect of dissolved hydrogen on the early corrosion behavior of 316 stainless steel in simulated PWR environments”. *Journal of Nuclear Materials*, 2024. **591**: p. 154907.
160. Zhu, T., et al., Local scaling of CaCO3 on carbon steel surface with different corrosion types. *Powder Technology*, 2019. **356**: p. 990-1000.
161. Linter, B.R. and G.T. Burstein, Reactions of pipeline steels in carbon dioxide solutions. *Corrosion Science*, 1999. **41**(1): p. 117-139.

162. Eklund, G.S., Initiation of Pitting at Sulfide Inclusions in Stainless Steel. *Journal of The Electrochemical Society*, 1974. **121**(4): p. 467.
163. Tachibana, M., et al., Determining factors for anodic polarization curves of typical structural materials of boiling water reactors in high temperature – high purity water. *Journal of Nuclear Science and Technology*, 2012. **49**(2): p. 253-262.
164. De Motte, R., et al., A study by electrochemical impedance spectroscopy and surface analysis of corrosion product layers formed during CO2 corrosion of low alloy steel. *Corrosion Science*, 2020. **172**: p. 108666.
165. Yu, H.-C., et al., Simulation of the diffusional impedance and application to the characterization of electrodes with complex microstructures. *Electrochimica Acta*, 2020. **354**: p. 136534.
166. Boukamp, B.A., Derivation of a Distribution Function of Relaxation Times for the (fractal) Finite Length Warburg. *Electrochimica Acta*, 2017. **252**: p. 154-163.
167. Leem, D.-S., et al., Amount of retained austenite at room temperature after reverse transformation of martensite to austenite in an Fe–13%Cr–7%Ni–3%Si martensitic stainless steel. *Scripta Materialia*, 2001. **45**(7): p. 767-772.
168. Li, L., et al., Computational simulation of metastable pitting of stainless steel. *Electrochimica Acta*, 2009. **54**(26): p. 6389-6395.
169. Pistorius, P.C. and G.T. Burstein, Metastable pitting corrosion of stainless steel and the transition to stability. *Philosophical Transactions of the Royal Society of London, Series A: Physical and Engineering Sciences*, 1992. **341**(1662): p. 531-559.
170. Gutman, E.M., Mechanochemistry of materials. 1998: Cambridge Int Science Publishing.
171. Detriche, S., et al., XPS fast depth profile of the native oxide layers on AISI 304, 316 and 430 commercial stainless steels and their evolution with time. *Journal of Electron Spectroscopy and Related Phenomena*, 2020. **243**: p. 146970.
172. Wang, L., et al., Effect of microstructure on corrosion behavior of high strength martensite steel—A literature review. *International Journal of Minerals, Metallurgy and Materials*, 2021. **28**(5): p. 754-773.
173. Ye, H., et al., Visualization and simulation investigation of Copper-Nickel alloy and carbon steel galvanic corrosion in marine environment. *Journal of Electroanalytical Chemistry*, 2024. **953**: p. 118013.
174. Wang, Z., Z. Feng, and L. Zhang, Effect of high temperature on the corrosion behavior and passive film composition of 316 L stainless steel in high H2S-containing environments. *Corrosion Science*, 2020. **174**: p. 108844.

175. Cui, Z., et al., Influence of temperature on the electrochemical and passivation behavior of 2507 super duplex stainless steel in simulated desulfurized flue gas condensates. *Corrosion Science*, 2017. **118**: p. 31-48.
176. Bösing, I., Modeling electrochemical oxide film growth—passive and transpassive behavior of iron electrodes in halide-free solution. *npj Materials Degradation*, 2023. **7**(1): p. 53.
177. Feng, X., et al., Degradation of passive film on 304 stainless steel in a simulated concrete pore solution under alternating temperature condition. *Cement and Concrete Composites*, 2020. **112**: p. 103651.
178. Azimi, G. and V.G. Papangelakis, The solubility of gypsum and anhydrite in simulated laterite pressure acid leach solutions up to 250°C. *Hydrometallurgy*, 2010. **102**(1-4): p. 1-13.
179. Chen, T., et al., Thermodynamic modeling of calcium carbonate scale precipitation: aqueous Na+-Ca2+-Cl−-HCO3−-CO32−-CO2 system. *Fluid Phase Equilibria*, 2022. **552**: p. 113263.
180. Moghadasi, J., et al. Scale Formation in Oil Reservoir and Production Equipment during Water Injection (Kinetics of CaSO4 and CaCO3 Crystal Growth and Effect on Formation Damage). in *SPE European Formation Damage Conference*. 2003.
181. Levanyuk, O., et al. A 3-Year Results of Application a Combined Scale Inhibition and Hydraulic Fracturing Treatments using a Novel Hydraulic Fracturing Fluid, Russia. in *SPE International Conference on Oilfield Scale*. 2012.
182. Mansoori, H., et al., Influence of calcium and magnesium ions on CO2 corrosion of carbon steel in oil and gas production systems - A review. *Journal of Natural Gas Science and Engineering*, 2018. **59**: p. 287-296.
183. Plummer, L.N. and E. Busenberg, The solubilities of calcite, aragonite and vaterite in CO2-H2O solutions between 0 and 90°C, and an evaluation of the aqueous model for the system CaCO3-CO2-H2O. *Geochimica et Cosmochimica Acta*, 1982. **46**(6): p. 1011-1040.
184. Azimi, G. and V.G. Papangelakis, Mechanism and kinetics of gypsum–anhydrite transformation in aqueous electrolyte solutions. *Hydrometallurgy*, 2011. **108**(1-2): p. 122-129.
185. Luo, K., et al., Influence of temperature and solution composition on the formation of calcium sulfates. *Particuology*, 2010. **8**(3): p. 240-244.
186. Ruiz-Agudo, E., et al., Crystallographic Control in the Replacement of Calcite by Calcium Sulfates. *Crystal Growth & Design*, 2016. **16**(9): p. 4950-4959.
187. Cuesta Mayorga, I., et al., Epitactic Overgrowths of Calcite (CaCO3) on Anhydrite (CaSO4) Cleavage Surfaces. *Crystal Growth & Design*, 2018. **18**(3): p. 1666-1675.

188. Li, J. and Z. Duan, A thermodynamic model for the prediction of phase equilibria and speciation in the H2O–CO2–NaCl–CaCO3–CaSO4 system from 0 to 250°C, 1 to 1000 bar with NaCl concentrations up to halite saturation. *Geochimica et Cosmochimica Acta*, 2011. **75**(15): p. 4351-4376.
189. Xu, J., et al., Testing the cation-hydration effect on the crystallization of Ca-Mg-CO3 systems. *Proc Natl Acad Sci U S A*, 2013. **110**(44): p. 17750-5.
190. Alsaiari, H.A.A., A. Kan, and M.B.B. Tomson, Effect of Calcium and Iron (II) Ions on the Precipitation of Calcium Carbonate and Ferrous Carbonate. *SPE Journal*, 2010. **15**(02): p. 294-300.
191. Rizzo, R., et al., Corrosion of carbon steel under CO2 conditions: Effect of CaCO3 precipitation on the stability of the FeCO3 protective layer. *Corrosion Science*, 2020. **162**: p. 108214.
192. Navabzadeh Esmaeely, S., et al., Effect of Calcium on the Formation and Protectiveness of Iron Carbonate Layer in CO2 Corrosion. *Corrosion*, 2013. **69**(9): p. 912-920.
193. Hua, Y., et al., Protectiveness, morphology and composition of corrosion products formed on carbon steel in the presence of Cl−, Ca2+ and Mg2+ in high pressure CO2 environments. *Applied Surface Science*, 2018. **455**: p. 667-682.
194. Yue, X., L. Zhang, and Y. Hua, Fundamental insights into the stabilisation and chemical degradation of the corrosion product scales. *npj Materials Degradation*, 2021. **5**(1): p. 8.
195. Wang, C., et al., Anti-corrosion characteristics of FeCO3 and FexCayMgzCO3 scales on carbon steel in high-PT CO2 environments. *Chemical Engineering Journal*, 2022. **431**: p. 133484.
196. Nielsen, L.C., J.J. De Yoreo, and D.J. DePaolo, General model for calcite growth kinetics in the presence of impurity ions. *Geochimica et Cosmochimica Acta*, 2013. **115**: p. 100-114.
197. Tang, H., et al., Heterogeneous Nucleation and Growth of CaCO3 on Calcite (104) and Aragonite (110) Surfaces: Implications for the Formation of Abiogenic Carbonate Cements in the Ocean. *Minerals*, 2020. **10**(4): p. 294.
198. Zhu, G.Y., Y.Y. Li, and G.A. Zhang, Interaction between crevice and galvanic corrosion of X65 carbon steel in the CO2-saturated NaCl solution under the coupling of crevice and galvanic effects. *Journal of Electroanalytical Chemistry*, 2022. **918**: p. 116482.
199. Zuo, Y., H. Wang, and J. Xiong, The aspect ratio of surface grooves and metastable pitting of stainless steel. *Corrosion Science*, 2002. **44**(1): p. 25-35.

200. Wang, G., et al., Influence of Milling–Electrochemical Polishing on Corrosion Resistance of NiTi Shape Memory Alloy. *Micromachines*, 2022. **13**(12): p. 2204.
201. Daniel, E.F., et al., Synergistic effect of crevice corrosion and galvanic coupling on 304SS fasteners degradation in chloride environments. *npj Materials Degradation*, 2023. **7**(1): p. 11.
202. Kim, J.-G., et al., Effects of Flow Velocity, pH, and Temperature on Galvanic Corrosion in Alkaline-Chloride Solutions. *Corrosion*, 2003. **59**(2): p. 121-129.
203. Wei, L., et al., L21-strengthened face-centered cubic high-entropy alloy with well pitting resistance. *Corrosion Science*, 2023. **215**: p. 111043.
204. Li, W. and D.Y. Li, Variations of work function and corrosion behaviors of deformed copper surfaces. *Applied Surface Science*, 2005. **240**(1): p. 388-395.
205. Stanislaw, H. and D. Tomasz, Work functions of elements expressed in terms of the Fermi energy and the density of free electrons. *Journal of Physics: Condensed Matter*, 1998. **10**(48): p. 10815.
206. Ishii, R., et al., Work function of binary alloys. *Applied Surface Science*, 2001. **169-170**: p. 658-661.
207. Dai, C., et al., Tailoring the microstructural characteristic and improving the corrosion rate of Mg-Gd-Ni alloy by heat treatment with different volume fraction of LPSO phase. *Corrosion Science*, 2023. **210**: p. 110806.
208. Pan, H., et al., Effect of alloyed Sr on the microstructure and corrosion behavior of biodegradable Mg-Zn-Mn alloy in Hanks' solution. *Corrosion Science*, 2019. **157**: p. 420-437.